The Age and Character of Alteration and Mineralization at the Buckhorn

Gold Skarn, Okanogan County, Washington, USA


by


Brendan Alfred Scorrar


B.Sc., The University of Alberta, 2008


A THESIS SUBMITTED IN PARTIAL FULFILLMENT OF

THE REQUIREMENTS FOR THE DEGREE OF


MASTER OF SCIENCE

in

The Faculty of Graduate Studies

(Geological Sciences)


THE UNIVERSITY OF BRITISH COLUMBIA

(Vancouver)


August 2012

**Abstract**

Located in Okanogan County, Washington, USA the Buckhorn mine is one of the largest gold skarns in North America (2.15 Mt at 14 ppm Au).

Buckhorn is hosted in Permian Anarchist Group metasedimentary rocks and Jurassic Elise Formation metavolcanic rocks. Monzodiorite comagmatic with the metavolcanic rocks is Jurassic in age (192.4 Ma) confirming the correlation. Two suites of granitoids intrude the local stratigraphy. The Middle Jurassic (170.4 Ma) post-accretionary Buckhorn Intrusive Suite is genetically related to skarn alteration and gold mineralization and comprised of a granodiorite stock, marginal diorite, and several generations of dikes. The Eocene Roosevelt Intrusive Suite (50.5 Ma) is comprised of a small (~0.03 km$^2$) granodiorite stock that post-dates skarn alteration and gold mineralization.

Skarn alteration is zoned from dominantly magnetite-garnet in the proximal Magnetic Mine, to equal portions of magnetite-garnet-pyroxene in the Gold Bowl, and pyroxene dominated in the distal Southwest Ore-Zone. The Southwest Ore-Zone contains the majority of the gold mineralization and consists of massive calcic, Fe-rich, reduced skarn alteration along a low-angle shear zone at the contact between the carbonate metasedimentary rocks and the overlying metavolcanic rocks. Skarn alteration is divided into three categories based on the prograde mineralogy: pyroxene, garnet and magnetite skarn. Pyroxene skarn is further subdivided based on the retrograde mineralogy: amphibole-pyroxene, magnetite-pyroxene, and epidote-pyroxene skarn. Gold mineralization occurs in fractures in and intercrystalline space between skarn minerals and is intimately associated with bismuth. Re-Os geochronology of molybdenite bearing skarn confirms the Middle Jurassic age of skarn alteration and gold mineralization (162.8-165.5 Ma).

Based on the mineralogy, the hydrothermal fluids that caused prograde alteration were between 430-500° C, fO2=-25 to -20, fS2=-8 to -4.5, and near neutral pH. Fluids responsible for retrograde alteration were cooler (300-430° C), more reduced (fO2<-26), and had lower sulfur fugacity (fS2=-15 to -6). Gold mineralization occurred at the end of retrograde alteration. Gold was transported as bisulfide complexes in even cooler (241-300°C) and more reduced (fO2=-42 to -36) fluids than earlier retrograde alteration. Gold was scavenged by a bismuth melt and precipitated due to cooling and local retrograde oxidation reactions.

# Table of Contents

# List of Tables

# List of Figures

## List of Abbreviations

**Amph:**     Amphibole

**And:**     Andradite garnet

**Asp:**     Arsenopyrite

**Bdi:**     Buckhorn diorite

**BGdi:**     Buckhorn Granodiorite

**Bi:**     Native bismuth

**Bi Min:**     Bismuth bearing mineral other than native bismuth and bismuthinite

**Bio:**     Biotite

**BIS:**     Buckhorn Intrusive Suite

**Bis:**     Bismuthinite

**BMS:**     Buckhorn Mountain Sequence

**BMV:**     Buckhorn Mountain Volcanic Sequence

**BSE:**     Back scatter electrons

**Ca:**     Calcite

**Chl:**     Chlorite

**CL:**     Cathodoluminescence microscopy

**Cpy:**     Chalcopyrite

**EDiD:**     Early diorite dike

**EDS:**     Energy-Dispersive X-Ray Spectroscopy

**EMP:**     Electron microprobe

**Ep:**     Epidote

**Felds:**     Feldspar

**Fg:**     Fine-grained

**Fol:**     Foliation

**GDiD:**     Granodiorite dikes

**Hbl:**     Hornblende

**Hed:**     Hedenbergite pyroxene

**HFSE:**     High field strength elements

**HREE:**     Heavy Rare Earth Elements (Gadolinium to Lutetium)

**Hyd Fe-Sil:**     Hydrated Iron Silicate minerals such as Ekmanite $(Fe,Mg,Mn)_3(Si,Al)_4O_{10}(OH)_2$-$2(H_2O)$, Ferrostilpnomelane $K(Fe,Mg)_8Si_{10}Al_2O_{24}(OH)_3$-$2(H_2O)$, Greenalite $Fe_2Si_2O_5(OH)_4$, and Minnesotaite $(Fe,Mg)_3Si_4O_{10}(OH)_2$

**Ilm:**     Ilmenite

**K-Spar:**     Potassium feldspar

**LA-ICP-MS:**     Laser Ablation Inductively Coupled Plasma Mass Spectrometry

**Mag:**     Magnetite

**Mo:**     Molybdenite

**Pie:**     Piemontite

**Plag:**     Plagioclase feldspar

**Po:**     Pyrrhotite

**PPL:**        Plane polarized light in microscopy

**Px:**        Pyroxene

**Py:**        Pyrite

**QP dike:**        Quartz Porphyry Dike

**Qtz:**        Quartz

**RGDi:**        Roosevelt Granodiorite

**RIS:**        Roosevelt Intrusive Suite

**RL:**        Reflected plane polarized light in microscopy

**SEM:**        Scanning electron microscope

**Sphal:**        Sphalerite

**SWOZ:**        Southwest Ore-Zone

**XPL:**        Cross polarized light in microscopy

**Acknowledgements**

# Chapter 1.  Introduction

## 1.1  Rationale for Study

Skarn deposits that contain gold occur throughout the world in a variety of geologic settings, but the most well-understood are associated with reduced plutons that were emplaced into shallow levels of the earth's crust (Meinert, 2000). These reduced gold skarns are typified by the Nickel Plate deposit (Billingsley and Hume, 1941; Ettlinger et al., 1992; Ray and Dawson, 1994). Other examples of reduced gold skarns include Fortitude, USA (Meinert, 2000; Theodore et al., 1973; Wotruba et al., 1986), El Valle - Boinas and Carles, Rio Narcea district, Spain (Cepedal et al., 2000; Martin-Izard et al., 2000), and Buckhorn, USA (Gaspar, 2005). These deposits are characterized by early widespread hornfels alteration, intense calcic pyroxene-garnet metasomatic alteration, a reduced sulfide assemblage (Po>Py), and an Au-Bi-Te-As geochemical signature (Meinert, 2000), however, due to their relative rarity the variations between them are poorly understood.

Further research of reduced gold skarns is needed to better understand the geologic and geochemical characteristics of the skarn alteration and gold mineralization and determine the controls on alteration and mineralization. For example the Au-Bi-Te-As geochemical signature in gold skarns is well documented (Cepedal et al., 2006; Ettlinger et al., 1992; Meinert et al., 2005), but the relationship between gold mineralization and the major and trace elements is poorly documented. Additionally, the mechanism for gold precipitation in reduced gold skarns is ambiguous, and the role of bismuth and tellurium in the gold mineralization process is not established. It is also unclear if there is a continuum between reduced and oxidised gold skarns in terms of mineralogy and/or conditions of formation.

To this end the Buckhorn gold skarn is the subject of this research to determine the geologic, geochemical, and geochronological characteristics of the deposit. This research will lead to (1) a better defined deposit model for the Buckhorn gold skarn, (2) a better understanding of the variations in the classification, and (3) will aid in exploration for similar deposits in both new and mature districts. These goals are accomplished through a detailed petrographic study of the host rocks and local intrusive rocks complemented by a U-Pb geochronological study to determine their character and ages. The mineralogical and textural characteristics of skarn alteration are investigated with detailed optical petrography followed by targeted scanning electron microscopy (SEM) of the skarn alteration and electron microprobe (EMP) analysis of certain prograde and retrograde minerals. Geochemical

analysis of the skarn alteration complements the mineralogical and textural characterization, and Re-Os geochronology of rare molybdenite hosted in the skarn alteration is used to constrain its age.

## 1.2   Background

The Buckhorn gold skarn is located in Okanogan County in north-central Washington (48° 57' N, 118° 59' W) (Figure 1.1). It originally contained approximately 2.15 Mt at 14 ppm gold, for about 1 Moz contained gold (Cooper et al., 2008). It is owned and operated by Kinross Gold Corporation and is being mined underground at a rate of approximately 1,000 tons per day, for an expected 7 year mine life from 2008 to 2015 (Cooper et al., 2008).

Skarn alteration has been known to occur at Buckhorn since the early 1900's (Umpleby, 1911), but gold mineralization was not discovered until 1988 and the Southwest Ore-Zone (SWOZ), the largest ore body, was not discovered until 1992 (Cooper et al., 2008). Buckhorn has been the focus of numerous government, academic and industry studies through the years including the work of Broughton (1943), McMillen (1979), Moen (1980), Hickey(1990, 1992), Jones (1992), Gaspar (2005), Gaspar et al. (2008), and Cooper et al. (2008). The early studies (Pre 1988) focused on the mine scale stratigraphy and the iron-copper skarn mineralization located in the Magnetic Mine area. Hickey's work in the early 1990's focused on the skarn alteration and gold mineralization in the Gold Bowl, which currently makes up a subordinate portion of the economic gold mineralization. Buckhorn has been the subject of one academic study, Gaspar (2005), since the discovery of the SWOZ, but it was completed before the majority of the diamond drilling and any underground mining took place. For his PhD, Gaspar (2005) focused on the mineral chemistry and through microprobe analysis determined the composition of the skarn alteration minerals. Gaspar (2005) also completed an early description of the skarn alteration and gold mineralization. With the benefit of greater access to the SWOZ than the previous studies, due to additional drilling and underground mining, the current work is able to provide a more detailed and comprehensive study of the geologic, geochemical, and geochronological characteristics of the skarn alteration and gold mineralization.

**Figure 1.1:** (A) Simplified terrane map of the Canadian cordillera modified from Cauldron and Nelson (2011). (B) Simplified geologic map of the southern Canadian cordillera modified from Gaspar (2005) after Tripper et al. (1981), Wheeler and McFeely, (1991), Nelson and Colpron (2007), and Colpron and Nelson (2011).
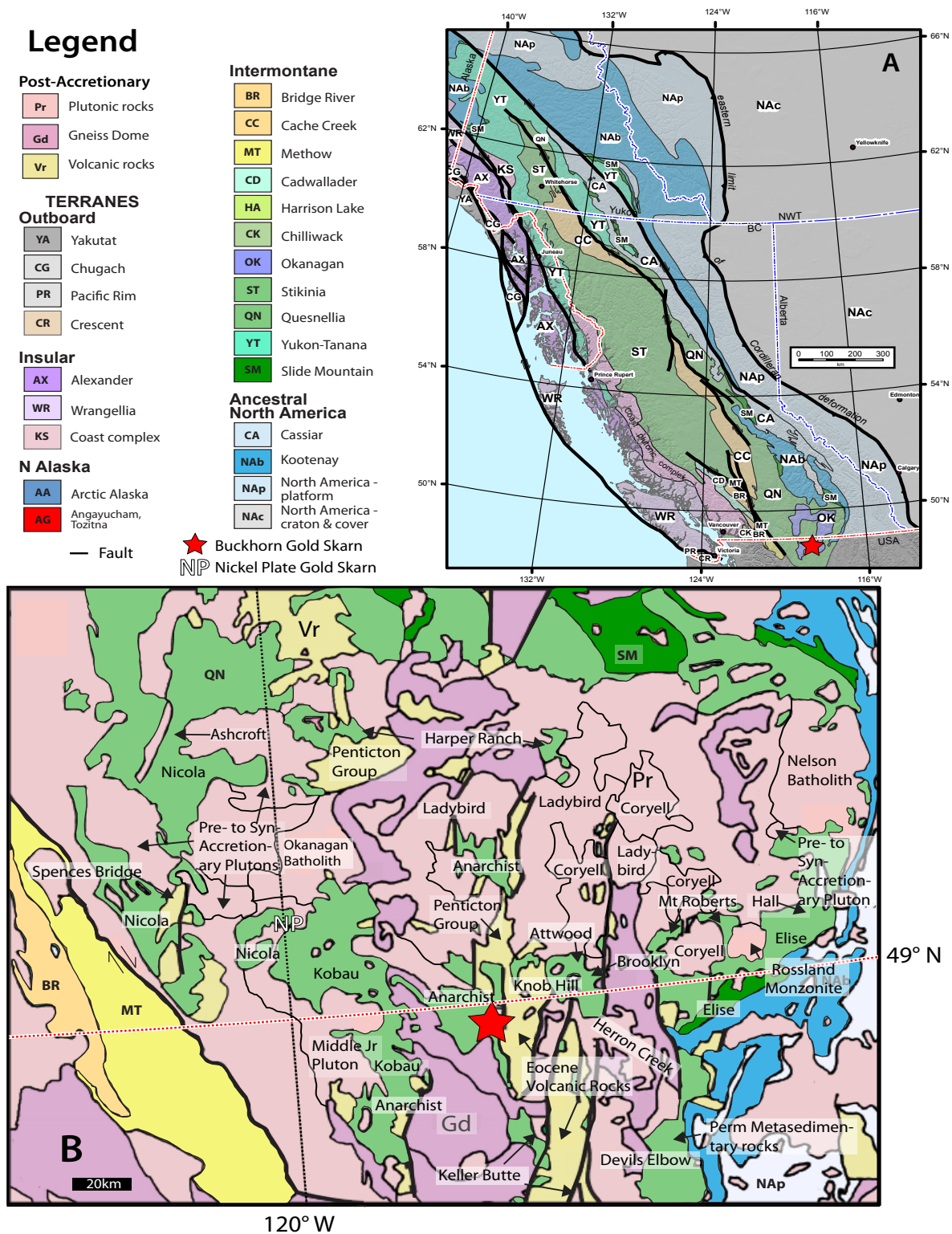
## 1.3  Thesis Objectives

This thesis aims to answer questions regarding the character, genesis, and age of skarn alteration and gold mineralization at Buckhorn that past studies left unanswered. It does this by focusing on two main questions.

(1) What is the geologic and geochemical character of skarn alteration and gold mineralization and what is their relationship to the host rocks, intrusive rocks, deformation, and metamorphism?

(2) How old are the host rocks and intrusive rocks? How old is the deformation, skarn alteration, and gold mineralization? The study also resolves confusion regarding the correlation of Buckhorn rocks with the regional stratigraphy.

Answering these questions helps construct an accurate deposit model for Buckhorn, which is compared to Nickel Plate and other gold skarns to determine how Buckhorn fits into the gold skarn deposit model. The refined Buckhorn deposit model can be used to improve exploration targeting for similar deposits around the world.

## 1.4  Thesis Organization

This thesis is arranged in seven chapters. Chapter 1 introduces the study and provides a brief history of the Buckhorn gold skarn.

Chapter 2 summarizes the tectonic evolution and geology of the southern Canadian cordillera, with particular attention paid to the Quesnel terrane that hosts Buckhorn. This summary is followed by a detailed description of the Buckhorn geology that focuses on the spatial and temporal relationships between the geologic units, metamorphism, deformation, and both skarn alteration and gold mineralization. This chapter provides context for the remainder of the thesis and correlates the Buckhorn rocks with the regional stratigraphy with the help of the geochronology presented in Chapter 3.

Chapter 3 presents a U-Pb geochronology study that aims to confirm the age of the metavolcanic host rocks and local intrusive rocks and to constrain the age of deformation and skarn alteration at Buckhorn. Chapter 3 also includes a Re-Os geochronology study of molybdenite-bearing skarn alteration to further constrain the age of skarn alteration and gold mineralization.

Chapter 4 presents detailed and thorough thin section and hand sample descriptions of the skarn alteration and gold mineralization at Buckhorn. Preliminary descriptions were done by Gaspar

(2005), but this study greatly benefits from additional drilling, and underground mining that has taken place since that study. This chapter focuses on characterizing the skarn alteration assemblages and settings of gold mineralization, and determining their relationship to each other, deformation and the local intrusions. Major element microprobe analysis of pyroxene and amphibole is included and complements the geologic characterization of the skarn alteration, and aims to determine any relationship between mineral composition and gold mineralization.

Chapter 5 characterizes the major, trace and Rare Earth Element geochemical signature of the host rocks, skarn alteration and gold mineralization, thus complementing the geologic descriptions and mineral geochemistry presented in Chapter 4. This chapter also includes a geochemical comparison of Buckhorn and other skarn deposits around the world to document the geochemical variation present and distinguish different types of skarn deposits.

Chapter 6 draws conclusions from the aforementioned work. It also presents ideas for future research and explains the implication regarding exploration for similar deposits.

Chapter 7 contains a summary of the theses. The chapters are followed by Appendix A and B that contain the results of the microprobe mineral analysis and the geochemical analysis respectively.

# Chapter 2.   Regional and Mine Scale Geology of the Buckhorn Mountain Gold Skarn

## 2.1   Introduction

The following work summarizes the regional geology and tectonic evolution of the southern Canadian cordillera, with particular attention paid to the Quesnel Terrane, which hosts the Buckhorn gold skarn. This provides geologic context for the remainder of the thesis and helps correlate the Buckhorn geology with the regional stratigraphy. The summary of the regional geology is followed by a detailed description of the Buckhorn geology that focuses on the relationships between the geologic units, deformation, alteration, and both skarn alteration and gold mineralization. Particular attention is paid to the regional geology because, while character of the mine scale geology is generally agreed upon, a consensus on its place in the regional stratigraphy has not been reached

## 2.2   Regional Geology

The Canadian cordillera is made up of tectonic blocks known as terranes that were accreted on to the North American continental margin during the Mesozoic (Figure 1.1). The tectonic evolution of the Canadian cordillera has been the subject of several review papers, (Monger and Price, 2002; Nelson and Colpron, 2007), which are summarized below.

The Canadian cordillera originated with the breakup of the supercontinent Rodinia in the Neoproterozoic, which lead to the development of a passive margin on the attenuated western margin of the North American craton (Monger and Price, 2002). The passive margin existed from about the Cambrian until the Middle Devonian, when a convergent inter-plate boundary formed off shore with subduction under the North American craton (Monger and Price, 2002). The Middle Devonian plate margin was characterized by a string of island arcs separated from North America by a back arc basin (Monger and Price, 2002). Sedimentary and volcaniclastic assemblages were deposited into this back arc basin, and they dominate the late Paleozoic rocks in the Quesnel Terrane (Nelson and Colpron, 2007). Accretion of the island arcs onto the North American craton started during the Middle Triassic and was completed by the Early Jurassic (Monger and Price, 2002). In the Quesnel Terrane the Middle Triassic is characterised by voluminous arc-related volcanic rocks with coeval and cogenetic plutons (Nelson and Colpron, 2007). Plutonism continued after accretion and new arcs were built on both the original continent and the newly accreted material (Monger and Price, 2002). The arc-related plutonic activity in the southern Canadian cordillera persisted until the Late Cretaceous when

there was a marked decline in activity (Nelson and Colpron, 2007). The tectonics of the southern Canadian cordillera changed in the Eocene from a compressional to transtensional environment. This changed resulted in strike-slip faults and volcanism that accompanied crustal extension, the exhumation of metamorphic core complexes, and the formation of volcano-sedimentary basins (Nelson and Colpron, 2007).

### 2.2.1 Quesnel Terrane

The Quesnel Terrane covers approximately 85,000 $km^2$, an area about the size of Ireland, from northern Washington State to the central Yukon (Figure 1.1).The Quesnel Terrane is made up of late Paleozoic to middle Mesozoic volcanic and sedimentary strata and plutonic rocks. On the east the Quesnel Terrane structurally and stratigraphically overlies the pericratonic Cassiar and Kootenay terranes and the dominantly oceanic Slide Mountain Terrane (Monger et al., 1991). Structurally to the west of the Quesnel Terrane is the Cache Creek Terrane, composed of rocks of an oceanic affinity (Monger et al., 1991).

The pre- to syn-accretionary strata of the Quesnel Terrane can be split into three main divisions: late Paleozoic assemblages, Early Mesozoic volcanic assemblages, and Jurassic sedimentary assemblages (Monger et al., 1991). Post-accretionary strata formed in the Cretaceous and Paleogene (Souther, 1991). The post-accretionary rocks include metamorphic core complexes that were exhumed in the Eocene (Kruckenberg et al., 2008). Plutonic activity in Quesnel Terrane can be split into four main magmatic episodes: Late Triassic to Early Jurassic, Middle to Late Jurassic, Cretaceous and Paleogene (Ghosh, 1995, and references therein). The description of the Quesnel Terrane that follows is compiled from the work of numerous authors (Beatty, 2003; Cheney et al., 1994; Dostal et al., 2001; Hoy and Dunne, 1997; Monger et al., 1991; Mortimer, 1987).

### 2.2.1.1 Late Paleozoic Assemblages

The late Paleozoic strata of the Quesnel Terrane in southern British Columbia and northern Washington are relatively poorly understood and have many local names. Monger et al. (1991) split them into the Okanagan and Harper Ranch Subterranes on the basis of the lithological assemblages. The Harper Ranch Group is the most complete example of the Harper Ranch Subterrane and is predominately made up of carbonate, siliciclastic and volcaniclastic rocks (Beatty, 2003; Monger et al., 1991). The Harper Ranch Group likely formed in an island arc and can been correlated with a number of other units including the Attwood and Anarchist Groups and the Mount Roberts Formation

(Beatty, 2003; Cheney et al., 1994; Hoy and Dunne, 1997). In Washington the Anarchist is made up of slate, metasiltstone, metasandstone, metalimestone, and metaconglomerate, with a Permian faunal assemblage (Rinehart and Fox, 1972). The Okanagan Subterrane is made up of limestone, greenstone, chert and ultramafic bodies that were likely formed in an oceanic or marginal basin setting (Monger et al., 1991). Hoy and Dunne (1997) include the ophiolites and greenstones of the Knob Hill and Kobau Groups of the Greenwood area in the Okanagan Subterrane. Although treated as separate units the relationship between the two Subterranes is unclear (Monger et al., 1991).

### 2.2.1.2 Early Mesozoic Volcanogenic Assemblages

Unconformably overlying the late Paleozoic strata is an extensive assemblage of early Mesozoic volcanogenic rocks (Monger et al., 1991). This assemblage is characterized by the Nicola Group which is composed of Late Triassic and Early Jurassic volcanic and sedimentary rocks that are intruded by co-magmatic plutons (Monger et al., 1991). Geochemical analysis shows that the Nicola Group volcanic rocks become more alkaline to the east indicating that they formed in a west-facing volcanic island arc (Monger et al., 1991). The Nicola Group also has increasing sedimentary input to the east, locally grading into a sedimentary sequence of argillite and siltstone (Monger et al., 1991). The Nicola Group can be correlated with the Triassic Brooklyn Formation in the Greenwood area (Beatty, 2003) and the Jurassic Elise Formation in the Nelson-Rossland area (Cheney et al., 1994; Monger et al., 1991; Mortimer, 1987a). The Elise Formation is composed of mafic pyroclastic and epiclastic rocks, dominated by augite porphyry flows and lesser mafic tuff (Hoy and Dunne, 1997). Some authors do correlate the Triassic and Jurassic rocks and instead split the Jurassic volcanic rocks into a separate group (Beatty, 2003; Hoy and Dunne, 1997). Regardless of the exact correlations, the early Mesozoic strata of the Quesnel Terrane are dominated by arc-related volcanic and sedimentary rocks.

### 2.2.1.3 Jurassic Sedimentary Assemblages

Early to Middle Jurassic marine sedimentary rocks unconformably overly portions of the Nicola Group rocks and Early Mesozoic plutons (Monger et al., 1991). Lacking volcanic rocks, the sedimentary rocks are dominantly conglomerate, sandstone, shale and siltstone indicating that they were deposited in a post-arc marine basin (Hoy and Dunne, 1997; Monger et al., 1991). Facies analysis indicates that the sediments were deposited in a submarine fan with an eastern sediment source that included eroding granodiorite, diorite and syenite presumably from Early Mesozoic plutons (Monger et al., 1991). These sedimentary rocks have been classified as the Hall Formation in east and the Ashcroft Formation in the west (Hoy and Dunne, 1997; Monger et al., 1991). Ranging in age from Early

Pliensbachian to Bajocian (190-168 Ma) the Hall and Ashcroft Formations represent the last marine incursion onto the Quesnel Terrane (Monger et al., 1991).

**2.2.1.4 Post-Accretionary Cretaceous Assemblages**

In the southern Quesnel Terrane, the Spences Bridge Group dominates the Cretaceous post-accretionary assemblage (Souther, 1991). Made up of basaltic to rhyolitic lavas intercalated with volcaniclastic rocks the Spences Bridge Group is located near the western margin of the Quesnel Terrane (Thorkelson and Smith, 1989) where it unconformably overlies the Triassic Nicola Group and earlier Mesozoic plutonic rocks (Irving and Thorkelson, 1990). The Spences Bridge Group is Early Cretaceous (104 Ma) and was deposited in a terrestrial environment during a time of east dipping subduction (Irving and Thorkelson, 1990; Souther, 1991).

**2.2.1.5 Post-Accretionary Paleogene Assemblages**

In south-central British Columbia, Eocene volcanism in the Quesnel Terrane is characterized by the widespread calc-alkalic Kamloops Group and the alkaline Penticton Assemblage (Souther, 1991). The Kamloops Group is composed of volcanic and sedimentary rocks preserved in complex basins that are the surface expression of high angle reverse faults. Geochemical analysis of the Kamloops Group rocks indicates that they formed in a subduction related continental arc setting. A similar setting is proposed for the Penticton Group rocks to the south-east (Souther, 1991). The Penticton Group is primarily made up of highly alkaline lavas and breccias of the Marron Formation, which are equivalent to the 54 Ma to 48 Ma volcanic rocks of the Sanpoil Formation in north-east Washington State (Holder, 1989; Souther, 1991). The Eocene volcanism was coeval with regional extension related to dextral, transcurrent movement on the Northern Rocky Mountain Trench fault system (Holder, 1989, and references therein; Souther, 1991).

The volcanism and extension is also coeval with the age of exhumation of the Okanogan gneiss dome, one of many metamorphic core complexes in the Canadian cordillera (Kruckenberg et al., 2008). These metamorphic core complexes are comprised of Mesozoic and older, poly-deformed, high grade paragneiss and variably deformed Cretaceous and Eocene granitoid rocks (Gabrielse, 1991). The granitoids predominately occur in normal faults and shear zones associated with the core complexes. These faults and shears form a regional network that accommodated significant extension and formed the basins that host the Eocene volcanic rocks (Gabrielse, 1991).

**2.2.1.6 Late Triassic to Early Jurassic Plutonism**

Early Mesozoic plutonism in the Quesnel Terrane ranges from the Late Triassic to Early Jurassic (Ghosh, 1995). It is pre-accretionary and represents the roots of the Nicola Arc, and ranges from alkalic to calc-alkalic in composition (Ghosh, 1995). Examples include the Bromley batholiths, Mount Riordan stock and the Hedley intrusions; the latter is associated with local gold skarn mineralization (Ray and Dawson, 1994). Plutons of this age are also prospective for porphyry mineralization. Porphyry deposits associated with pre-accretionary plutonism include the Highland Valley and Copper Mountain mining districts, which are associated with the Guichon Creek Batholith and the Copper Mountain Stock respectively (Mortensen et al., 1995; Woodsworth et al., 1991). In other mining districts such as the Greenwood and Nelson-Rossland areas the Late Triassic to Early Jurassic intrusions are volumetrically minor and more mafic in composition (Fyles, 1990; Hoy and Dunne, 2001). Examples include a microdiorite from the Greenwood area that are interpreted as the intrusive equivalent of the Brooklyn Formation, and has a K-Ar age of 206±8 Ma (Church, 1986). In the Nelson-Rossland area examples include the Katie and Shaft monzogabbro plutons that are interpreted as sub-volcanic intrusions, comagmatic with the Early Jurassic Elise Formation (Hoy and Dunne, 2001). The plutons in the Nelson-Rossland area have not been dated, but they are expected to be Sinemurian (197 Ma to 190 Ma) the same age as the Elise formation (Hoy and Dunne, 1997).

**2.2.1.7 Middle to Late Jurassic Plutonism**

Middle to Late Jurassic plutonism in the Quesnel Terrane was syn- to post-accretionary, and it represents the continued subduction of the Cache Creek Ocean, and the obduction and onlap of the eastern side of the Quesnel Terrane onto the North American craton (Hoy and Dunne, 1997). The syn- to post-accretionary plutons display a general compositional trend through time from alkali through calc-alkalic to two mica granitoids (Woodsworth et al., 1991). Located north of Nelson, BC, the Kuskanax Suite intrusions represent the earliest Middle Jurassic magmatism (Ghosh, 1995). The Kuskanax is a homogenous leucocratic quartz-pyroxene monzonite batholith that has a minimum age of 173 ± 5 Ma (Woodsworth et al., 1991, and references therein). The widespread and economically important Nelson Suite intrusions are slightly younger than the Kuskanax suite (Woodsworth et al., 1991). The Nelson Intrusive Suite is made up of the Nelson, Bonnington and Trail batholiths, as well as numerous smaller stocks including the Rossland monzonite (Hoy and Dunne, 2001). The Nelson Intrusive Suite is made up of granodiorite with lesser diorite and granite, and ranges from coarse-grained equigranular to porphyritic (Ghosh, 1995; and references therein). These rocks were

emplaced during the Middle Jurassic (173 Ma to 160 Ma) in a continental arc setting and have undergone considerable crustal contamination (Ghosh, 1995; Hoy and Dunne, 2001). The Middle to Late Jurassic intrusive rocks are associated with a number of types of mineralization including porphyries, skarns and polymetallic veins along the borders of the Nelson Batholith, as well as molybdenite skarn and gold-copper veins that are related to the Rossland monzonite (Hoy and Dunne, 2001).

### 2.2.1.8 Cretaceous Plutonism

Cretaceous plutonism is abundant in the southern Canadian cordillera predominately forming west of the Quesnel Terrane and to a lesser extent within it (Woodsworth et al., 1991). Plutonism in the Quesnel Terrane is characteristically more felsic and peraluminous than the intrusions to the west and the dominant rock types are biotite or biotite-muscovite granite and granodiorite (Driver et al., 2000, and references therein). Examples of Cretaceous plutons in the south-eastern Quesnel Terrane include the White Creek, Bayonne, Okanagan Range and the Whatson batholiths (Ghosh, 1995; Hurlow and Nelson, 1993; Woodsworth et al., 1991). In the south-western Quesnel Terrane Cretaceous plutonism is represented by the Verde and Summers Creek stocks, which are leucogranites that cut the Early Cretaceous Spences Bridge Group, and have been interpreted as its hypabyssal equivalent (Ghosh, 1995; Woodsworth et al., 1991).

### 2.2.1.9 Paleogene Plutonism

Paleocene and Eocene plutonism is widespread in southern British Columbia and northern Washington State (Holder and McCarley Holder, 1988; Woodsworth et al., 1991). In British Columbia the most areally extensive are the Lady Bird Suite and the younger Coryell plutons. Rocks of the Ladybird Suite were emplaced between 62 and 52 Ma, possibly from a crustal source, and occur as late kinematic to post-kinematic, I-type biotite leucogranite plutons and batholiths (Carr, 1992). Rocks of the Ladybird suite are compositionally similar to the Keller Butte Suite of the Colville Batholith in Washington, and the two are correlated based on composition and tectonic setting (Carr, 1992; Holder, 1989; Holder and McCarley Holder, 1988). The Devils Elbow Suite was emplaced after the Ladybird/Keller Butte Suite and has an intermediate composition between the earlier Ladybird/Keller Butte Suite and the later Coryell Batholith (Holder and McCarley Holder, 1988). The Devils Elbow Suite has not been correlated with equivalent rocks in British Columbia, but Holder (1989) suggested that it is equivalent to the lower Sanpoil Formation and possibly the Marron Formation. The youngest major Eocene intrusive suite is the Coryell batholiths that are characterized by high-level alkaline porphyritic syenites and lesser granite, diorite and monzonite (Woodsworth et al., 1991). The Coryell

batholiths are genetically related to the wide spread Marron Formation rocks and equivalent to the Herron Creek Intrusive Suite in Washington State (Holder, 1989; Woodsworth et al., 1991).

## 2.3   Buckhorn Geology

The geology of the Buckhorn gold skarn has been described by numerous authors, (Cheney et al., 1994; Gaspar, 2005; Hickey, 1990, 1992; Jones, 1992; McMillen, 1979; Stoffel, 1990a, b) and is generally agreed upon. However, there are still aspects that are poorly understood including the timing of skarn alteration relative to the various intrusions, the age of deformation and its timing relative to skarn alteration, and the correlation of mine units with the regional stratigraphy. The understanding of the area is complicated by the fact that the Buckhorn host rocks have all undergone several stages of metamorphism, deformation and skarn alteration, which locally makes identifying their original character impossible. To address these points the following section presents a thorough description of the different mine scale geologic units followed by a summary of the metamorphism, deformation, and briefly of skarn alteration. The character of the skarn alteration is thoroughly described in Chapter 4.

The Buckhorn gold skarn is hosted in metamorphosed carbonate and clastic sedimentary rocks that are unconformably overlain by mafic volcanic flows and intruded by several felsic granitoid stocks and associated dikes (Figure 2.1 and Figure 2.2). This host stratigraphy occurs elsewhere in the southern Quesnel Terrane, for example in the Nelson-Rossland, Greenwood and Hedley areas (Cheney et al., 1994; Church, 1986; Fyles, 1990; Hoy and Dunne, 1997; Ray and Dawson, 1994). The Buckhorn stratigraphy is fault-bound on all sides, on the east by a major NNE normal fault that is the western boundary of the Eocene rocks that fill the Toroda Creek half graben (Suydam and Gaylord, 1997). To the west and north the Chesaw thrust places ophiolite rocks of the Permian Knob Hill Group are over the younger pelitic Buckhorn rocks (Cheney et al., 1994; Fyles, 1990). The southern edge of the Buckhorn rocks is defined by a detachment fault at the edge of the Okanogan metamorphic core complex (Cheney et al., 1994).
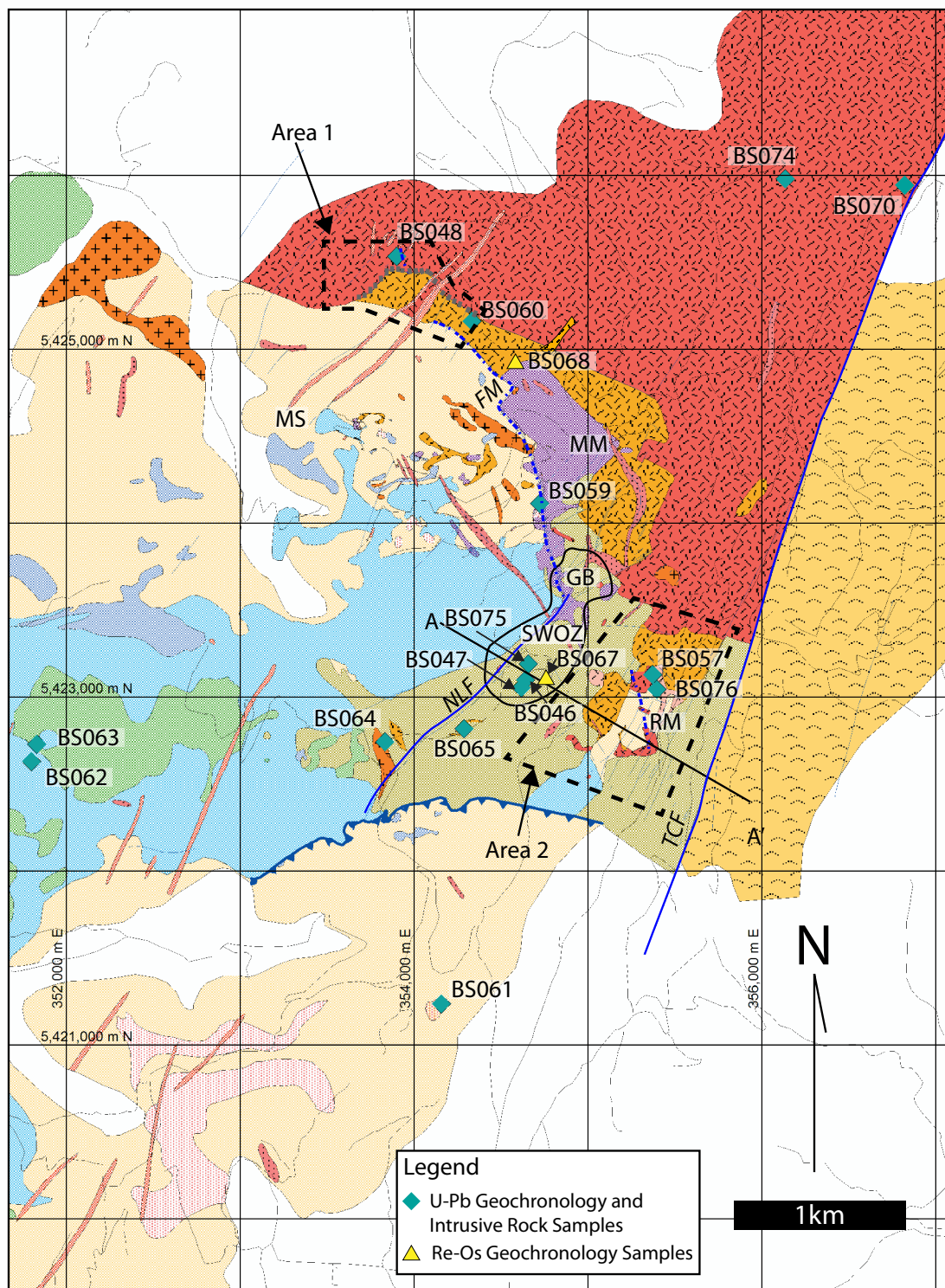
**Figure 2.1:** Geologic map of Buckhorn Mountain with sample locations highlighted. Based on data from this study (Areas 1 & 2), and modified from Kinross Gold Corporation maps. Coordinate system: UTM NAD27, Zone 11U. Map legend on following page.

## Sedimentary and Volcanic Rocks

### Volcanic Rocks

Challis Suite/Penticton group

### Buckhorn Mountain Volcanic Sequence (BMV)

Volcaniclastic rocks
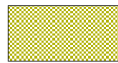
Volcanic flows and conglomerates

### Buckhorn Mountain Sequence (BMS)

Carbonate rocks

Mixed clastic-carbonate rocks

Metarhyolite

Clastic rocks

## Linear Features

——— Normal fault

▲▲▲ Thrust fault

----- Shear zone

⁓⁓⁓ Gradational Contact
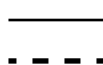
——— Deposit Outline
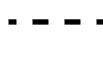
- - - Outline of area mapped for this study

## Locations

Southwest Ore-Zone (SWOZ)
Gold Bowl Ore-Zone (GB)
North Lookout Fault (*NLF*)
Footwall Mylonite (*FM*)

Toroda Creek Graben Fault (*TCF*)
Magnetite Mine (MM)
Roosevelt Mine (RM)
Mike's Skarn (MS)

## Intrusive Rocks

### Roosevelt Intrusive Suite

Roosevelt granodiorite

### Buckhorn Intrusive Suite

Quartz porphyry dikes

Granodiorite dikes

Buckhorn diorite

Buckhorn granodiorite

### BMV Intrusive Rocks

Equigranular intrusive

Porphyritic intrusive

## Mineralized Rocks

Skarn

**Figure 2.1 Continued:** Legend for the Geologic map of Buckhorn

14
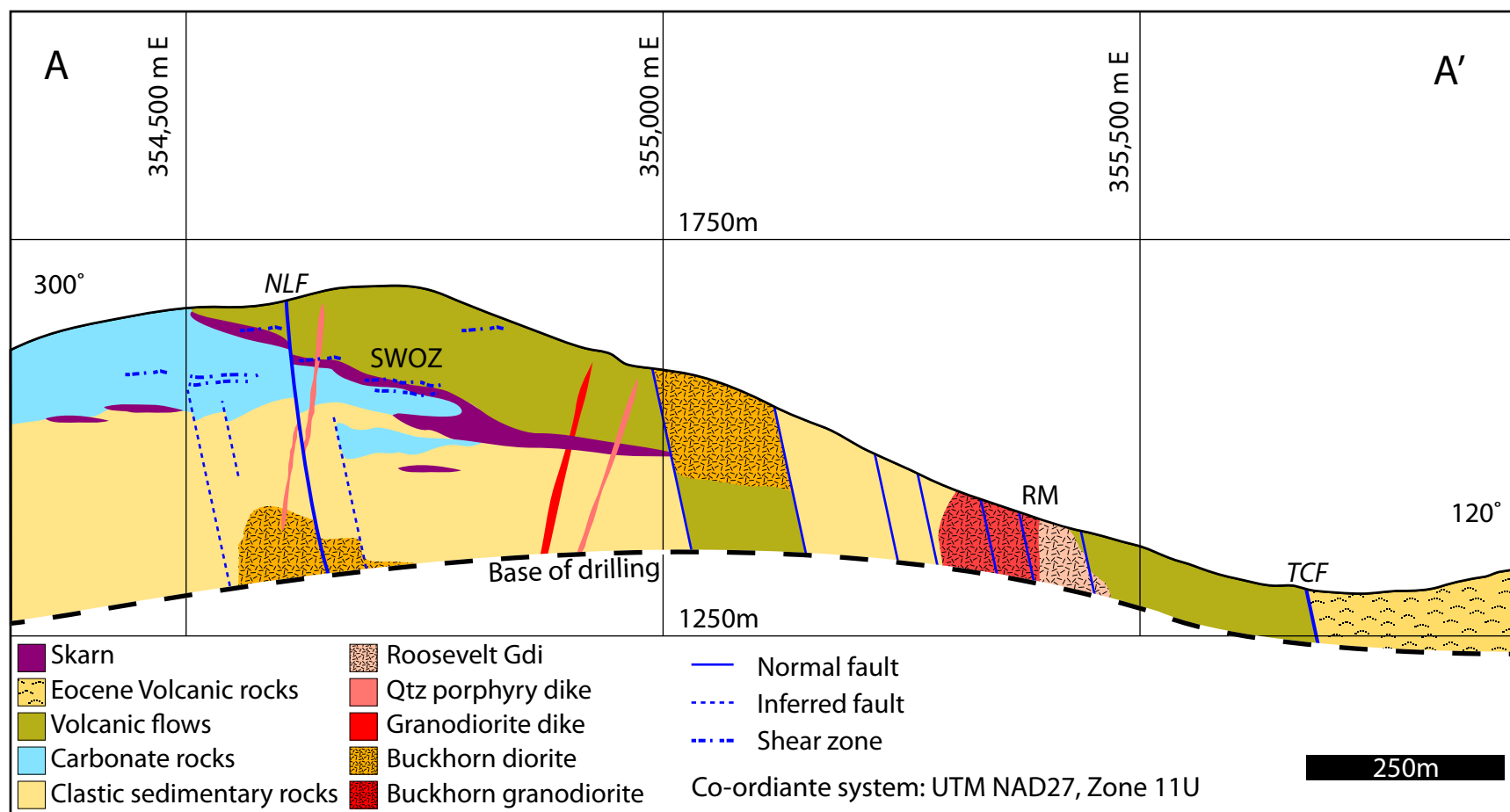
**Figure 2.2:** Geologic cross-section of the South-West Ore Zone and Roosevelt Mine area looking NNE. Based on data from this study and Kinross Gold Corporation drilling

### 2.3.1 Metasedimentary Rocks

Metasedimentary rocks are the oldest rocks in the local stratigraphy and have a thickness of at least 500 m. Locally known as the Buckhorn Mountain Sequence (BMS), the rocks are dominantly argillite, siltstone and lesser sandstone with rare conglomerate. The clastic sedimentary rocks are intercalated with volcaniclastic sedimentary rocks and capped by a carbonate dominated member (Figure 2.2).

Clastic rocks in the BMS were originally siltstones and sandstones, argillite with lesser black shale (McMillen, 1979). Greenschist facies metamorphism and later intense hornfels alteration masks the original sedimentary textures and minerals (Figure 2.3). The metasedimentary rocks are currently finely laminated to massive and range in colour from very dark brown to green to white (Figure 2.3). They are variably altered to epidote-zoisite-amphibole or biotite-chlorite-sericite assemblages, both with minor remnant quartz and lesser feldspar grains. The rocks have minor (<1%) disseminated magnetite and sulfides, predominately pyrrhotite and chalcopyrite, which may be associated with alteration of mafic minerals to amphibole.

The least abundant, but most recognizable sedimentary rocks in the BMS are the conglomerates, which mostly occur in the Gold Bowl area where they dip gently to the south-east. Based on drilling, the thickness of the conglomerates ranges from several metres up to 10's of metres. The conglomerates are heterolithic and texturally variable, and can be clast or matrix supported. The clasts are rounded to rarely subangular and range in size from 1 to >10 cm. The clasts are typically chert, but may also be igneous, volcanic or carbonate rocks. When altered, the clasts are usually replaced by an epidote-zoisite assemblage and mafic minerals in the matrix by chlorite (Figure 2.4).
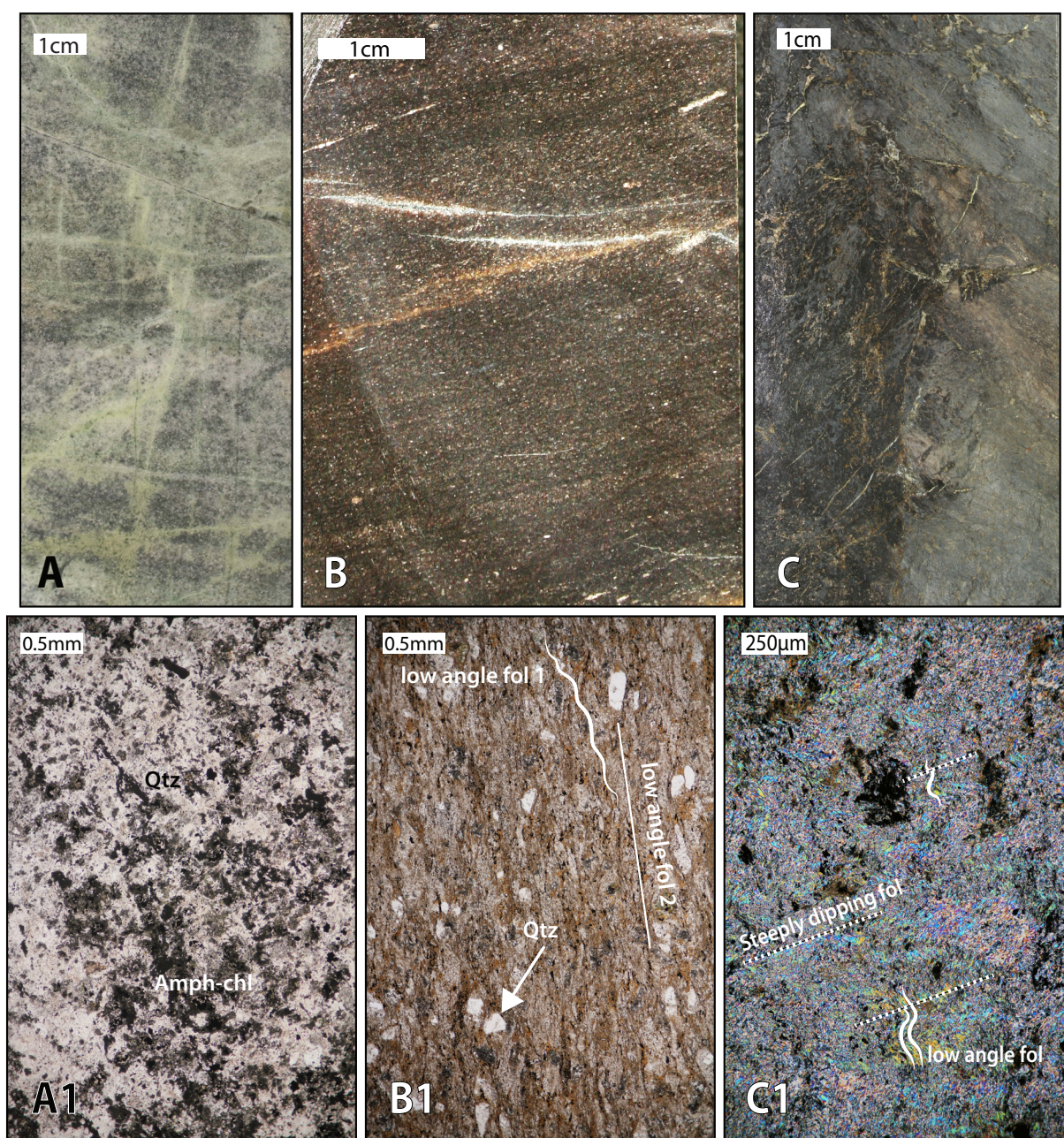
**Figure 2.3:** Examples of BMS metasedimentary rocks that have been variably hornfels altered that demonstrate its texture, mineralogy, and character and variation in alteration and deformation (A, B, and C hand samples; A1 and B1 PPL photomicrograph; C1 XPL photomicrograph). See text for further discussion.

**Figure 2.4:** Examples of the BMS conglomerate that demonstrate its texture, mineralogy, and character and variation in alteration and deformation. (A hand sample; A1 PPL photomicrograph) See text for further discussion.

The upper carbonate member of the BMS is a dark grey-blue to white calcic marble that is conformable with the underlying clastic sedimentary rocks (Figure 2.5). It is up to about 300 m thick, and crops out on the west side of Buckhorn Mountain, covering an area of approximately 4.5 km². It underwent nearly complete recrystallization during contact metamorphism followed by deformation and has a wide range of crystal sizes from 10 μm to over 3 cm. Smaller crystals usually occur in intensely strained portions whereas the very large crystals are in massive zones. A minor component of the upper carbonate member is fossiliferous, with crinoid stems being the most abundant fossil, however, fusulinids, ostracods, bivalves and coral have also been reported by other authors (Gaspar, 2005; Hickey, 1990; McMillen, 1979).
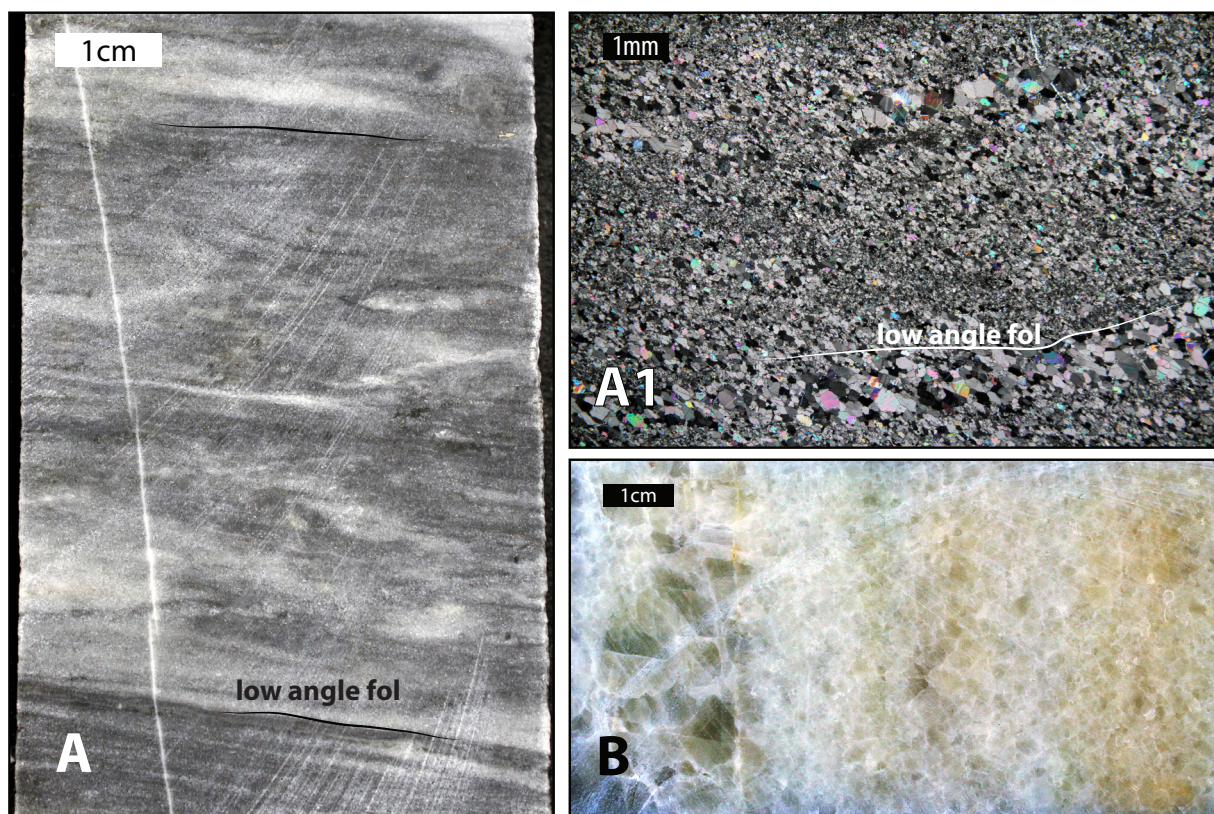
**Figure 2.5:** Examples of the upper carbonate member of the BMS that demonstrate its texture, mineralogy, and character and variation in alteration and deformation (A and B hand sample; A1 XPL photomicrograph). See text for further discussion.

The BMS is correlated with the Permian Anarchist Group rocks based on a Late Paleozoic age determined for corals from a graphitic, calcareous, pyritic, quartz-sericite phyllite that were examined by W. J. Sando of the U.S. Geological Survey (McMillen, 1979). More recently this same age was determined from fusulinids by Dr. Sarah Fowell of the University of Alaska at Fairbanks (M. Deal personal communication, 2011). As described in the regional geology section, the Anarchist Group is equivalent to other late Paleozoic strata in southern British Columbia including the Harper Ranch Group in the Kamloops area, the Attwood Group in the Greenwood area, and the Mount Roberts Formation in the Nelson-Rossland area (Beatty, 2003; Cheney et al., 1994; Hoy and Dunne, 1997; Monger et al., 1991).

### 2.3.2 Metavolcanic Rocks

Rocks of the Buckhorn Mountain Volcanic Sequence (BMV) unconformably overlie the BMS and are the uppermost host rock package. They cover 1.7 km² on the top and east side of Buckhorn Mountain (Figure 2.1). The nature of the contact with the underlying BMS has been disputed in the past. Some authors, (Hickey, 1990, 1992; McMillen, 1979), describe the contact as a thrust fault,

while others, (Cheney et al., 1994; Gaspar, 2005), consider the contact to be a disconformity. Current core logging and local underground mapping suggests that the contact is a disconformity, which matches with the stratigraphy at nearby locations such as the Nelson-Rossland area. The BMV is mostly made up of sub-horizontal porphyritic flows and autobreccias with minor tuffs, dikes, sills, and plugs.

The porphyritic flows of the BMV are massive and blocky in outcrop. They are typified by coarse grained augite phenocrysts in a fine grained to aphanitic mafic groundmass. The augite crystals range in size from 0.1-1 cm and are altered to amphibole and chlorite. The groundmass is very fine grained to aphanitic and altered to chlorite, amphibole and epidote. There are rare oval to spherical amygdules in some flows that are filled with epidote and later chlorite. The flows usually contain a trace amount of chalcopyrite and sphalerite that may be associated with epidote and/or zoisite alteration (Figure 2.6).
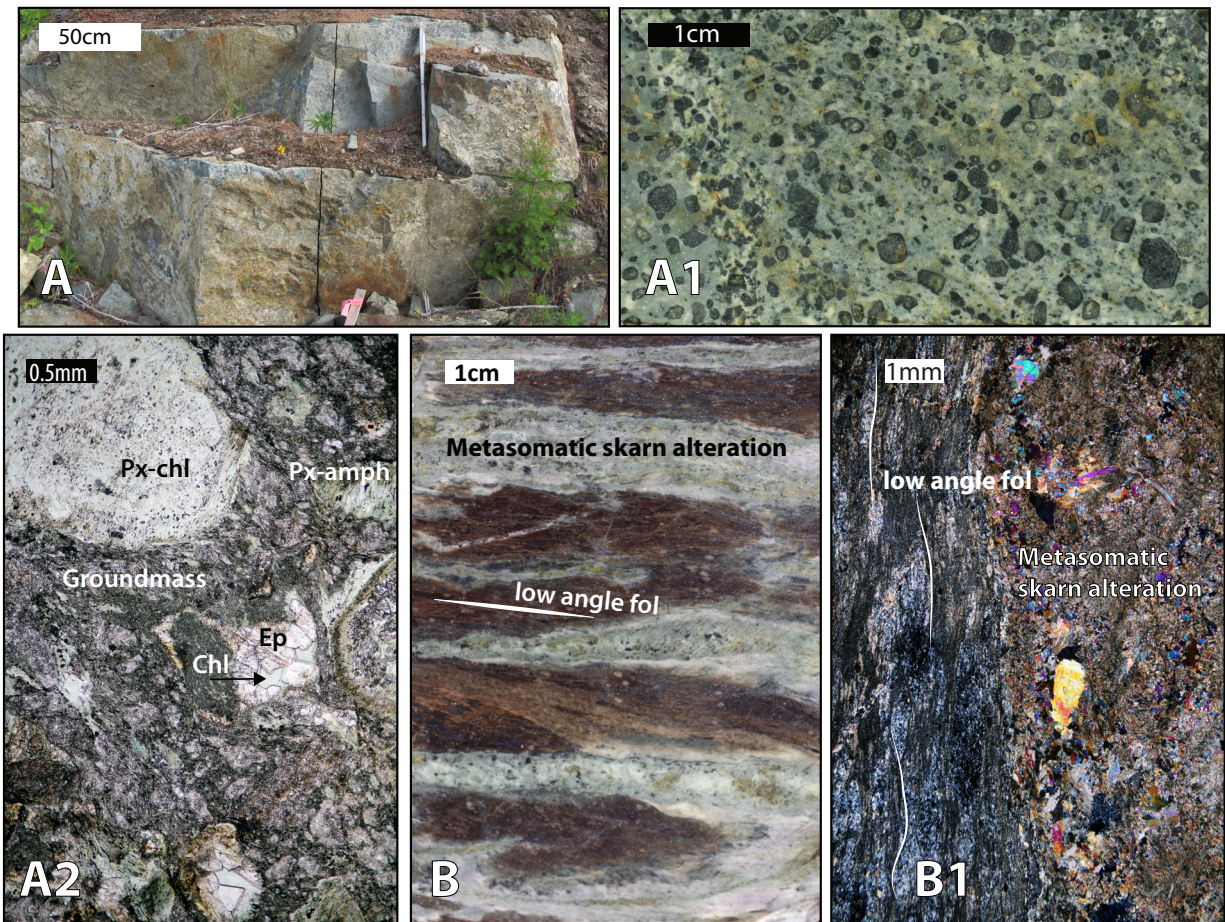


**Figure 2.6:** Examples of the pyroxene porphyry flow member of the BMV that demonstrate its texture, mineralogy, and character and variation in alteration and deformation (A outcrop; A1 and B hand sample; A2 PPL photomicrograph; B1 XPL photomicrograph). See text for further discussion.

Autobreccias form a subordinate amount of the BMV. They are monolithic, only containing clasts from volcanic flows, and clast supported with minor fine grained matrix. Minor flow banding of the groundmass around the clasts has been noted. A small proportion of the autobreccias contain clasts from more than one type of flow, as seen in Figure 2.7. The clasts are subangular to subrounded and range in size from 2 mm to greater than 10 cm. The clasts and matrix have a similar composition, but the groundmass is typically more altered than the clasts. Pyroxene phenocrysts are nearly completely altered to chlorite and amphibole.
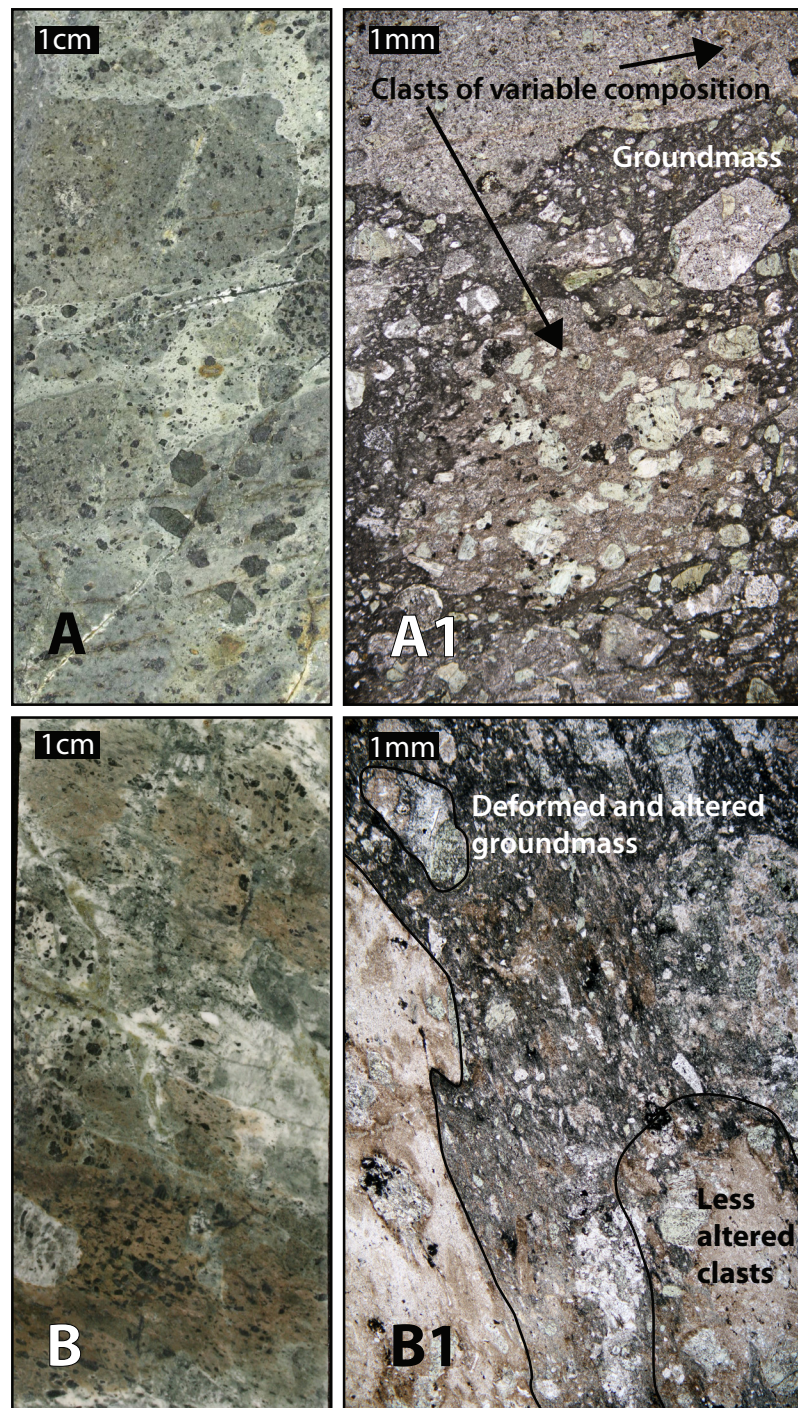
**Figure 2.7:** Examples of autobreccia in the BMV that demonstrate its texture, mineralogy, and character and variation in alteration and deformation (A and B hand samples; A1 and B1 PPL photomicrograph). See text for further discussion.

The intrusive members of the BMV range in composition from diorite to monzodiorite and typically occur in sill-, dike- and plug-like bodies. Based on texture, two varieties have been identified: the equigranular variety and the porphyritic variety. The equigranular variety typically forms as plug like intrusions that more commonly occur on the west side of Buckhorn Mountain, where they

intrude through upper carbonate member of the BMS. The equigranular variety is predominately composed of 0.4-1.5 mm, subhedral plagioclase (70 %) crystals. Mafic minerals make up about 30 % of the rock, and are dominantly pyroxene with lesser amphibole, which are both pervasively altered to chlorite and lesser biotite. Accessory minerals include quartz, potassium feldspar and up to 1 % magnetite. The rocks have also undergone minor carbonate alteration (Figure 2.8).

The porphyritic variety is less abundant and less well documented than the equigranular variety. It has a similar mineralogy to the equigranular variety, but with more potassium feldspar (15 %) and quartz (5 %). The porphyritic variety is distinguished based on texture, having plagioclase and altered mafic phenocrysts that make up about 50 % of the rock, with the remainder being very fine grained chlorite-feldspar-quartz groundmass. The porphyritic intrusive BMV also has minor epidote alteration of the mafic minerals, but no magnetite (Figure 2.8).
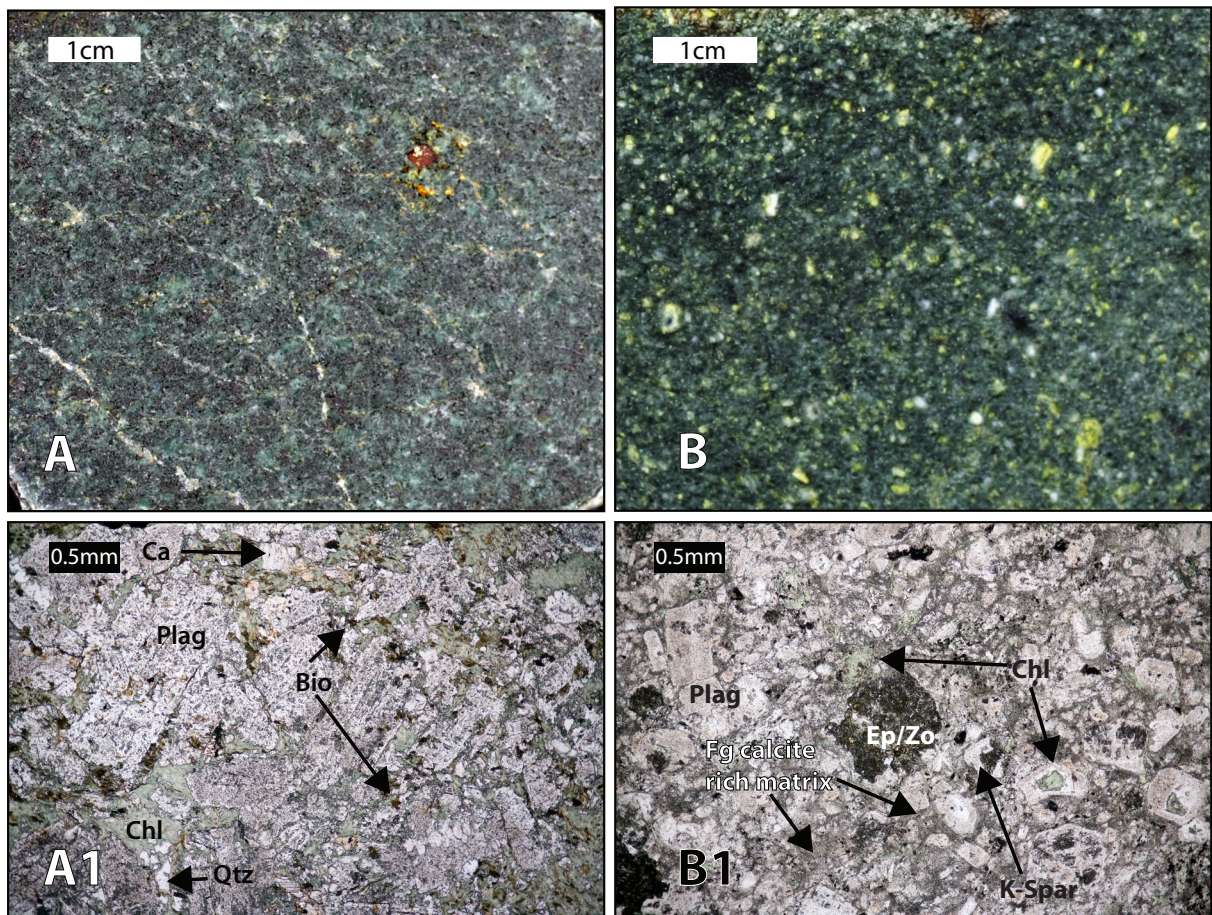


**Figure 2.8:** Examples of intrusive rocks comagmatic with the BMV that demonstrate its texture, mineralogy, and character and variation in alteration and deformation (A and B hand sample; A1 and B1 PPL photomicrograph). (A, A1) The equigranular variety and (B, B1) the porphyritic variety. See text for further discussion.

Samples from a pyroxene porphyry flow and an equigranular and porphyritic intrusion were collected for U-Pb zircon geochronology and the latter sample was dated at 192.4 ± 1.0 Ma (Figure 3.3). This age, combined with major and trace element geochemistry from Gaspar (2005) indicates that the BMV is equivalent to the Jurassic Elise formation of the Nelson-Rossland area as described by Hoy and Dunne (1997). This resolves the long-standing disagreement over their age and place in the regional stratigraphy, as past correlations of the BMV have included a number of different units in southern British Columbia and northern Washington: McMillen (1979), Hickey (1990, 1992) and Stoffel (1990a) correlate them with the Permian-Triassic Kobau or Knob Hill Group; McMillen (1979) also correlated a portion of the BMV with the Triassic Brooklyn Formation, whereas Cheney et al. (1994) and Gaspar (2005) correlate them with the Jurassic Elise Formation.

### 2.3.3 Metamorphism and Skarn Alteration in the BMS and BMV

Siliciclastic rocks of the BMS and volcanic rocks of the BMV are affected by chlorite and epidote alteration, indicative of greenschist facies metamorphism (Figure 2.3, Figure 2.4, Figure 2.6, Figure 2.7, and Figure 2.8). The metamorphism in the BMS has been mostly obscured by subsequent hornfels alteration resulting from contact metamorphism. In the BMV the greenschist facies metamorphism is characterised by the alteration of clinopyroxene to amphibole, epidote and chlorite. In the flows and autobreccias, the alteration preferentially affects the pyroxene phenocrysts and matrix (Figure 2.6 and Figure 2.7).This greenschist facies metamorphism occurred before the Middle Jurassic as it is overprint by hornfels alteration during contact metamorphism related to the emplacement of the Buckhorn Intrusive Suite (BIS). The contact metamorphism caused extensive hornfels alteration of the BMS rocks that is characterised by fine grained biotite growth in the siliciclastic sedimentary rocks and amphibole and pyroxene growth in the calcareous sedimentary rocks (Figure 2.3). In the dominantly carbonate rocks the contact metamorphism caused recrystallization of limestone into marble (Figure 2.5). Contact metamorphism and related hornfels alteration is less prominent in the BMV, and is characterized by similar mineralogical changes as in the clastic sedimentary rocks of the BMS (Figure 2.6). This type of hornfels alteration is typical for isochemical contact metamorphism in skarn systems (Meinert et al., 2005).

Several stages of deformation affected the host metasedimentary rocks after the greenschist and contact metamorphism. This deformation produced two low angle and one steeply dipping foliation that occur in local shear zones (Figure 2.3). The deformation was previously thought to predate the BMV and intrusive rocks (McMillen, 1979), but this study documents the foliations in all rock Meso-

zoic and Paleozoic rock types. A complete description of the deformation and how it manifests in the different rock types is described below in section 2.3.4.3.1

Following the onset of deformation, metasomatic skarn alteration locally overprints the isochemical hornfels alteration in the BMS and BMV. The skarn alteration is characterized by variable prograde pyroxene, garnet and magnetite and retrograde amphibole, epidote and pyrrhotite alteration. Skarn alteration is more intense along shear zones in the BMV and BMS, most notable along the contact between the upper carbonate member of the BMS and the overlying BMV (Figure 2.2). The location skarn alteration is also spatially associated with the Granodiorite dikes. For example in the Mike's Skarn area skarn alteration only occurs in the BMS rocks adjacent to the Granodiorite dikes, and not in the more distal BMS rocks (Figure 2.9) (G.E. Ray, Personal Communication 2010). The skarn alteration may be massive or foliated in hand sample, and in thin section is seen to be brittlely and/or ductilely deformed, suggesting that skarn alteration was coeval with the deformation.
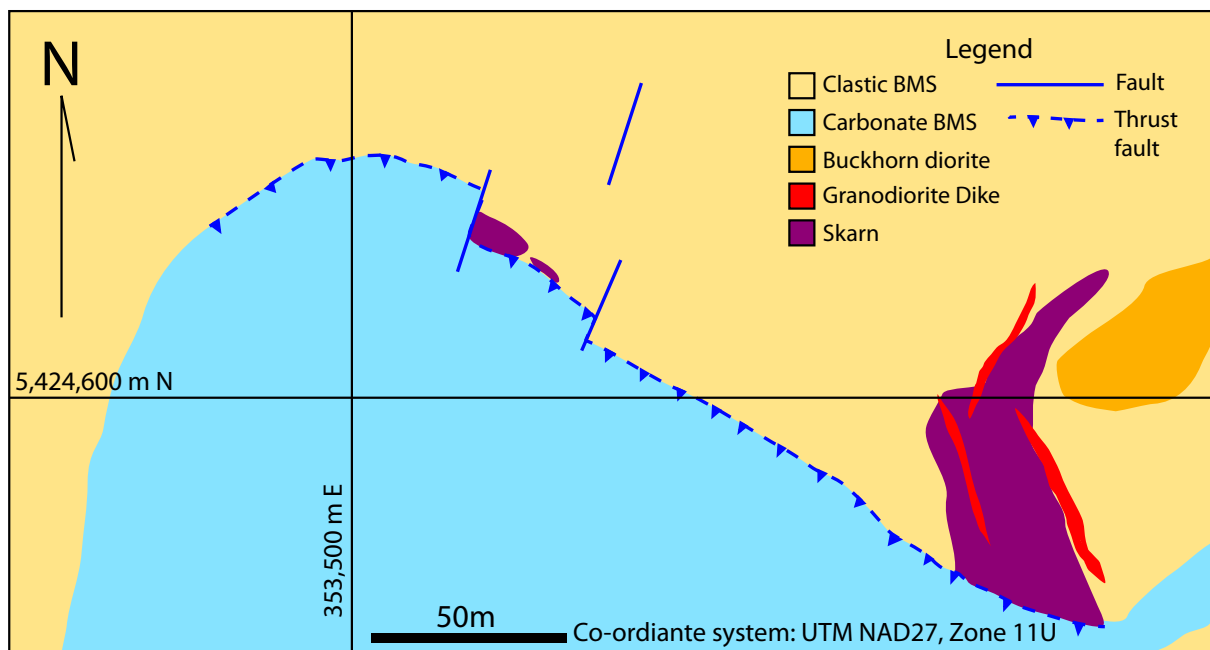


**Figure 2.9:** Simplified geologic map of the Mike's Skarn area. Skarn alteration is spatially related to the Granodiorite dikes in the south-east corner of the map. The clastic metasedimentary rocks distal to the dikes have not been skarn altered. Modified from mapping done by G.E. Ray (2010)

Gold mineralization is spatially associated with the skarn alteration, although a significant portion of the skarn alteration is not gold mineralized. The gold mineralization is associated with bismuth mineralization and can be petrographically shown to be part of the retrograde alteration assemblage. The mineralogical, textural and geochemical characteristics of skarn alteration and gold mineralization are the subject of Chapters 4 and 5.

The last stage of deformation at Buckhorn is characterised by late NNE oriented normal faults that cut the skarn alteration, deformation, and metamorphism. The two most prominent of these faults are the North Lookout fault, which offsets skarn alteration and gold mineralization, and the Toroda Creek Graben Fault, which forms the eastern margin of the Buckhorn stratigraphy. These faults affect all rock types at Buckhorn and are discussed, along with the foliations in more detail in section 2.3.4.3.1.

**2.3.4 Intrusive Rocks**

Intrusive rocks at Buckhorn can be split into two distinct intrusive suites: The Buckhorn Intrusive Suite (BIS) and the Roosevelt Intrusive Suite (RIS). The Middle Jurassic BIS is more voluminous than the Eocene RIS, and rocks of the BIS have undergone similar alteration and deformation to the host rocks, whereas the RIS rocks are less altered and deformed and have only been subjected to the final stage of deformation. The relationship between the two intrusive suites with mineralization is disputed. Early authors, (Hickey, 1990, 1992; McMillen, 1979) suggested that mineralization was related to the BIS, while Gaspar (2005) stated it was related to the RIS. This study resolves this ambiguity.

**2.3.4.1 Buckhorn Intrusive Suite (BIS)**

The BIS includes several distinct rock types: Buckhorn Granodiorite, Mafic Diorite, Buckhorn Diorite, Early Diorite dikes, Granodiorite dikes, and Quartz Porphyry dikes. The orientation of some of the dikes make be influenced by Paleozoic syn-sedimentray NNE striking normal faults that are inferred from drilling below the SWOZ (Figure 2.1 and Figure 2.2).

**2.3.4.1.1    Buckhorn Granodiorite**

The Buckhorn Granodiorite is the dominant intrusive phase in the Buckhorn area. It outcrops on the northeast side of Buckhorn Mountain and into southern British Columbia covering an area of approximately 19 km$^2$ (Figure 2.1) (Gaspar, 2005; Massey et al., 2005; Schuster and Carutherers, 2005). The Buckhorn Granodiorite has an intrusive contact with both the BMS and BMV.

The Buckhorn Granodiorite is a grey-weathering massive, heterogeneous, fine to coarse grained, heterogranular to rarely porphyritic granodiorite pluton. It contains about 30 % quartz, 40 % plagioclase, 15 % potassium feldspar, 10 % hornblende, 5 % biotite and a trace amount of magnetite, pyrite and zircon. Quartz occurs as clear, anhedral interstitial crystals. Potassium feldspar is subhedral and plagioclase is nearly euhedral with polysynthetic twinning. Biotite forms as 2-3 mm euhedral

hexagonal crystals and hornblende forms smaller (1mm) subhedral crystals. Trace euhedral magnetite crystals occur with biotite and potassium feldspar (Figure 2.10).

The intensity of alteration that affects the Buckhorn Granodiorite is variable. Much of it is relatively unaltered with only minor chlorite-epidote alteration of the mafic minerals and sericite alteration of the plagioclase. Potassic alteration also occurs and is characterized by secondary biotite and octahedral magnetite (Figure 2.10). Locally there is intense alteration of the mafic minerals to chlorite and lesser amphibole, and of the plagioclase and lesser potassium feldspar to sericite. Where cut by the steeply northeast dipping shear zones the Buckhorn Granodiorite is intensely altered to a quartz-amphibole-chlorite assemblage (Figure 2.10).

Skarn alteration is rare but does locally occur in the Buckhorn Granodiorite where it is cut by the later Granodiorite dikes (Figure 2.11). This skarn alteration is less intense that in the Early Diorite dikes, BMV or BMS and is characterized by the development of prograde clinopyroxene and retrograde amphibole.

The Buckhorn Granodiorite was originally assumed to be Cretaceous (Hickey, 1990, 1992; McMillen, 1979), but U-Pb dating done in Chapter 3 confirms that it was emplaced during the Middle Jurassic with an age of 170.4 ± 1.1 Ma. (Figure 3.5) This allows its correlation with several plutons of similar age and composition in the southern Canadian cordillera: The Cahill Creek Pluton (168.9 ±9 Ma) in the Hedley district (Ray and Dawson, 1994, and references therein); The Nelson (167 Ma), Trail (169±3 Ma) and Bonnington (167 Ma) Plutons and the Rossland Monzonite (167.5±0.5 Ma) in the Nelson-Rossland area (Hoy and Dunne, 2001, and references therein) (Figure 1.1). It was originally proposed as the mineralizing intrusive (Hickey, 1990, 1992; Jones, 1992; McMillen, 1979), but based on the skarn alteration around cross-cutting dikes, it is now shown to predate the skarn alteration.
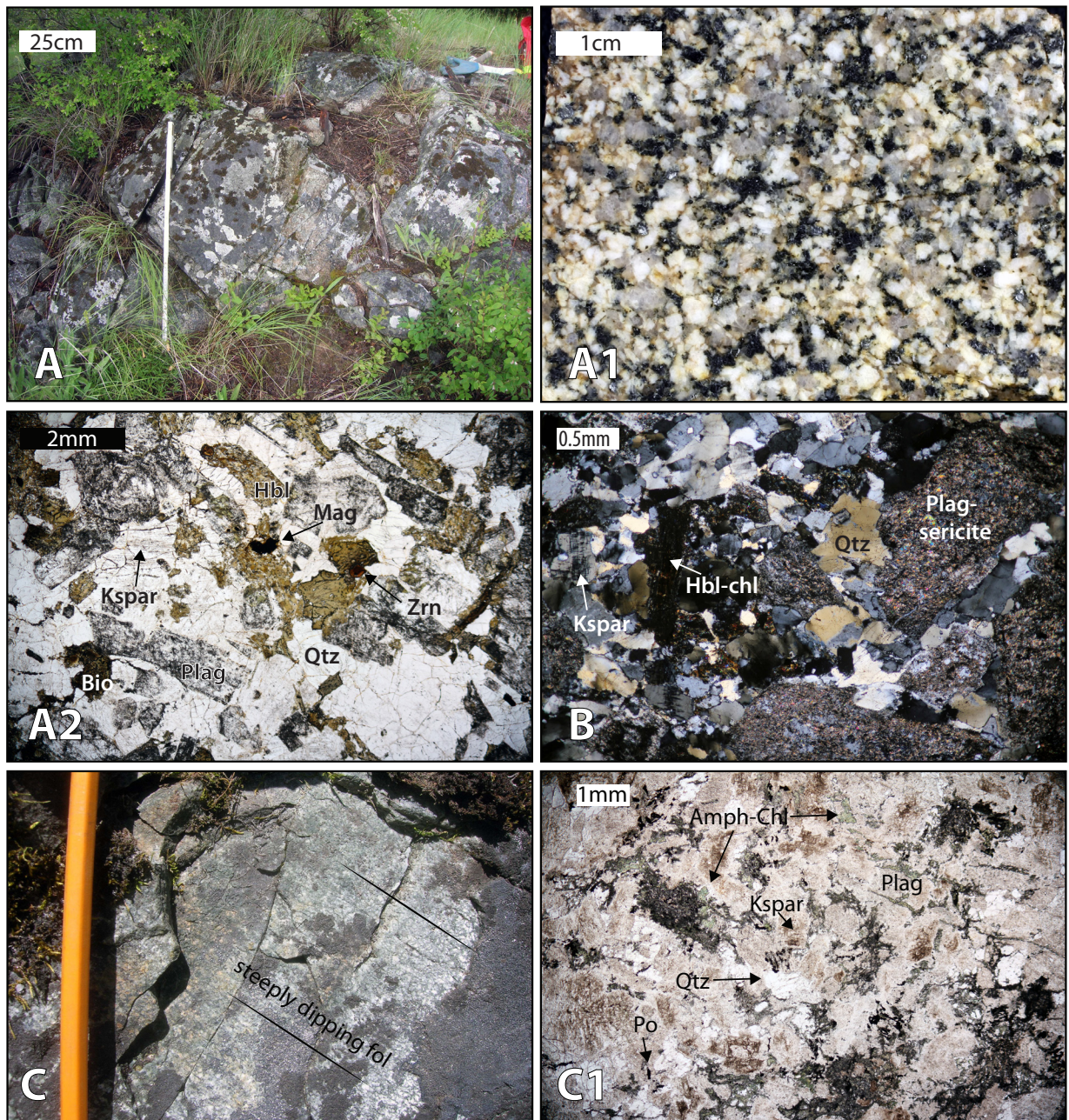
**Figure 2.10:** Examples of the Buckhorn Granodiorite that demonstrate its texture, mineralogy, and character and variation in alteration and deformation (A and C outcrop; A1 hand sample; A2 and C1 PPL photomicrograph; B XPL photomicrograph). See text for further discussion.
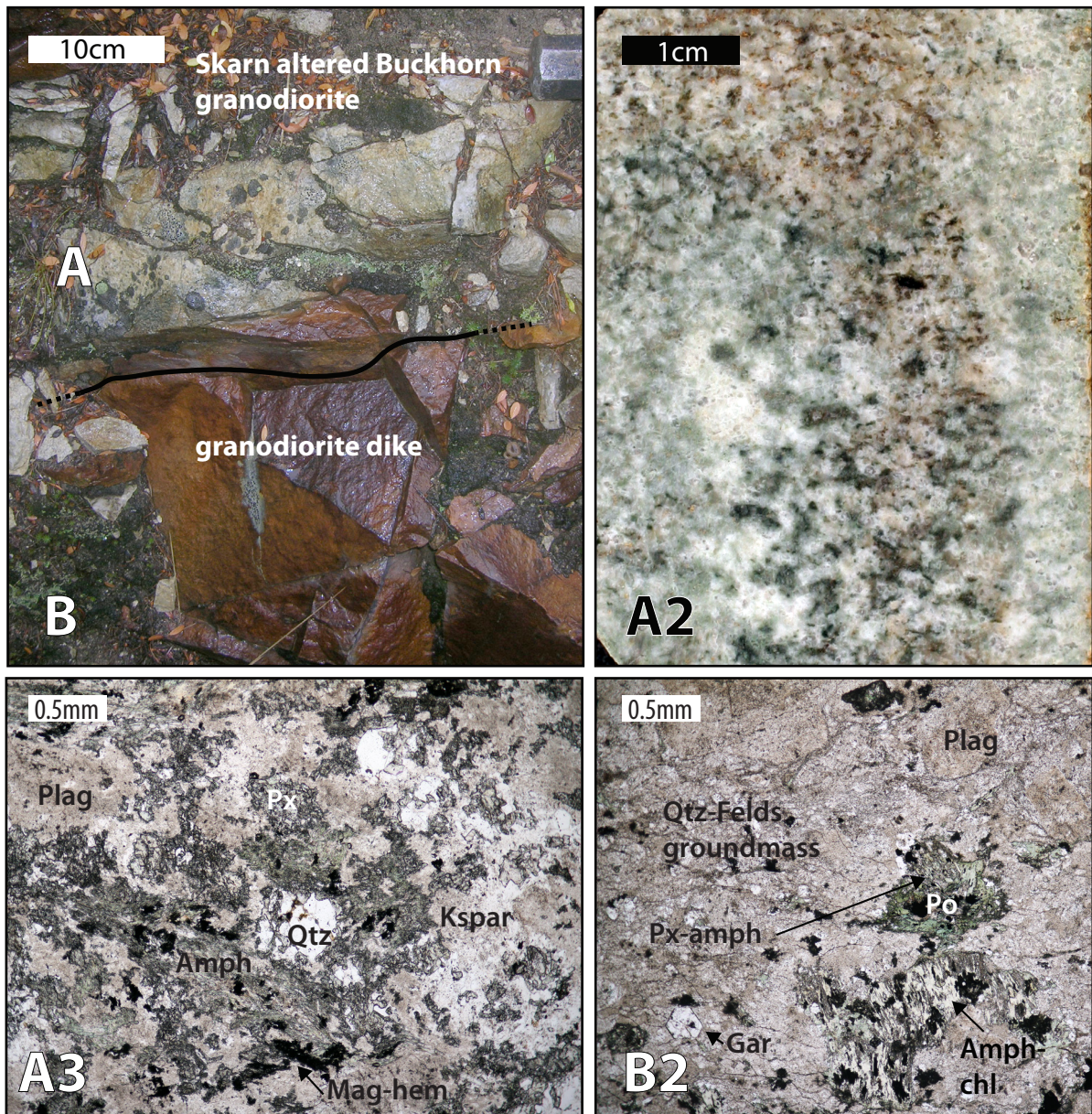
**Figure 2.11:** Example of a Granodiorite dike cross-cutting the Buckhorn Granodiorite that demonstrates the mineralogy and texture of the local skarn alteration (A/B outcrop; A2 hand sample; A3 and B2 PPL photomicrograph). See text for further discussion.

### 2.3.4.1.2    Mafic Diorite

The Mafic Diorite is a volumetrically minor and poorly understood intrusive rock type found in the Buckhorn area. It was identified during a geochemical study of the local intrusive rocks and its extent is not known. It is defined based on its high titanium and low silica content compared to the other intrusive rocks (M. Deal, personal communication 2011). The Mafic Diorite occurs as dikes that cross cut the Buckhorn Granodiorite, however, it has not been found in contact with any other intrusive rocks, so its age cannot be further constrained.

The Mafic Diorite is black to very dark green in hand sample with up to 40 % euhedral white plagioclase crystals that are 400 μm to 2.5 mm in length. Amphibole (5 %) forms 100 μm, and rarely 500 μm, anhedral to subhedral crystals. Primary clinopyroxene (4 %) forms 100 μm anhedral to subhedral crystals. Ilmenite is the only primary opaque mineral and makes up about 1 % of the rock, as irregular wormy grains spatially associated, or possibly intergrown, with primary clinopyroxene and amphibole (Figure 2.12).

Amphibole is the most abundant alteration mineral (50 %) replacing the larger primary amphibole crystals with many smaller fibrous crystals and rarely pseudomorphing the primary amphibole (Figure 2.12). Plagioclase is also affected by amphibole alteration that preferentially alters the edges of the crystals giving them a rounded appearance (Figure 2.12). Sericite alteration of the plagioclase also occurs, and is typically pervasive and weak, affecting less than 5 % of a plagioclase crystal (Figure 2.12). Pyrrhotite is the most abundant sulfide with less chalcopyrite and pyrite; together the sulphides make up a trace amount of the rock (Figure 2.12). The Mafic Diorite is locally altered to epidote in centimetre scale bands, and rarely hosts minor prograde pyroxene skarn alteration at its contact with skarn altered metasedimentary rocks. In general the Mafic Diorite appears massive and undeformed in hand sample, but plagioclase and other primary minerals have minor fractures.

The age of the Mafic Diorite is unknown. Its age can be constrained by its cross-cutting relationship with the Buckhorn Granodiorite, which requires that it was emplaced after 170.4 ± 1.1 Ma (Figure 3.5), and the presence of skarn alteration suggests that it is older than the Granodiorite dikes at 167.5 ± 0.8 Ma (Figure 3.15). Based on these ages constrains the Mafic Diorite is interpreted as an early dike phase of the BIS.
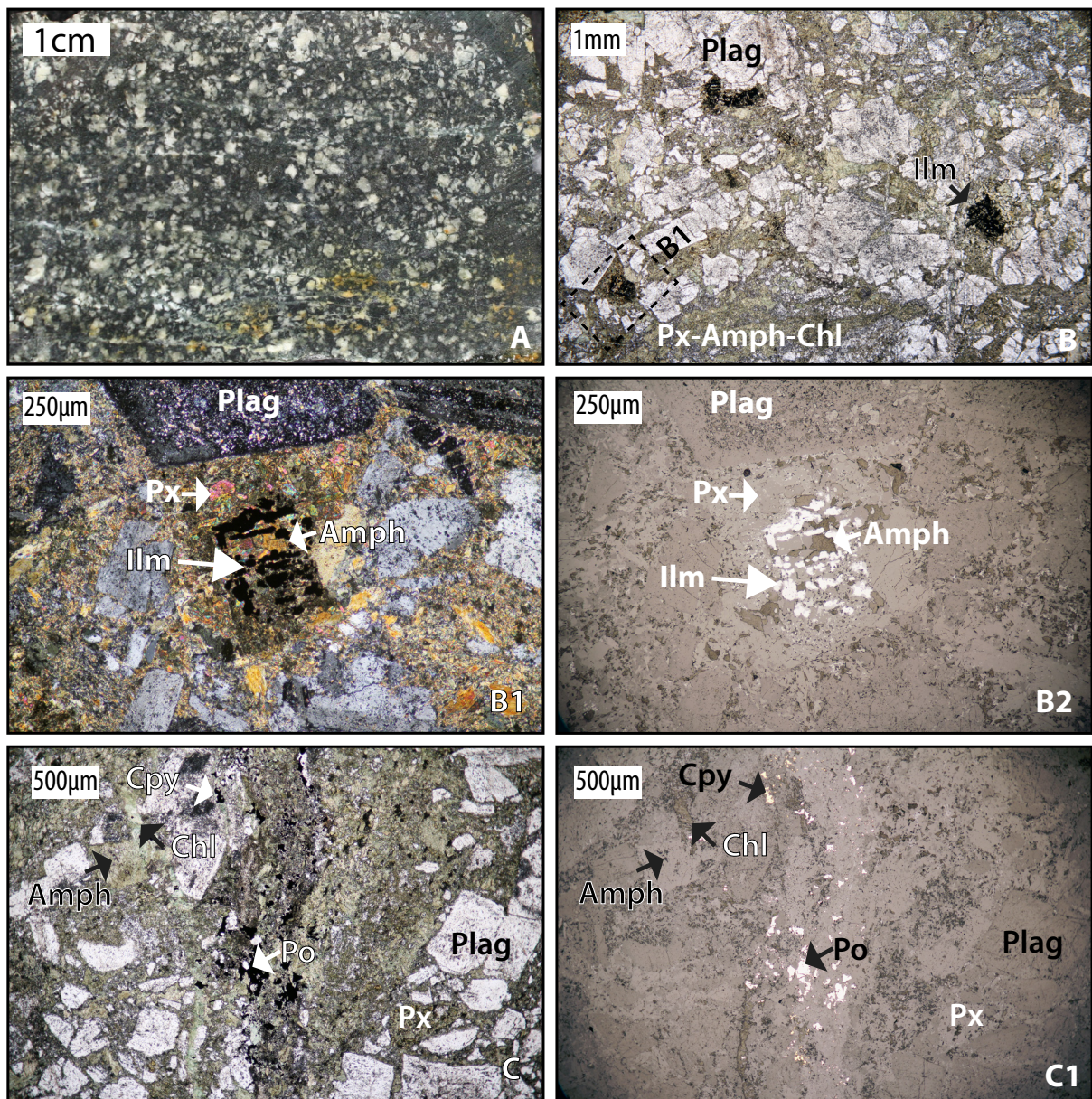
**Figure 2.12:** Examples of the Mafic Diorite that demonstrate its texture, mineralogy, and character of alteration and deformation. (A hand sample; B and C PPl photomicrograph; B1 XPL photomicrograph; B2 and C1 RL photomicrograph). See text for further discussion.

### 2.3.4.1.3 Buckhorn Diorite

The Buckhorn Diorite is a massive mafic intrusive phase that covers 0.8 km$^2$ and crops out on the northeast side of the Buckhorn Mountain between the Buckhorn Granodiorite and the Magnetic Mine skarn (Figure 2.1). It has a gradational contact with the Buckhorn Granodiorite to the north and east (Figure 2.1). On its southwestern side the Footwall Mylonite, a major steeply northeast dipping shear zone, puts the Buckhorn Diorite in contact with the BMS. It has an intrusive contact with metasedimentary and metavolcanic rocks along its southern margin. The Buckhorn Diorite is cross

cut by the Quartz Porphyry dikes, however its timing relative to the Early Diorite dikes is unknown. While it is labelled as diorite it is compositionally a quartz-monzodiorite, but for the sake of consistency with older work it will continue to be referred to as the Buckhorn Diorite.

The Buckhorn Diorite is a coarse-grained heterogranular to porphyritic quartz monzodiorite made up of coarse-grained amphibole (25 %) and biotite (10 %), fine grained plagioclase (15 %) and alkali feldspar (5 %) in a matrix of fine grained quartz (7 %), plagioclase (25 %) and alkali feldspar (13 %). The Buckhorn Diorite has undergone similar alteration to the Buckhorn Granodiorite. Amphibole and biotite are altered to secondary hydrothermal amphibole, chlorite and epidote. Trace euhedral magnetite is now altered to hematite, and occurs with the secondary mafic minerals (Figure 2.13).

Current mapping shows a gradational contact between the Buckhorn Diorite and the Buckhorn Granodiorite (Figure 2.1). As well, the mineralogical differences, more abundant mafic minerals and less quartz when compared to the Buckhorn Granodiorite, are those expected in the margin of a zoned pluton (Pitcher, 1997). U-Pb zircon geochronology also supports the classification as a marginal phase, showing that the Buckhorn Diorite 169.0 ± 0.9 Ma, (Figure 3.13) is the same age as the Buckhorn Granodiorite. Early workers (Hickey, 1990, 1992; McMillen, 1979) drew a similar conclusion from their work and labelled the Buckhorn Diorite as a border phase of the Buckhorn Granodiorite, but that genetic relationship was later questioned (Gaspar, 2005). However based on mapping and geochronology from this study, the Buckhorn Diorite is classified as a marginal phase of the Buckhorn Granodiorite.
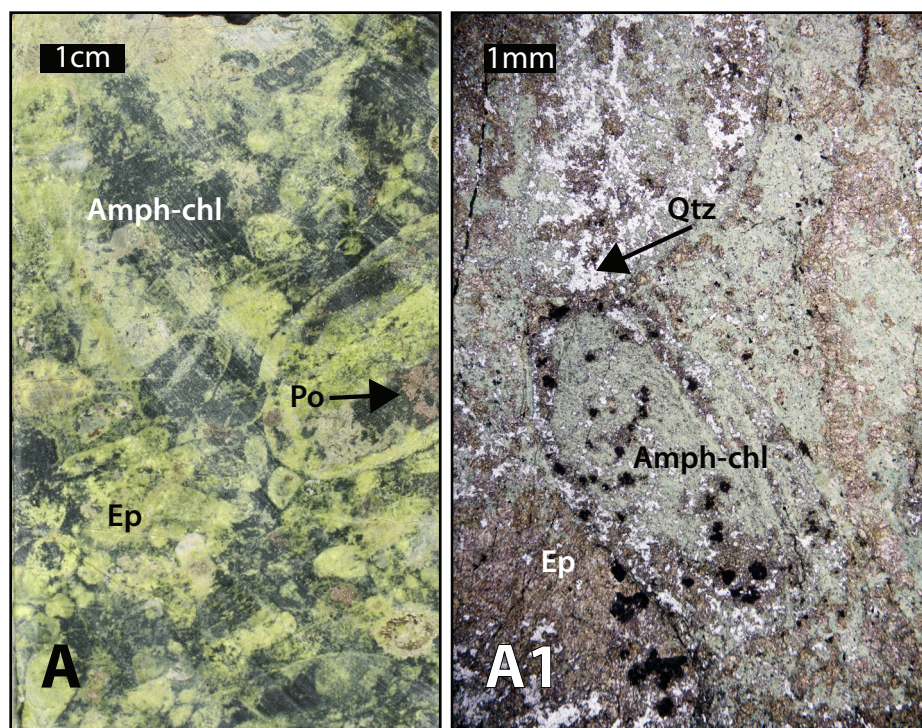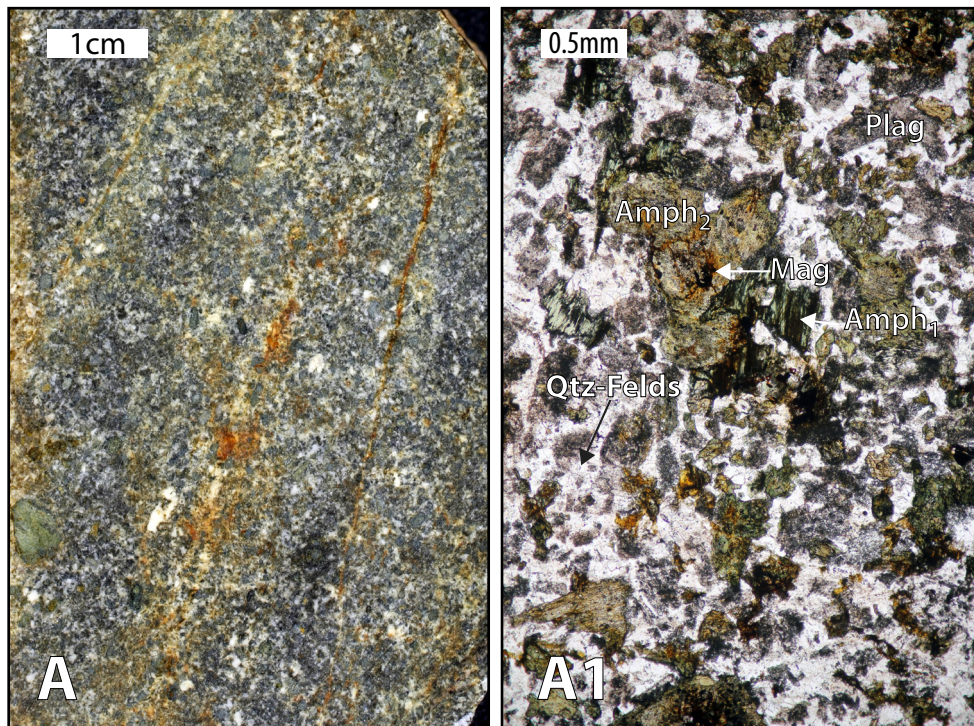
**Figure 2.13:** Examples of the Buckhorn Diorite that demonstrate its texture, mineralogy, and character of alteration and deformation. (A hand sample; A1 PPL photomicrograph). See text for further discussion

### 2.3.4.1.4 Early Diorite Dikes

The Early Diorite dikes are lithologically similar to the Buckhorn Diorite and are distinguished from the Buckhorn Diorite on the basis of their porphyritic and endoskarn altered nature (G.E. Ray, personal communication, 2009). They appear to be volumetrically the smallest of the BIS rocks, and their intrusion style is poorly defined. They form predominately in dikes, but may also form as sills and small plugs. They were not found in contact with other intrusive rocks, and their distribution is unknown.

The Early Diorite dikes are porphyritic and texturally distinct from the Buckhorn Diorite with coarse-grained lath-shaped plagioclase phenocrysts that form about 30 % of the rock. The plagioclase phenocrysts have abundant, very fine grained inclusions of amphibole and/or pyroxene. Coarse grained clinopyroxene phenocrysts are also present, forming about 15 % of the rock. The remaining 55 % of the rock is made up of sub-micron scale feldspar/quartz groundmass with very fine grained amphibole and/or pyroxene inclusions similar to those in the plagioclase phenocrysts (Figure 2.14).

The Early Diorite dikes are the most intensely endoskarn altered rocks in the Buckhorn area. They often host pervasive garnet, amphibole and epidote alteration and minor gold mineralization

(Figure 2.14). Less altered examples are characterized by moderate amphibole alteration of pyroxene phenocrysts and sericite alteration of the plagioclase phenocrysts (Figure 2.14).

The Early Diorite dikes predate skarn mineralization and have been dated by U-Pb zircon geochronology to 169.4 ± 1.3 Ma (Figure 3.10). Based on the mineralogical similarities with the Buckhorn Diorite, and U-Pb geochronology they are interpreted as an early dikes phase of the BIS.
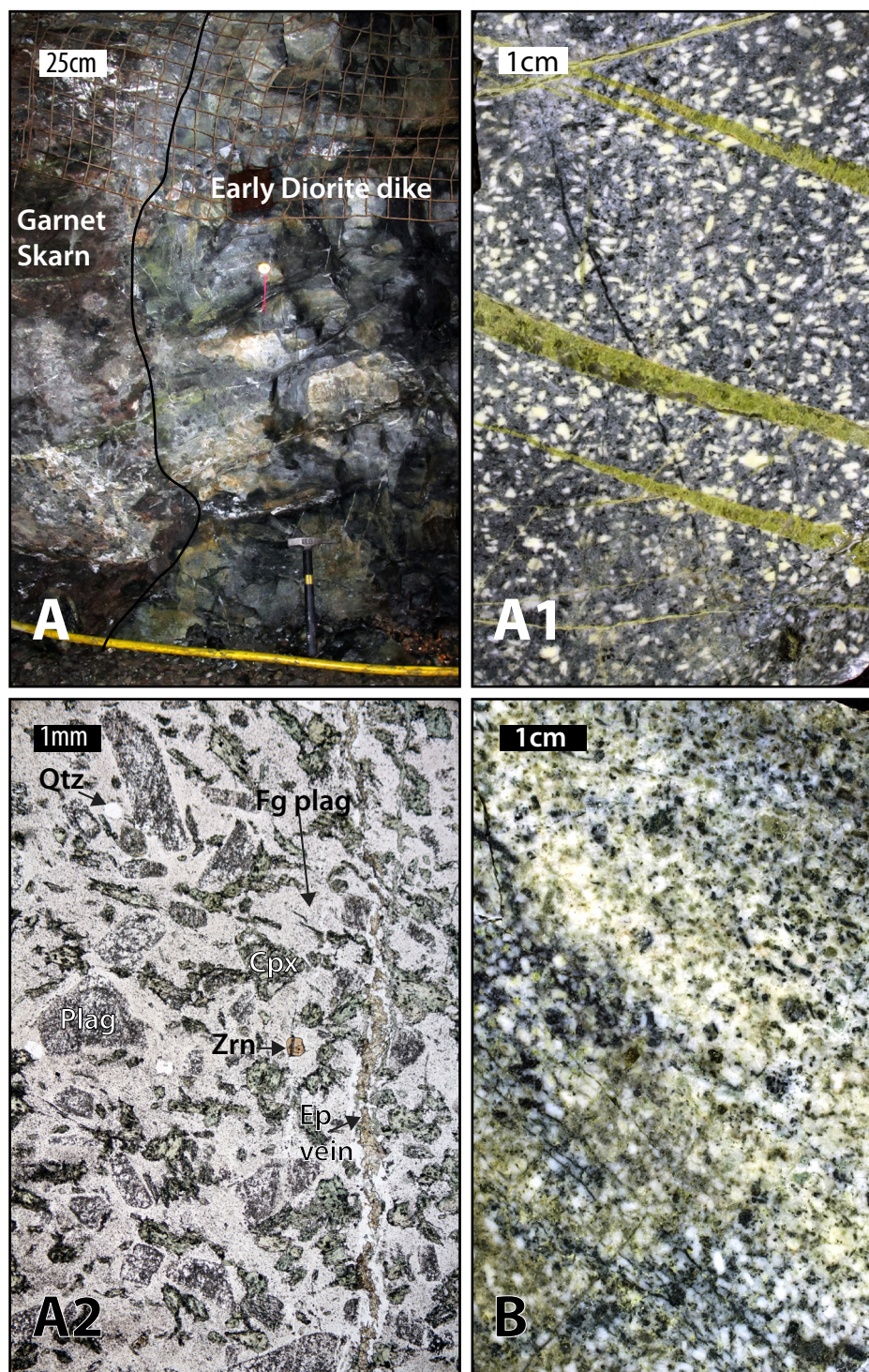
**Figure 2.14:** Examples of the Early Diorite dikes that demonstrate the intrusive style, texture, mineralogy, character and variation in alteration and deformation.(A outcrop; A1 and B hand sample; A2 PPL photomicrograph). See text for further discussion.

### 2.3.4.1.5    Granodiorite dikes

The Granodiorite dikes have a NNE or WNW orientation and occur throughout the Buckhorn area (Figure 2.1) (Gaspar, 2005). The Granodiorite dikes cross-cut the BMS, BMV, and the Buckhorn Granodiorite, but they have not been found in contact with the other types of dikes, so the relative timing could not be determined.

The Granodiorite dikes are mineralogically and texturally similar to the Buckhorn Granodiorite, but contain quartz phenocrysts (Figure 2.15). Most of the dikes are massive with minor chlorite alteration of the mafic minerals, however, a few intensely deformed examples have been documented. When altered, the quartz phenocrysts, and very rarely feldspar grains, are the only original minerals to survive, and the rest of the rock is made up of very fine grained to aphanitic recrystallized quartz and lesser biotite, muscovite, and chlorite.

The Granodiorite dikes host minor skarn alteration, which is characterized by a pyroxene-garnet-amphibole-pyrrhotite-chalcopyrite mineral assemblage (Figure 2.11). In addition to being skarn altered, the Granodiorite dikes are also spatially related to the location of skarn alteration and gold mineralization in other rock types. As documented in sections 2.3.4.1.1 and 2.3.3, where the Granodiorite dikes cross cut the Buckhorn Granodiorite (Figure 2.11) or the BMS (Figure 2.9) there may be local skarn alteration.

The Granodiorite dikes were dated at 167.5 ± 0.8 Ma (Figure 3.15), confirming their association with the Buckhorn Granodiorite. Based on their spatial association with local skarn alteration their age also provides a maximum age for skarn alteration at Buckhorn.
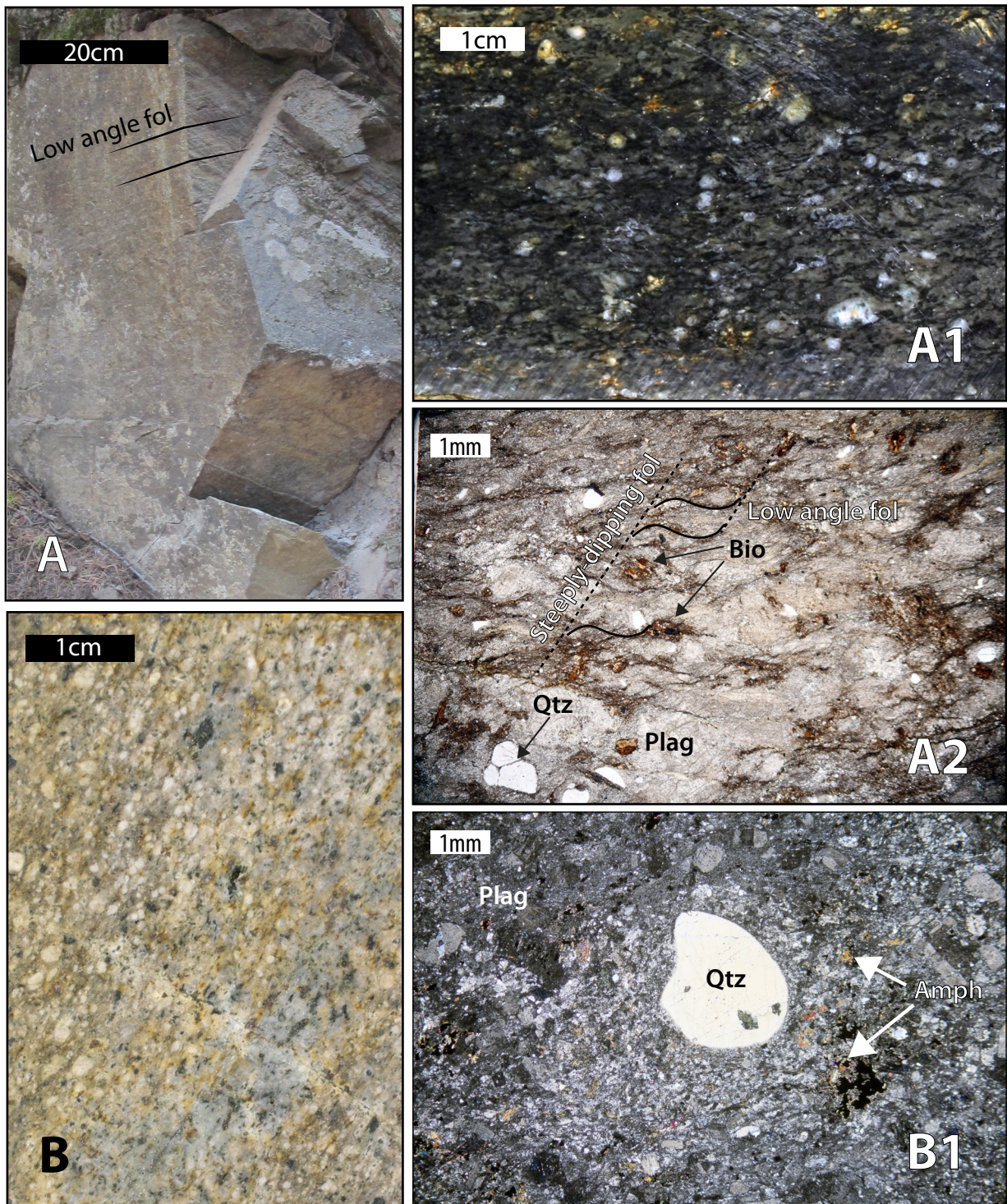
**Figure 2.15:** Examples of the Granodiorite dikes that demonstrate the intrusive style, texture, mineralogy, character and variation in alteration and deformation. (A and B1 hand sample; B outcrop; B2 PPL photomicrograph). See text for further discussion.

### 2.3.4.1.6        Quartz Porphyry Dikes

The Quartz Porphyry dikes are the most abundant dikes in the Buckhorn area, they occur in NNE and WNW striking swarms (Figure 2.1). The Quartz Porphyry dikes cross-cut the BMS, the BMV, the Buckhorn Granodiorite and the Buckhorn Diorite. Relationships with the Early Diorite dikes or the Granodiorite dikes are not apparent, so the relative timing of the different types of dikes is uncertain.

The Quartz Porphyry dikes are white to tan coloured, with distinctive 0.5-1.5 mm subhedral quartz phenocrysts. The groundmass is made up of 10-20 μm anhedral quartz crystals and lesser plagioclase, potassium feldspar and muscovite (Figure 2.16).

The Quartz Porphyry dikes are pervasively altered with minor carbonate and muscovite-epidote-chlorite alteration. They are locally skarn altered, hosting a garnet-epidote assemblage (Figure 2.17). Gaspar (2005) reported that gold was recovered during heavy mineral separation indicating that they may be mineralized. The skarn alteration and mineralization is very rare and has only been documented in a small number of drill holes (~5).

The Quartz Porphyry dikes were dated to 163.57±0.8 Ma (Gaspar, 2005), and are the youngest of the Jurassic intrusive rocks.
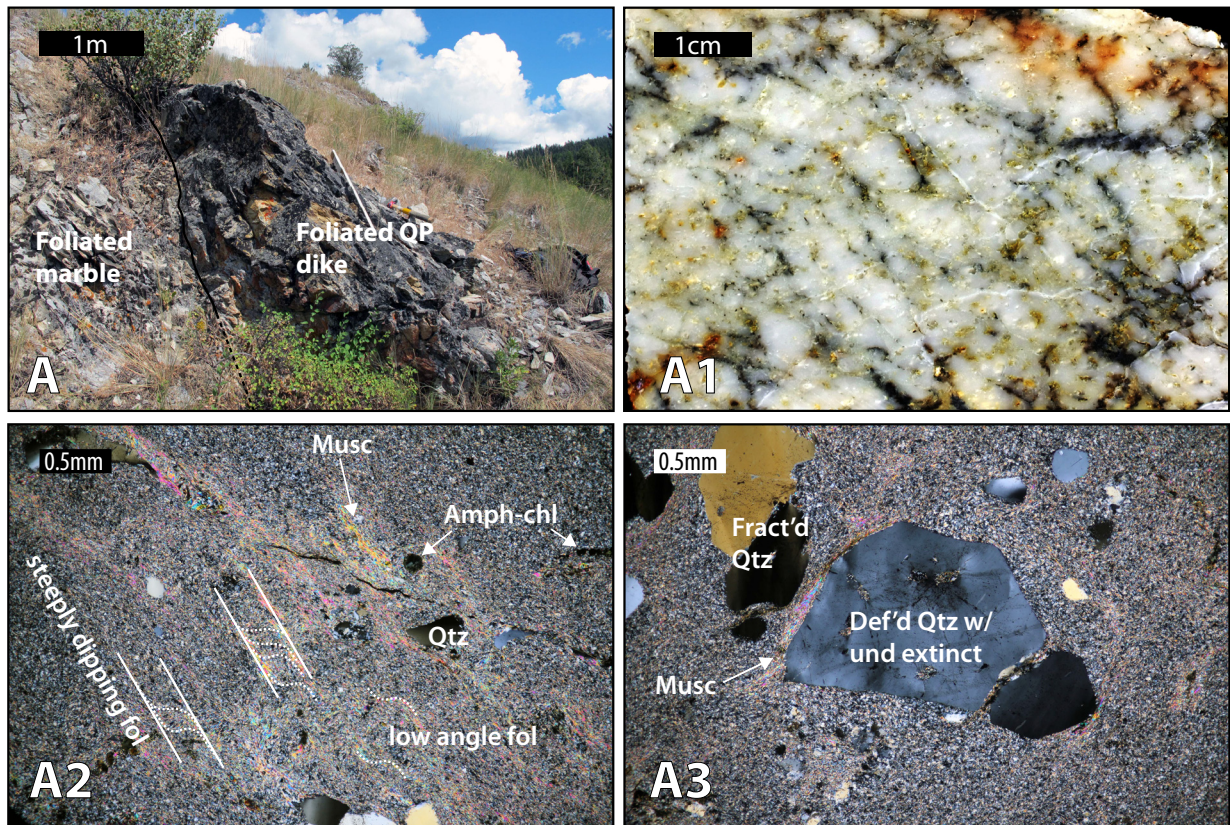
**Figure 2.16:** Examples of the Quartz Porphyry dikes that demonstrate the intrusive style, texture, mineralogy, character and variation in alteration and deformation.(A outcrop; A1 hand sample; A2 and A3 XPL photomicrograph). See text for further discussion.
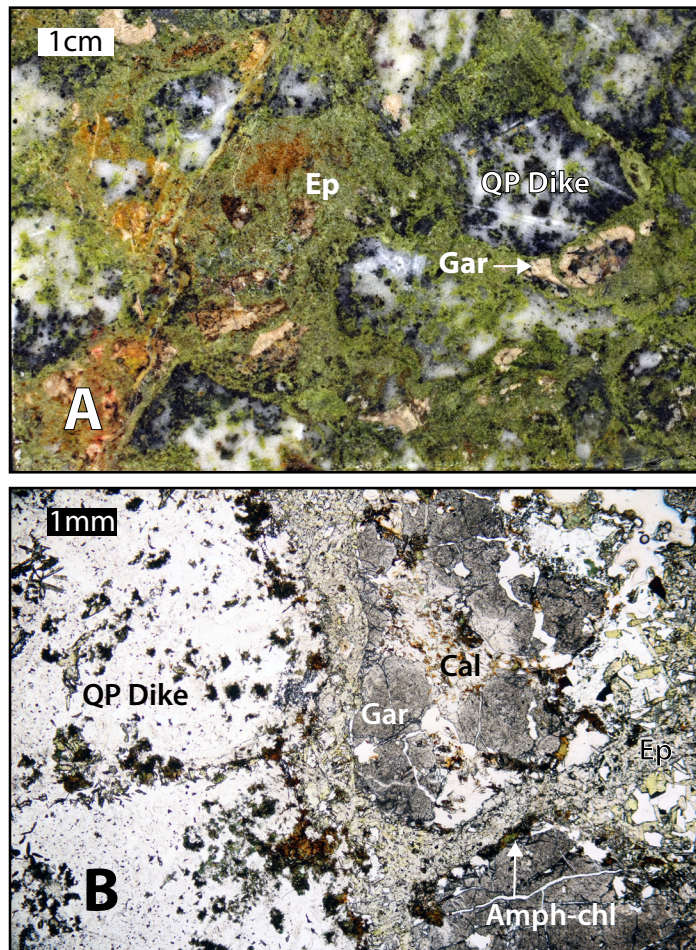
**Figure 2.17:** Example of skarn alteration in the Quartz Porphyry dike that demonstrate the texture, mineralogy, character and variation in skarn alteration.(A hand sample; B PPL photomicrograph). See text for further discussion.

### 2.3.4.2 The Roosevelt Intrusive Suite (RIS)

Originally mapped as part of the Buckhorn Granodiorite or border diorite (Hickey, 1990, 1992; McMillen, 1979), the Roosevelt Intrusive Suite (RIS) is made up of the Roosevelt Granodiorite and the Pink Granite.

The Roosevelt Granodiorite is a small massive intrusion (0.03 km²) on the east side of Buckhorn Mountain that intrudes the Buckhorn Granodiorite, BMS, and BMV (Figure 2.1).

The Roosevelt Granodiorite is similar to the Buckhorn Granodiorite, but it is darker in hand sample with minor mafic clusters that may be xenoliths but do not have chilled or resorbed margins (Figure 2.18). The Roosevelt Granodiorite appears equigranular in hand sample, but in thin section it is clearly porphyritic with abundant plagioclase, amphibole and biotite phenocrysts in a fine-grained feldspar and quartz matrix. The rock also has minor primary magnetite (<1 %).

The Roosevelt Granodiorite is less altered than the nearby Buckhorn Granodiorite, having only minor secondary biotite and mild secondary amphibole and chlorite alteration of the primary mafic minerals.

The Roosevelt Granodiorite was dated at 50.5 ± 3.0 Ma (Figure 3.17). The Eocene age suggests that it is the intrusive equivalent of the Sanpoil volcanic rocks that fill the adjacent Toroda Creek half graben (Gaspar, 2005; Suydam and Gaylord, 1997). Based on petrography, geochemistry and age data, the Roosevelt Granodiorite is correlated with the Devils Elbow Suite Intrusions that are part of the Colville Igneous Complex (Holder and McCarley Holder, 1988; Suydam and Gaylord, 1997).
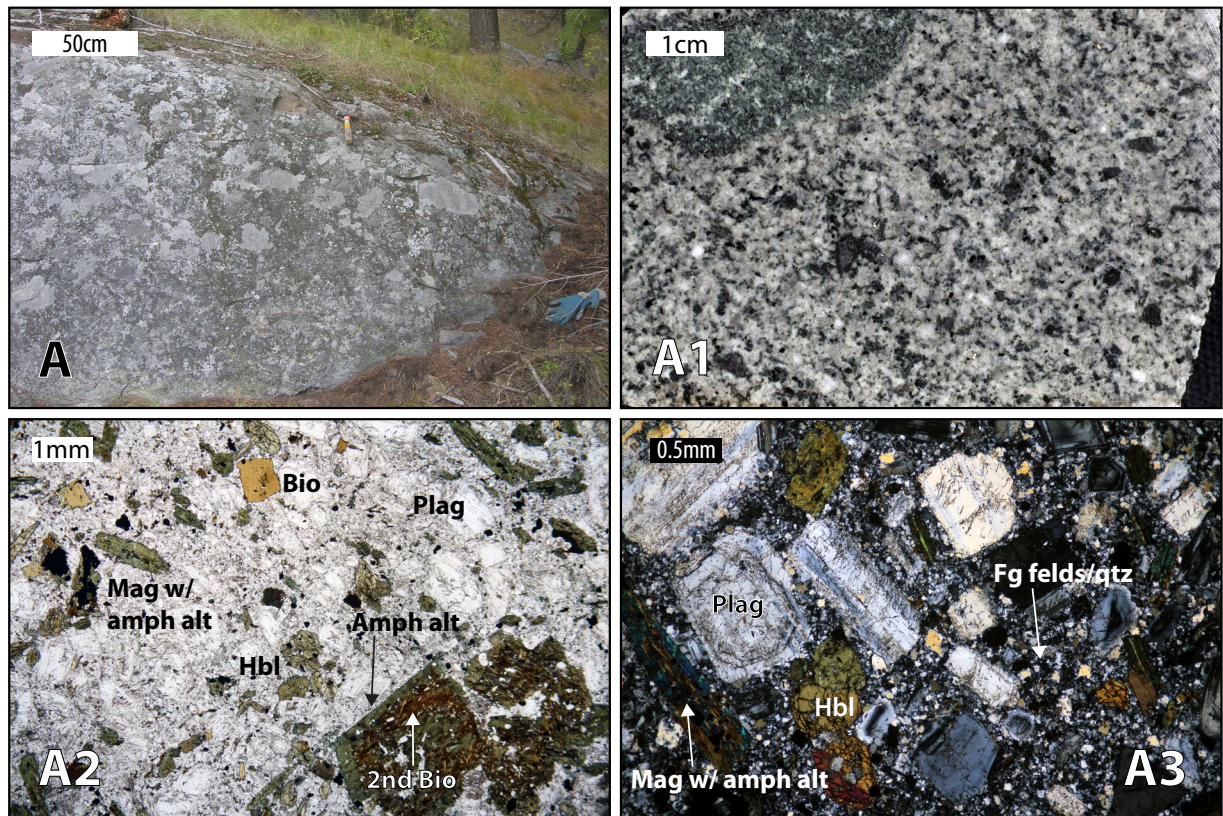


**Figure 2.18:** Examples of the Roosevelt Granodiorite that demonstrate the intrusive style, texture, mineralogy, and character of alteration and deformation.(A outcrop; A1 hand sample; A2 PPL photomicrograph; A3 XPL photomicrograph). See text for further discussion.

The Pink Granite has only been found in a small number of diamond drill holes in the Roosevelt Mine area, and no outcrops were found there during detailed mapping. Gaspar (2005) found the Pink Granite in contact with the Buckhorn Granodiorite in a drill hole and described it as medium-grained pink coloured equigranular granite with minor mafic content.

### 2.3.4.3 Alteration in the Intrusive Rocks

During the development of hornfels alteration in the metasedimentary and metavolcanic rocks, the BIS rocks underwent various types of alteration. The first stage is characterized by secondary biotite, magnetite and lesser potassium feldspar (Figure 2.10).The second stage is characterized by the development of amphibole and lesser plagioclase (Figure 2.10, Figure 2.12, and Figure 2.13). The final stage of alteration is characterized by the replacement of hornblende by chlorite, amphibole and epidote and the replacement plagioclase by sericite (Figure 2.10, Figure 2.12, Figure 2.13, and Figure 2.16). Based on the mineralogical characteristics the three stages are classified as potassic, sodic-calcic and propylitic alteration. All three types of alteration are unevenly developed in the BIS rocks, and are best preserved in the Buckhorn Granodiorite and the Buckhorn Diorite (Figure 2.10, Figure 2.13, and Figure 2.14).

Skarn alteration is locally developed in the BIS rocks, and is the most intense in the Early Diorite dikes and the Buckhorn Diorite, but has been documented in every rock type. Skarn alteration is dominantly composed of pyroxene-garnet prograde alteration and amphibole-epidote-pyrrhotite retrograde alteration (Figure 2.11 and Figure 2.17). Most of the skarn alteration is texturally destructive, leaving only small patches with igneous textures, and masking any earlier alteration. Skarn alteration in the BIS is spatially related to the emplacement of the Granodiorite dikes.

The RIS is much less altered than the other units in the Buckhorn area. The Roosevelt Granodiorite has undergone minor chloritic, sericite and potassic alteration, which is characterized by chlorite and sericite alteration of the mafic minerals and feldspars, along with minor secondary biotite development (Figure 2.18). The relative timing of the three alteration assemblages is unclear but likely progressed from potassic to sericite and chloritic alteration. Gaspar (2005) described the Pink Granite as being even less altered than the Roosevelt Granodiorite, having only undergone deuteric alteration.

### 2.3.4.3.1 Deformation

Deformation in the Buckhorn area is characterized by two low angle and one steeply northeast dipping foliations, and NNE normal faults. The low angle foliation and steeply dipping foliations occur in shear zones throughout the Buckhorn area, in all rock types except the Eocene RIS. The relative timing of skarn alteration and the foliations is ambiguous suggesting that they are coeval (Figure 4.4). The NNE normal faults post date the foliations and occur in all rock types, cutting all of the aforementioned metamorphism, alteration and deformation.

The two low angle foliations, and the corresponding shear zones, are the earliest, most prominent, and most abundant. Both low angle foliations are nearly flat lying and are sub-parallel to each other, and the second foliation may crenulate the first foliation (Figure 2.19). The exact orientation of these foliations has not been determined, so when only one low angle foliation is visible it is impossible to determine which one it is. The most prominent low angle shear zone occurs near the contact between the upper carbonate member of the BMS and the overlying BMV. This shear zone is nearly flat lying, cross cuts the contact, and affects both the carbonate and the volcanic rocks. The steeply northeast dipping foliation and shear zones are less abundant than the low angle variety. The most prominent of the steeply dipping shear zones is the Footwall Mylonite, which occurs between the SWOZ and the Gold Bowl, and also forms the southwestern edge of the Magnetic Mine (Figure 2.1). Elsewhere the northeast dipping shear zones cut the Buckhorn Granodiorite and related rocks.

In the clastic metasedimentary, volcanic, and intrusive rocks the foliations are defined by the alignment and deformation of metamorphic phyllosilicate minerals, whereas in the carbonate rocks the foliations are denoted by grain size variation and compositional bands (Figure 2.3, Figure 2.6, Figure 2.15, Figure 2.16, Figure 2.5, and Figure 2.19). In the intrusive rocks the foliations may locally be accompanied by increased propylitic alteration (Figure 2.10). The foliations have similar characteristics in the skarn alteration, where they are defined by the alignment and deformation of amphibole (Figure 4.4).
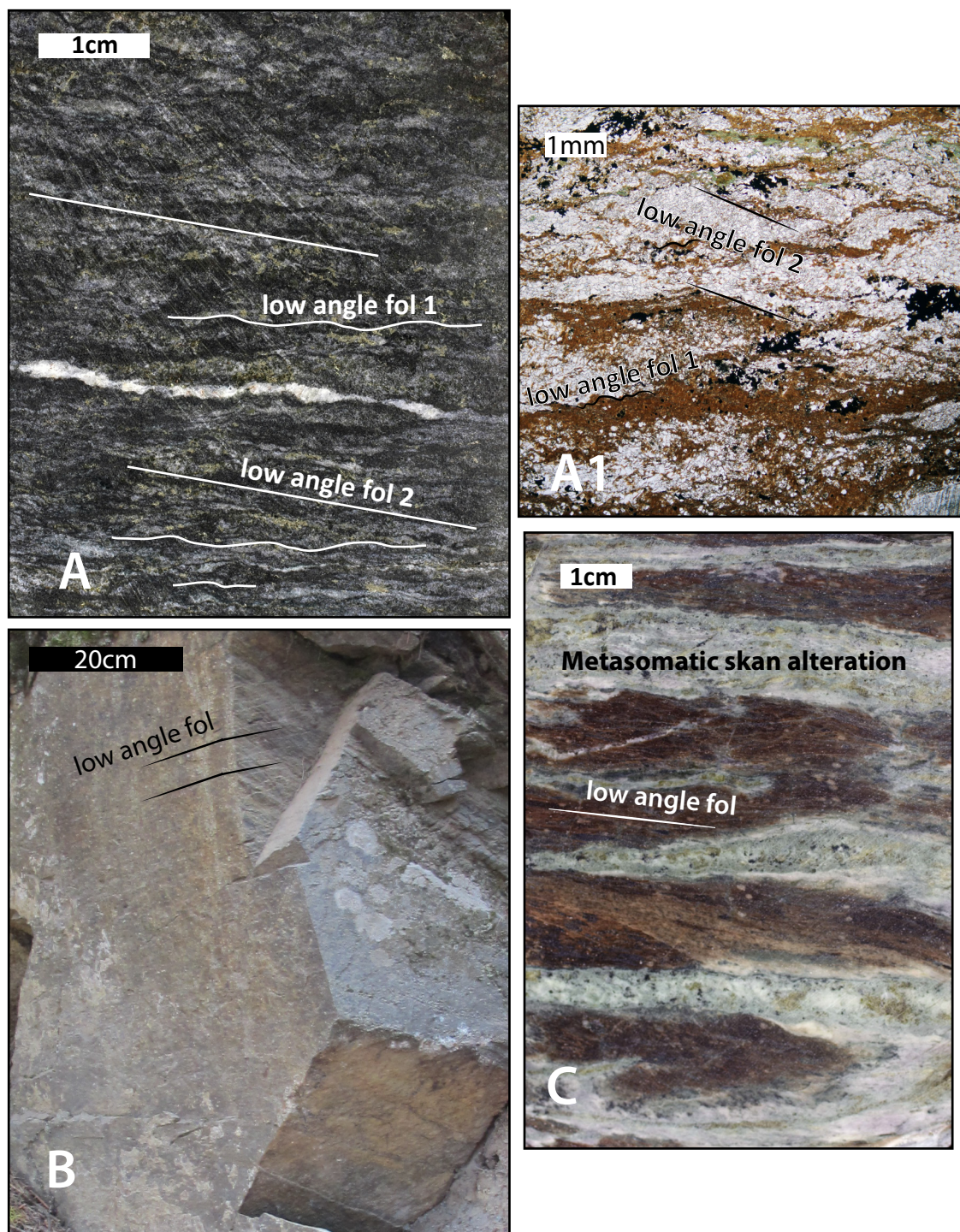
**Figure 2.19:** Examples of the two low angle foliations that demonstrates their characteristics at a variety of scale and in different rock types. (A and C hand samples of foliated metasedimentary and metavolcanic rocks; A1 PPL photomicrograph of foliated metasedimentary rock; B outcrop of a foliated Granodiorite dike).

The final stage of deformation to affect the BMS is characterized by steeply-dipping NNE oriented normal faults. The normal faults usually have low displacement (<30 m), and are more abundant on the east side of the Buckhorn area (Figure 2.1). The NNE normal faults cut all of the

rocks at Buckhorn, and postdate all of the metamorphism, alteration and deformation. The faults are subparallel to the Toroda Creek Graben Fault that forms the eastern margin of the Buckhorn rocks. The North Lookout Fault is the most important of the NNE normal faults as it offsets skarn alteration in the SWOZ (Figure 2.2). Several NNE striking normal faults can be inferred from drill hole data below the SWOZ, however some of these faults do not appear to offset the adjacent volcanic rocks (Figure 2.2), suggesting that some of the faults were active prior to volcanism during sedimentation in the late Paleozoic (Gaspar, 2005). Similar syn-sedimentary faults have been recognized in the Late Paleozoic strata of Nelson-Rossland area (Hoy and Dunne, 1997) and the Hedley district (Ray and Dawson, 1994).

## 2.4   Conclusions

The Buckhorn host rocks can be correlated with a number of other units of the Quesnel Terrane in southern British Columbia and northern Washington. The BMS is age equivalent to the Harper Ranch, Attwood, and Anarchist Groups, as well as the Mount Roberts Formation. All of these units are made up of carbonate, siliciclastic and volcanic rocks indicative of an arc environment, which is the expected depositional setting for late Paleozoic rocks in the Quesnel Terrane (Beatty, 2003; Cheney et al., 1994; Hoy and Dunne, 1997). Unconformably overlying the BMS is the BMV, which is correlated with the Elise formation. The BMV and the Elise formation have the same age (Figure 3.3), chemistry (Gaspar, 2005), and are composed of arc-related volcanic rocks that are characteristic for early Mesozoic rocks in the Quesnel Terrane (Hoy and Dunne, 1997). Prior to the emplacement of the BIS in the Middle Jurassic the host metasedimentary and metavolcanic rocks underwent greenschist facies metamorphism.

Intrusion of the BIS started with the Buckhorn Granodiorite (170.4 Ma), followed by the Mafic Diorite, Early Diorite dikes (169.4 Ma), Buckhorn Diorite (169.0 Ma), Granodiorite dikes (167.5 Ma), and finally the Quartz Porphyry dikes (163.3 Ma). Contact metamorphism related to the Buckhorn Granodiorite caused hornfels alteration in the host rocks that over print the greenschist facies metamorphism and obscured the original depositional textures in the BMS and to a lesser extent in the BMV. Two low angle and one steeply dipping foliations where developed in shear zones during the emplacement of the BIS, locally affecting all rock types. The shear zones were planes of higher permeability that focused the flow of skarn forming fluids, and partially controlled the location of skarn alteration.

Skarn alteration is related to the intrusion of the Granodiorite dikes, and has a diverse mineralogy that is made up of variable amounts or prograde pyroxene, garnet and magnetite, followed by retrograde amphibole, epidote, and pyrrhotite alteration. The association of skarn alteration with the Granodiorite dikes is similar to the Nickel Plate deposit in the Hedley Mining camp where dikes and sills acted as conduits for the mineralizing fluids (Ettlinger et al., 1992).The skarn alteration is coeval with the three foliations and both overprints foliated rock and is itself foliated. The skarn alteration also overprints the preceding stages of metamorphism and hornfels alteration, and affects all of the BIS rocks.

The Roosevelt Granodiorite of the RIS intruded the Buckhorn Granodiorite, Buckhorn Diorite, BMS and BMV in the Eocene (50.5 Ma). Following potassic, sodic-calcic and propylitic alteration the RIS was cut by the NNE normal faults, which also form the eastern margin of the Buckhorn rocks and offset skarn alteration in the SWOZ.

# Chapter 3.   U-Pb Geochronology

## 3.1   Introduction

The aim of this study is to confirm the age of the metavolcanic host rocks and local intrusive rocks at the Buckhorn gold skarn, and to constrain the age of deformation and skarn alteration at the deposit. The outcome of this work will aid in the proper correlation of the host rocks with the regional stratigraphy, and has implications for the genesis of the Buckhorn gold skarn. Age dating was accomplished through the determination of isotopic ratios of U-Pb in zircon by Laser Ablation Inductively Coupled Plasma Mass Spectrometry (LA-ICP-MS). The U-Pb isotopic system in zircon was chosen for its high closure temperature, about 900° C (Cherniak and Watson, 2001), which allows it to retain its magmatic age through metamorphism and a give reliable crystallization age for igneous rocks. The high closure temperature is necessary because the area experienced regional extension and intrusion of several granitoid stocks during the Eocene, which could have reset isotopic systems with lower closure temperatures. LA-ICP-MS was chosen for its high spatial resolution, which makes it possible to avoid the inclusions and fractures in the zircons, and its short analysis time that allows a larger number of samples to be analysed (Kosler and Sylvester, 2003).

### 3.1.1 Background

The Buckhorn gold skarn is hosted in a package of clastic and carbonate metasedimentary rocks, known as the Buckhorn Mountain Sequence (BMS), which are overlain by a package of metavolcanic rocks known as the Buckhorn Mountain Volcanic Sequence (BMV) (Gaspar, 2005). These rocks host several igneous stocks and associated dikes. Skarn alteration was preferentially developed along the foliated contact between the BMV and BMS and is spatially related to the Granodiorite dike phase of the Buckhorn Intrusive Suite (BIS) (Figure 2.2 and Figure 2.11). A detailed description of the Buckhorn area stratigraphy, including descriptions of the rock types and their geologic relationships, is in Chapter 2. Five igneous rock types have previously been dated: (1) the Buckhorn Granodiorite, (2) the Quartz Porphyry dikes, (3) the Granodiorite dikes, (4) the Roosevelt Granodiorite and (5) the Pink granite (Gaspar, 2005). The ages of four additional igneous rock types were previously unknown: (6) the Buckhorn Diorite, (7) the Early Diorite dikes, (8) the Mafic Diorite, and (9) an intrusive equivalent of the BMV.

Samples were collected from all of the aforementioned intrusive rocks as well as two examples of intrusions comagmatic with the BMV, except the Pink granite. Samples were also collected from a

pyroxene porphyry flow member of the BMV and from a conformable rhyolite layer in the BMS to constrain the age of these host rocks (Figure 2.1 and Table 3.1).

### 3.1.2 Sample Preparation

The samples were run through a crushing and grinding circuit that reduced the samples to approximately silt-sized fragments. They were then processed on a Wilfley® Concentrating Table to remove the least dense minerals, and separated using Methylene Iodide to remove minerals with a density less than 3.32 g/cm³. The dense minerals were then run through a Frantz® Magnetic Separator to remove the magnetic minerals. Zircons were picked by hand from the least magnetic separates with the aid of a binocular microscope. 25 to 55 of the largest, clearest and most inclusion free zircon grains from each sample were chosen for analysis. Depending on the number of grains selected, two or three samples were mounted in an epoxy cylinder with approximately 10 internationally recognized standards (Plešovice Zircon, Sláma et al., 2008), and 10 in-house standards. The cylinders were then polished and carbon-coated and taken to the scanning electron microscope (SEM) for imaging with back scatter electrons (BSE). Inclusions detected during BSE imaging were avoided during the laser ablation. Before the isotopic analysis the mounts were re-polished and washed with dilute nitric acid for ten minutes and then rinsed with high purity water.

### 3.1.3 Analytical Method and Data Reduction

The analyses were performed at the Pacific Centre for Isotopic and Geochemical Research (PCI-GR), at the University of British Columbia, employing the standard PCIGR methods as described by Tafti et al. (2009) and summarized below. Following imaging the mounts were loaded into a New Wave "Supercell" ablation chamber and ablated using a New Wave 213 nm Nd-YAG laser. The samples were then analyzed using a Finnigan Element2, single collector, double-focusing, magnetic sector high resolution ICP-MS.

Two zircon reference standards were used, an internationally recognized standard, Plešovice Zircon (Sláma et al., 2008) with an age of 337 Ma, and an internal standard with an age of 197 Ma. Twenty or more analyses were performed per sample using a 15 to 30 μm spot with 45 % laser power. High quality portions of each grain, free of alteration, inclusions, or inherited cores were selected for analysis. Line scans were done rather than spot analyses in order to minimize within-run elemental fractionation. Background levels were measured with the laser shutter closed for ten seconds, followed by data collection with the laser firing for approximately 35 seconds.

Corrections for mass and elemental fractionation were made by bracketing analyses of unknown grains with replicate analyses of the Plešovice zircon standard. A typical analytical session at the PCI-GR consists of four analyses of the Plešovice standard zircon, followed by two analyses of the in-house zircon standard, five analyses of unknown zircons, two standard analyses, five unknown analyses, etc., and finally two in-house zircon standards and four Plešovice standard analyses. The 197 Ma in-house zircon standard was analysed as an unknown in order to monitor the reproducibility of the age determinations on a run-to-run basis. The time-integrated signals were analysed using GLITTER software (Griffin et al., 2008; van Achterbergh et al., 2001), which automatically subtracts background measurements, propagates all analytical errors, and calculates isotopic ratios and ages. The time-integrated data was carefully examined to identify and avoid portions of the signal that reflected lead loss, the analysis of older inherited cores or altered zones in the zircon or a combination of all three.

Final interpretation and plotting of the analytical results employed the ISOPLOT v. 4.13 software of Ludwig (2009). The ages reported are concordant ages and weighted average $^{206}Pb/^{238}U$ ages. These ages were chosen as they are the most accurate and precise for Phanerozoic rocks. Errors for the calculated isotopic ratios are given at the 1 sigma level and errors on calculated ages are given at the 2 sigma level.

Analyses were excluded from the final interpretation with ISOPLOT if they fell into one of five categories discussed in Campbell et al. (2006). These categories are as follows: analysis that exhibit (1) internal age zoning, (2) discordant ages, (3) indication of the zircon being a xenocryst, (4) indication of the zircon being affected by post crystallization lead loss, or (5) evidence of subtle inheritance. The objective criteria modified from Campbell et al. (2006) were used to reject analyses and return the most accurate and precise age possible.

Internal age zoning was detected by analysing the time integrated signals in GLITTER prior to interpretation in ISOPLOT. It was performed by choosing portions of the signal with consistent $^{206}Pb/^{238}U$ and $^{207}Pb/^{235}U$ ratios, and portions with mixed signals were discarded. Analyses were deemed discordant if their $^{207}Pb/^{235}U$ age divided by their $^{206}Pb/^{238}U$ age was greater or less than 1 ± 0.1. Approximately 8 % of the analyses were discordant. If an analysis returned an age that was clearly older than the crystallization age of the rock it was deemed a xenocryst. With the exception of sample BS076, this was easily determined because the xenocrysts were usually at least 180 million years older than the average age determined for the rock. The specifics of BS076 are discussed later in the chapter.

Evidence for post crystallization lead loss and/or subtle inheritance affecting the zircons was present in analyses from each sample. The subtle lead loss or inheritance was objectively detected using linear cumulative probability plots. Linear cumulative probability plots are designed to show data with a normal distribution in a straight line with a positive slope. Different populations will appear as straight lines separated by inflection points. Figure 3.1 shows a linear cumulative probability plot for sample BS057 that shows the analysis of zircon that have been affected by both subtle lead loss and inheritance.

Following dating, select zircons were imaged using cathodoluminescence microscopy (CL). This was done on samples where complex inheritance was detected in the age results. Imaging with CL showed more complex growth patterns than was detected with BSE imaging and aided the interpretation of those samples. In retrospect, due to the complexity of the growth patterns detected by post dating CL imaging and the inheritance and leads loss detected in the age dates, it would have been beneficial to image all the zircons from all the samples with CL prior to dating. Unfortunately a CL imaging apparatus was not available to use at the time of dating.

**Table 3.1:** Summary of analysis quality

| Unit/ Sample no. | $^{206}Pb/^{238}U$ Age (Ma) | ±2σ(Ma) | Analyses Used (n) | Total Analyses (N) | Grains Excluded | | | | |
| --- | --- | --- | --- | --- | --- | --- | --- | --- | --- |
| | | | | | MSWD | Xenocrysts | Discord | Lead Loss | Inheritance |
| Intrusion comagmatic with the BMV | | | | | | | | | |
| BS064 | 193.5 | 1.2 | 37 | 55 | 1.4 | | 4 | 10 | 4 |
| Buckhorn Granodiorite (BGdi) | | | | | | | | | |
| BS048 | 170.4 | 1.7 | 12 | 20 | 2 | 2 | | 6 | |
| BS074 | 167.8 | 1.5 | 8 | 20 | 0.91 | 2 | 2 | 8 | |
| BS057 | 165.99 | 0.97 | 15 | 20 | 0.86 | | 1 | 3 | 1 |
| Early Diorite (EDiD) | | | | | | | | | |
| BS046 | 168.15 | 0.7 | 14 | 20 | 0.32 | 3 | | 2 | 1 |
| BS075 | 169.3 | 1.5 | 14 | 20 | 1.2 | | 3 | | 3 |
| Buckhorn Diorite (BDi) | | | | | | | | | |
| BS060 | 168.94 | 0.86 | 15 | 20 | 1.05 | | 1 | 1 | 3 |
| Granodiorite dikes (GDiD | | | | | | | | | |
| BS059 | 167.51 | 0.72 | 17 | 20 | 0.98 | 1 | | 2 | |
| Roosevelt Granodiorite (RGDi) | | | | | | | | | |
| BS076 | 50.8 | 2.9 | 2 | 20 | 0.025 | 12 | 6 | | |
| Total | | | 134 | 215 | | 20 | 17 | 32 | 12 |
| Percentages | | | 62.3% | | | 9.3% | 7.9% | 14.9% | 5.6% |
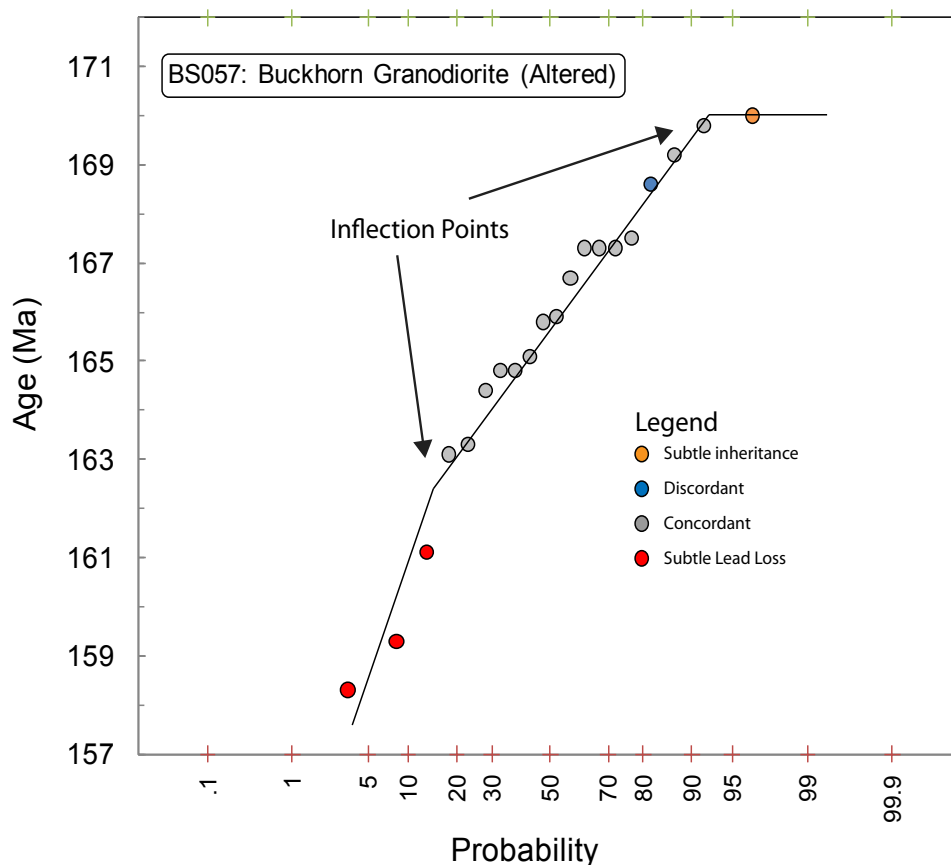
**Figure 3.1:** Linear cumulative probability plot of sample BS057. The analyses affected by subtle lead loss and inheritance are highlighted. The colour scheme will be used in subsequent figures.

## 3.2   Samples and Results

### 3.2.1 Buckhorn Mountain Volcanic Sequence (BMV)

Gold mineralization and skarn alteration at Buckhorn are hosted in the metavolcanic rocks of the BMV and the metasedimentary rocks of the BMS. As described in Chapter 2 the BMV is predominately made up of sub-aerial porphyritic flows and autobreccias, with minor tuffs, and dike- and plug-like comagmatic intrusions (Figure 2.6, Figure 2.7, and Figure 2.8). Rocks of the BMV have not been previously isotopically dated and there is a long standing disagreement over their age. McMillen (1979), Hickey (1990, 1992), and Stoffel (1990a) correlate them with the Permian-Triassic Kobau or Knob Hill Group; McMillen (1979) also suggests a portion of the BMV may be equivalent to the Triassic Brooklyn Formation, where as Cheney et al. (1994) and Gaspar (2005) correlate them with the Jurassic Elise Formation. Determining the age of the BMV resolves this disagreement. Three samples were collected for dating; two from different intrusive rocks comagmatic with the BMV, and a third from a pyroxene porphyry flow. Sample BS063 was selected from a plug-like body of the equigranular

variety of intrusive BMV that cross cuts the upper carbonate member of the BMS. Sample BS064 was selected from a dike-like body of the porphyritic variety of the intrusive BMV that cross-cuts the BMV flows. Sample BS065 was selected from a pyroxene porphyry flow.

Only the porphyritic intrusive sample, BS064, yielded zircons. The zircons are subhedral to nearly euhedral. Most grains are about 100 μm, but about 10 % are 200 to 350 μm. BSE imaging shows that both size fractions have inclusions and fractures, but growth zoning and inherited cores are not visible (Figure 3.2). Sample BS064 yielded a concordant age of 192.4 ± 1.0 Ma and a weighted average $^{206}Pb/^{238}U$ age of 193.5 ± 1.2 Ma (Figure 3.3), based on thirty-seven of the fifty-five zircons analysed. Ten of the eighteen zircons excluded from the age calculations were affected by subtle lead loss, four by subtle inheritance, and four were discordant (Table 3.2 and Figure 3.2). Analyses of zircons from both size fractions are included in the results, and there was no correlation between the size of the zircon and its age.

The concordant data provide the first isotopically determined age for the BMV, which allows the BMV to be compared to age equivalent rocks in southern British Columbia. In the Nelson area several plutons and other small plugs, dikes and sills have been interpreted as comagmatic with the Elise Formation. These comagmatic intrusions have not been dated, but they are expected to be approximately the same age as the Elise Formation, which was deposited in the late Sinemurian (197-190 Ma) (Hoy and Dunne, 1997). As explained previously (Chapter 2) the BMV is mineralogically, texturally and geochemically similar to the Elise Formation. Based on the overlap of depositional age of the Elise Formation and the intrusive age of sample BS064, it is the likely that the porphyritic intrusive sample of the BMV is equivalent to the intrusive equivalents of the Elise Formation, and the BMV is therefore equivalent to the Elise Formation.
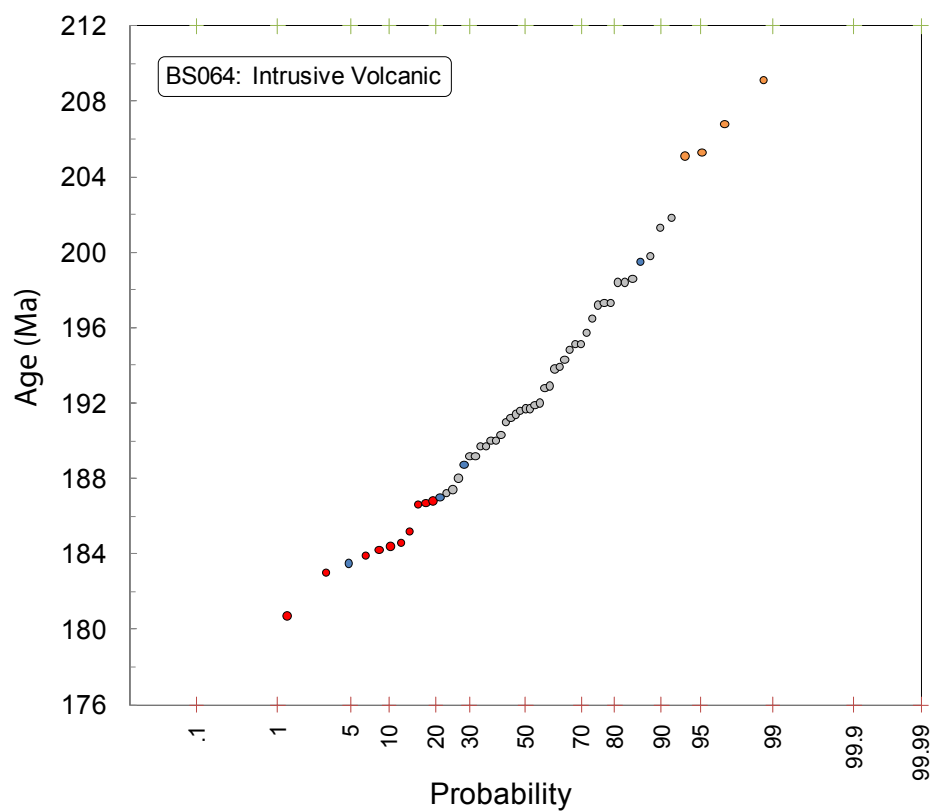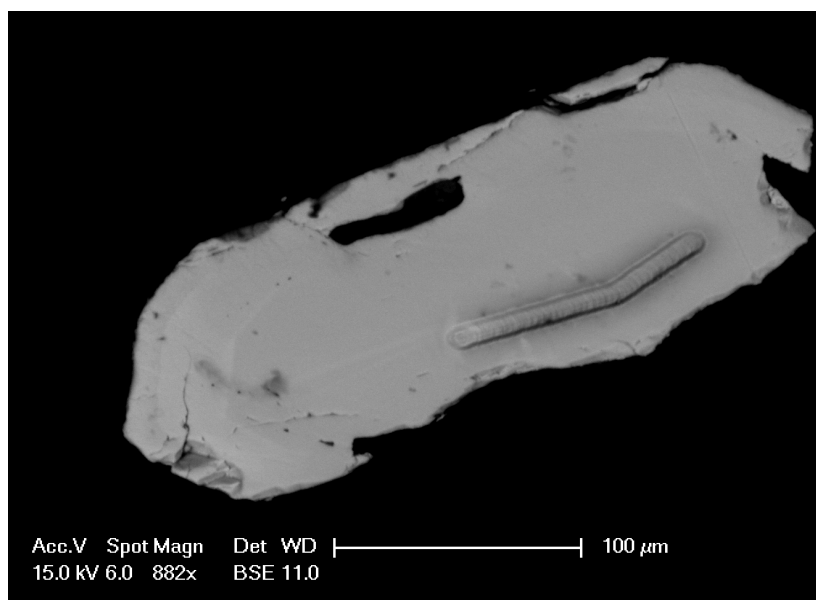
**Figure 3.2:** BSE image of a representative zircon and linear cumulative probability plot for sample BS064

**Table 3.2:** Isotope ratios and age estimates for sample BS064, porphyritic intrusion comagmatic with the BMV

| | Table 3.2 | | | | | | | | U/Pb LA-ICP-MS data and calculated ages | | | | | | |
|---|---|---|---|---|---|---|---|---|---|---|---|---|---|---|---|

| | | Isotopic ratios | | | | | | | Age estimates (Ma) | | | | | | |
| Rock Type | Sample-analysis | $^{207}Pb/^{206}Pb$ | ± 1σ | $^{207}Pb/^{235}U$ | ± 1σ | $^{206}Pb/^{238}U$ | ± 1σ | Rho | $^{207}Pb/^{206}Pb$ | ± 1σ | $^{207}Pb/^{235}U$ | ± 1σ | $^{206}Pb/^{238}U$ | ± 1σ | Dis-cord. | Comments |
|---|---|---|---|---|---|---|---|---|---|---|---|---|---|---|---|---|
| BMV | BS064-1 | 0.0421 | 0.0034 | 0.1719 | 0.0140 | 0.0297 | 0.0007 | 0.30 | 0.1 | 0 | 161.1 | 12.14 | 188.7 | 4.52 | 0.854 | Discordant |
| BMV | BS064-2 | 0.0539 | 0.0023 | 0.2263 | 0.0099 | 0.0310 | 0.0005 | 0.36 | 368.1 | 92.04 | 207.1 | 8.21 | 196.5 | 3.04 | 1.054 | |
| BMV | BS064-3 | 0.0646 | 0.0101 | 0.2658 | 0.0418 | 0.0289 | 0.0014 | 0.30 | 761.9 | 298.16 | 239.3 | 33.54 | 183.5 | 8.67 | 1.304 | Discordant |
| BMV | BS064-4 | 0.0540 | 0.0018 | 0.2246 | 0.0078 | 0.0302 | 0.0004 | 0.36 | 368.6 | 72.76 | 205.7 | 6.46 | 191.7 | 2.35 | 1.073 | |
| BMV | BS064-5 | 0.0493 | 0.0054 | 0.1985 | 0.0218 | 0.0295 | 0.0009 | 0.29 | 160.8 | 235.82 | 183.9 | 18.46 | 187.4 | 5.86 | 0.981 | |
| BMV | BS064-6 | 0.0507 | 0.0013 | 0.2066 | 0.0056 | 0.0290 | 0.0003 | 0.36 | 225.5 | 57.88 | 190.7 | 4.72 | 184.2 | 1.74 | 1.035 | Pb Loss |
| BMV | BS064-7 | 0.0505 | 0.0015 | 0.2037 | 0.0064 | 0.0294 | 0.0003 | 0.36 | 218.6 | 68.01 | 188.2 | 5.42 | 186.8 | 2.05 | 1.007 | Pb Loss |
| BMV | BS064-8 | 0.0524 | 0.0022 | 0.2090 | 0.0091 | 0.0290 | 0.0004 | 0.35 | 301.4 | 92.99 | 192.7 | 7.61 | 184.4 | 2.76 | 1.045 | Pb Loss |
| BMV | BS064-9 | 0.0517 | 0.0026 | 0.2049 | 0.0105 | 0.0284 | 0.0005 | 0.34 | 272.7 | 110.3 | 189.3 | 8.83 | 180.7 | 3.1 | 1.048 | Pb Loss |
| BMV | BS064-10 | 0.0494 | 0.0018 | 0.1950 | 0.0075 | 0.0291 | 0.0004 | 0.35 | 166 | 84.81 | 180.9 | 6.4 | 185.2 | 2.46 | 0.977 | Pb Loss |
| BMV | BS064-11 | 0.0466 | 0.0095 | 0.2230 | 0.0459 | 0.0323 | 0.0016 | 0.25 | 26 | 426.22 | 204.4 | 38.12 | 205.1 | 10.23 | 0.997 | Inheritance |
| BMV | BS064-12 | 0.0506 | 0.0063 | 0.2017 | 0.0254 | 0.0290 | 0.0011 | 0.29 | 222.8 | 264.53 | 186.6 | 21.46 | 184.6 | 6.64 | 1.011 | Pb Loss |
| BMV | BS064-13 | 0.0523 | 0.0062 | 0.2328 | 0.0279 | 0.0305 | 0.0011 | 0.31 | 299.8 | 248.15 | 212.5 | 22.97 | 193.8 | 7.02 | 1.096 | |
| BMV | BS064-14 | 0.0502 | 0.0025 | 0.2116 | 0.0110 | 0.0317 | 0.0006 | 0.35 | 202.6 | 112.77 | 194.9 | 9.2 | 201.3 | 3.59 | 0.968 | |
| BMV | BS064-15 | 0.0498 | 0.0017 | 0.2127 | 0.0076 | 0.0313 | 0.0004 | 0.35 | 186.3 | 77.91 | 195.8 | 6.38 | 198.6 | 2.41 | 0.986 | |
| BMV | BS064-16 | 0.0468 | 0.0032 | 0.1945 | 0.0136 | 0.0313 | 0.0007 | 0.32 | 38 | 156.28 | 180.5 | 11.55 | 198.4 | 4.32 | 0.910 | |
| BMV | BS064-17 | 0.0496 | 0.0047 | 0.2116 | 0.0206 | 0.0326 | 0.0010 | 0.30 | 175.8 | 208.87 | 194.9 | 17.24 | 206.8 | 6 | 0.942 | Inheritance |
| BMV | BS064-18 | 0.0477 | 0.0022 | 0.2019 | 0.0096 | 0.0311 | 0.0005 | 0.34 | 81.5 | 106.56 | 186.7 | 8.11 | 197.3 | 3.12 | 0.946 | |
| BMV | BS064-19 | 0.0518 | 0.0014 | 0.2144 | 0.0063 | 0.0301 | 0.0003 | 0.35 | 275.2 | 61.85 | 197.2 | 5.24 | 191 | 1.94 | 1.032 | |
| BMV | BS064-20 | 0.0540 | 0.0037 | 0.2259 | 0.0159 | 0.0307 | 0.0007 | 0.34 | 370 | 147.71 | 206.8 | 13.17 | 194.8 | 4.64 | 1.062 | |
| BMV | BS064-21 | 0.0474 | 0.0017 | 0.1940 | 0.0073 | 0.0301 | 0.0004 | 0.34 | 69.4 | 84.55 | 180 | 6.23 | 191.2 | 2.46 | 0.941 | |
| BMV | BS064-22 | 0.0507 | 0.0018 | 0.2133 | 0.0081 | 0.0305 | 0.0004 | 0.34 | 225 | 81.96 | 196.3 | 6.78 | 193.9 | 2.53 | 1.012 | |
| BMV | BS064-23 | 0.0514 | 0.0017 | 0.2193 | 0.0074 | 0.0308 | 0.0004 | 0.35 | 259.9 | 72.35 | 201.4 | 6.2 | 195.7 | 2.3 | 1.029 | |
| BMV | BS064-24 | 0.0517 | 0.0024 | 0.2105 | 0.0102 | 0.0288 | 0.0005 | 0.35 | 270.8 | 103.8 | 193.9 | 8.53 | 183 | 3.04 | 1.060 | Pb Loss |

Table 3.2 — U/Pb LA-ICP-MS data and calculated ages

| Rock Type | Sample-analysis | Isotopic ratios | | | | | | | Age estimates (Ma) | | | | | | | Comments |
|---|---|---|---|---|---|---|---|---|---|---|---|---|---|---|---|---|
| | | $^{207}Pb/^{206}Pb$ | ± 1σ | $^{207}Pb/^{235}U$ | ± 1σ | $^{206}Pb/^{238}U$ | ± 1σ | Rho | $^{207}Pb/^{206}Pb$ | ± 1σ | $^{207}Pb/^{235}U$ | ± 1σ | $^{206}Pb/^{238}U$ | ± 1σ | Dis-cord. | |
| BMV | BS064-25 | 0.0410 | 0.0065 | 0.1893 | 0.0304 | 0.0304 | 0.0012 | 0.25 | 0.1 | 73.26 | 176 | 25.94 | 192.9 | 7.78 | 0.912 | |
| BMV | BS064-26 | 0.0493 | 0.0021 | 0.2089 | 0.0091 | 0.0299 | 0.0005 | 0.35 | 161.4 | 95.03 | 192.6 | 7.63 | 190 | 2.81 | 1.014 | |
| BMV | BS064-27 | 0.0570 | 0.0050 | 0.2474 | 0.0220 | 0.0330 | 0.0010 | 0.33 | 490.7 | 181.69 | 224.5 | 17.88 | 209.1 | 6.14 | 1.074 | Inheritance |
| BMV | BS064-28 | 0.0530 | 0.0046 | 0.2028 | 0.0180 | 0.0301 | 0.0009 | 0.33 | 327.2 | 187.13 | 187.5 | 15.2 | 191.4 | 5.47 | 0.980 | |
| BMV | BS064-29 | 0.0546 | 0.0066 | 0.2100 | 0.0258 | 0.0298 | 0.0012 | 0.31 | 395.9 | 251.45 | 193.6 | 21.62 | 189.2 | 7.21 | 1.023 | |
| BMV | BS064-30 | 0.0492 | 0.0016 | 0.2039 | 0.0072 | 0.0311 | 0.0004 | 0.35 | 156.9 | 76.4 | 188.4 | 6.05 | 197.2 | 2.36 | 0.955 | |
| BMV | BS064-31 | 0.0507 | 0.0031 | 0.2029 | 0.0129 | 0.0296 | 0.0006 | 0.33 | 225.2 | 137.32 | 187.6 | 10.88 | 188 | 3.9 | 0.998 | |
| BMV | BS064-32 | 0.0488 | 0.0023 | 0.2108 | 0.0101 | 0.0306 | 0.0005 | 0.34 | 138.2 | 104.71 | 194.2 | 8.45 | 194.3 | 3.1 | 0.999 | |
| BMV | BS064-33 | 0.0475 | 0.0030 | 0.2040 | 0.0131 | 0.0307 | 0.0007 | 0.33 | 72 | 142.93 | 188.5 | 11.06 | 195.1 | 4.15 | 0.966 | |
| BMV | BS064-34 | 0.0482 | 0.0023 | 0.2020 | 0.0101 | 0.0302 | 0.0005 | 0.33 | 106.9 | 110.68 | 186.8 | 8.55 | 192 | 3.13 | 0.973 | |
| BMV | BS064-35 | 0.0507 | 0.0022 | 0.2039 | 0.0091 | 0.0300 | 0.0005 | 0.35 | 227.3 | 96.43 | 188.4 | 7.68 | 190.3 | 2.93 | 0.990 | |
| BMV | BS064-36 | 0.0486 | 0.0019 | 0.2016 | 0.0082 | 0.0302 | 0.0004 | 0.34 | 128.4 | 89.32 | 186.5 | 6.94 | 191.7 | 2.61 | 0.973 | |
| BMV | BS064-37 | 0.0530 | 0.0030 | 0.2149 | 0.0127 | 0.0289 | 0.0006 | 0.35 | 329.4 | 124.96 | 197.6 | 10.6 | 183.9 | 3.67 | 1.074 | Pb Loss |
| BMV | BS064-38 | 0.0500 | 0.0022 | 0.2086 | 0.0095 | 0.0299 | 0.0005 | 0.34 | 197 | 98.45 | 192.4 | 7.96 | 189.7 | 2.9 | 1.014 | |
| BMV | BS064-39 | 0.0533 | 0.0018 | 0.2222 | 0.0080 | 0.0294 | 0.0004 | 0.35 | 340 | 75.77 | 203.8 | 6.68 | 186.6 | 2.32 | 1.092 | Pb Loss |
| BMV | BS064-40 | 0.0497 | 0.0027 | 0.2008 | 0.0113 | 0.0298 | 0.0006 | 0.34 | 182 | 122.82 | 185.8 | 9.58 | 189.2 | 3.57 | 0.982 | |
| BMV | BS064-41 | 0.0439 | 0.0054 | 0.1950 | 0.0242 | 0.0302 | 0.0011 | 0.29 | 0.1 | 160.26 | 180.8 | 20.54 | 191.6 | 6.81 | 0.944 | |
| BMV | BS064-42 | 0.0436 | 0.0038 | 0.1967 | 0.0173 | 0.0313 | 0.0008 | 0.29 | 0.1 | 68.65 | 182.3 | 14.7 | 198.4 | 5.04 | 0.919 | |
| BMV | BS064-43 | 0.0478 | 0.0029 | 0.2059 | 0.0130 | 0.0307 | 0.0006 | 0.32 | 90.2 | 140.66 | 190.1 | 10.97 | 195.1 | 3.86 | 0.974 | |
| BMV | BS064-44 | 0.0493 | 0.0022 | 0.2072 | 0.0098 | 0.0311 | 0.0005 | 0.34 | 162.3 | 102.94 | 191.2 | 8.23 | 197.3 | 3.11 | 0.969 | |
| BMV | BS064-45 | 0.0440 | 0.0036 | 0.1845 | 0.0154 | 0.0314 | 0.0008 | 0.30 | 0.1 | 78.94 | 171.9 | 13.19 | 199.5 | 4.91 | 0.862 | Discordant |
| BMV | BS064-46 | 0.0506 | 0.0026 | 0.1976 | 0.0103 | 0.0294 | 0.0005 | 0.35 | 221.3 | 112.41 | 183.1 | 8.71 | 186.7 | 3.31 | 0.981 | Pb Loss |
| BMV | BS064-47 | 0.0499 | 0.0018 | 0.2182 | 0.0083 | 0.0324 | 0.0004 | 0.34 | 192.1 | 81.5 | 200.4 | 6.9 | 205.3 | 2.63 | 0.976 | Inheritance |
| BMV | BS064-48 | 0.0505 | 0.0019 | 0.2085 | 0.0082 | 0.0304 | 0.0004 | 0.34 | 219.8 | 84.46 | 192.3 | 6.9 | 192.8 | 2.57 | 0.997 | |
| BMV | BS064-49 | 0.0507 | 0.0023 | 0.2127 | 0.0100 | 0.0315 | 0.0005 | 0.35 | 226.2 | 100.79 | 195.8 | 8.35 | 199.8 | 3.17 | 0.980 | |

Table 3.2　　　　　　　　　　　　　　　　　　　　　　　　　U/Pb LA-ICP-MS data and calculated ages

| Rock Type | Sample-analysis | Isotopic ratios | | | | | | | Age estimates (Ma) | | | | | | | Comments |
|---|---|---|---|---|---|---|---|---|---|---|---|---|---|---|---|---|
| | | $^{207}Pb/^{206}Pb$ | ± 1σ | $^{207}Pb/^{235}U$ | ± 1σ | $^{206}Pb/^{238}U$ | ± 1σ | Rho | $^{207}Pb/^{206}Pb$ | ± 1σ | $^{207}Pb/^{235}U$ | ± 1σ | $^{206}Pb/^{238}U$ | ± 1σ | Dis-cord. | |
| BMV | BS064-50 | 0.0506 | 0.0018 | 0.2128 | 0.0082 | 0.0302 | 0.0004 | 0.34 | 220.3 | 82.15 | 195.9 | 6.84 | 191.9 | 2.49 | 1.021 | |
| BMV | BS064-51 | 0.0520 | 0.0032 | 0.2017 | 0.0128 | 0.0295 | 0.0006 | 0.33 | 284.9 | 135.04 | 186.6 | 10.78 | 187.2 | 3.87 | 0.997 | |
| BMV | BS064-52 | 0.0575 | 0.0041 | 0.2323 | 0.0171 | 0.0294 | 0.0008 | 0.35 | 511.6 | 151.1 | 212.1 | 14.12 | 187 | 4.68 | 1.134 | Discordant |
| BMV | BS064-53 | 0.0510 | 0.0020 | 0.2121 | 0.0088 | 0.0299 | 0.0004 | 0.35 | 240.9 | 88.68 | 195.3 | 7.37 | 190 | 2.67 | 1.028 | |
| BMV | BS064-54 | 0.0531 | 0.0023 | 0.2204 | 0.0098 | 0.0299 | 0.0005 | 0.35 | 333.3 | 93.71 | 202.3 | 8.18 | 189.7 | 2.87 | 1.066 | |
| BMV | BS064-55 | 0.0488 | 0.0023 | 0.2013 | 0.0098 | 0.0318 | 0.0005 | 0.34 | 137.7 | 106.85 | 186.3 | 8.32 | 201.8 | 3.3 | 0.923 | |
| Weighted average (95% confidence level) | | | | | | | | | | | **192.9** | **2.7** | **193.5** | **1.2** | | |
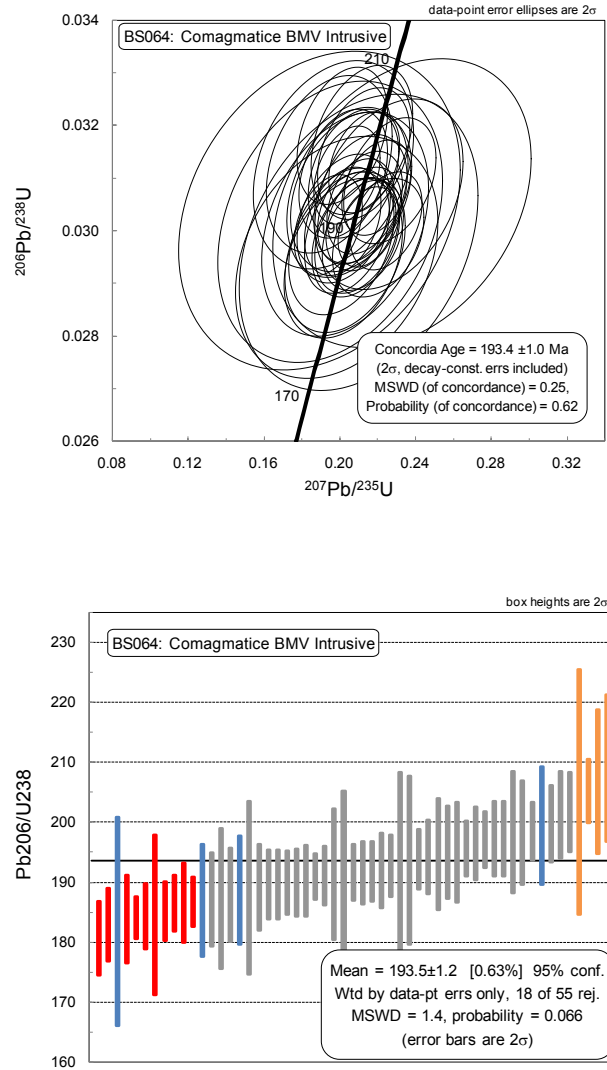
**Figure 3.3:** Concordia and weighted average diagrams for sample BS064

### 3.2.2 Buckhorn Granodiorite

The Buckhorn Granodiorite covers an area of approximately 19 km² northeast of the Buckhorn gold skarn (Figure 2.1). The Buckhorn Granodiorite is the largest component of the BIS, which also includes the Buckhorn Diorite and several generations of dikes. To determine if there is significant variability in age within the stock and to more precisely date Buckhorn Granodiorite, three samples were evaluated. Sample BS048 was collected about 85 m from the intrusive contact, and approximately 10 m from a steeply-dipping northeast oriented shear zone. Sample BS074 was collected near the center of the stock, about 1.7 km from its margin, and has intense sericite and chlorite alteration. Sample BS057 is intensely deformed and altered and was collected from near the Roosevelt Mine. The

deformation in sample BS057 is dominated by the steeply north-east dipping foliation that occurs throughout the entire BS057 outcrop for over 10 m. Sample BS057 is also affected by intense sericite and chlorite alteration. Samples BS048 and BS057 will also provide a maximum age for the deformation event responsible for the steeply dipping foliation and the Footwall Mylonite.

The zircons from samples BS048 and BS074 are clear, near euhedral elongate crystals about 100 µm wide and up to 300 µm long. A few inherited cores and inclusions were detected by BSE imaging, and were avoided during analysis. A few concentric growth zones and fractures were also visible with BSE imaging; the latter was avoided during analysis to minimize the potential of lead loss (Figure 3.4). BS048 gives a concordant age of 170.4 ± 1.1 Ma and a weighted average $^{206}Pb/^{238}U$ age of 170.4 ± 1.7 Ma (Figure 3.5). These ages are based on twelve of the twenty zircons analysed. Two of the zircons analysed were xenocrysts, and have ages of about 350 Ma and 1.05 Ga, the remaining six had experienced subtle lead loss (Table 3.3 and Figure 3.5). Sample BS074 gives a concordant age of 167.8 ± 1.5 Ma and an identical weighted average $^{206}Pb/^{238}U$ age of 167.8 ± 1.5 Ma (Figure 3.5). Twelve of the twenty analyses were excluded from the age calculations. Two zircons, with ages of approximately 1.4 and 1.8 Ga, are interpreted as xenocrysts. Two of the zircons had discordant ages, and eight had been affected by subtle lead loss (Table 3.4 and Figure 3.5).

In contrast to the other granodiorite samples, the zircons from BS057 are mostly subhedral and near equant crystals that range from 100 to 200 µm. Clear in transmitted light, growth zoning was rarely visible and a single core was detected with BSE imaging. Zircons from sample BS057 have inclusions that are up to 20 µm (Figure 3.7). The analysis gives a concordant age of 166.0 ± 1.0 Ma and a weighted average $^{206}Pb/^{238}U$ age of 166.0 ± 1.0 Ma (Figure 3.8). These ages are based on fifteen of the twenty zircons analysed. Three of the excluded zircons had experienced subtle lead loss, one was discordant and the fifth was affected by subtle inheritance (Table 3.5 and Figure 3.7).

These results more precisely and accurately constrain the maximum age of the Buckhorn Granodiorite compared to the 169.4 ± 2.3 Ma age determined by Gaspar (2005). They also clearly indicate that the development of the steeply dipping shear zones occurred after 170.4 Ma and that the deformation event responsible for them persisted until at least 166.0 Ma. These results are also important because they show that the BIS experienced alteration and deformation on a large scale, and not only in meter-scale shear zones as previously thought (Gaspar, 2005). The difference in absolute ages between the three samples can be explained in two ways. The first explanation is that samples BS074

and BS057 are younger phases of granodiorite, rather than truly part of the Buckhorn Granodiorite stock. The intensity of alteration and deformation in the two younger samples makes their positive identification as dikes uncertain. However, their ages and the geochemistry of BS074, which deviates from the expected zoning of the stock (M. Deal, personal communication 2011), suggest that samples BS057 and BS074 are Granodiorite dikes. The second possibility is that, as the ages overlap at the 2 sigma level, all three samples represent the same intrusion, and the difference in chemistry is due to the intensity of alteration in sample BS074. This conclusion is supported by the fact that intrusive contacts were not identified during mapping of the sample locations.
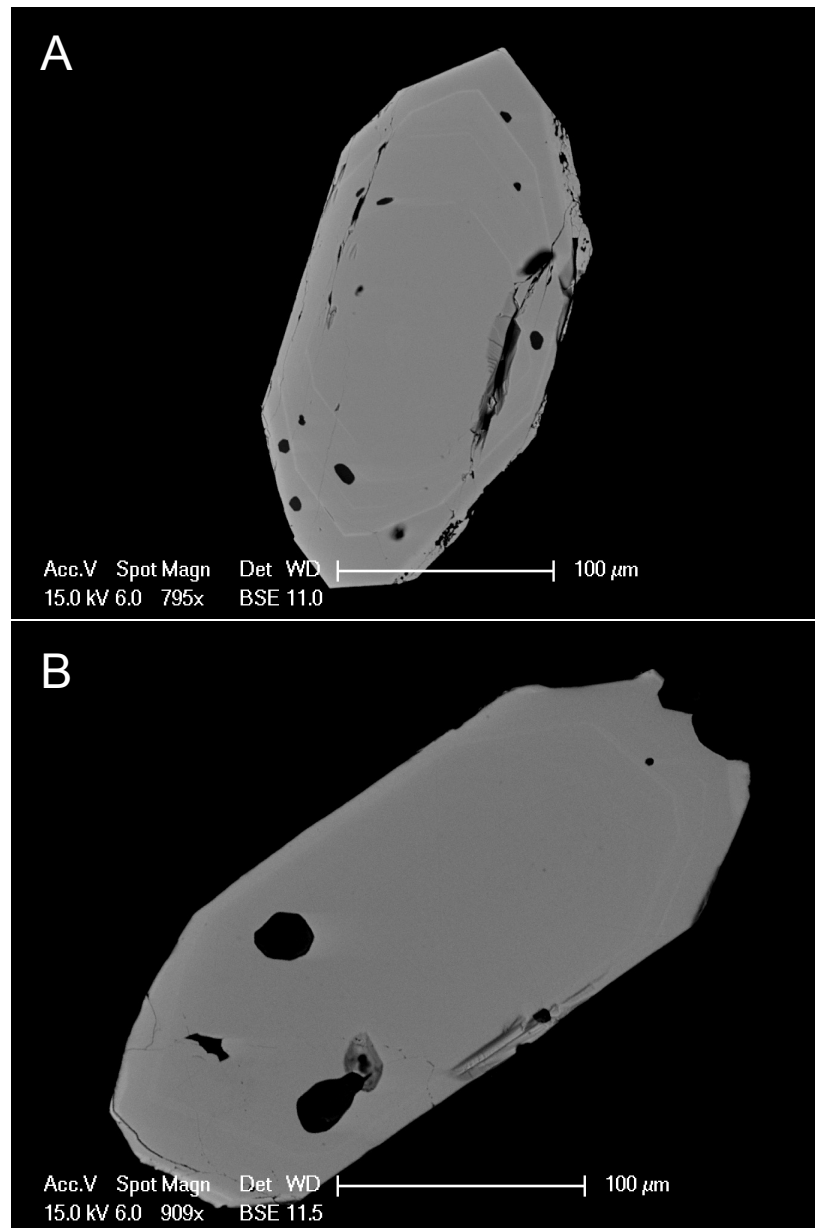


**Figure 3.4:** BSE image of representative zircons from samples BS048 (A) and BS074 (B)
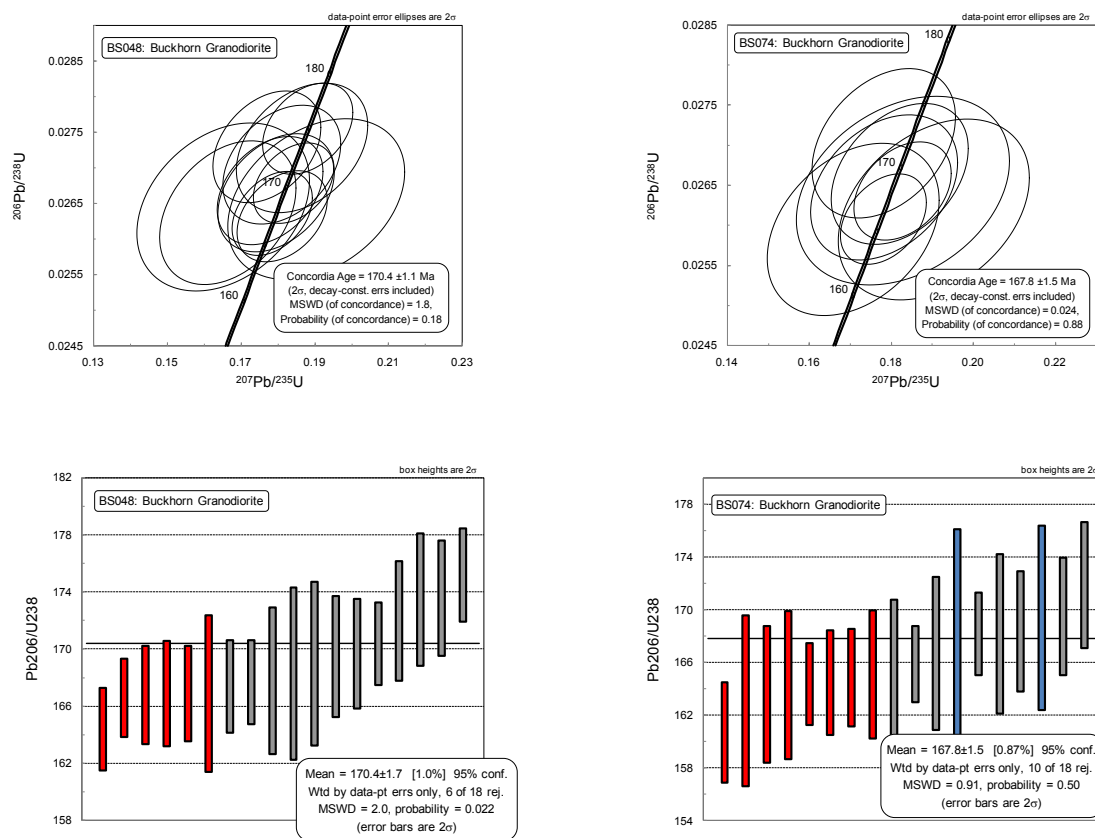
**Figure 3.5:** Concordia and weighted average diagrams for BS048 and BS074. Rejected analyses coloured according to the legend in Figure 3.1. Only concordant data was used for the age calculations and plotted on the Concordia diagrams.
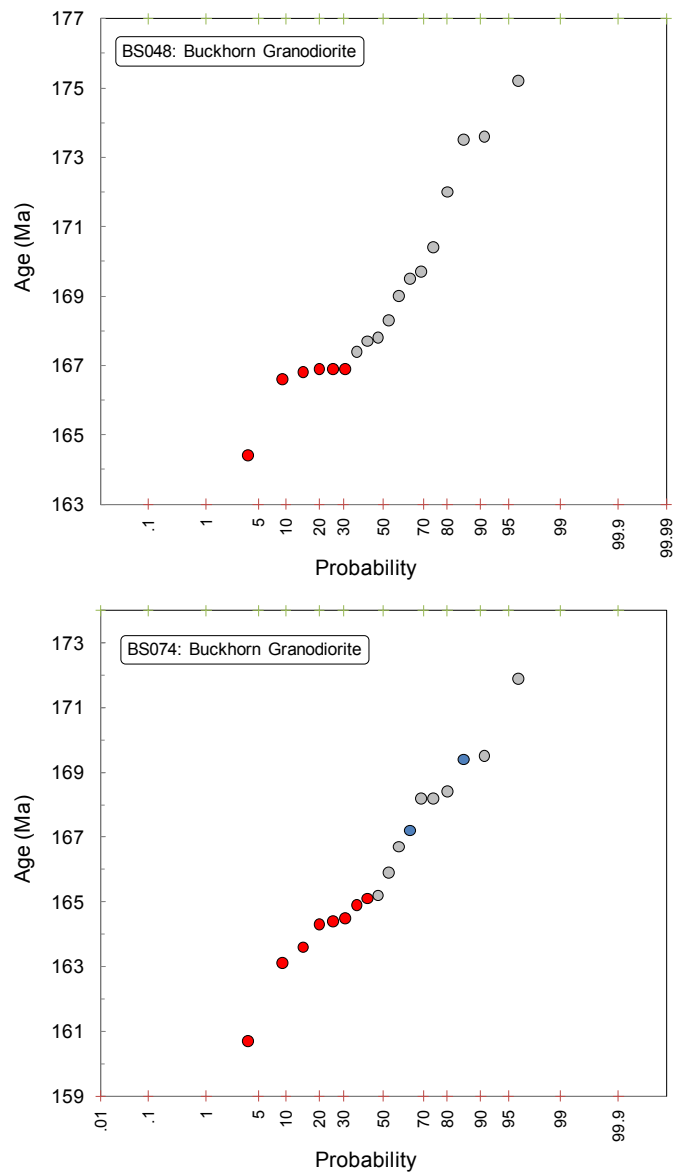
**Figure 3.6:** Linear cumulative probability plots for samples BS048 and BS074

**Table 3.3:** Isotope ratios and age estimates for BS048

| Table 3.3 | | | | | | | | | U/Pb LA-ICP-MS data and calculated ages | | | | | | | |
|---|---|---|---|---|---|---|---|---|---|---|---|---|---|---|---|---|
| | | Isotopic ratios | | | | | | | Age estimates (Ma) | | | | | | | |
| Rock Type | Sample-analysis | $^{207}Pb/^{206}Pb$ | ± 1σ | $^{207}Pb/^{235}U$ | ± 1σ | $^{206}Pb/^{238}U$ | ± 1σ | Rho | $^{207}Pb/^{206}Pb$ | ± 1σ | $^{207}Pb/^{235}U$ | ± 1σ | $^{206}Pb/^{238}U$ | ± 1σ | Dis-cord. | Com-ments |
| BGdi | BS048-a | 0.0515 | 0.0016 | 0.1936 | 0.0061 | 0.0262 | 0.0003 | 0.37 | 262.5 | 68.08 | 179.7 | 5.15 | 166.9 | 1.85 | 1.08 | Pb Loss |
| BGdi | BS048-b | 0.0440 | 0.0027 | 0.1651 | 0.0095 | 0.0265 | 0.0005 | 0.31 | 34.3 | 130.51 | 155.2 | 8.31 | 168.3 | 3.02 | 0.92 | |
| BGdi | BS048-c | 0.0440 | 0.0012 | 0.1842 | 0.0044 | 0.0268 | 0.0002 | 0.36 | 188.7 | 53.21 | 171.7 | 3.79 | 170.4 | 1.44 | 1.01 | |
| BGdi | BS048-d | 0.0440 | 0.0025 | 0.1903 | 0.0098 | 0.0266 | 0.0005 | 0.34 | 212.8 | 111.86 | 176.9 | 8.34 | 169 | 2.87 | 1.05 | |
| BGdi | BS048-e | 0.0440 | 0.0012 | 0.1881 | 0.0050 | 0.0276 | 0.0003 | 0.36 | 136.3 | 58.77 | 175 | 4.24 | 175.2 | 1.63 | 1.00 | |
| BGdi | BS048-f | 0.0440 | 0.0015 | 0.1778 | 0.0059 | 0.0267 | 0.0003 | 0.35 | 89.1 | 75.2 | 166.2 | 5.05 | 169.7 | 1.93 | 0.98 | |
| BGdi | BS048-g | 0.0440 | 0.0020 | 0.1664 | 0.0076 | 0.0264 | 0.0004 | 0.34 | 0.1 | 77.59 | 156.3 | 6.57 | 167.8 | 2.56 | 0.93 | |
| BGdi | BS048-h | 0.0491 | 0.0012 | 0.1769 | 0.0044 | 0.0258 | 0.0002 | 0.36 | 150.8 | 55.9 | 165.4 | 3.82 | 164.4 | 1.44 | 1.01 | Pb Loss |
| BGdi | BS048-i | 0.0440 | 0.0019 | 0.1865 | 0.0073 | 0.0273 | 0.0004 | 0.35 | 180 | 86.03 | 173.7 | 6.22 | 173.5 | 2.32 | 1.00 | |
| BGdi | BS048-j | 0.0440 | 0.0013 | 0.1811 | 0.0050 | 0.0263 | 0.0003 | 0.36 | 195.5 | 61.04 | 169 | 4.3 | 167.4 | 1.63 | 1.01 | |
| BGdi | BS048-k | 0.0440 | 0.0012 | 0.1784 | 0.0045 | 0.0264 | 0.0002 | 0.36 | 124.7 | 55.91 | 166.7 | 3.84 | 167.7 | 1.48 | 0.99 | |
| BGdi | BS048-l | 0.0440 | 0.0017 | 0.1811 | 0.0065 | 0.0270 | 0.0003 | 0.35 | 152.3 | 80.04 | 169 | 5.61 | 172 | 2.1 | 0.98 | |
| BGdi | BS048-m | 0.0440 | 0.0015 | 0.1770 | 0.0060 | 0.0273 | 0.0003 | 0.35 | 47.9 | 76.49 | 165.5 | 5.14 | 173.6 | 2.02 | 0.95 | |
| BGdi | BS048-n | 0.0440 | 0.0009 | 0.3990 | 0.0078 | 0.0560 | 0.0004 | 0.36 | 318 | 39.13 | 340.9 | 5.67 | 351.4 | 2.37 | 0.97 | Xenocryst |
| BGdi | BS048-o | 0.0480 | 0.0014 | 0.1762 | 0.0054 | 0.0262 | 0.0003 | 0.34 | 100.8 | 68.5 | 164.8 | 4.63 | 166.8 | 1.71 | 0.99 | Pb Loss |
| BGdi | BS048-p | 0.0440 | 0.0014 | 1.8026 | 0.0505 | 0.1772 | 0.0015 | 0.31 | 1051.7 | 36.9 | 1046.4 | 18.29 | 1051.5 | 8.33 | 1.00 | Xenocryst |
| BGdi | BS048-q | 0.0478 | 0.0013 | 0.1697 | 0.0048 | 0.0262 | 0.0003 | 0.35 | 88.8 | 64.56 | 159.1 | 4.15 | 166.9 | 1.66 | 0.95 | Pb Loss |
| BGdi | BS048-r | 0.0440 | 0.0022 | 0.1639 | 0.0084 | 0.0262 | 0.0004 | 0.33 | 0.1 | 7.31 | 154.1 | 7.36 | 166.9 | 2.75 | 0.92 | Pb Loss |
| BGdi | BS048-s | 0.0440 | 0.0017 | 0.1795 | 0.0064 | 0.0267 | 0.0003 | 0.36 | 132 | 79.62 | 167.6 | 5.53 | 169.5 | 2.13 | 0.99 | |
| BGdi | BS048-t | 0.0479 | 0.0011 | 0.1763 | 0.0042 | 0.0262 | 0.0002 | 0.36 | 93.8 | 54.04 | 164.8 | 3.59 | 166.6 | 1.38 | 0.99 | Pb Loss |
| **Weighted average (95% confidence level)** | | | | | | | | | | | **168.6** | **2.9** | **170.4** | **1.7** | | |

**Table 3.4:** Isotope ratios and age estimates for BS074

| | | Isotopic ratios | | | | | | | Age estimates (Ma) | | | | | | | |
| | Table 3.4 | | | | | | | | U/Pb LA-ICP-MS data and calculated ages | | | | | | | |
| Rock Type | Sample-analysis | $^{207}Pb$ $/^{206}Pb$ | ± 1σ | $^{207}Pb$ $/^{235}U$ | ± 1σ | $^{206}Pb$ $/^{238}U$ | ± 1σ | Rho | $^{207}Pb$ $/^{206}Pb$ | ± 1σ | $^{207}Pb$ $/^{235}U$ | ± 1σ | $^{206}Pb$ $/^{238}U$ | ± 1σ | Dis-cord. | Comments |
|---|---|---|---|---|---|---|---|---|---|---|---|---|---|---|---|---|
| BGdi | BS074-a | 0.1145 | 0.0026 | 5.1927 | 0.2526 | 0.3377 | 0.0042 | 0.26 | 1871.3 | 40.18 | 1851.4 | 41.42 | 1875.5 | 20.4 | 0.99 | Xenocryst |
| BGdi | BS074-b | 0.0415 | 0.0036 | 0.1463 | 0.0128 | 0.0263 | 0.0007 | 0.31 | 0.1 | 0 | 138.6 | 11.31 | 167.2 | 4.48 | 0.83 | Discordant |
| BGdi | BS074-c | 0.0493 | 0.0018 | 0.1821 | 0.0068 | 0.0266 | 0.0004 | 0.36 | 160.5 | 83.1 | 169.9 | 5.86 | 169.5 | 2.23 | 1.00 | |
| BGdi | BS074-d | 0.0493 | 0.0013 | 0.1827 | 0.0048 | 0.0264 | 0.0003 | 0.36 | 161 | 58.85 | 170.4 | 4.15 | 168.2 | 1.57 | 1.01 | |
| BGdi | BS074-e | 0.0499 | 0.0022 | 0.1798 | 0.0082 | 0.0257 | 0.0004 | 0.35 | 191.9 | 100.81 | 167.9 | 7.09 | 163.6 | 2.59 | 1.03 | Pb Loss |
| BGdi | BS074-f | 0.0934 | 0.0013 | 3.1816 | 0.0720 | 0.2483 | 0.0017 | 0.31 | 1496 | 25.99 | 1452.7 | 17.47 | 1429.9 | 8.91 | 1.02 | Xenocryst |
| BGdi | BS074-g | 0.0496 | 0.0013 | 0.1776 | 0.0047 | 0.0258 | 0.0003 | 0.37 | 177.5 | 58.31 | 166 | 4.02 | 164.4 | 1.56 | 1.01 | Pb Loss |
| BGdi | BS074-h | 0.0509 | 0.0025 | 0.1904 | 0.0096 | 0.0262 | 0.0005 | 0.35 | 237.4 | 108.8 | 176.9 | 8.14 | 166.7 | 2.9 | 1.06 | |
| BGdi | BS074-i | 0.0511 | 0.0016 | 0.1800 | 0.0060 | 0.0253 | 0.0003 | 0.36 | 243.5 | 72.5 | 168 | 5.12 | 160.7 | 1.9 | 1.05 | Pb Loss |
| BGdi | BS074-j | 0.0507 | 0.0016 | 0.1844 | 0.0058 | 0.0259 | 0.0003 | 0.36 | 227.7 | 69.1 | 171.8 | 4.98 | 164.9 | 1.85 | 1.04 | Pb Loss |
| BGdi | BS074-k | 0.0500 | 0.0021 | 0.1750 | 0.0074 | 0.0259 | 0.0004 | 0.36 | 192.9 | 92.92 | 163.7 | 6.37 | 165.1 | 2.43 | 0.99 | Pb Loss |
| BGdi | BS074-l | 0.0479 | 0.0019 | 0.1783 | 0.0073 | 0.0265 | 0.0004 | 0.34 | 91.5 | 93.16 | 166.6 | 6.31 | 168.4 | 2.29 | 0.99 | |
| BGdi | BS074-m | 0.0497 | 0.0012 | 0.1781 | 0.0043 | 0.0261 | 0.0002 | 0.37 | 179.2 | 53.07 | 166.5 | 3.69 | 165.9 | 1.45 | 1.00 | |
| BGdi | BS074-n | 0.0472 | 0.0016 | 0.1712 | 0.0059 | 0.0259 | 0.0003 | 0.35 | 59.8 | 78.68 | 160.5 | 5.14 | 164.5 | 1.98 | 0.98 | Pb Loss |
| BGdi | BS074-o | 0.0504 | 0.0028 | 0.1817 | 0.0105 | 0.0256 | 0.0005 | 0.35 | 215.1 | 125.24 | 169.5 | 8.99 | 163.1 | 3.24 | 1.04 | Pb Loss |
| BGdi | BS074-p | 0.0549 | 0.0032 | 0.2034 | 0.0122 | 0.0266 | 0.0006 | 0.35 | 407.5 | 125.37 | 188 | 10.3 | 169.4 | 3.5 | 1.11 | Discordant |
| BGdi | BS074-q | 0.0486 | 0.0019 | 0.1782 | 0.0071 | 0.0270 | 0.0004 | 0.35 | 127.8 | 88.97 | 166.5 | 6.14 | 171.9 | 2.4 | 0.97 | |
| BGdi | BS074-r | 0.0482 | 0.0024 | 0.1707 | 0.0086 | 0.0260 | 0.0004 | 0.34 | 108.7 | 111.75 | 160 | 7.41 | 165.2 | 2.79 | 0.97 | |
| BGdi | BS074-s | 0.0486 | 0.0028 | 0.1828 | 0.0106 | 0.0264 | 0.0005 | 0.31 | 130.3 | 128.38 | 170.5 | 9.12 | 168.2 | 3.02 | 1.01 | |
| BGdi | BS074-t | 0.0472 | 0.0023 | 0.1653 | 0.0082 | 0.0258 | 0.0005 | 0.35 | 58.7 | 111.55 | 155.3 | 7.11 | 164.3 | 2.81 | 0.95 | Pb Loss |
| | **Weighted average (95% confidence level)** | | | | | | | | | | **168.1** | **3.9** | **167.8** | **1.5** | | |
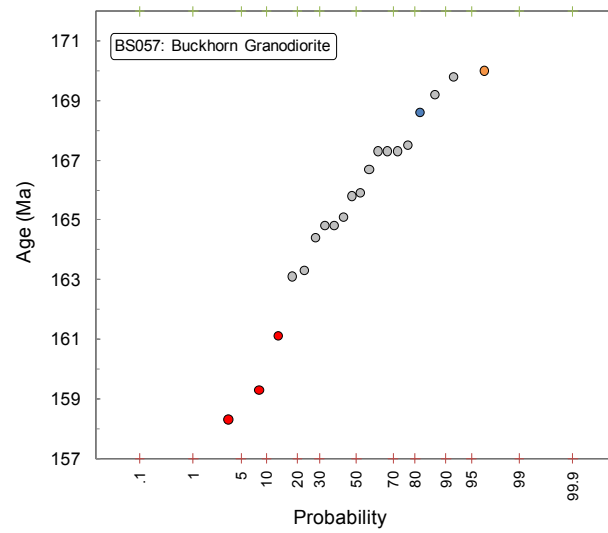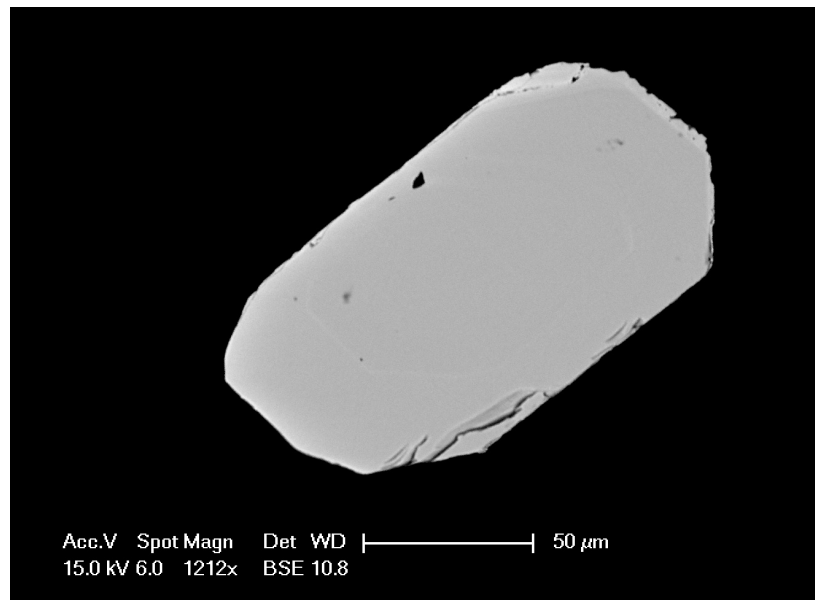
**Figure 3.7:** BSE image of a representative zircon and linear cumulative probability plot for BS057
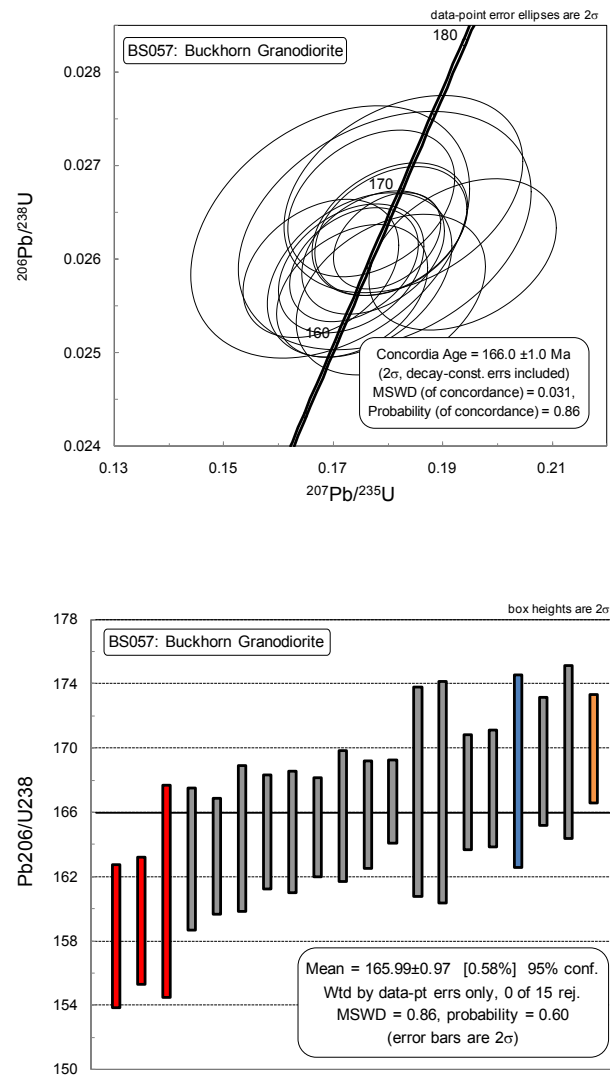
**Figure 3.8:** Concordia and weighted average and diagram for BS057

**Table 3.5:** Summary of isotope ratios and age estimates for BS057

| | | Isotopic ratios | | | | | | | Age estimates (Ma) | | | | | | | |
|---|---|---|---|---|---|---|---|---|---|---|---|---|---|---|---|---|
| Rock Type | Sample-analysis | $^{207}Pb/^{206}Pb$ | ± 1σ | $^{207}Pb/^{235}U$ | ± 1σ | $^{206}Pb/^{238}U$ | ± 1σ | Rho | $^{207}Pb/^{206}Pb$ | ± 1σ | $^{207}Pb/^{235}U$ | ± 1σ | $^{206}Pb/^{238}U$ | ± 1σ | Discord. | Comments |
| BGdi | BS057-1 | 0.0573 | 0.0028 | 0.2102 | 0.0105 | 0.0265 | 0.0005 | 0.36 | 501.1 | 102.77 | 193.7 | 8.79 | 168.6 | 2.99 | 1.149 | Discordant |
| BGdi | BS057-2 | 0.0484 | 0.0015 | 0.1733 | 0.0055 | 0.0259 | 0.0003 | 0.34 | 117 | 70.6 | 162.3 | 4.71 | 164.8 | 1.77 | 0.985 | |
| BGdi | BS057-3 | 0.0480 | 0.0029 | 0.1739 | 0.0106 | 0.0253 | 0.0005 | 0.34 | 97 | 136.52 | 162.8 | 9.2 | 161.1 | 3.31 | 1.011 | Pb Loss |
| BGdi | BS057-4 | 0.0503 | 0.0019 | 0.1748 | 0.0069 | 0.0258 | 0.0004 | 0.35 | 208.9 | 87.08 | 163.6 | 5.97 | 164.4 | 2.26 | 0.995 | |
| BGdi | BS057-5 | 0.0517 | 0.0018 | 0.1936 | 0.0070 | 0.0261 | 0.0003 | 0.35 | 271.6 | 78.33 | 179.7 | 5.95 | 165.8 | 2.05 | 1.084 | |
| BGdi | BS057-6 | 0.0496 | 0.0015 | 0.1772 | 0.0053 | 0.0261 | 0.0003 | 0.34 | 175.7 | 66.87 | 165.6 | 4.59 | 165.9 | 1.67 | 0.998 | |
| BGdi | BS057-7 | 0.0480 | 0.0013 | 0.1737 | 0.0048 | 0.0259 | 0.0003 | 0.35 | 96 | 63.55 | 162.6 | 4.15 | 165.1 | 1.55 | 0.985 | |
| BGdi | BS057-8 | 0.0491 | 0.0011 | 0.1799 | 0.0040 | 0.0262 | 0.0002 | 0.36 | 153.4 | 49.59 | 167.9 | 3.43 | 166.7 | 1.3 | 1.007 | |
| BGdi | BS057-9 | 0.0495 | 0.0016 | 0.1804 | 0.0058 | 0.0263 | 0.0003 | 0.34 | 170.8 | 71.75 | 168.4 | 5 | 167.5 | 1.82 | 1.005 | |
| BGdi | BS057-10 | 0.0490 | 0.0016 | 0.1734 | 0.0056 | 0.0257 | 0.0003 | 0.35 | 145.6 | 72.78 | 162.3 | 4.88 | 163.3 | 1.81 | 0.994 | |
| BGdi | BS057-11 | 0.0498 | 0.0019 | 0.1804 | 0.0071 | 0.0256 | 0.0004 | 0.35 | 184.5 | 86.22 | 168.4 | 6.07 | 163.1 | 2.21 | 1.032 | |
| BGdi | BS057-12 | 0.0493 | 0.0029 | 0.1793 | 0.0109 | 0.0263 | 0.0005 | 0.32 | 162.4 | 133.33 | 167.5 | 9.4 | 167.3 | 3.26 | 1.001 | |
| BGdi | BS057-13 | 0.0494 | 0.0020 | 0.1664 | 0.0067 | 0.0249 | 0.0004 | 0.35 | 164.6 | 90.15 | 156.3 | 5.87 | 158.3 | 2.23 | 0.987 | Pb Loss |
| BGdi | BS057-14 | 0.0469 | 0.0016 | 0.1677 | 0.0058 | 0.0259 | 0.0003 | 0.34 | 44.9 | 78.8 | 157.5 | 5.03 | 164.8 | 1.9 | 0.956 | |
| BGdi | BS057-15 | 0.0481 | 0.0018 | 0.1675 | 0.0062 | 0.0250 | 0.0003 | 0.33 | 104.2 | 83.65 | 157.3 | 5.41 | 159.3 | 1.98 | 0.987 | Pb Loss |
| BGdi | BS057-16 | 0.0476 | 0.0029 | 0.1694 | 0.0104 | 0.0263 | 0.0006 | 0.34 | 80.2 | 137.21 | 158.9 | 9.02 | 167.3 | 3.45 | 0.950 | |
| BGdi | BS057-17 | 0.0481 | 0.0013 | 0.1767 | 0.0050 | 0.0267 | 0.0003 | 0.35 | 103.4 | 64.01 | 165.2 | 4.34 | 170 | 1.68 | 0.972 | Inheritance |
| BGdi | BS057-18 | 0.0483 | 0.0023 | 0.1828 | 0.0089 | 0.0267 | 0.0004 | 0.33 | 116.1 | 108.05 | 170.4 | 7.63 | 169.8 | 2.69 | 1.004 | |
| BGdi | BS057-19 | 0.0507 | 0.0016 | 0.1805 | 0.0057 | 0.0263 | 0.0003 | 0.34 | 225.1 | 69.55 | 168.5 | 4.9 | 167.3 | 1.79 | 1.007 | |
| BGdi | BS057-20 | 0.0484 | 0.0017 | 0.1770 | 0.0062 | 0.0266 | 0.0003 | 0.34 | 117 | 78.92 | 165.5 | 5.37 | 169.2 | 1.98 | 0.978 | |
| **Weighted average (95% confidence level)** | | | | | | | | | | | **165.7** | **2.6** | **165.99** | **0.97** | | |

### 3.2.3 Early Diorite Dikes

The Early Diorite dikes were identified during mapping (G.E. Ray, Personal communication 2009). They are plagioclase- and pyroxene-porphyritic diorite dikes that are so-named because they predate the prograde skarn alteration. Many of the Early Diorite dikes are intensely skarn-altered to a garnet-epidote and lesser pyroxene-amphibole assemblage. Because of the intensity of alteration two samples of the Early Diorite dikes were collected to ensure a dependable age could be determined. Sample BS046, is moderately skarn altered to pyroxene-amphibole-epidote and is about 1 m from intense garnet skarn alteration; sample BS075 is weakly skarn altered to the same mineral assemblage and is about 3 m from garnet skarn alteration. A date from this rock type will provide the first isotopic age for the Early Diorite dikes and a maximum age for skarn alteration.

Zircons from the two samples are similar. They are clear in transmitted light, near euhedral crystals with moderate concentric zoning and no inherited cores visible with BSE imaging. The zircons average between 100 and 200 μm in length and about 100 μm in width, and have a few inclusions and fractures (Figure 3.9). The more intensely endoskarn altered sample, BS046, has a concordant age of 168.2 ± 0.7 Ma and a weighted average $^{206}Pb/^{238}U$ age of 168.2 ± 0.7 Ma (Figure 3.10). These results are based on fourteen of the twenty zircons analysed. The results from three zircons were excluded because the crystals are xenocrysts reflecting crustal contamination by the country rocks during emplacement. The three xenocrysts have concordant ages, two at approximately 1.85 Ga, and the third at about 1.1 Ga. Two analyses were excluded because the zircons experienced subtle lead loss, and the last was affected by subtle inheritance (Table 3.7 and Figure 3.11). The less endoskarn altered sample, BS075, has a concordant age of 169.4 ± 1.3 Ma and a weighted average $^{206}Pb/^{238}U$ age of 169.3 ± 1.5 Ma (Figure 3.10). These ages are based on fourteen of the twenty zircons analyzed. Of the rejected zircon analyses, three were discordant and three had been affected by subtle inheritance (Table 3.7 Figure 3.11).

The ages of the two skarn-altered Early Diorite dikes agree within error of each other and within the age of the Buckhorn Granodiorite. This work provides an age for a previously undated rock type, which can be used along with its geologic relationships to show that the Early Diorite dikes are likely a mafic dike phase of the Buckhorn stock. Also, as the Early Diorite dikes are usually skarn-altered, their emplacement must have predated skarn alteration and gold mineralization and their age of 168.2 ± 0.7 Ma can therefore be used as a maximum age of mineralization.
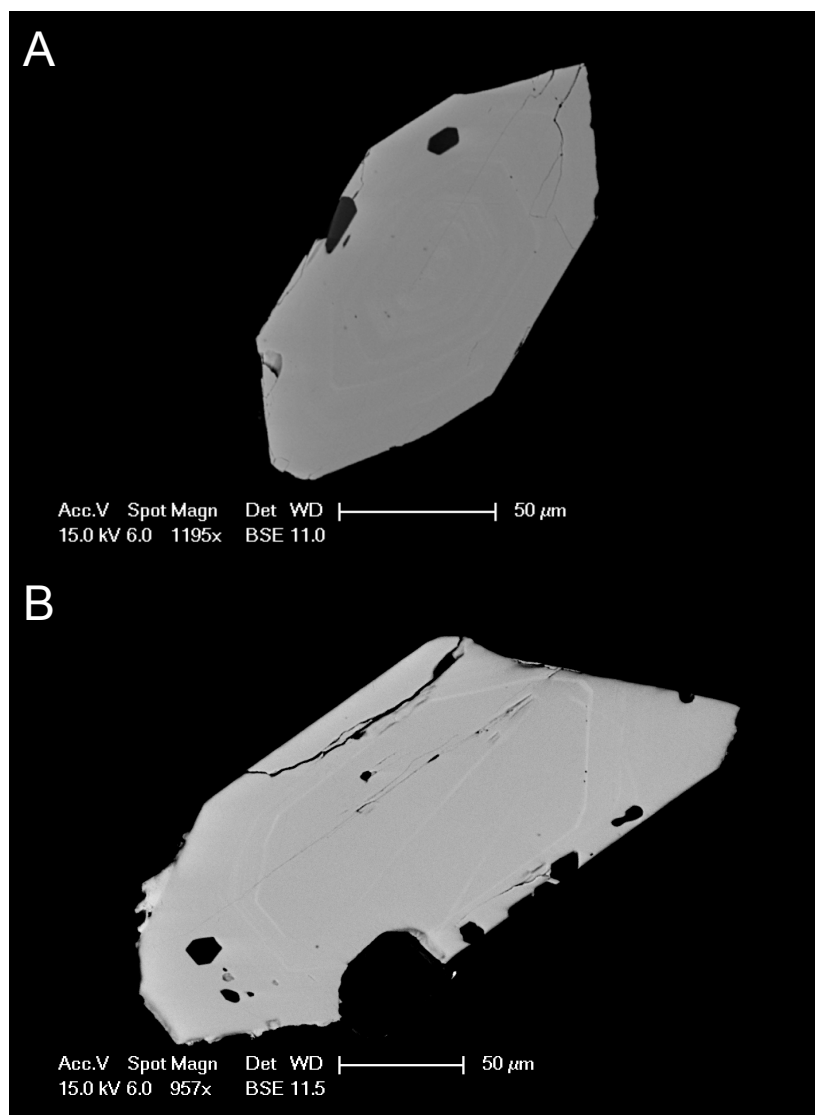
**Figure 3.9:** BSE images of representative zircons from sample BS046 (A) and BS075 (B)
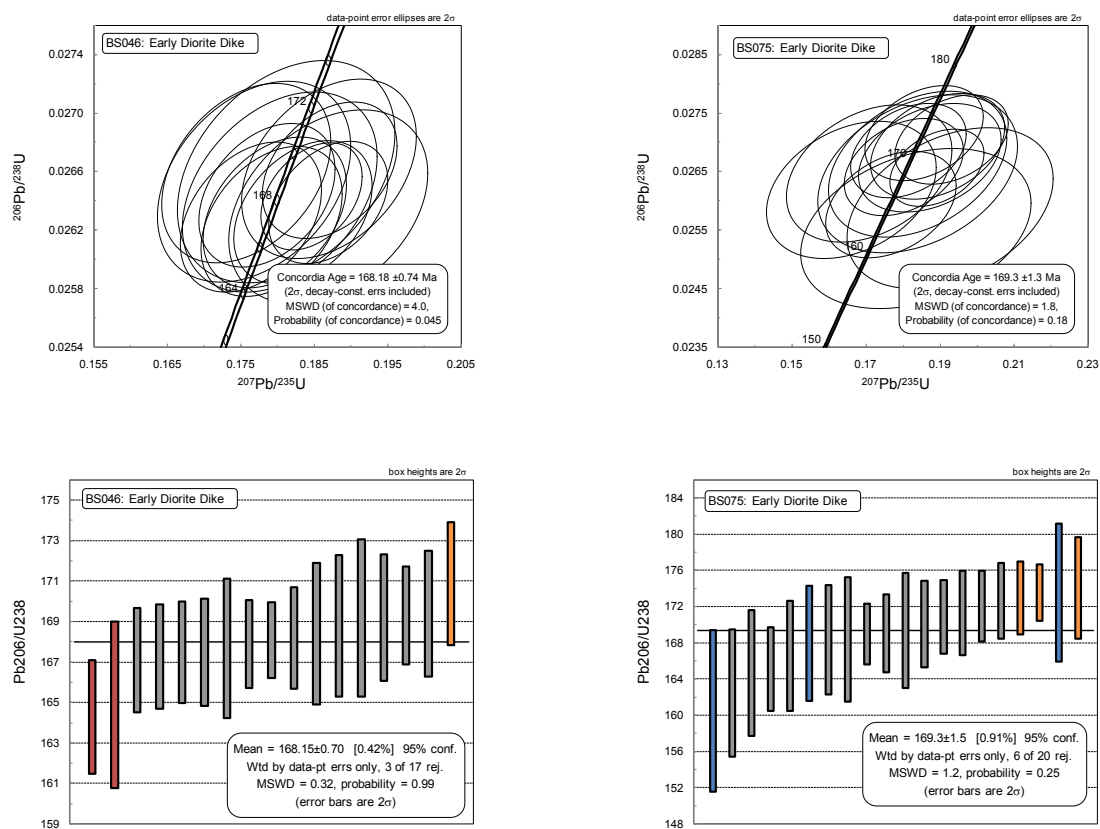
**Figure 3.10:** Concordia and weighted average diagrams from sample BS046 and BS075
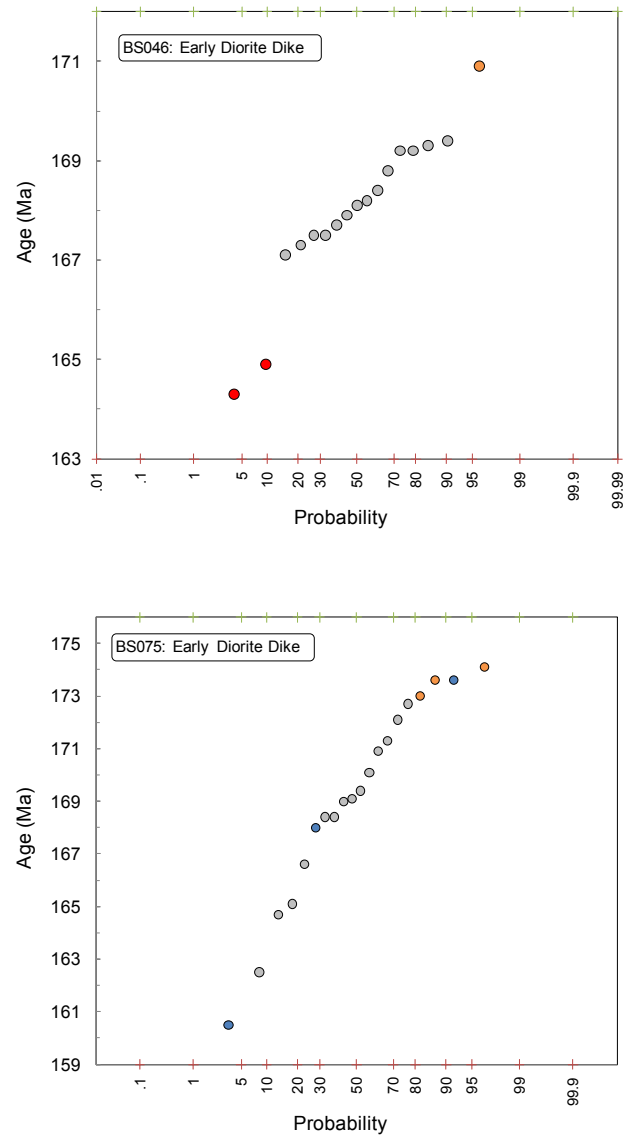
**Figure 3.11:** Linear cumulative probability plots for sample BS046 and BS075

**Table 3.6:** Isotope ratios and age estimates for sample BS046

Table 3.6 — U/Pb LA-ICP-MS data and calculated ages

| Rock Type | Sample-analysis | Isotopic ratios | | | | | | | | Age estimates (Ma) | | | | | | | | |
|---|---|---|---|---|---|---|---|---|---|---|---|---|---|---|---|---|---|---|
| | | $^{207}Pb/^{206}Pb$ | $\pm 1\sigma$ | $^{207}Pb/^{235}U$ | $\pm 1\sigma$ | $^{206}Pb/^{238}U$ | $\pm 1\sigma$ | Rho | $^{207}Pb/^{206}Pb$ | $\pm 1\sigma$ | $^{207}Pb/^{235}U$ | $\pm 1\sigma$ | $^{206}Pb/^{238}U$ | $\pm 1\sigma$ | Discord. | Comments |
| EDiD | BS046-1 | 0.0510 | 0.0015 | 0.1869 | 0.0055 | 0.0264 | 0.0003 | 0.35 | 240.4 | 65.24 | 174 | 4.74 | 167.7 | 1.72 | 1.038 | |
| EDiD | BS046-2 | 0.0516 | 0.0009 | 0.1869 | 0.0033 | 0.0264 | 0.0002 | 0.36 | 269.1 | 38.96 | 174 | 2.83 | 167.9 | 1.09 | 1.036 | |
| EDiD | BS046-3 | 0.0507 | 0.0012 | 0.1804 | 0.0043 | 0.0258 | 0.0002 | 0.36 | 227.5 | 53.03 | 168.4 | 3.72 | 164.3 | 1.4 | 1.025 | Pb loss |
| EDiD | BS046-4 | 0.0495 | 0.0017 | 0.1817 | 0.0065 | 0.0259 | 0.0003 | 0.35 | 173.4 | 79.82 | 169.6 | 5.62 | 164.9 | 2.05 | 1.029 | Pb loss |
| EDiD | BS046-5 | 0.0502 | 0.0010 | 0.1871 | 0.0038 | 0.0266 | 0.0002 | 0.36 | 205.6 | 44.52 | 174.2 | 3.21 | 169.3 | 1.21 | 1.029 | |
| EDiD | BS046-6 | 0.0496 | 0.0012 | 0.1859 | 0.0047 | 0.0269 | 0.0002 | 0.35 | 174.8 | 56.18 | 173.2 | 4.02 | 170.9 | 1.52 | 1.013 | Inheritance |
| EDiD | BS046-7 | 0.0486 | 0.0016 | 0.1812 | 0.0061 | 0.0266 | 0.0003 | 0.35 | 129 | 74.76 | 169.1 | 5.2 | 169.2 | 1.94 | 0.999 | |
| EDiD | BS046-8 | 0.0505 | 0.0008 | 0.1846 | 0.0028 | 0.0264 | 0.0002 | 0.37 | 217.1 | 33.82 | 172 | 2.41 | 168.1 | 0.94 | 1.023 | |
| EDiD | BS046-9 | 0.0487 | 0.0011 | 0.1764 | 0.0039 | 0.0263 | 0.0002 | 0.36 | 133.8 | 50.27 | 165 | 3.4 | 167.3 | 1.29 | 0.986 | |
| EDiD | BS046-10 | 0.0509 | 0.0010 | 0.1835 | 0.0038 | 0.0263 | 0.0002 | 0.36 | 235.9 | 46.21 | 171 | 3.29 | 167.5 | 1.26 | 1.021 | |
| EDiD | BS046-11 | 0.0479 | 0.0014 | 0.1768 | 0.0054 | 0.0265 | 0.0003 | 0.35 | 92.3 | 69.79 | 165.3 | 4.64 | 168.8 | 1.75 | 0.979 | |
| EDiD | BS046-12 | 0.1105 | 0.0015 | 5.0777 | 0.1468 | 0.3267 | 0.0025 | 0.26 | 1806.9 | 24.33 | 1832.4 | 24.52 | 1822.2 | 12.17 | 1.006 | Xenocryst |
| EDiD | BS046-13 | 0.0791 | 0.0019 | 2.0061 | 0.0777 | 0.1866 | 0.0022 | 0.30 | 1174.6 | 46.6 | 1117.6 | 26.23 | 1103.1 | 11.66 | 1.013 | Xenocryst |
| EDiD | BS046-14 | 0.0479 | 0.0013 | 0.1758 | 0.0047 | 0.0266 | 0.0003 | 0.35 | 95 | 61.53 | 164.4 | 4.06 | 169.2 | 1.56 | 0.972 | |
| EDiD | BS046-15 | 0.0492 | 0.0010 | 0.1786 | 0.0038 | 0.0264 | 0.0002 | 0.36 | 158 | 47.42 | 166.8 | 3.26 | 168.2 | 1.26 | 0.992 | |
| EDiD | BS046-16 | 0.0504 | 0.0013 | 0.1870 | 0.0049 | 0.0266 | 0.0003 | 0.36 | 211.1 | 57.51 | 174.1 | 4.16 | 169.4 | 1.56 | 1.028 | |
| EDiD | BS046-17 | 0.0504 | 0.0011 | 0.1796 | 0.0040 | 0.0263 | 0.0002 | 0.36 | 211.3 | 49.07 | 167.7 | 3.42 | 167.5 | 1.33 | 1.001 | |
| EDiD | BS046-18 | 0.0497 | 0.0011 | 0.1792 | 0.0039 | 0.0263 | 0.0002 | 0.37 | 182.4 | 48.79 | 167.3 | 3.38 | 167.1 | 1.29 | 1.001 | |
| EDiD | BS046-19 | 0.0488 | 0.0014 | 0.1803 | 0.0054 | 0.0265 | 0.0003 | 0.35 | 139.3 | 66.96 | 168.3 | 4.64 | 168.4 | 1.75 | 0.999 | |
| EDiD | BS046-20 | 0.1112 | 0.0012 | 5.1297 | 0.1063 | 0.3353 | 0.0019 | 0.28 | 1819.4 | 18.8 | 1841 | 17.61 | 1864 | 9.33 | 0.988 | Xenocryst |
| **Weighted average (95% confidence level)** | | | | | | | | | | | **169.9** | **1.8** | **168.15** | **0.7** | | |

**Table 3.7:** Isotope ratios and age estimates for sample BS075

| | Table 3.7 | | | | | | | | U/Pb LA-ICP-MS data and calculated ages | | | | | | | |

| Rock Type | Sample-analysis | Isotopic ratios | | | | | | | Age estimates (Ma) | | | | | | | Comments |
|---|---|---|---|---|---|---|---|---|---|---|---|---|---|---|---|---|
| | | $^{207}Pb/^{206}Pb$ | ± 1σ | $^{207}Pb/^{235}U$ | ± 1σ | $^{206}Pb/^{238}U$ | ± 1σ | Rho | $^{207}Pb/^{206}Pb$ | ± 1σ | $^{207}Pb/^{235}U$ | ± 1σ | $^{206}Pb/^{238}U$ | ± 1σ | Discord. | |
| EDiD | BS075-a | 0.0486 | 0.0023 | 0.1767 | 0.0085 | 0.0274 | 0.0004 | 0.34 | 130.5 | 107.46 | 165.3 | 7.29 | 174.1 | 2.79 | 0.949 | Inheritance |
| EDiD | BS075-b | 0.0503 | 0.0021 | 0.1872 | 0.0079 | 0.0267 | 0.0004 | 0.34 | 209.7 | 92.94 | 174.2 | 6.71 | 170.1 | 2.39 | 1.024 | |
| EDiD | BS075-c | 0.0466 | 0.0026 | 0.1661 | 0.0094 | 0.0262 | 0.0005 | 0.33 | 26.4 | 128.88 | 156 | 8.15 | 166.6 | 3.03 | 0.936 | |
| EDiD | BS075-d | 0.0474 | 0.0025 | 0.1708 | 0.0091 | 0.0265 | 0.0005 | 0.34 | 66.4 | 121.66 | 160.1 | 7.92 | 168.4 | 3.02 | 0.951 | |
| EDiD | BS075-e | 0.0588 | 0.0030 | 0.2163 | 0.0111 | 0.0264 | 0.0005 | 0.37 | 560.5 | 106.32 | 198.9 | 9.25 | 168 | 3.17 | 1.184 | Discordant |
| EDiD | BS075-f | 0.0508 | 0.0019 | 0.1893 | 0.0074 | 0.0269 | 0.0004 | 0.35 | 232.9 | 85.9 | 176.1 | 6.3 | 171.3 | 2.33 | 1.028 | |
| EDiD | BS075-g | 0.0507 | 0.0030 | 0.1839 | 0.0110 | 0.0265 | 0.0006 | 0.35 | 229.1 | 130.62 | 171.4 | 9.41 | 168.4 | 3.43 | 1.018 | |
| EDiD | BS075-h | 0.0508 | 0.0016 | 0.1931 | 0.0062 | 0.0271 | 0.0003 | 0.35 | 233.1 | 71.34 | 179.2 | 5.31 | 172.1 | 1.96 | 1.041 | |
| EDiD | BS075-i | 0.0507 | 0.0012 | 0.1933 | 0.0048 | 0.0273 | 0.0003 | 0.37 | 225.9 | 54.89 | 179.4 | 4.1 | 173.6 | 1.55 | 1.033 | Inheritance |
| EDiD | BS075-j | 0.0492 | 0.0017 | 0.1857 | 0.0065 | 0.0272 | 0.0003 | 0.35 | 157.7 | 78.19 | 172.9 | 5.56 | 172.7 | 2.1 | 1.001 | |
| EDiD | BS075-k | 0.0526 | 0.0014 | 0.1892 | 0.0052 | 0.0266 | 0.0003 | 0.37 | 311.4 | 59.61 | 175.9 | 4.44 | 169 | 1.69 | 1.041 | |
| EDiD | BS075-l | 0.0497 | 0.0020 | 0.1767 | 0.0072 | 0.0259 | 0.0004 | 0.35 | 179.7 | 90.64 | 165.2 | 6.2 | 165.1 | 2.31 | 1.001 | |
| EDiD | BS075-m | 0.0487 | 0.0017 | 0.1802 | 0.0066 | 0.0266 | 0.0003 | 0.35 | 134.3 | 81.82 | 168.2 | 5.65 | 169.1 | 2.15 | 0.995 | |
| EDiD | BS075-n | 0.0505 | 0.0027 | 0.1839 | 0.0098 | 0.0266 | 0.0005 | 0.36 | 219.7 | 117.4 | 171.4 | 8.43 | 169.4 | 3.18 | 1.012 | |
| EDiD | BS075-o | 0.0503 | 0.0035 | 0.1834 | 0.0127 | 0.0255 | 0.0006 | 0.32 | 206.8 | 151.92 | 171 | 10.93 | 162.5 | 3.5 | 1.052 | |
| EDiD | BS075-p | 0.0561 | 0.0046 | 0.1942 | 0.0159 | 0.0252 | 0.0007 | 0.34 | 456.9 | 170.9 | 180.2 | 13.54 | 160.5 | 4.46 | 1.123 | Discordant |
| EDiD | BS075-q | 0.0442 | 0.0032 | 0.1638 | 0.0118 | 0.0273 | 0.0006 | 0.31 | 0.1 | 67.94 | 154 | 10.33 | 173.6 | 3.82 | 0.887 | Discordant |
| EDiD | BS075-r | 0.0562 | 0.0033 | 0.1927 | 0.0114 | 0.0259 | 0.0006 | 0.37 | 458.6 | 125.01 | 178.9 | 9.69 | 164.7 | 3.49 | 1.086 | |
| EDiD | BS075-s | 0.0505 | 0.0016 | 0.1886 | 0.0061 | 0.0272 | 0.0003 | 0.36 | 219.4 | 71.7 | 175.4 | 5.25 | 173 | 2.01 | 1.014 | Inheritance |
| EDiD | BS075-t | 0.0489 | 0.0017 | 0.1815 | 0.0064 | 0.0269 | 0.0003 | 0.35 | 143.5 | 78.61 | 169.3 | 5.48 | 170.9 | 2.05 | 0.991 | |
| **Weighted average (95% confidence level)** | | | | | | | | | | | **171.6** | **3.4** | **169.3** | **1.5** | | |

### 3.2.4 Buckhorn Diorite

The Buckhorn Diorite is a fine-grained equigranular diorite that predominately occurs along the southwest margin of the Buckhorn Granodiorite stock. The Buckhorn Diorite has not been previously dated. It was originally labelled as a border phase of the Buckhorn Granodiorite (Hickey, 1990, 1992; McMillen, 1979), but that genetic relationship was later questioned (Gaspar, 2005). Current mapping shows a gradational contact between the two units (Figure 2.1) and a date will help to correlate it with the Buckhorn Granodiorite and distinguish it from the Early Diorite dikes.

The Buckhorn Diorite sample contained similar size zircons to the Buckhorn Granodiorite, but more were subhedral. The grains were near equant with poorly developed crystal faces; they ranged from 100 to 200 μm, and contained few inclusions. Fewer growth zones were visible with BSE imaging than in the Buckhorn Granodiorite samples, and few cores were detected (Figure 3.12). The sample had a concordant age of 169.0 ± 0.9 Ma and a weighted average $^{206}Pb/^{238}U$ age of 169.9 ± 0.9 Ma (Figure 3.13). Five of the twenty analyses were excluded from the age calculations. One analysis was of a zircon that experienced subtle lead loss, three were affected by subtle inheritance, and the final was discordant (Table 3.8 and Figure 3.12).

This work establishes the first age for the Buckhorn Diorite. The age falls within error of the Buckhorn Granodiorite, which supports the idea that it is a border phase of the granodiorite stock, and adds to the understanding of the genesis of the BIS. The age of the Buckhorn Diorite also falls within error of the Early Diorite dike samples; therefore the two diorites cannot be distinguished based on their age. Fortunately as was shown in Chapter 2 they are easily distinguished based on texture.
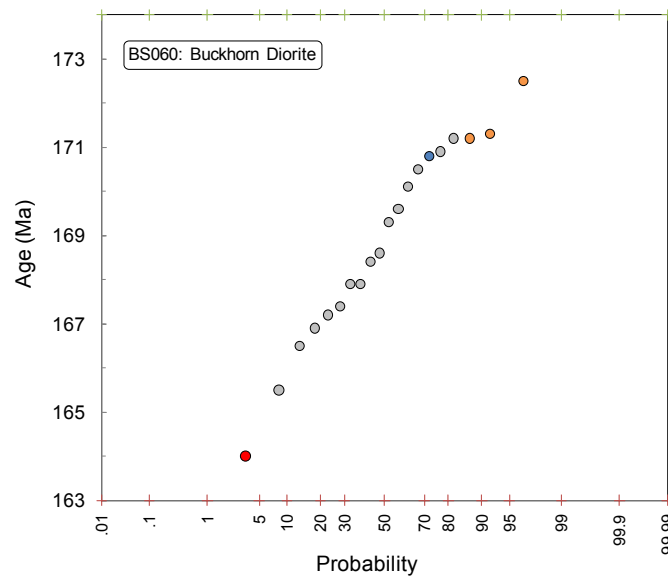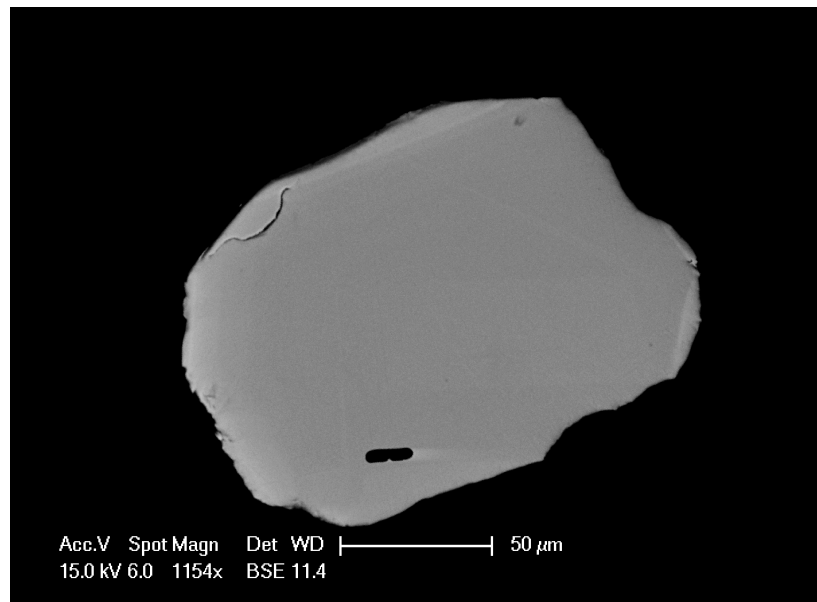
**Figure 3.12:** BSE image of a representative zircon and linear cumulative probability plot for BS060
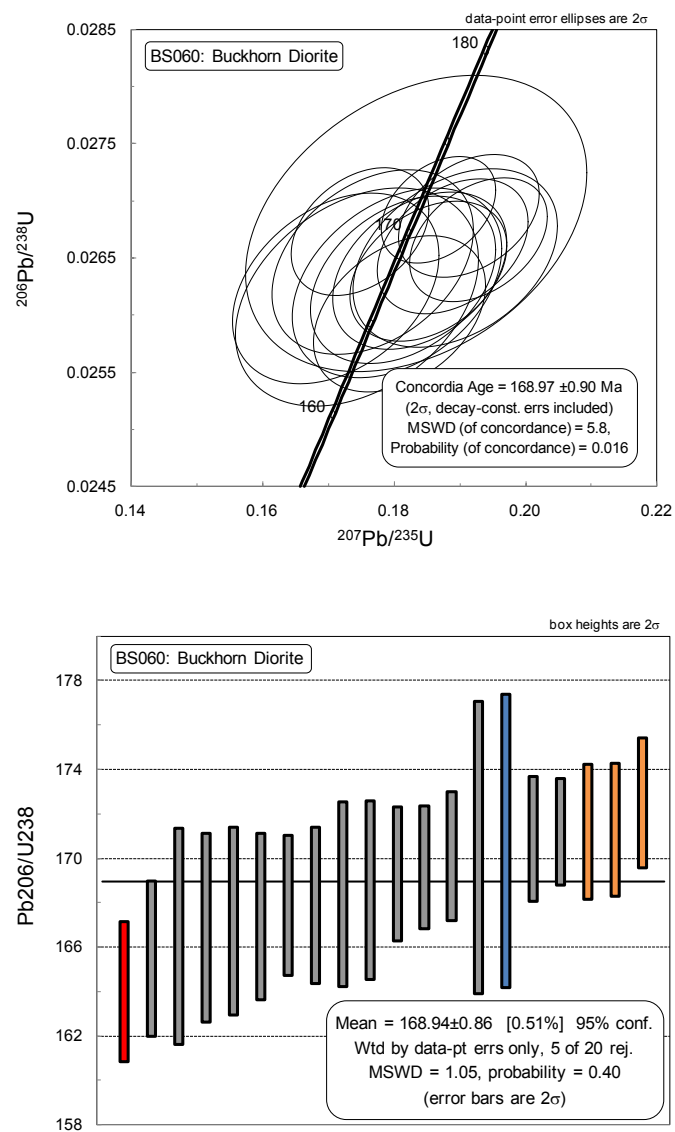
**Figure 3.13:** Concordia and weighted average diagrams for sample BS060

**Table 3.8:** Isotope ratios and age estimates for sample BS060

| | Table 3.8 | | | | | | | | | U/Pb LA-ICP-MS data and calculated ages | | | | | | | |
|---|---|---|---|---|---|---|---|---|---|---|---|---|---|---|---|---|---|
| | | Isotopic ratios | | | | | | | | | | Age estimates (Ma) | | | | | |
| Rock Type | Sample-analysis | $^{207}Pb$ $/^{206}Pb$ | ± 1σ | $^{207}Pb$ $/^{235}U$ | ± 1σ | $^{206}Pb$ $/^{238}U$ | ± 1σ | Rho | $^{207}Pb$ $/^{206}Pb$ | ± 1σ | $^{207}Pb$ $/^{235}U$ | ± 1σ | $^{206}Pb$ $/^{238}U$ | ± 1σ | Discord. | Comments |
| BDi | BS060-1 | 0.0508 | 0.0012 | 0.1952 | 0.0045 | 0.0271 | 0.0002 | 0.37 | 233 | 51.42 | 181 | 3.84 | 172.5 | 1.46 | 1.049 | Inheritance |
| BDi | BS060-2 | 0.0512 | 0.0013 | 0.1889 | 0.0047 | 0.0266 | 0.0002 | 0.36 | 247.7 | 55.18 | 175.7 | 4.01 | 169.3 | 1.51 | 1.038 | |
| BDi | BS060-3 | 0.0504 | 0.0011 | 0.1914 | 0.0044 | 0.0269 | 0.0002 | 0.36 | 214.1 | 50.87 | 177.8 | 3.72 | 170.9 | 1.4 | 1.040 | |
| BDi | BS060-4 | 0.0508 | 0.0012 | 0.1871 | 0.0045 | 0.0269 | 0.0002 | 0.37 | 233.5 | 53.74 | 174.1 | 3.86 | 171.3 | 1.49 | 1.016 | Inheritance |
| BDi | BS060-5 | 0.0504 | 0.0016 | 0.1813 | 0.0058 | 0.0263 | 0.0003 | 0.36 | 212.8 | 70.92 | 169.2 | 4.95 | 167.4 | 1.87 | 1.011 | |
| BDi | BS060-6 | 0.0503 | 0.0009 | 0.1868 | 0.0036 | 0.0269 | 0.0002 | 0.37 | 209.7 | 42.54 | 173.9 | 3.05 | 171.2 | 1.2 | 1.016 | |
| BDi | BS060-7 | 0.0506 | 0.0017 | 0.1893 | 0.0063 | 0.0265 | 0.0003 | 0.36 | 220.6 | 74.33 | 176 | 5.41 | 168.6 | 2.01 | 1.044 | |
| BDi | BS060-8 | 0.0505 | 0.0013 | 0.1852 | 0.0049 | 0.0264 | 0.0003 | 0.36 | 215.6 | 58.81 | 172.5 | 4.18 | 167.9 | 1.58 | 1.027 | |
| BDi | BS060-9 | 0.0509 | 0.0015 | 0.1839 | 0.0054 | 0.0264 | 0.0003 | 0.36 | 237.9 | 65.38 | 171.4 | 4.64 | 167.9 | 1.76 | 1.021 | |
| BDi | BS060-10 | 0.0501 | 0.0018 | 0.1804 | 0.0065 | 0.0263 | 0.0003 | 0.36 | 201 | 80.31 | 168.4 | 5.58 | 167.2 | 2.11 | 1.007 | |
| BDi | BS060-11 | 0.0522 | 0.0029 | 0.2074 | 0.0117 | 0.0269 | 0.0005 | 0.35 | 293.8 | 121.4 | 191.3 | 9.82 | 170.8 | 3.3 | 1.120 | Discordant |
| BDi | BS060-12 | 0.0485 | 0.0028 | 0.1833 | 0.0106 | 0.0268 | 0.0005 | 0.34 | 123.7 | 129.21 | 170.9 | 9.1 | 170.5 | 3.3 | 1.002 | |
| BDi | BS060-13 | 0.0473 | 0.0017 | 0.1711 | 0.0064 | 0.0262 | 0.0003 | 0.35 | 65.3 | 85.92 | 160.4 | 5.54 | 166.9 | 2.12 | 0.961 | |
| BDi | BS060-14 | 0.0496 | 0.0012 | 0.1869 | 0.0047 | 0.0269 | 0.0002 | 0.36 | 174.3 | 55.75 | 174 | 3.98 | 171.2 | 1.52 | 1.016 | Inheritance |
| BDi | BS060-15 | 0.0497 | 0.0014 | 0.1808 | 0.0054 | 0.0260 | 0.0003 | 0.36 | 181 | 66.28 | 168.8 | 4.6 | 165.5 | 1.75 | 1.020 | |
| BDi | BS060-16 | 0.0469 | 0.0016 | 0.1768 | 0.0063 | 0.0265 | 0.0003 | 0.35 | 46 | 81.67 | 165.3 | 5.41 | 168.4 | 2.07 | 0.982 | |
| BDi | BS060-17 | 0.0521 | 0.0011 | 0.1928 | 0.0043 | 0.0267 | 0.0002 | 0.37 | 291.2 | 48.32 | 179 | 3.62 | 169.6 | 1.38 | 1.055 | |
| BDi | BS060-18 | 0.0480 | 0.0012 | 0.1748 | 0.0043 | 0.0267 | 0.0002 | 0.35 | 99.2 | 56.75 | 163.6 | 3.69 | 170.1 | 1.45 | 0.962 | |
| BDi | BS060-19 | 0.0505 | 0.0013 | 0.1782 | 0.0048 | 0.0258 | 0.0003 | 0.36 | 217.7 | 59.72 | 166.5 | 4.11 | 164 | 1.58 | 1.015 | Pb Loss |
| BDi | BS060-20 | 0.0490 | 0.0021 | 0.1744 | 0.0076 | 0.0262 | 0.0004 | 0.34 | 145.6 | 97.27 | 163.2 | 6.52 | 166.5 | 2.44 | 0.980 | |
| | **Weighted average (95% confidence level)** | | | | | | | | | | **171.6** | **3.1** | **168.94** | **0.86** | | |

### 3.2.5 Granodiorite dikes

The Granodiorite dikes are typically mineralogically identical to the Buckhorn Granodiorite except coarser grained and containing quartz phenocrysts. The Granodiorite dikes are documented to control the location of skarn alteration in the Buckhorn Granodiorite and BMS (Figure 2.9 and Figure 2.11).The dikes may also be altered and deformed as is seen in sample BS059 chosen for dating (Figure 2.15). This example shows a low angle foliation, and a steeply dipping foliation, both defined by intense biotite alteration (Figure 2.15). In addition to dating the Granodiorite dikes this sample will also provide a maximum age for the prograde skarn alteration and the development of the foliations.

Sample BS059 contains many clear, elongate, near euhedral zircons that are 150 to 400 μm in length and 100 to 200 μm wide. Concentric growth zoning, inclusions and a few inherited cores were visible with BSE imaging (Figure 3.14). The sample gives a concordant age of 167.5 ± 0.8 Ma and a weighted average $^{206}Pb/^{238}U$ age of 167.5 ± 0.7 Ma (Figure 3.15). These ages are based on seventeen of the twenty zircons analysed. Of the three zircons excluded, one was a 2 Ga xenocryst, and two were affected by subtle lead loss (Table 3.9 and Figure 3.14).

The concordant data provide a reliable age for the emplacement of the Granodiorite dikes that control the location of skarn alteration and gold mineralization. The date is similar to that indicated by the earlier work of Gaspar (2005), but more precise. The date also provides a maximum age for deformation events responsible for the low angle and the steeply dipping foliation. The low angle foliations were originally thought to predate the Buckhorn Granodiorite and only affect the Paleozoic BMS host rock package (McMillen, 1979).
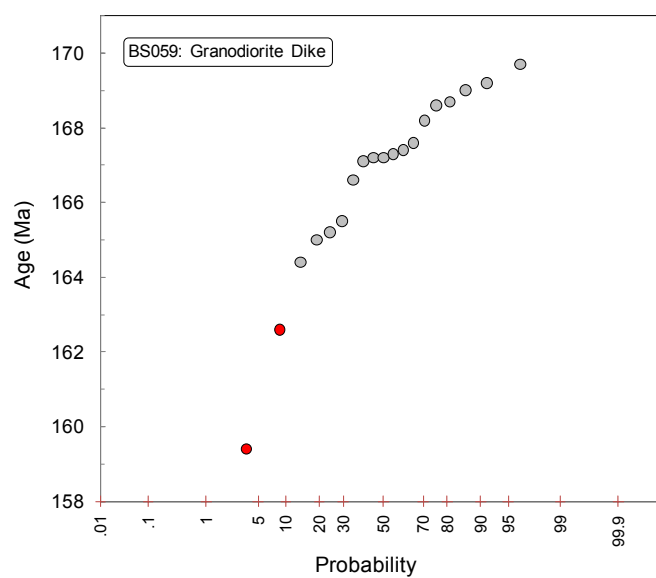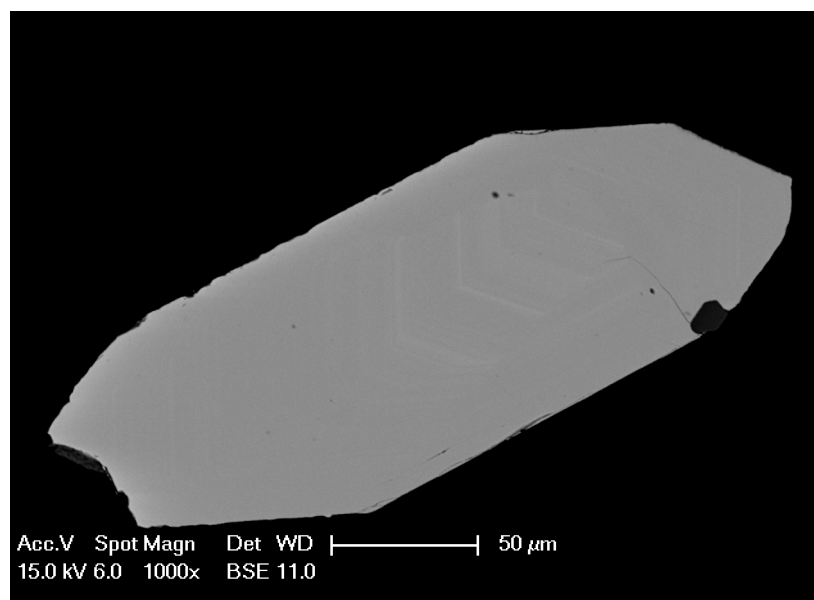
**Figure 3.14:** BSE image and linear cumulative probability plot for sample BS059
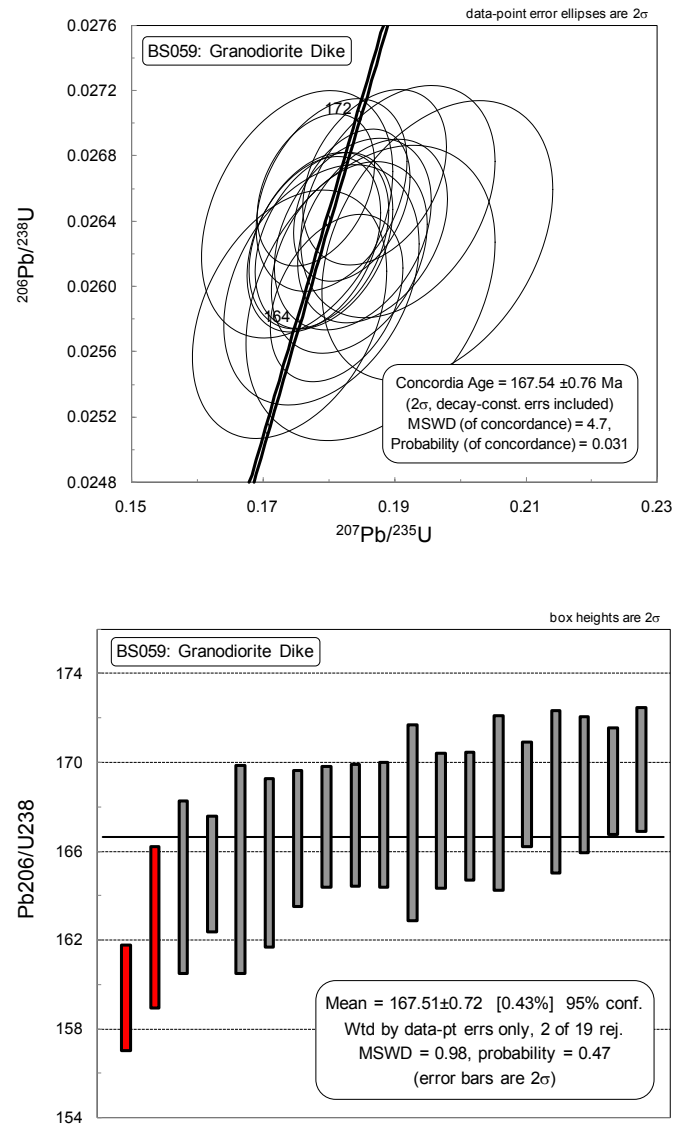
**Figure 3.15:** Concordia and weighted average diagrams for Granodiorite dike sample BS059

**Table 3.9:** Isotope ratios and age estimates for sample BS059

Table 3.9  U/Pb LA-ICP-MS data and calculated ages

| Rock Type | Sample-analysis | Isotopic ratios | | | | | | | Age estimates (Ma) | | | | | | | Comments |
| | | $^{207}Pb/^{206}Pb$ | $\pm 1\sigma$ | $^{207}Pb/^{235}U$ | $\pm 1\sigma$ | $^{206}Pb/^{238}U$ | $\pm 1\sigma$ | Rho | $^{207}Pb/^{206}Pb$ | $\pm 1\sigma$ | $^{207}Pb/^{235}U$ | $\pm 1\sigma$ | $^{206}Pb/^{238}U$ | $\pm 1\sigma$ | Dis-cord. | |
|---|---|---|---|---|---|---|---|---|---|---|---|---|---|---|---|---|
| GDiD | BS059-a | 0.0510 | 0.0010 | 0.1759 | 0.0037 | 0.0250 | 0.0002 | 0.36 | 241.40 | 46.16 | 164.50 | 3.18 | 159.40 | 1.19 | 1.032 | Pb Loss |
| GDiD | BS059-b | 0.0491 | 0.0011 | 0.1793 | 0.0043 | 0.0263 | 0.0002 | 0.35 | 152.80 | 52.87 | 167.40 | 3.66 | 167.20 | 1.37 | 1.001 | |
| GDiD | BS059-c | 0.0501 | 0.0015 | 0.1905 | 0.0060 | 0.0265 | 0.0003 | 0.35 | 201.00 | 69.57 | 177.10 | 5.14 | 168.70 | 1.82 | 1.050 | |
| GDiD | BS059-d | 0.0506 | 0.0013 | 0.1805 | 0.0047 | 0.0266 | 0.0002 | 0.35 | 224.40 | 57.09 | 168.40 | 4.02 | 169.00 | 1.53 | 0.996 | |
| GDiD | BS059-e | 0.0482 | 0.0016 | 0.1753 | 0.0059 | 0.0264 | 0.0003 | 0.35 | 107.00 | 75.93 | 164.00 | 5.13 | 168.20 | 1.97 | 0.975 | |
| GDiD | BS059-f | 0.0480 | 0.0016 | 0.1740 | 0.0060 | 0.0258 | 0.0003 | 0.35 | 97.90 | 79.03 | 162.90 | 5.21 | 164.40 | 1.95 | 0.991 | |
| GDiD | BS059-g | 0.0494 | 0.0012 | 0.1785 | 0.0044 | 0.0263 | 0.0002 | 0.34 | 167.50 | 54.28 | 166.80 | 3.75 | 167.20 | 1.41 | 0.998 | |
| GDiD | BS059-h | 0.0506 | 0.0020 | 0.1863 | 0.0077 | 0.0260 | 0.0004 | 0.34 | 223.30 | 90.55 | 173.50 | 6.61 | 165.20 | 2.35 | 1.050 | |
| GDiD | BS059-i | 0.0497 | 0.0011 | 0.1812 | 0.0041 | 0.0259 | 0.0002 | 0.36 | 179.60 | 50.21 | 169.10 | 3.53 | 165.00 | 1.31 | 1.025 | |
| GDiD | BS059-j | 0.0500 | 0.0012 | 0.1867 | 0.0047 | 0.0263 | 0.0002 | 0.35 | 192.60 | 55.24 | 173.80 | 4.00 | 167.60 | 1.45 | 1.037 | |
| GDiD | BS059-k | 0.1240 | 0.0023 | 6.1630 | 0.2682 | 0.3701 | 0.0041 | 0.26 | 2014.30 | 33.08 | 1999.20 | 38.01 | 2029.90 | 19.45 | 0.985 | Xenocryst |
| GDiD | BS059-l | 0.0504 | 0.0017 | 0.1789 | 0.0061 | 0.0260 | 0.0003 | 0.34 | 214.10 | 74.91 | 167.20 | 5.23 | 165.50 | 1.89 | 1.010 | |
| GDiD | BS059-m | 0.0503 | 0.0010 | 0.1835 | 0.0036 | 0.0265 | 0.0002 | 0.36 | 207.80 | 43.23 | 171.10 | 3.10 | 168.60 | 1.18 | 1.015 | |
| GDiD | BS059-n | 0.0487 | 0.0011 | 0.1778 | 0.0042 | 0.0263 | 0.0002 | 0.36 | 131.10 | 52.22 | 166.10 | 3.58 | 167.10 | 1.36 | 0.994 | |
| GDiD | BS059-o | 0.0505 | 0.0013 | 0.1831 | 0.0049 | 0.0262 | 0.0002 | 0.35 | 217.20 | 58.32 | 170.70 | 4.17 | 166.60 | 1.54 | 1.025 | |
| GDiD | BS059-p | 0.0481 | 0.0009 | 0.1781 | 0.0036 | 0.0266 | 0.0002 | 0.35 | 102.20 | 45.79 | 166.40 | 3.14 | 169.20 | 1.20 | 0.983 | |
| GDiD | BS059-q | 0.0506 | 0.0013 | 0.1837 | 0.0049 | 0.0263 | 0.0002 | 0.34 | 222.70 | 58.10 | 171.20 | 4.17 | 167.40 | 1.52 | 1.023 | |
| GDiD | BS059-r | 0.0505 | 0.0016 | 0.1844 | 0.0059 | 0.0255 | 0.0003 | 0.35 | 217.50 | 70.47 | 171.90 | 5.08 | 162.60 | 1.82 | 1.057 | Pb Loss |
| GDiD | BS059-s | 0.0493 | 0.0011 | 0.1870 | 0.0045 | 0.0267 | 0.0002 | 0.35 | 163.80 | 52.58 | 174.10 | 3.80 | 169.70 | 1.39 | 1.026 | |
| GDiD | BS059-t | 0.0539 | 0.0019 | 0.1966 | 0.0072 | 0.0263 | 0.0004 | 0.37 | 367.40 | 77.49 | 182.20 | 6.09 | 167.30 | 2.21 | 1.089 | |
| **Weighted average (95% confidence level)** | | | | | | | | | | | **169.60** | **1.90** | **167.51** | **0.72** | | |

### 3.2.6 Roosevelt Granodiorite

The Roosevelt Granodiorite is found in the Roosevelt Mine area approximately 500 m south east of the center of the SWOZ. It is a plagioclase, hornblende and biotite porphyritic granodiorite with a fine-grained quartz and feldspar matrix. Although, it has only been found in the Roosevelt Mine area and is areally minor, Gaspar (2005) suggested that it was the mineralizing intrusion. A sample was collected to confirm its age.

The sample contained a more diverse zircon population than the other rock types. The zircons were commonly subhedral or equant, and were usually moderately to intensely fractured. The zircons fell into two size categories. About 20 % of the grains were 200 to 300 μm with the remaining 80 % being 100 to 150 μm. Growth zoning and inherited cores were generally not visible with BSE imaging, but a few inclusions were found. Investigation with cathodoluminescence microscopy (CL) after dating revealed that the grains had more diversity than detected with BSE imaging. CL imaging showed that grains had concentric growth zones and up to two stages of core growth as seen in Figure 3.16. Analysis of the Roosevelt Granodiorite gives a concordant age of 50.5 ± 3.0 Ma and a weighted average $^{206}Pb/^{238}U$ age of 50.5 ± 2.9 Ma (Figure 3.17). These ages are based on the youngest two grains of the twenty analysed. Six of the grains had discordant ages and the rest were xenocrysts or suffered from inheritance. The xenocrysts have a wide range of ages that fall into six age divisions: 57 Ma, 67 Ma, 82 Ma, 168 Ma, 390 Ma and 1.5 Ga (Table 3.10, Figure 3.16, and Figure 3.17).

The reported age agrees within error with the previously determined age of 52.7 ± 1.1 Ma (Gaspar, 2005). It is clear from the inherited ages and the CL images (Figure 3.16) that the Roosevelt Granodiorite has had a more complex melting and emplacement history than the other igneous rock present at Buckhorn. Based on the inherited ages, the Roosevelt Granodiorite likely incorporated portions of the Paleozoic and Proterozoic country rock and Middle Jurassic BIS during emplacement. The zircons with Late Cretaceous and Early Paleogene ages were possibly incorporated from Keller Butte Suite rocks found adjacent to the nearby Toroda Creek half Graben (Holder and McCarley Holder, 1988; Suydam and Gaylord, 1997). A similar range of inherited ages was reported with the first dating of the Roosevelt Granodiorite (Gaspar, 2005). The cores visible with CL imaging are not always inherited. For example Figure 3.16 shows a grain that appears to have an inherited core, but had a concordant age of 50 Ma. These pseudo-cores are proposed to be the result of multiple stages of zircon growth and corrosion as described in Corfu et al. (2003). A correlation between the size of the

zircon and its age, or the quality of its analysis was not detected. These results confirm the Eocene age of the Roosevelt Granodiorite, as well as further describe its complex genesis.
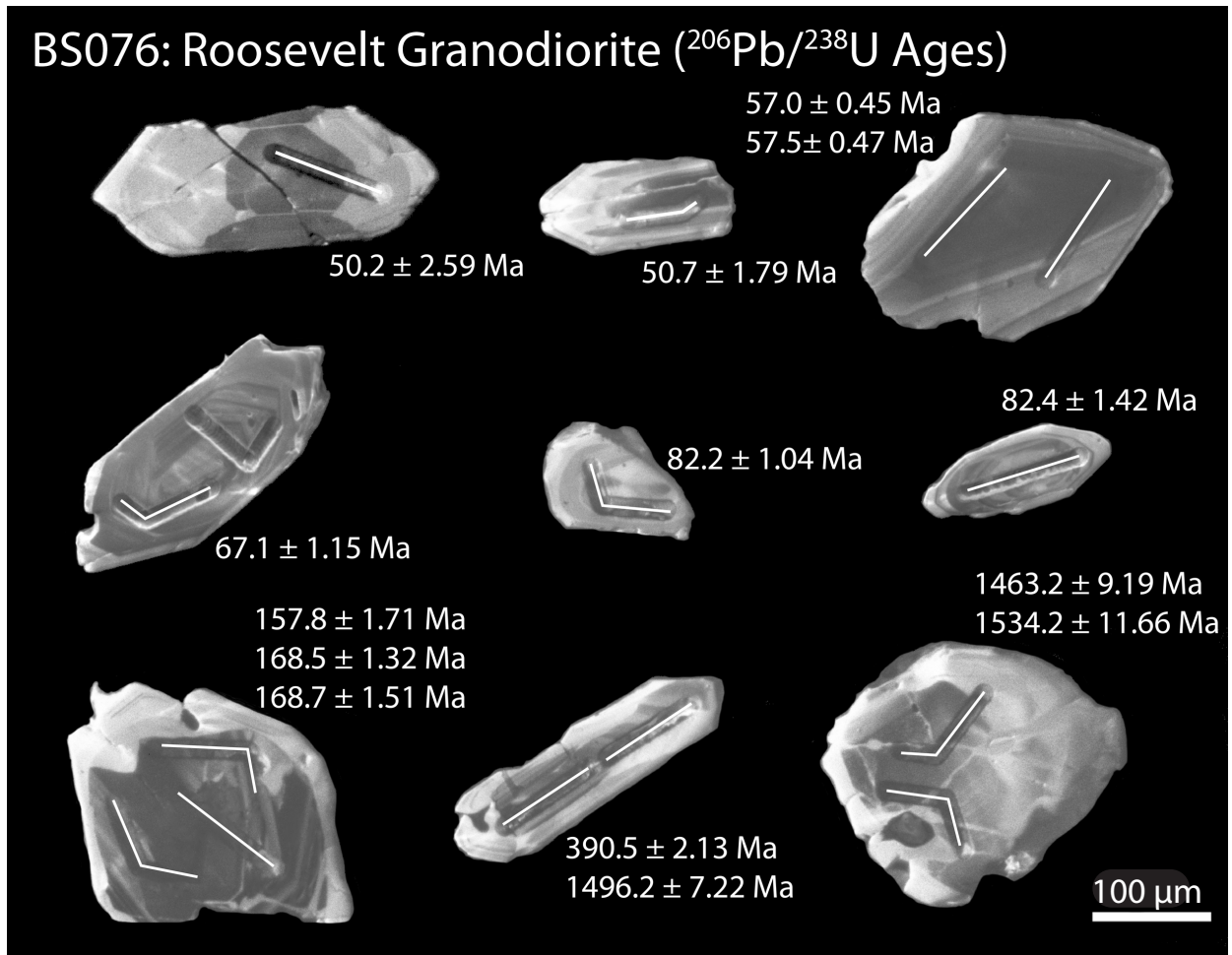


**Figure 3.16:** CL images and ages of all the concordant zircon crystals from sample BS076. Ablation lines are highlighted with white lines
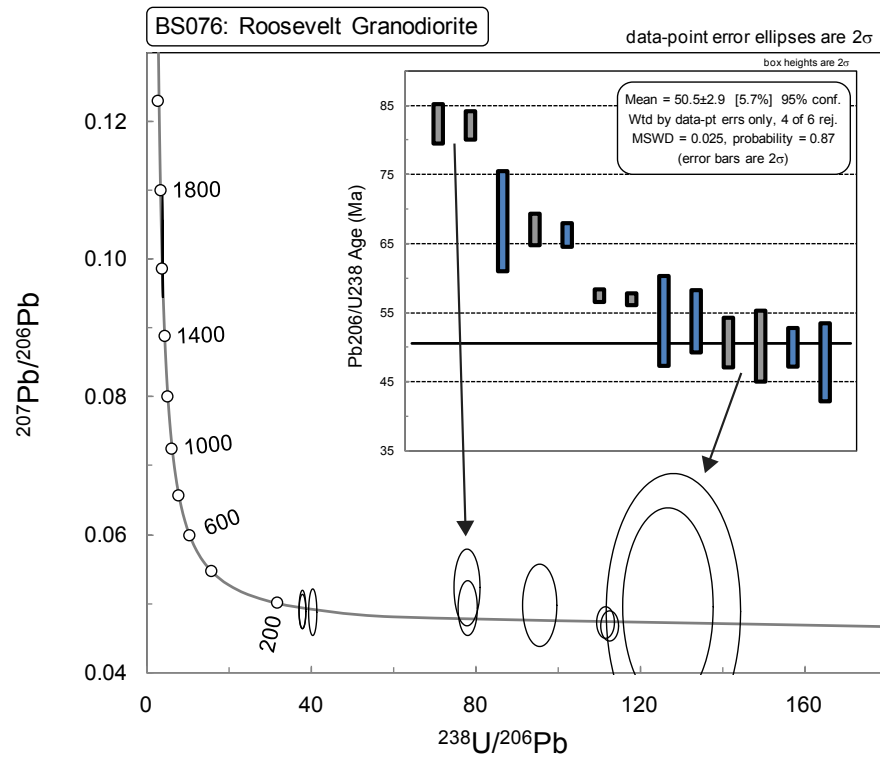
**Figure 3.17:** Tera-Wasserburg plot with weighted average diagram for sample BS076

**Table 3.10:** Isotope ratios and age estimates for sample BS076

| Table 3.10 | | | | | | | | U/Pb LA-ICP-MS data and calculated ages | | | | | | | |
|---|---|---|---|---|---|---|---|---|---|---|---|---|---|---|---|
| | | Isotopic ratios | | | | | | | Age estimates (Ma) | | | | | | |
| Rock Type | Sample-analysis | $^{207}Pb$ $/^{206}Pb$ | ± 1σ | $^{207}Pb$ $/^{235}U$ | ± 1σ | $^{206}Pb$ $/^{238}U$ | ± 1σ | Rho | $^{207}Pb$ $/^{206}Pb$ | ± 1σ | $^{207}Pb$ $/^{235}U$ | ± 1σ | $^{206}Pb$ $/^{238}U$ | ± 1σ | Discord. | Comments |
| RGDi | BS076-1 | 0.0484 | 0.0026 | 0.0718 | 0.0037 | 0.0105 | 0.0002 | 0.33 | 117.5 | 119.71 | 70.4 | 3.51 | 67.1 | 1.15 | 1.049 | Xenocryst |
| RGDi | BS076-2 | 0.0509 | 0.0019 | 0.0747 | 0.0027 | 0.0103 | 0.0001 | 0.38 | 235 | 82.56 | 73.2 | 2.53 | 66.3 | 0.87 | 1.104 | Discordant |
| RGDi | BS076-3 | 0.0959 | 0.0013 | 3.5121 | 0.0851 | 0.2548 | 0.0018 | 0.29 | 1546 | 25.06 | 1529.9 | 19.15 | 1463.2 | 9.19 | 1.046 | Xenocryst |
| RGDi | BS076-4 | 0.0974 | 0.0016 | 3.7752 | 0.1173 | 0.2687 | 0.0023 | 0.27 | 1574.4 | 30.25 | 1587.5 | 24.93 | 1534.2 | 11.66 | 1.035 | Xenocryst |
| RGDi | BS076-5 | 0.0491 | 0.0015 | 0.1664 | 0.0051 | 0.0248 | 0.0003 | 0.35 | 154.1 | 69.1 | 156.3 | 4.46 | 157.8 | 1.71 | 0.990 | Xenocryst |
| RGDi | BS076-6 | 0.0496 | 0.0010 | 0.1784 | 0.0039 | 0.0265 | 0.0002 | 0.37 | 177.8 | 48.1 | 166.7 | 3.31 | 168.5 | 1.32 | 0.989 | Xenocryst |
| RGDi | BS076-7 | 0.0488 | 0.0012 | 0.1797 | 0.0045 | 0.0265 | 0.0002 | 0.36 | 138.7 | 56.73 | 167.8 | 3.91 | 168.7 | 1.51 | 0.995 | Xenocryst |
| RGDi | BS076-8 | 0.0503 | 0.0091 | 0.0526 | 0.0092 | 0.0078 | 0.0004 | 0.30 | 210.7 | 370.74 | 52 | 8.88 | 50.2 | 2.59 | 1.036 | |
| RGDi | BS076-9 | 0.0484 | 0.0011 | 0.0585 | 0.0013 | 0.0090 | 0.0001 | 0.36 | 119.2 | 50.99 | 57.7 | 1.21 | 57.5 | 0.47 | 1.003 | Xenocryst |
| RGDi | BS076-10 | 0.0465 | 0.0010 | 0.0572 | 0.0012 | 0.0089 | 0.0001 | 0.38 | 23.7 | 49.94 | 56.5 | 1.15 | 57 | 0.45 | 0.991 | Xenocryst |
| RGDi | BS076-11 | 0.0561 | 0.0115 | 0.0605 | 0.0121 | 0.0075 | 0.0004 | 0.29 | 455.8 | 400.83 | 59.6 | 11.58 | 47.9 | 2.82 | 1.244 | Discordant |
| RGDi | BS076-12 | 0.0461 | 0.0058 | 0.0540 | 0.0067 | 0.0079 | 0.0003 | 0.29 | 2 | 279.06 | 53.4 | 6.42 | 50.7 | 1.79 | 1.053 | |
| RGDi | BS076-13 | 0.0419 | 0.0125 | 0.0487 | 0.0144 | 0.0084 | 0.0005 | 0.21 | 0.1 | 385.41 | 48.3 | 13.89 | 53.9 | 3.26 | 0.896 | Discordant |
| RGDi | BS076-14 | 0.0626 | 0.0101 | 0.0984 | 0.0155 | 0.0106 | 0.0006 | 0.34 | 694.7 | 309.97 | 95.3 | 14.28 | 68.3 | 3.61 | 1.395 | Discordant |
| RGDi | BS076-15 | 0.1000 | 0.0010 | 3.6196 | 0.0597 | 0.2612 | 0.0014 | 0.33 | 1624.2 | 18.92 | 1553.8 | 13.11 | 1496.2 | 7.22 | 1.038 | Xenocryst |
| RGDi | BS076-16 | 0.0605 | 0.0008 | 0.5243 | 0.0075 | 0.0625 | 0.0004 | 0.39 | 620 | 26.96 | 428 | 5.02 | 390.5 | 2.13 | 1.096 | Xenocryst |
| RGDi | BS076-17 | 0.0519 | 0.0025 | 0.0928 | 0.0044 | 0.0129 | 0.0002 | 0.36 | 282.2 | 105.76 | 90.1 | 4.04 | 82.4 | 1.42 | 1.093 | Xenocryst |
| RGDi | BS076-18 | 0.0476 | 0.0017 | 0.0873 | 0.0031 | 0.0128 | 0.0002 | 0.35 | 76.8 | 83.76 | 85 | 2.88 | 82.2 | 1.04 | 1.034 | Xenocryst |
| RGDi | BS076-19 | 0.0572 | 0.0048 | 0.0626 | 0.0051 | 0.0078 | 0.0002 | 0.35 | 499.1 | 175.46 | 61.6 | 4.86 | 50 | 1.41 | 1.232 | Discordant |
| RGDi | BS076-20 | 0.0312 | 0.0073 | 0.0353 | 0.0082 | 0.0084 | 0.0004 | 0.18 | 0.1 | 0 | 35.2 | 8.03 | 53.8 | 2.24 | 0.654 | Discordant |
| **Weighted average (95% confidence level)** | | | | | | | | | | | 53 | 10 | 50.5 | 2.9 | | |

### 3.2.7 Samples with Inconclusive Results

Two samples, BS047 and BS062, of Quartz Porphyry dike were collected to confirm the age of the unit and constrain the timing of deformation and skarn alteration. Based on cross-cutting relationships and the previous dating done by Gaspar (2005), the Quartz Porphyry dikes are the youngest of the Jurassic intrusions. They usually cross-cut skarn mineralization, but as shown in Chapter 2 may be skarn altered. Sample BS062 has at least one of the two low angle foliations (Figure 2.16).

Sample BS062 contained a single zircon that was large enough for analysis. The grain was approximately 75 by 200 μm and was subhedral. Minor zoning was noted from BSE imaging, but a core was not visible. However, an inherited core was clearly visible with CL imaging performed after dating (Figure 3.18). Three ablation lines were done on the grain; they were affected by the inherited core and returned ages of approximately 177 Ma, 1795 Ma and 1829 Ma (Table 3.11). The first age is interpreted as a mixing age between the core and the rim, and the latter two as the age of the core. Similar age xenocrysts were found when Gaspar (2005) determined a weighted average $^{206}Pb/^{238}U$ age of 163.6 ± 0.8 Ma for the Quartz Porphyry dikes. Sample BS047 contained five zircons, but they were not large enough for dating.

Sample BS061 was collected from a rhyolite layer that is conformable with the BMS rocks (Figure 2.1). It was chosen to provide a date for the BMS, which has not been dated isotopically, and is one of the host rocks for the gold mineralization and skarn alteration. The sample did not contain any zircons and therefore could not be dated. The Permian ages assigned based on the faunal assemblage remains the best age for the BMS.

Sample BS099 was selected for U-Pb geochronology from the Mafic Diorite, which is presumed to be an early dike phase of the BIS. The sample did not contain any zircons, so it could not be dated. In the absence of contradictory evidence the Mafic Diorite will continue to be presumed to be Middle Jurassic in age and an early dike phase of the BIS.

A

Acc.V Spot Magn Det WD ├──────────┤ 50 μm
15.0 kV 6.0 1342x BSE 10.8

B

BS062
MAG: 1388 x HV: 15.0 kV WD: 11.0 mm       40 μm
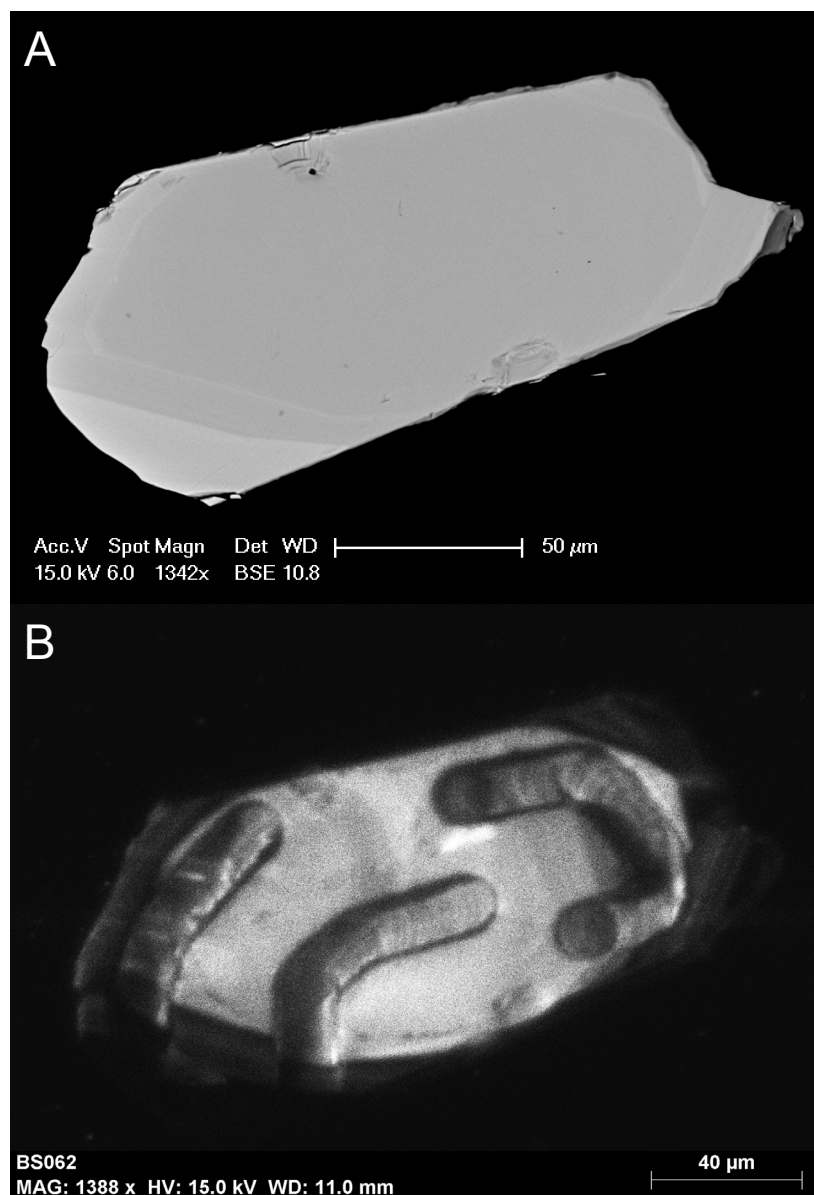
**Figure 3.18:** BSE (A) and CL (B) image of the zircon recovered from sample BS062

**Table 3.11:** Isotope ratios and age estimates for sample BS062

| Rock Type | Sample-analysis | Isotopic ratios | | | | | | | Age estimates (Ma) | | | | | | | Comments |
|---|---|---|---|---|---|---|---|---|---|---|---|---|---|---|---|---|
| | | $^{207}Pb$ $/^{206}Pb$ | ± 1σ | $^{207}Pb$ $/^{235}U$ | ± 1σ | $^{206}Pb$ $/^{238}U$ | ± 1σ | Rho | $^{207}Pb$ $/^{206}Pb$ | ± 1σ | $^{207}Pb$ $/^{235}U$ | ± 1σ | $^{206}Pb$ $/^{238}U$ | ± 1σ | Dis-cord. | |
| QP | BS062-aa | 0.0470 | 0.0009 | 0.1793 | 0.0038 | 0.0279 | 0.0002 | 0.36 | 47 | 46.28 | 167.5 | 3.23 | 177.3 | 1.32 | 0.9447 | Inheritance |
| QP | BS062-bb | 0.1050 | 0.0024 | 4.3908 | 0.2007 | 0.3211 | 0.0040 | 0.27 | 1713.7 | 40.75 | 1710.6 | 37.8 | 1795 | 19.55 | 0.9530 | Xenocryst |
| QP | BS062-cc | 0.1080 | 0.0023 | 4.9746 | 0.2293 | 0.3280 | 0.0040 | 0.26 | 1765.3 | 38.88 | 1815 | 38.97 | 1828.6 | 19.27 | 0.9926 | Xenocryst |

Table 3.11 — U/Pb LA-ICP-MS data and calculated ages

## 3.3   Re-Os Geochronology of Molybdenite

### 3.3.1 Introduction and Methods

Prior to this study there was uncertainty regarding the age of gold mineralization at Buckhorn. Early authors correlated the skarn alteration and gold mineralization with the Middle Jurassic Buckhorn Intrusive Suite (Hickey, 1990, 1992) whereas the more recent work (Gaspar, 2005) suggests that alteration and mineralization are related to the Eocene Roosevelt Intrusive Suite. Local small scale mapping and petrography (Figure 2.9 and Figure 2.11), combined with U-Pb geochronology showed that the skarn alteration is spatially related to the Granodiorite dikes and has a maximum age of 167.5 ± 0.8 Ma (Figure 3.15), however a definitive minimum age was not determined. Re-Os geochronology was performed on two samples of rare molybdenite mineralization that postdates the skarn alteration, the resulting ages were used to define the minimum age of skarn alteration and gold mineralization.

The Re-Os geochronology was performed by Dr. Roberta A Creaser's lab at the University of Alberta following their protocol as outlined in Lawley et al. (2010) and summarized below. Molybdenite concentrates were generated using modified mineral separation techniques that minimized contact with metal. Samples were pulverized in a porcelain disc mill and magnetic minerals were removed using a Frantz isodynamic magnetic separator. Molybdenite was separated using a combination of heavy liquids and flotation with high purity water. Final molybdenite concentrates were handpicked under a microscope as a last step in quality control. Molybdenite is the preferred mineral for Re-Os geochronology because of its tendency to incorporate large concentrations of Re and insignificant non-radiogenic Os at the time of crystallization (Stein et al., 2001). This property allows a Re-Os model age to be calculated from the simplified isotope equation, $t = \ln(^{187}Os/\ ^{187}Re + 1)/\lambda$, where t = model age, and $\lambda = ^{187}Re$ decay constant, $1.666 \times 10^{-11}$ yr$^{-1}$; (Smoliar et al., 1996). $^{187}Re$ and $^{187}Os$ were measured using isotope dilution mass spectrometry following the methods of Selby and Creaser (2004). Mass-dependent fractionation during analysis was corrected by using a mixed double spike (Markey et al., 2007). Samples were equilibrated with the Re-Os tracer using the Carius tube method. Purified Re and Os concentrates were then loaded onto barium-coated Pt filaments and the respective isotopic concentrations were measured using negative thermal ionization mass spectrometry (Creaser et al., 1991). Total procedure blanks are on the order of <5 pg for Re and <2 pg for Os. Re-Os model age errors are reported at 2σ and account for uncertainties in mass spectrometry measurements, spike and standard Re-Os isotope compositions, and the Re-Os decay constant of Smoliar et al. (1996).

### 3.3.2 Molybdenite in Skarn Altered Diorite

The skarn sample with the highest molybdenite content is sample BS068, an example of epidote-pyroxene skarn with a Buckhorn Diorite protolith. BS068 was collected from a diamond drill hole, D09-513, north of the Magnetic Mine (Figure 2.1). The sample is made up of intense prograde pyroxene and retrograde epidote alteration with abundant late molybdenite and minor pyrrhotite and chalcopyrite. The molybdenite occurs in intercrystalline space between the silicate skarn minerals or in vein-like bands and locally makes up approximately 1% of the rock (Figure 3.19). Chalcopyrite and pyrrhotite make up a trace amount of the rock and occur with quartz in intercrystalline space between skarn minerals (Figure 3.19). Based on its location between prograde and retrograde minerals the molybdenite formed towards the end of retrograde alteration. Sample BS068 was not gold mineralized and molybdenite was not found in contact with the other sulfides, so the timing of molybdenite alteration relative to the typical sulfide alteration and gold mineralization is unknown. However, as gold mineralization was documented to also occur towards the end of retrograde alteration the molybdenite is assumed to be approximately coeval with gold mineralization.

### 3.3.3 Molybdenite in Skarn Altered Metasedimentary Rocks

A second sample of molybdenite-bearing skarn, BS067, was collected from a diamond drill hole, D08-484, below the SWOZ. Sample BS067 contains less molybdenite than sample BS068, but the former is closer in character to typical gold-bearing skarn in the SWOZ. Sample BS067 is made up of garnet and lesser pyroxene prograde alteration with moderate amphibole and minor hydrated Fe-silicate retrograde alteration (Figure 3.19). Unlike the typical skarn sample BS067 contains a trace amount of molybdenite that occurs as 20 to 200 μm anhedral crystals. The molybdenite preferentially occurs along quartz crystal boundaries in intercrystalline space between prograde and retrograde minerals. The molybdenite rims rare pyrrhotite in the sample, and therefore postdates the majority of retrograde alteration (Figure 3.19). The sample did not contain any gold grains so the relative timing of molybdenite and gold is unknown, but as noted with sample BS068, based on its place in the paragenesis molybdenite is presumed to be approximately coeval with gold.
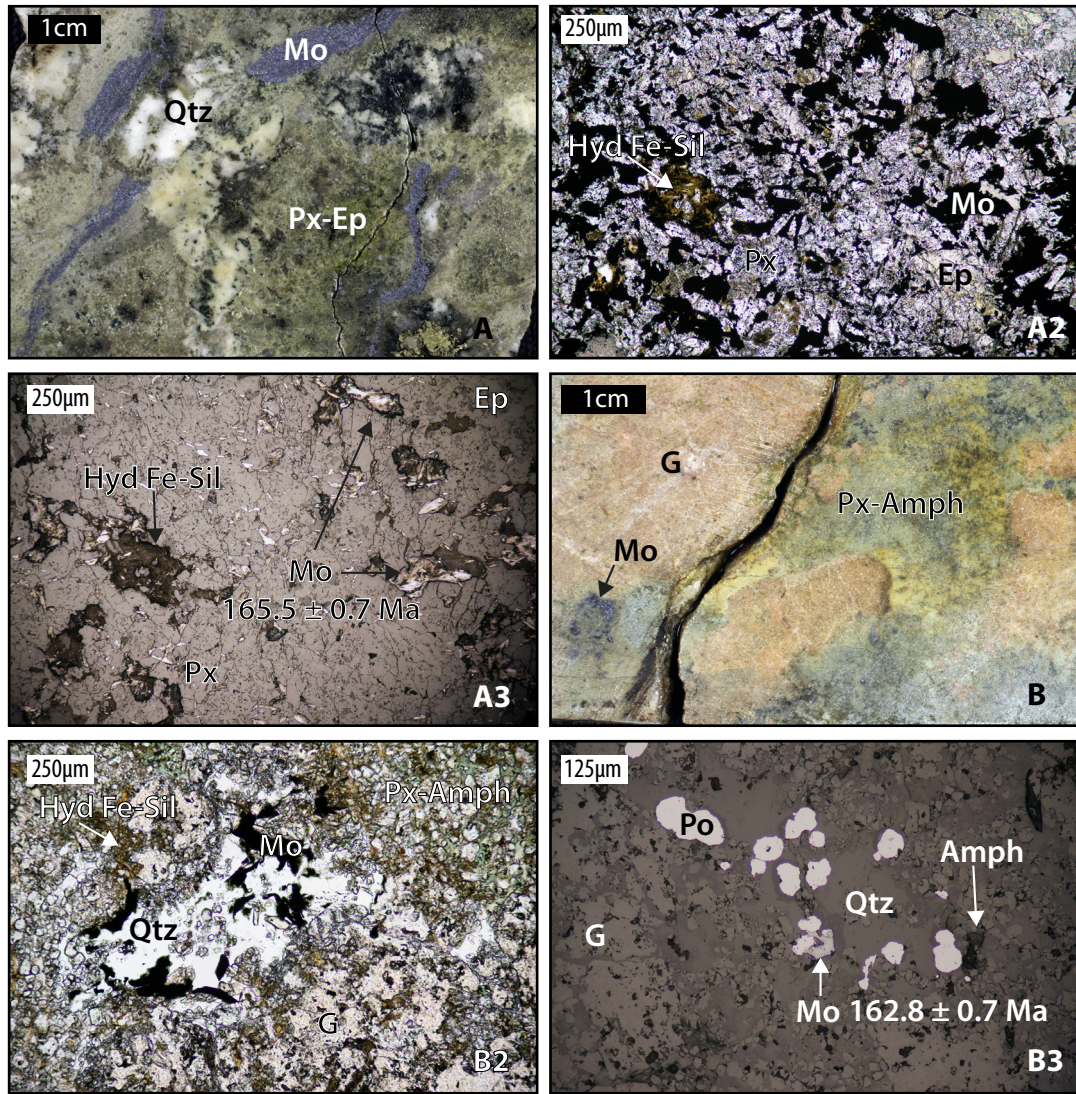
**Figure 3.19:** Examples of molybdenite bearing skarn. The photograph (A), PPL photomicrograph (A2), and RL photomicrograph (A3) show sample BS068 an example of Px-Ep endoskarn. This sample was dated by Re-Os geochronology in molybdenite at 165 ± 0.7 Ma (Table 3.12). The photograph (B), PPL photomicrograph (B2), and RL photomicrograph (B3) show sample BS067 an example of garnet skarn from the BMS below the SWOZ. The sample was dated to 162.8 ± 0.7 Ma by Re-Os geochronology of molybdenite (Table 3.12). See text for further discussion

### 3.3.4 Results of Re-Os Geochronology

The results of the Re-Os geochronology on the molybdenite in samples BS068 and BS067 are shown in Table 3.12. The analysis returned a model age of 165.5 ± 0.7 Ma for sample BS068 and 162.8 ± 0.7 Ma for sample BS067. Analyzed Re and Os concentrations in sample BS068 were 58.58 ppm and 101.65 ppb respectively, and 24.87 ppm and 42.47 ppb for sample BS067 (Table 3.12).

**Table 3.12:** Re-Os isotope data for molybdenite samples from Buckhorn

| Sample no. | Location | Re (ppm) | ± 2σ | ¹⁸⁷Re (ppm) | ± 2σ | ¹⁸⁷Os (ppb) | ± 2σ | Common Os (pg) | Model Age ( Ma) | ± 2σ with λ (Ma) |
|---|---|---|---|---|---|---|---|---|---|---|
| BS068 | Epidote-Pyroxene endoskarn with Buckhorn Diorite protolith | 58.58 | 0.15 | 36.82 | 95 | 101.65 | 0.08 | 4 | 165.5 | 0.7 |
| BS067 | Garnet Skarn with BMS protolith | 24.87 | 0.08 | 15.63 | 47 | 42.47 | 0.07 | 33 | 162.8 | 0.7 |

## 3.4   Summary and Discussion

The current dating has added to the understanding of the host rocks and intrusive rocks at the Buckhorn gold skarn in several ways. It has confirmed the Middle Jurassic age of the BIS, with a more precise age for the Buckhorn Granodiorite at 170.4 ± 1.7 Ma. The dating has added to the understanding of the BIS by showing that the Buckhorn Diorite, 168.9 ± 0.9 Ma, is within error of the age of the Buckhorn Granodiorite and is therefore likely a marginal phase of the pluton. It also determined that there are four generations of dikes. The Mafic Diorite was not dated, but based on geochemistry, petrography and mineralogy is clearly distinct from the other dikes. The Early Diorite dikes (168.2 ± 0.7 Ma) were originally thought to predate the pluton, but they are shown to be the statistically the same age as the Granodiorite dikes and the Buckhorn Diorite. A more precise age was determined for the Granodiorite dikes of 167.5 ± 0.7 Ma. As skarn alteration was shown to occur in the halos of the Granodiorite dikes (Figure 2.9 and Figure 2.11), their new age provides a precise maximum age for skarn alteration and gold mineralization. A new age was not determined for the Quartz Porphyry dikes as insufficient zircons were present, but based on the cross-cutting relationships and the age (163.6 ± 0.8 Ma) determined by Gaspar (2005) they are interpreted as the youngest expression of the Middle Jurassic BIS. The new dates also confirm the Eocene age of the porphyritic Roosevelt Granodiorite, at 50.5 ± 2.9 Ma.

The Re-Os geochronology provides the first age dates for sulfide alteration at Buckhorn and helps bracket the age of gold mineralization. In both samples the molybdenite forms after the prograde and retrograde alteration, so the dates provide definitive minimum ages for the skarn alteration at both sample locations. The paragenetic relationship between gold and molybdenite is unknown as the two minerals were not found in contact with each other, but as shown in Chapter 4 both gold and molybdenite occur towards the end of retrograde alteration and are therefore assumed to be approximately coeval. Based on this assumption the ages determined for the molybdenite also provide minimum ages for the gold mineralization. When combined with the U-Pb geochronology of local

intrusive rocks the Re-Os dates constrain the age of the skarn alteration and gold mineralization at Buckhorn to a 4.7 million year window in the Middle Jurassic between 167.5 Ma and 162.8 Ma (Figure 3.20). Based on these ages, the petrography and the small scale mapping presented in Chapter 2, it is clear that the skarn alteration and gold mineralization at Buckhorn is genetically related to the Buckhorn Intrusive Suite.
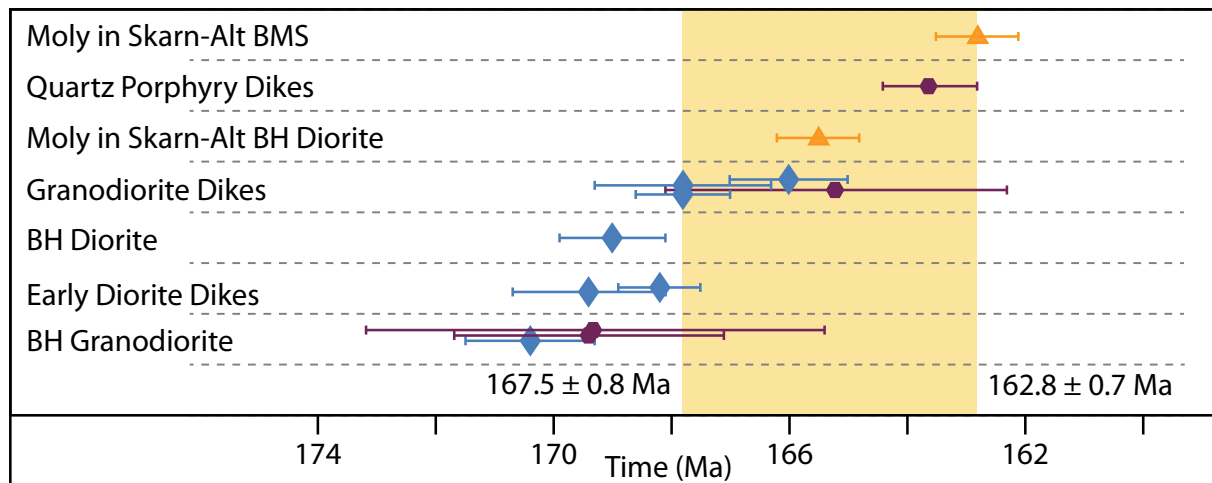


**Figure 3.20:** Summary of isotopically determined Middle Jurassic ages at Buckhorn. The range of possible ages for skarn alteration and gold mineralization is denoted by the gold box. Error bars are 2σ, See text for further discussion.

The U-Pb dating has also constrained the age of the onset of deformation. Prior to this study it was unclear when the deformation events affecting the Buckhorn area occurred. The low angle foliations are most intensely developed in the host BMS rocks leading some authors to suggest that their development predated the emplacement of the BMV and the intrusive rocks (McMillen, 1979). The poly-deformed Granodiorite dike, sample BS059, however, shows that the low angle and steeply-dipping foliations formed after the emplacement of the Granodiorite dikes at 167.5 ± 0.72 Ma. This contrasts earlier work that proposed that only the high angle foliation post-dated the igneous rocks and affected the skarn alteration (Gaspar, 2005; McMillen, 1979).

Another significant outcome of the present work is the new age of the BMV. The BMV rocks have previously been correlated with a number of units with a wide range of ages including the Permian Kobau Formation (Hickey, 1990, 1992; McMillen, 1979), the Triassic Brooklyn Formation

(McMillen, 1979), and the Jurassic Elise Formation (Cheney et al., 1994; Gaspar, 2005). Based on geochemical and geologic similarities Gaspar (2005) concluded that they were likely equivalent to the Jurassic Elise Formation, but said that they were also compositionally similar to varieties of the Permian Attwood Group and the Triassic Brooklyn Formation. Based on the Early Jurassic age of 193.5 ± 1.2 Ma for an intrusion comagmatic with the BMV it is now clear that the BMV, is equivalent to the Jurassic Elise Formation.

# Chapter 4.   Skarn Alteration and Gold Mineralization

## 4.1   Categories of Gold Skarns

Gold skarns can be categorized as reduced, oxidised, magnesian, or metamorphic. These categories are defined based the mineralogy of the prograde and retrograde alteration, the character of the intrusive and host rocks, and the regional tectonic setting (Meinert et al., 2005).

Reduced gold skarns are the highest grade and best studied of the gold skarn categories (Meinert et al., 2005). Their prograde mineralogy is dominated by Fe-rich pyroxene (>Hd50), but can contain significant grossular-andradite garnet in proximal zones. The retrograde mineralogy is more diverse and is composed of K-feldspar, scapolite, vesuvianite, apatite, amphibole, and abundant sulfide minerals dominated by pyrrhotite and arsenopyrite (Meinert et al., 2005).The reduced gold skarns typically form from clastic-rich protoliths and are associated with diorite-granodiorite plutons and dike-sill complexes (Meinert, 2000). These intrusive rocks are typically emplaced at shallow depths (<5km) and arc related (Meinert, 2000). Other features of reduced gold skarns include their Au-Bi-Te-As geochemical signature, early and/or distal hornfels alteration, and lack of economic concentrations of metals other than gold (Meinert et al., 2005).

Oxidized gold skarns are lower grade but have produced more gold than reduced gold skarns (Meinert, 2000). They are characterized by a prograde mineral assemblage composed of Fe poor garnet with lesser pyroxene, and a retrograde assemblage that is made up of abundant K-feldspar and quartz, with lesser pyrite, pyrrhotite and minor but ubiquitous chalcopyrite, sphalerite, and galena (Meinert et al., 2005). Oxidized gold skarns form in similar host rocks as the reduced gold skarns, but are associated with more oxidized and silicic plutons that were emplaced at a similar depth and in a similar tectonic setting (Meinert, 2000). Oxidized gold skarns have the same Au-Bi-Te-As geochemical signature, early and/or distal hornfels alteration, and lack of economic concentrations of metals other than gold (Meinert, 2000).

Magnesian gold skarns are less abundant that reduced and oxidised gold skarns. They are distinguished from the latter two on the basis of their magnesium rich mineralogy, which is dominated by forsterite, spinel, and serpentine (Meinert et al., 2005). Magnetite is the most abundant spinel mineral and most of the magnesian gold skarns are mined for their Fe content in addition to gold (Meinert et al., 2005). Magnesian gold skarns form from dolomitic protoliths and can form in the

same tectonic setting, associated with similar intrusive rocks to the reduced and oxidised gold skarns (Meinert, 1998; Meinert et al., 2005).

Metamorphic gold skarns are distinguished from the other categories of gold skarn primarily on the basis of their tectonic setting (Meinert et al., 2005). Metamorphic skarns occur in orogenic belts where the skarn alteration is associated with both plutonism and high-temperature and high-pressure metamorphism. This contrasts the skarns in the aforementioned categories that have a clear genetic relationship with relatively shallow Phanerozoic plutons that intruded into previously unmetamorphosed sedimentary rocks (Meinert et al., 2005). Some of the metamorphic gold skarns occur in Precambrian terranes and are not associated with intrusive rocks (Meinert et al., 2005). The metamorphic gold skarns typically have a reduced mineralogy made up of Fe-rich almandine-spessartine garnet, hedenbergite pyroxene, and Fe-rich amphibole. The mineralogy may be controlled by Fe-rich protoliths such as Fe formations, komatiites, and metabasalts (Meinert et al., 2005). These deposits typically have the same Au-As-Bi-Te geochemical signature as the reduced, oxidised, and magnesian gold skarns (Meinert et al., 2005).

## 4.2   Introduction

Skarn alteration at Buckhorn dominates at three locations: The Southwest Ore-Zone (SWOZ), the Gold Bowl Ore Zone and the Magnetic Mine (Figure 2.2). The SWOZ is two sub-parallel, sub-horizontal zones located along the upper and lower contact of the upper carbonate member of the BMS (Figure 2.4). The majority of the skarn alteration in the SWOZ forms as a relatively thin (1-15m) layer replacing both the metasedimentary and metavolcanic rocks along the upper contact. A subordinate portion of the SWOZ replaces both carbonate and clastic metasedimentary rocks along the lower contact of the carbonate member. In addition to these locations, a minor amount of skarn is developed in lenses within the BMS below the SWOZ (Figure 2.4). Skarn alteration in the Gold Bowl is thicker, up to 200 m, and patchy compared to the SWOZ. The Gold Bowl skarn alteration occurs in clastic metasedimentary and igneous rocks in the hanging wall of the footwall mylonite. The Magnetic Mine skarn has a larger areal extent than the Gold Bowl skarn and occurs in metasedimentary rocks at the contact with the southwest margin of the Buckhorn Diorite (Figure 2.2). In addition to these locations, lesser amounts of skarn alteration occur elsewhere in the Buckhorn area, such as at Mike's Skarn and in alteration halos around Granodiorite dikes (Figure 2.2).

Gold mineralization at Buckhorn is predominately hosted in skarn altered rocks. The majority of economic gold mineralization occurs in the upper and lower SWOZ, with additional economic mineralization in the Gold Bowl (Cooper et al., 2008). Gold mineralization is unevenly distributed through the skarn, and significant portions of skarn alteration in the SWOZ and Gold Bowl are not gold mineralized. Gold has also been discovered in non skarn-altered rocks, although not in economic abundances. The Magnetic Mine does not host economic gold mineralization, but was mined during the first half or the 20th century for small amounts of iron, copper, silver, gold and magnesium (Moen, 1980). Gold mineralization also occurs in some of the minor skarn occurrences in the BMS, such as at Mike's Skarn, but none of these are currently considered to be economic.

To better understand the skarn alteration and gold mineralization at Buckhorn detailed optical petrography was performed on 55 samples from the SWOZ and Gold Bowl (Figure 4.1 and Table 4.1). To complement the petrography, back-scattered electron (BSE) imaging was done on 7 skarn-altered samples and major element microprobe analysis was performed on pyroxene and amphibole from 5 skarn-altered samples. Diamond drill holes were logged and small scale underground mapping was also performed in the SWOZ. This work has five main goals: (1) to define the character of the skarn alteration assemblages, including the zonation and paragenesis; (2) to determine the relative timing of skarn alteration, deformation, and gold mineralization; (3) to describe the character of gold-bearing, non skarn-hosted rocks; (4) to define different settings of gold mineralization and to determine their relative age relationships; and (5) to describe the differences and similarities between Buckhorn and other gold skarns. In particular, to compare Buckhorn to the Nickel Plate deposit in the Hedley mining district, one of the largest and best studied reduced gold skarns located approximately 90 km to the northwest (Figure 1.1).

The descriptions that follow are first divided by the three major skarn assemblages and then further subdivided based on retrograde alteration mineral assemblages. With the benefit of greater access to the SWOZ than the previous studies, due to additional drilling and underground mining, the current work is able to provide a more detailed and comprehensive description of the skarn alteration and gold mineralization at Buckhorn.

**Table 4.1:** Table of diamond drill holes and skarn samples selected for petrographic analysis

| Drill Hole | Location | Samples | Types of Skarn Alteration | Analysis Performed | Range of Gold Grade (ppm) |
|---|---|---|---|---|---|
| D07-323 | SWOZ | BS007-09 | Pyroxene and Magnetite | Petrography | 0.2 - 21.7 |
| D07-325 | SWOZ | BS020-21 | Pyroxene | Petrography | 11.1 - 27.4 |
| D07-326 | SWOZ | BS010-12 | Pyroxene | Petrography | 0.1 - 31.8 |
| D07-327 | SWOZ | BS005-06 | Pyroxene | Petrography | <0.1 - 2.8 |
| D07-329 | SWOZ | BS002-04 | Pyroxene and Magnetite | Petrography | 9.7 - 319.8 |
| D07-358 | SWOZ | BS018-19 | Pyroxene | Petrography | 0.6 - 20.5 |
| D07-369 | SWOZ | BS082-84 | Pyroxene, Garnet, and Magnetite | Geochemistry and Petrography | <0.1 - 62.0 |
| D07-394 | SWOZ | BS022-23 | Pyroxene and Garnet | Petrography | <0.1 - 0.1 |
| D08-409 | SWOZ | BS024 | Garnet | Petrography | 36.0 |
| D08-410 | SWOZ | BS090-94 | Pyroxene, Garnet, and Magnetite | Geochemistry, Microprobe Analysis, and Petrography | <0.1 - 51.1 |
| D08-413 | SWOZ | BS016-17, BS085-88 | Pyroxene, Garnet, and Magnetite | Geochemistry and Petrography | <0.1 - 117.5 |
| D08-414 | SWOZ | BS013-15 | Magnetite and Pyroxene | Petrography | <0.1 - 172 |
| D08-420 | SWOZ | BS025-28 | Pyroxene | Petrography | 0.6 - 6.9 |
| D08-443 | GB | BS077-79, BS089 | Pyroxene and Garnet | Geochemistry, EDS, and Petrography | <0.1 - 53.7 |
| D08-480 | SWOZ | BS030 | Garnet | Petrography | 0.1 |
| D08-484 | SWOZ | BS067 | Molybdenite bearing Garnet | Re-Os Geochronology and Petrography | |
| D09-490 | SWOZ | BS033-34 | Pyroxene | Petrography | 30.0 - 67.2 |
| D09-513 | SWOZ | BS068 | Molybdenite bearing Epidote-Pyroxene | Re-Os Geochronology and Petrography | |
| D09-536 | North of GB | BS080-81 | Pyroxene, Garnet, and Magnetite | Geochemistry and Petrography | <0.1 - 0.7 |
| D10-569 | Below SWOZ | BS095-96 | Skarn veins | Geochemistry and Petrography | <0.1 - 24.1 |
| D10-595 | Below SWOZ | BS097-98 | Skarn veins | Geochemistry and Petrography | <0.1 - 3.5 |
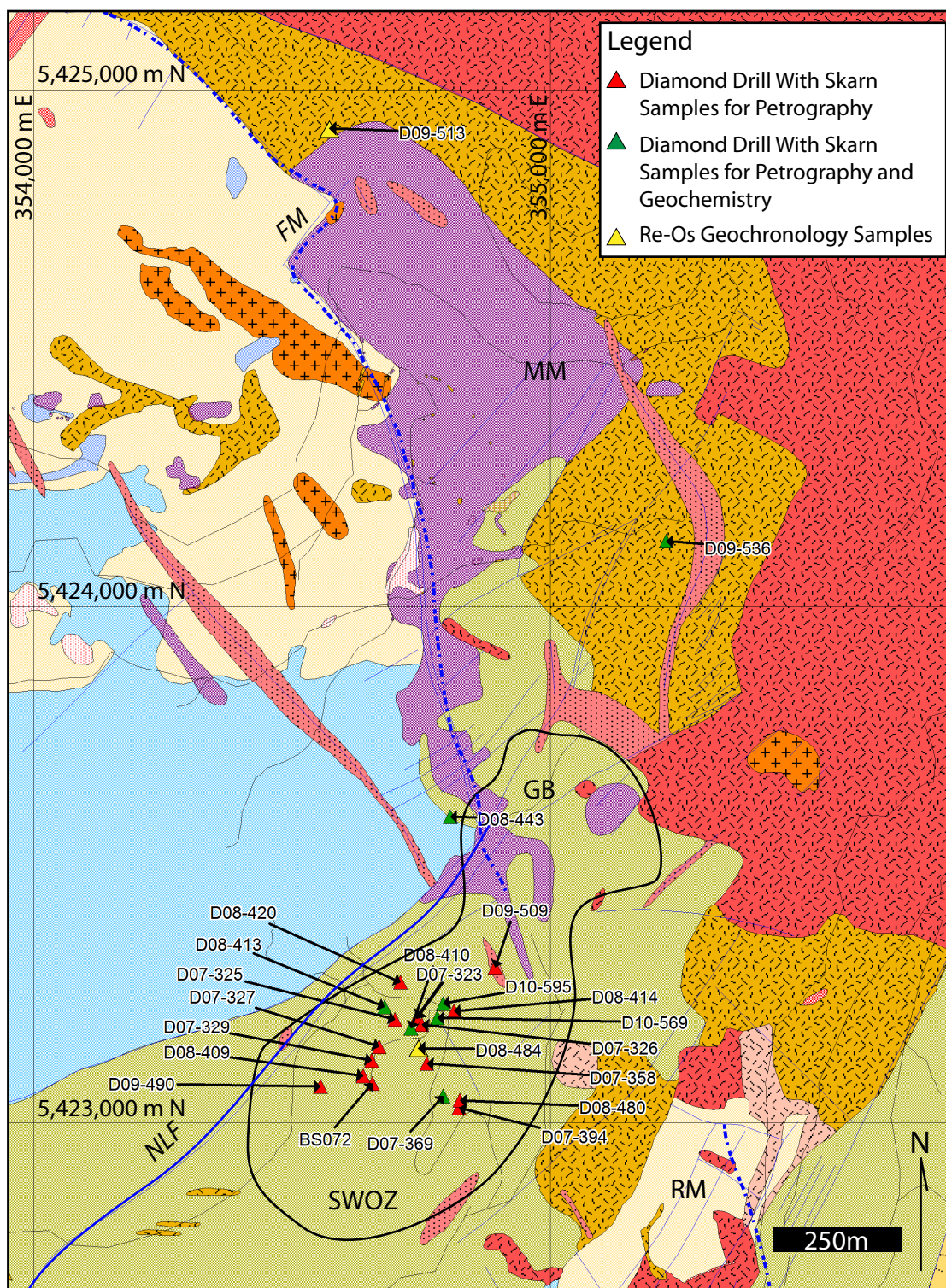
**Figure 4.1:** Geologic map of Buckhorn Mountain with the skarn petrography, skarn geochemistry and Re-Os geochronology sample locations highlighted. Based on data from this study and modified from Kinross Gold Corporation maps. See   for map legend.

**Table 4.2:** Mineral compositions at Buckhorn as determined by microprobe analysis, performed by Gaspar (2005). In this thesis, minerals will be referred to by their category, except where the distinction can be made based on optical properties.

| Mineral Category | End Member Minerals at Buckhorn | End Member Mineral Formula | |
|---|---|---|---|
| Pyroxene | Diopside$_{(64)}$ | Diopside | $CaMgSi_2O_6$ |
| | Hedenbergite$_{(93)}$ | Hedenbergite | $CaFeSi_2O_6$ |
| Garnet | Grossular$_{(70)}$ | Grossular | $Ca_3Al_2(SiO_4)_3$ |
| | Andradite$_{(99)}$) | Andradite | $Ca_3Fe_2(SiO4)_3$ |
| Epidote | Clinozoisite (XFe=14) | Clinozoisite | $Ca_2Al_3(SiO_4)_3(OH)$ |
| | Epidote (XFe=33) | Epidote | $Ca_2(Fe,Al)_3(SiO_4)_3(OH)$ |
| Amphibole | Tremolite | $Ca_2Mg_5(Si_8O_{22})(OH)_2$ | |
| | Fe-Actinolite | $Ca_2Fe_5(Si_8O_{22})(OH)_2$ | |
| | Fe-hornblende | $Ca_2Fe_4(Al,Fe)(Si_7AlO_{22})(OH)_2$ | |
| | Fe-Tschermakite | $Ca_2Fe_3AlFe(Si_6Al_2O_{22})(OH)_2$ | |
| | Hastingsite | $NaCa_2Fe_4(Al,Fe)(Si_6Al_2O_{22})(OH)_2$ | |
| | Grunerite | $Fe_7(Si_8O_{22})(OH)_2$ | |
| Hydrated Fe-silicate | Ekmanite | $(Fe,Mg,Mn)_3(Si,Al)_4O_{10}(OH)_2-2(H2O)$ | |
| | Ferrostilpnomelane | $K(Fe,Mg)_8Si_{10}Al_2O_{24}(OH)_3-2(H_2O)$ | |
| | Greenalite | $Fe_2Si_2O_5(OH)_4$ | |
| | Minnesotaite | $(Fe,Mg)_3Si_4O_{10}(OH)_2$ | |
| Bismuth phases | Native Bi | Bi | |
| | Bismuthinite | $Bi_2S_3$ | |
| | Joseite | $Bi_4TeS_2$ | |
| | Pilsenite | $Bi_4Te_3$ | |
| | Sulphotsumoite | $Bi_3Te_2S$ | |
| | Tetradymite | $Bi_2Te_2S$ | |
| | Joseite-B | $Bi_4Te_2S$ | |
| | Tsumoite | BiTe | |
| | unknown Bi Sulfide | $(Bi,Pb)_6AuS_5$ | |
| Gold | Gold | $Au_{(100)}$ | |
| | Electrum | $Au_{(88)}Ag_{(12)}$ | |

XFe = 100*($Fe^{3+}$/( $Fe^{3+}$ + Al))
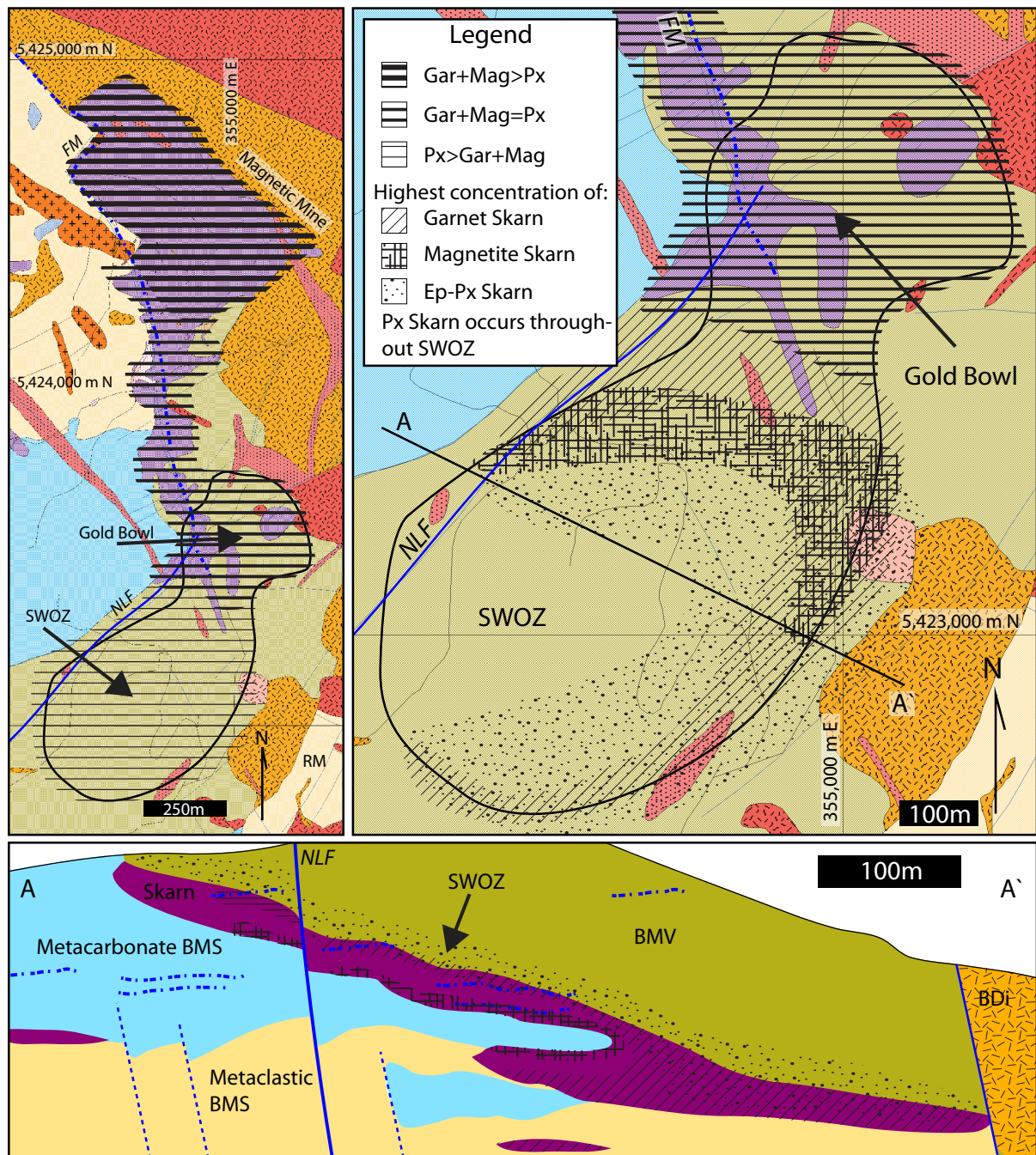
**Figure 4.2:** Geologic map and cross-section of Buckhorn Mountain with the schematic skarn zonation highlighted. Pyroxene skarn occurs throughout the SWOZ. The thickness of skarn alteration on cross-section is exaggerated by a factor of 2 to more clearly illustrate zoning. Based on data from this study and modified from Kinross Gold Corporation maps. See   and Figure 2.2 for map and cross-section legends.

### 4.3   Pyroxene Skarn

Pyroxene skarn is the most abundant skarn type at Buckhorn, composing the majority of the SWOZ and a significant portion of the Gold Bowl. Pyroxene skarn is more prevalent near the west and south margins of the SWOZ and near the base of the Gold Bowl, but does occur throughout both ore bodies (Figure 4.2). Pyroxene skarn formation is texturally destructive; making identification of the protolith difficult to impossible. Based on the intensity and type of retrograde alteration the pyroxene skarn can be classified into three sub-categories: (1) Amphibole-Pyroxene, (2) Magnetite-Pyroxene, and (3) Epidote-Pyroxene.

### 4.3.1 Amphibole-Pyroxene Skarn

Amphibole-pyroxene skarn is the most abundant variety of pyroxene skarn at Buckhorn. This type of skarn has a prograde assemblage composed of greater than 90 % pyroxene along with minor garnet (<10 %) and magnetite (<10 %). Retrograde alteration is dominated by amphibole, which replaces 20 to 80 % of the pyroxene. Other retrograde and accessory minerals such as epidote, hydrated Fe-silicates, calcite and quartz occur in minor amounts, however, in rare locations calcite may compose up to 40 % of the rock. Sulfide minerals are part of the retrograde assemblage and usually compose up to about 10 % of the rock. Pyrrhotite is the most abundant sulfide mineral (5-10 %), and is accompanied by lesser pyrite and chalcopyrite, and trace sphalerite, gold, native bismuth and other Bi-minerals. In hand sample the amphibole-pyroxene skarn is moderate to dark green depending on the amphibole content, with the darker specimens corresponding to higher amphibole contents (Figure 4.3 and Figure 4.4).
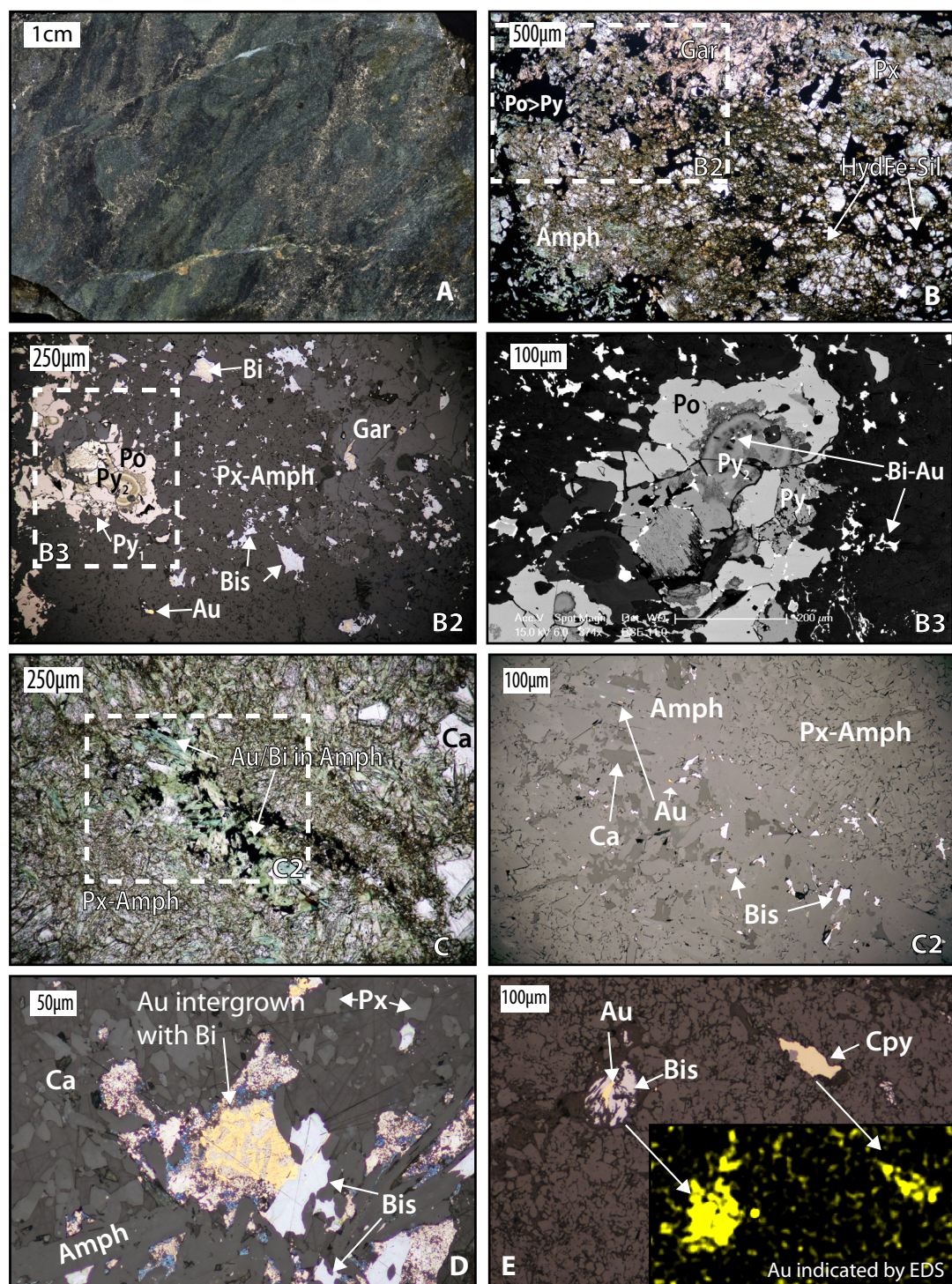
**Figure 4.3:** Examples of amphibole-pyroxene skarn. The photograph (A), PPL photomicrographs (B, C), RL photomicrograph (B2, C2, D, E), BSE image (B3), and EDS elemental map (E) show the mineralogy, texture and paragenesis of the skarn alteration and gold mineralization. See text for further discussion.

Pyroxene occurs as 100 μm to 1 mm, subhedral to euhedral stubby prismatic crystals (Figure 4.3 and Figure 4.4). Pyroxene typically forms in a decussate, polygonal or web texture with poikiloblastic calcite and minor quartz. When present, garnet occurs as near euhedral, anisotropic, concentrically and/or hexagonally zoned crystals that rarely include pyroxene (Figure 4.3 and Figure 4.4). The garnet crystals are typically larger than pyroxene, and range from 200 μm to 2 mm in diameter. Garnet crystals tend to be concentrated in discrete masses, rather than evenly distributed through the skarn (Figure 4.3 and Figure 4.4). Magnetite occurs as subhedral to anhedral near equant 50 μm crystals that are found as discrete grains or masses irregularly distributed through the pyroxene (Figure 4.3 and Figure 4.4).

The paragenesis of prograde minerals is consistent for all the amphibole-pyroxene skarn samples collected. Pyroxene was the first mineral to form followed by garnet and magnetite. The relative timing of garnet and magnetite alteration in amphibole-pyroxene skarn is ambiguous because they are not in contact with each other, but their relative timing can be interpreted from other varieties of skarn in which garnet formed before magnetite (Figure 4.3 and Figure 4.4).

Amphibole is the most abundant retrograde mineral and occurs as elongate to fibrous, subhedral to anhedral crystals that are typically smaller than the prograde pyroxene. Amphibole alteration replaces and overgrows pyroxene and in many cases destroys the prograde texture. Amphibole alteration continues through the retrograde alteration, and some of the later stages of amphibole alteration are intergrown with gold mineralization (Figure 4.3). Epidote is the next most abundant retrograde silicate mineral. Most of the epidote occurs as anhedral aggregates replacing pyroxene and/or garnet, however, some of the epidote crystals are subhedral hexagonal or rectangular crystals. Sulfide minerals form a minor portion of the retrograde alteration. Pyrrhotite is the most abundant sulfide mineral, and it is accompanied by lesser amounts of chalcopyrite, sphalerite and two types of pyrite/marcasite. Pyrrhotite occurs in fractures and/or cleavage planes through the prograde minerals or in the intercrystalline space between prograde minerals (Figure 4.3 and Figure 4.4). A lesser amount of pyrrhotite is intergrown with amphibole and/or epidote (Figure 4.3 and Figure 4.4). Chalcopyrite and sphalerite occur together in trace amounts in the same settings as pyrrhotite. In one example gold-bearing chalcopyrite was documented by the use of an elemental map generated by Energy-Dispersive X-Ray Spectroscopy (EDS) (Figure 4.3). The gold-bearing chalcopyrite is optically indistinguishable from the barren chalcopyrite, and the specific location of gold in the chalcopyrite is unknown. It is unclear how widespread the gold-bearing chalcopyrite is, but geochemical analysis of the skarn alteration pre-

sented in Chapter 5 suggests that it is a relatively rare phenomenon. The most abundant style of pyrite is a very fine grained pyrite/marcasite phase that forms with a colloform texture and partially replaces some of the pyrrhotite grains (Figure 4.3). The other style of pyrite is characterized by skeletal grains that occur in similar settings to the other sulfides (Figure 4.3).

Retrograde alteration in the amphibole-pyroxene skarn has a consistent paragenesis. Amphibole is the first retrograde mineral to form, followed by epidote and sulfide minerals. The majority of sulfide minerals formed contemporaneously with the retrograde silicate alteration and before the gold mineralization. The skeletal style of pyrite was the first sulfide to form followed by pyrrhotite-chalcopyrite-sphalerite and finally the fine grained colloform pyrite/marcasite (Figure 4.3).

Gold mineralization occurs as 5 to 100 µm gold grains preferentially located in areas with more intense amphibole alteration. Gold may be intergrown with a generation of amphibole that is typically more fibrous and coarser-grained that the other amphibole alteration in the rock (Figure 4.3). The gold may also occur in intercrystalline space between prograde and retrograde minerals, or rarely in fractures in prograde minerals (Figure 4.3). Much of the gold is finely intergrown with bismuth. The intergrowth with bismuth occurs on the micron scale, and typically with a symplectic texture (Figure 4.3). Bismuthinite and other Bi-minerals typically rim the gold and native bismuth grains (Figure 4.3). Gold mineralization in amphibole-pyroxene skarn occurs after the sulfide mineralization.

A volumetrically minor amount of hydrated Fe-silicate alteration, (Table 4.2), occurs in two stages after gold mineralization. The hydrated Fe-silicate alteration is patchy and irregularly distributed. It fills intercrystalline space between and partially replaces prograde and retrograde minerals. This stage of hydrated Fe-silicate alteration forms as the alteration product of magnetite, pyroxene, and amphibole (Figure 4.3 and Figure 4.4). A later stage occurs as less than 1 mm veins that typically contain calcite. The veins cut the replacement style of hydrated Fe-silicate alteration and the prograde and earlier retrograde alteration, and formed after gold mineralization (Figure 4.3 and Figure 4.4). In addition to the hydrated Fe-silicate veins there are also several generations of sulfide, sulfide-calcite and calcite veins (Figure 4.3). The relative timing of these veins is ambiguous, but they appear to postdate gold mineralization.

Deformation of the amphibole-pyroxene skarn is separated in the three end member categories. Most of the amphibole-pyroxene skarn is massive and not foliated in hand sample, but brittle deformation is evident at the thin section scale. The brittle deformation occurs in the prograde minerals

and the retrograde minerals are generally unaffected (Figure 4.3). In some locations retrograde altera-tion is more intense in the brittle fracture zones, and the fractures in prograde pyroxene may host gold mineralization (Figure 4.3). A lesser amount of the amphibole-pyroxene skarn appears foliated in hand sample but in thin section the minerals are not ductilely deformed. This pseudo-foliation is proposed to be the result of the skarn alteration overprinting a foliated protolith. In hand samples of the pseudo-foliated amphibole-pyroxene skarn a low angle foliation is defined by variation in the skarn mineralogy and grain size. In thin section it is clear that the pseudo-foliated skarn experienced the same brittle deformation that affected the prograde minerals in other samples, but no foliation is present (Figure 4.4). Finally, a moderate amount of the amphibole-pyroxene skarn was foliated dur-ing or after the retrograde alteration. The foliation is more prevalent in amphibole-rich skarn where it is defined by the deformation and alignment of amphibole (Figure 4.4). The foliated areas may have higher sulfide content than usual, but the sulfide minerals do not show signs of deformation. Evidence for ductile deformation is also seen in calcite grains that can have deformed twin lamella and in numerous skarn minerals (pyroxene, quartz, garnet) that have undulatory extinction (Figure 4.3 and Figure 4.4).
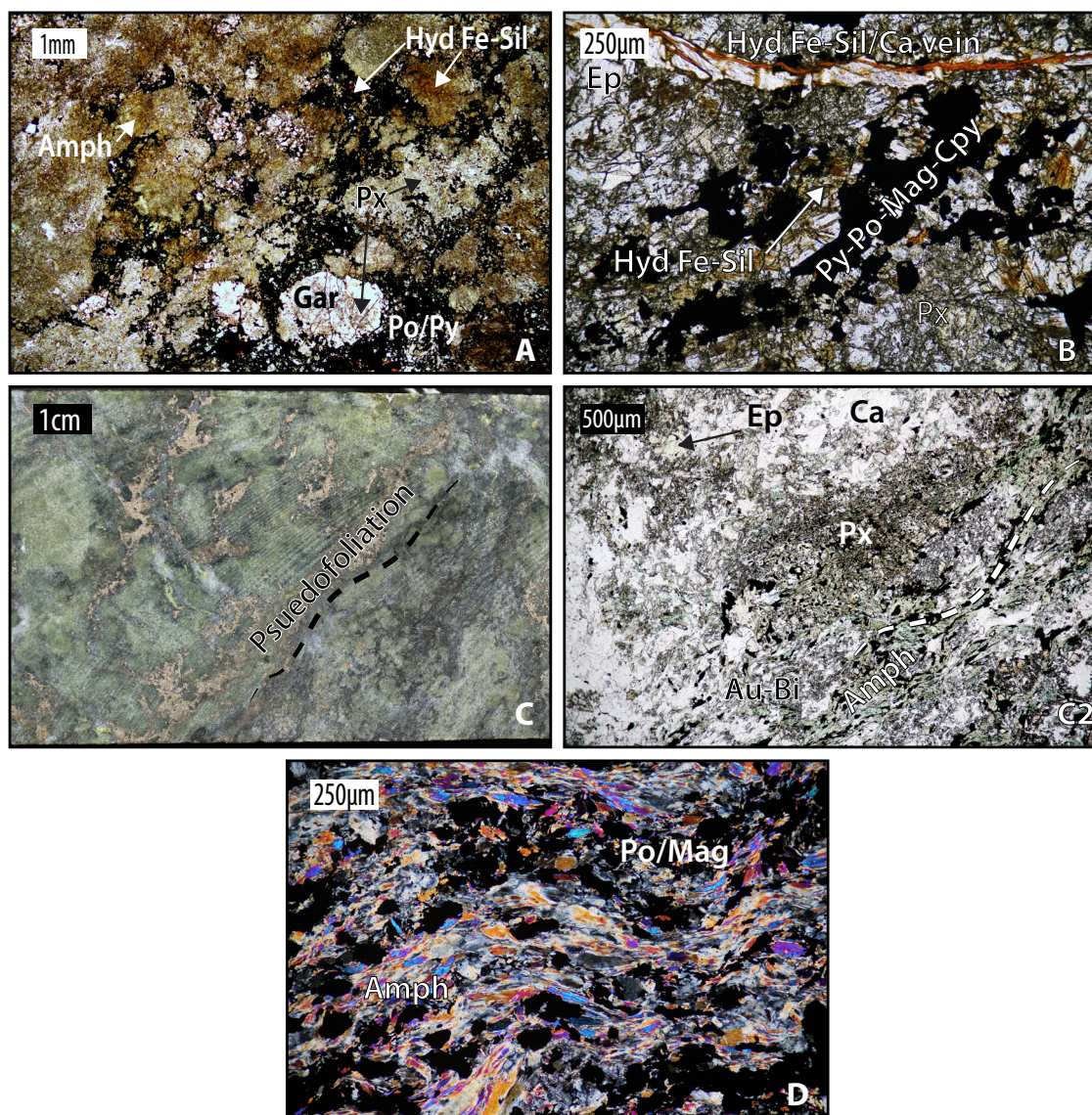
**Figure 4.4:** Examples of amphibole-pyroxene skarn. The PPL photomicrographs (A, B, C1), photograph (C) and XPL photomicrograph (D) show the mineralogy, texture and paragenesis of the retrograde alteration and the various types of deformation. See text for further discussion.

### 4.3.2 Magnetite-Pyroxene Skarn

Magnetite-pyroxene skarn occurs as a lesser component throughout the pyroxene skarn. It has similar mineralogy to the amphibole-pyroxene skarn but with higher magnetite content. There is a continuum of compositions between the two end members. The magnetite-pyroxene skarn typically has a prograde assemblage made up of between 10 and 30 % magnetite, 30 and 60 % pyroxene and trace garnet. Pyroxene is variably retrograde altered to amphibole, which accounts for between 30 and 50 % of the magnetite-pyroxene skarn assemblage. Trace amounts of other retrograde minerals such as epidote and hydrated Fe-silicates also occur. Sulfide minerals (<5 %) occur with the other retro-

grade minerals and are dominated by pyrrhotite with lesser pyrite, chalcopyrite and trace gold, native bismuth and Bi-minerals. Calcite is locally a major component of the rock (40 %). Due to the high magnetite content, the rock is black to mottled black-green in hand sample (Figure 4.5).

The magnetite-pyroxene skarn is made up of the same minerals as the amphibole-pyroxene skarn, but the minerals developed with different characteristics. Pyroxene occurs as 100 μm to 1 mm euhedral to subhedral crystals that form in a range of textures from decussate, to polygonal or web texture with poikiloblastic calcite (Figure 4.5). Magnetite crystals range in shape from near euhedral cubic crystals to irregular anhedral shapes that form interstitial to pyroxene (Figure 4.5). In the magnetite-pyroxene skarn, garnet occurs as anhedral crystals between well formed pyroxene crystals and may partially include magnetite (Figure 4.5).

The paragenetic sequence of prograde minerals in the magnetite-pyroxene skarn is different than the amphibole-pyroxene skarn. Pyroxene was the first mineral to form followed by magnetite and then garnet. All three prograde minerals appear to have formed at the same time for much of the prograde alteration (Figure 4.5).

Retrograde alteration in the magnetite-pyroxene skarn is similar to the amphibole-pyroxene skarn. Pyroxene was altered to amphibole, which replaced between 5 and 90 % of the pyroxene. Trace epidote locally formed as an alteration of pyroxene. A minor amount of sulfide minerals filled fractures and intercrystalline space between the prograde and earlier retrograde minerals. The sulfide minerals formed with similar relative abundances to the amphibole-pyroxene skarn (Po>Py>Cpy) (Figure 4.5). The paragenesis of retrograde alteration in the magnetite-pyroxene skarn for both the silicate and sulfide minerals is the same as the amphibole-pyroxene skarn.

Similar to the amphibole-pyroxene skarn, gold mineralization in magnetite-pyroxene skarn follows the main period of sulfide formation and is accompanied by native bismuth and Bi-minerals (Figure 4.5). Gold, bismuth and Bi-minerals are intergrown with amphibole and fill intercrystalline space or fractures in prograde minerals (Figure 4.5). In magnetite-pyroxene skarn the amphibole that is intergrown with gold is typically more fibrous and coarser-grained than the rest of the amphibole in the rock. The fracture-hosted style of gold mineralization primarily occurs in magnetite, which has abundant fractures. The three styles of gold mineralization may be proximal to each other (<200 μm) and have a similar mineral assemblage of gold + bismuth ± Bi-minerals.

The magnetite-pyroxene skarn was subjected to less intense alteration after gold mineralization than the amphibole-pyroxene skarn. There is minor hydrated Fe-silicate alteration of some of the magnetite, but unlike the amphibole-pyroxene skarn, hydrated Fe-silicate veining is absent (Figure 4.5). The magnetite-pyroxene skarn is also less deformed that the amphibole-pyroxene skarn. It is massive in hand sample and thin section, and lacks any pseudo-foliations, true foliations or signs of ductile deformation, but it was brittlely deformed after the prograde alteration. The magnetite and to a lesser extent pyroxene crystals are locally intensely fractured and these fractured zones may correlate with increased retrograde alteration (Figure 4.5).
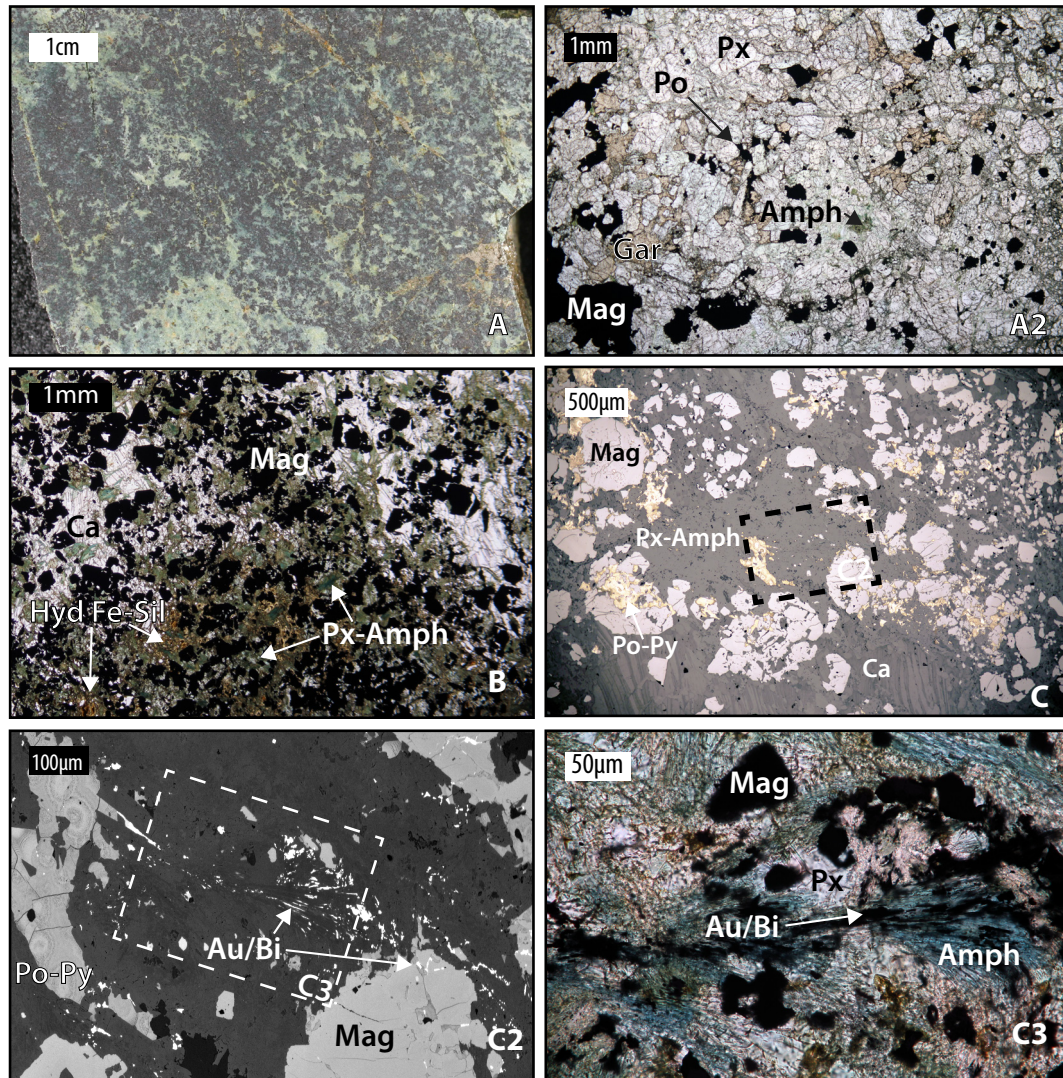


**Figure 4.5:** Examples of magnetite-pyroxene skarn. The photograph (A), PPL photomicrographs (A2, B, C3), RL photomicrograph and BSE image (C2) show the mineralogy, texture and paragenesis of the skarn alteration and gold mineralization. C2 and C3 are of particular importance because they shown gold mineralization inter-grown with a late stage of amphibole alteration. See text for further discussion.

### 4.3.3 Epidote-Pyroxene Skarn

Whereas there is a continuum in composition between amphibole-pyroxene skarn and magnetite-pyroxene skarn the epidote-pyroxene skarn is distinct from the other varieties of pyroxene skarn. It makes up a lesser component of the pyroxene skarn and usually occurs close to the outer margin of the skarn alteration, especially towards the northern and eastern margins of the SWOZ and above it in the BMV (Figure 4.2). The prograde assemblage is comprised entirely of pyroxene that was intensely retrograde altered to epidote-clinozoisite, which makes up between 20 and 40 % of the rock. Calcite and hydrated Fe-silicate content is variable, but less than 5 %. Sulfide alteration and gold mineralization are generally absent, but have been documented in rare locations. Because of the high epidote and pyroxene content the epidote-pyroxene skarn tends to be pale to bright green in hand sample, but is locally mottled pink-green. The pink colour is due to the local abundance of pink epidote, which may be the manganese-rich variety called piemontite (Figure 4.6). In addition to occurring as exoskarn, epidote-pyroxene skarn occurs as endoskarn in the Early Diorite dikes and the Buckhorn Diorite (Figure 4.6)

Pyroxene occurs as 50-200 μm near euhedral blocky crystals many of which have clearly visible pyroxene cleavages. Pyroxene usually forms with a polygonal texture leaving little intercrystalline space, but may also form with a decussate texture (Figure 4.6).

Retrograde alteration is dominated by the intense development of epidote-clinozoisite. Epidote is more abundant than clinozoisite and the two mineral occur in a 9:1 ratio. In some samples a significant portion (20 %) of the epidote-clinozoisite is a probably piemontite the manganese-rich end member. The possible piemontite is pinkish in hand sample and has pink-violet interference colours and pinkish pleochroism in thin section (Figure 4.6). The majority of the epidote-clinozoisite occurs as anhedral crystals replacing pyroxene, with a lesser amount pseudomorphing pyroxene. Rare calcite-quartz veins also occur and cut the prograde and retrograde skarn. Locally epidote-clinozoisite formed during an early stage of vein fill with euhedral crystal terminations pointing towards the center of the veins (Figure 4.6). The calcite – quartz ± epidote veins are less than a millimetre wide and are discontinuous and irregularly shaped (Figure 4.6). Typically the epidote-pyroxene skarn lacks any sulfide alteration or gold mineralization, but was affected by the hydrated Fe-silicate alteration that postdates sulfide alteration and gold mineralization in other skarn varieties. The hydrated Fe-silicate minerals tend to form in the intercrystalline space between pyroxene and/or epidote crystals, likely replacing

one of these minerals or possibly intercrystalline calcite (Figure 4.6). Hydrated Fe-silicate minerals rarely form in veins that cut the calcite – quartz ± epidote veins (Figure 4.6).

Sulfide bearing epidote-pyroxene skarn is rare, but locally formed from a Buckhorn Diorite protolith. It contains the same prograde and retrograde alteration assemblages as the other examples of epidote-pyroxene skarn, except with abundant sulfide minerals (minor molybdenite and trace chalcopyrite and pyrrhotite). The molybdenite occurs in intercrystalline space between the silicate skarn minerals or in vein-like bands and makes up approximately 1 % of the rock (Figure 4.6). The traces of chalcopyrite and pyrrhotite occur with quartz in intercrystalline space (Figure 4.6). Based on its location between prograde and retrograde minerals the molybdenite formed towards the end of retrograde alteration. However, the molybdenite-bearing sample was not gold mineralized and molybdenite was not found in contact with the other sulfides, so its timing relative to the typical sulfide alteration and gold mineralization is uncertain. The molybdenite was dated by Re-Os geochronology to constrain the age of skarn alteration at Buckhorn and returned an age of 165.5 ± 0.7 Ma (Figure 3.19 and Table 3.12). The results of this study are discussed in Chapter 3.

The epidote-pyroxene skarn is characteristically massive in hand sample and does not show any signs of foliation or pseudo-foliation. The prograde pyroxene is typically less fractured compared to the other pyroxene skarn varieties, although, there are several generations of brittle calcite – quartz ± epidote veins that developed after most of the retrograde alteration (Figure 4.6).
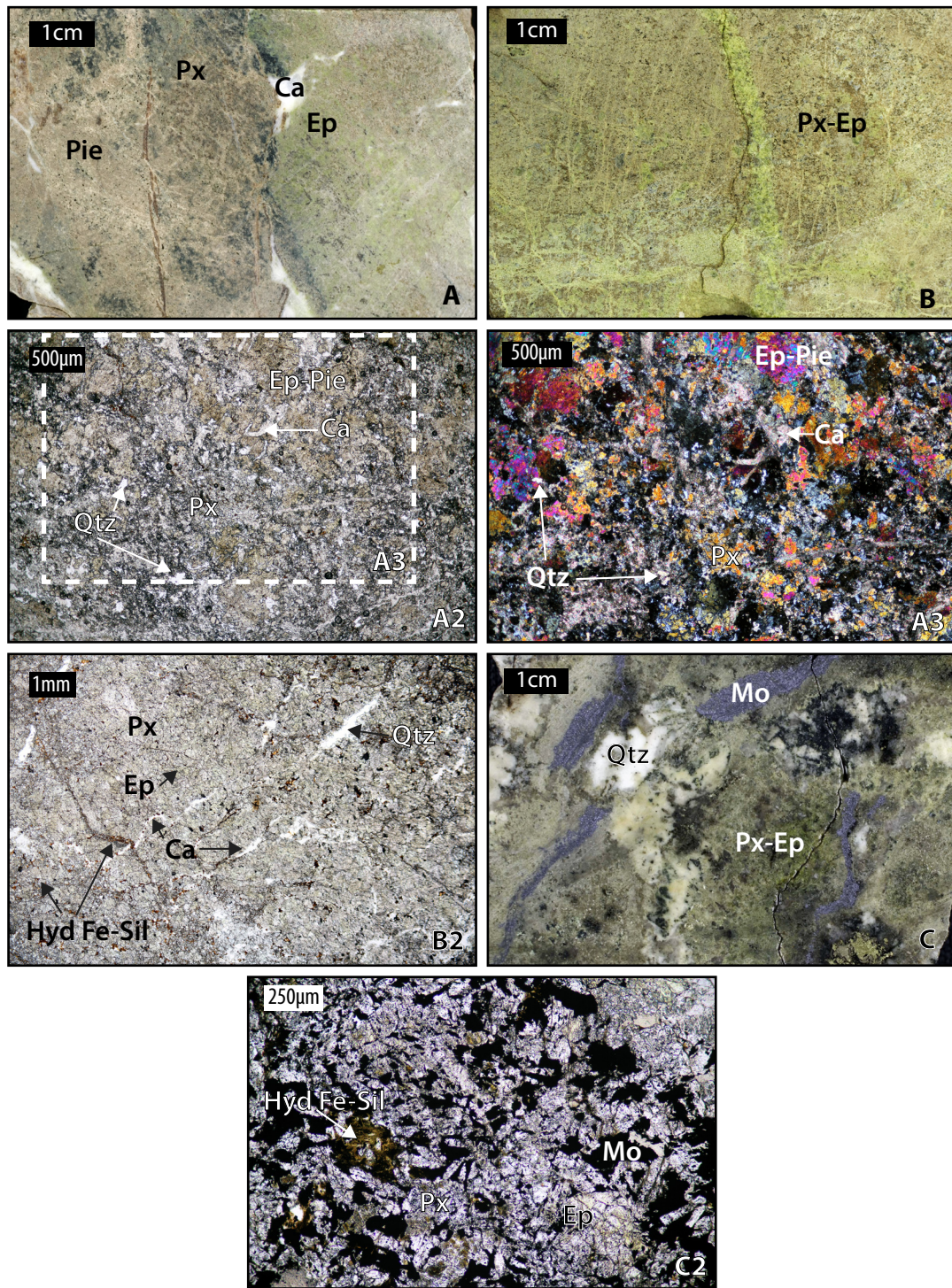
**Figure 4.6:** Examples of epidote-pyroxene skarn. The photographs (A, B, C), PPL photomicrographs (A2, B2, C2) and XPL photomicrograph (A3) show the mineralogy, texture and paragenesis of the prograde and retrograde alteration. C and C1 show an exceptional endo-skarn sample with significant molybdenite mineralization.

### 4.3.4 Microprobe Analysis of Pyroxene and Amphibole from Pyroxene Skarn

### 4.3.4.1 Introduction and Methods

The major element composition of prograde pyroxene and retrograde amphibole was investigated with an electron microprobe (EMP) to further characterize the pyroxene skarn alteration and to document any relationship between variations in mineral composition and gold grade. Five samples from drill hole D08-410 through the SWOZ were chosen for analysis because their pyroxene skarn alteration has high pyroxene and amphibole content that allowed uncomplicated analysis and their wide spread of gold grades (0.2 to 51.1 ppm) gives a greater chance of detecting any variation in mineral chemistry related to gold mineralization. This study builds on the work of Gaspar (2005), which contained an extensive microprobe study that determined the composition of the skarn alteration minerals, but did not document the relationship between the minerals analyzed and gold mineralization.

After detailed optical petrography the samples selected for major element analysis by EMP were carbon coated and BSE imaged with the SEM. The BSE imaging was performed to select the specific pyroxene and amphibole crystals that would be analysed.

Electron-probe micro-analyses of pyroxene were done on a fully automated CAMECA SX-50 instrument, operating in the wavelength-dispersion mode with the following operating conditions: excitation voltage, 15 kV; beam current, 20 nA; peak count time, 20 s; background count-time, 10 s; spot diameter, 5 μm. Data reduction was done using the 'PAP' $\Phi(\rho Z)$ method (Pouchou and Pichoir, 1985). For the elements considered, the following standards, X-ray lines and crystals were used: albite, NaKα, TAP; kyanite, AlKα, TAP; diopside, MgKα, TAP; diopside, SiKα, TAP; diopside, CaKα, PET; rutile, TiKα, PET; synthetic magnesiochromite, CrKα, LIF; synthetic rhodonite, MnKα, LIF; synthetic fayalite, FeKα, LIF; synthetic Ni2SiO4, NiKα, LIF.

Electron-probe micro-analyses of amphibole were also done on a fully automated CAMECA SX-50 instrument, operating in the wavelength-dispersion mode with the following operating conditions: excitation voltage, 15 kV; beam current, 20 nA; peak count time, 20 s (40 s for F, Cl); background count-time, 10 s (20 s for F, Cl); spot diameter, 5 μm. Data reduction was done using the 'PAP' $\Phi(\rho Z)$ method (Pouchou and Pichoir, 1985). For the elements considered, the following standards, X-ray lines and crystals were used: synthetic phlogopite, FKα, TAP; albite, NaKα, TAP; kyanite, AlKα, TAP; diopside, MgKα, TAP; diopside, SiKα, TAP; scapolite, ClKα, PET; orthoclase, KKα,

PET; diopside, CaKα, PET; rutile, TiKα, PET; synthetic magnesiochromite, CrKα, LIF; synthetic rhodonite, MnKα, LIF; synthetic fayalite, FeKα, LIF. The structural formulas of both amphibole and pyroxene were calculated from the corrected chemical data and are located in Appendix A.

### 4.3.4.2 Mineral Chemistry

The range of compositions determined for prograde pyroxene from the SWOZ is shown in Figure 4.7 and as expected from the work of Gaspar (2005) they are dominantly hedenbergite with lesser augite. This range of pyroxene compositions is characteristic of reduced gold skarns (Meinert et al., 2005), and indicates that the samples occurred more distal to the source of skarn forming fluids compared to diopside pyroxene that Gaspar (2005) noted at the eastern margin of the SWOZ and Hickey (1990) noted in the Gold Bowl. Figure 4.7 also demonstrates that there is no relationship between pyroxene composition and gold grade, which is consistent with the petrography that shows that the gold mineralization postdates the pyroxene alteration (Figure 4.3).

The compositions of amphiboles formed during retrograde alteration are plotted in Figure 4.8, which shows that the amphiboles range from ferrohornblende to ferroactinolite. The work confirms the compositions determined by Gaspar (2005), and matches with the range expected for gold skarns (Meinert et al., 2005). Unlike pyroxene there is a relationship between gold grade and amphibole composition. Amphiboles from gold rich samples have higher magnesium numbers (Mg/(Mg + Fe$^{2+}$) and more silicon in the mineral formula, which corresponds with a decrease in iron and aluminum-titanium respectively. These changes in amphibole chemistry are also seen in the correlation matrix (Table 4.3) where there is a positive correlation between gold-silicon and gold-magnesium, and a negative correlation between gold-aluminum and gold-iron.

The amphibole intergrown with gold mineralization is petrographically distinct from the rest of the amphibole alteration in a specific sample and because of the difference in composition they are assumed to reflect different alteration events. Based on the position of gold mineralization in the skarn paragenesis the barren samples are presumed to represent an earlier stage of retrograde alteration that was locally followed by a later stage of amphibole alteration and gold mineralization. The change in amphibole composition from the barren to gold mineralizing stage is suggestive of a cooling and/or oxidising trend (Blundy and Holland, 1990; Holland and Blundy, 1994; Spear, 1981). The change in amphibole composition was likely affected by both factors, as the temperature of skarn formation

typically decreases with time, and oxidising conditions occurred at the end of skarn alteration at Buckhorn as indicated by the presence of hydrated Fe-silicate minerals (Meinert et al., 2005).
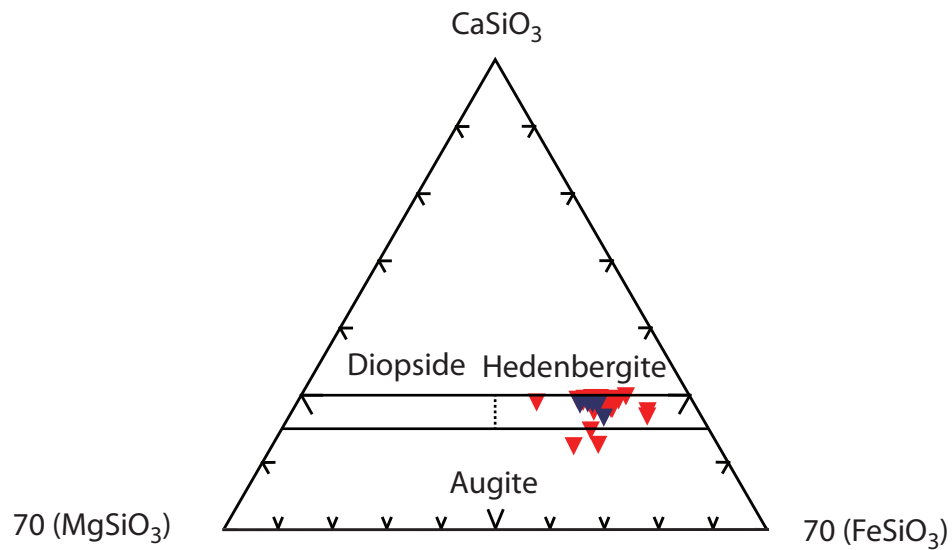


**Figure 4.7:** Composition of pyroxene from the SWOZ. Hedenbergite is the most abundant type of pyroxene at Buckhorn and is characteristic for reduced gold skarns (Meinert et al. (2005)). There is no compositional difference between pyroxene from gold-rich rocks (red triangles) and barren rocks (blue triangles). See text for further discussion.
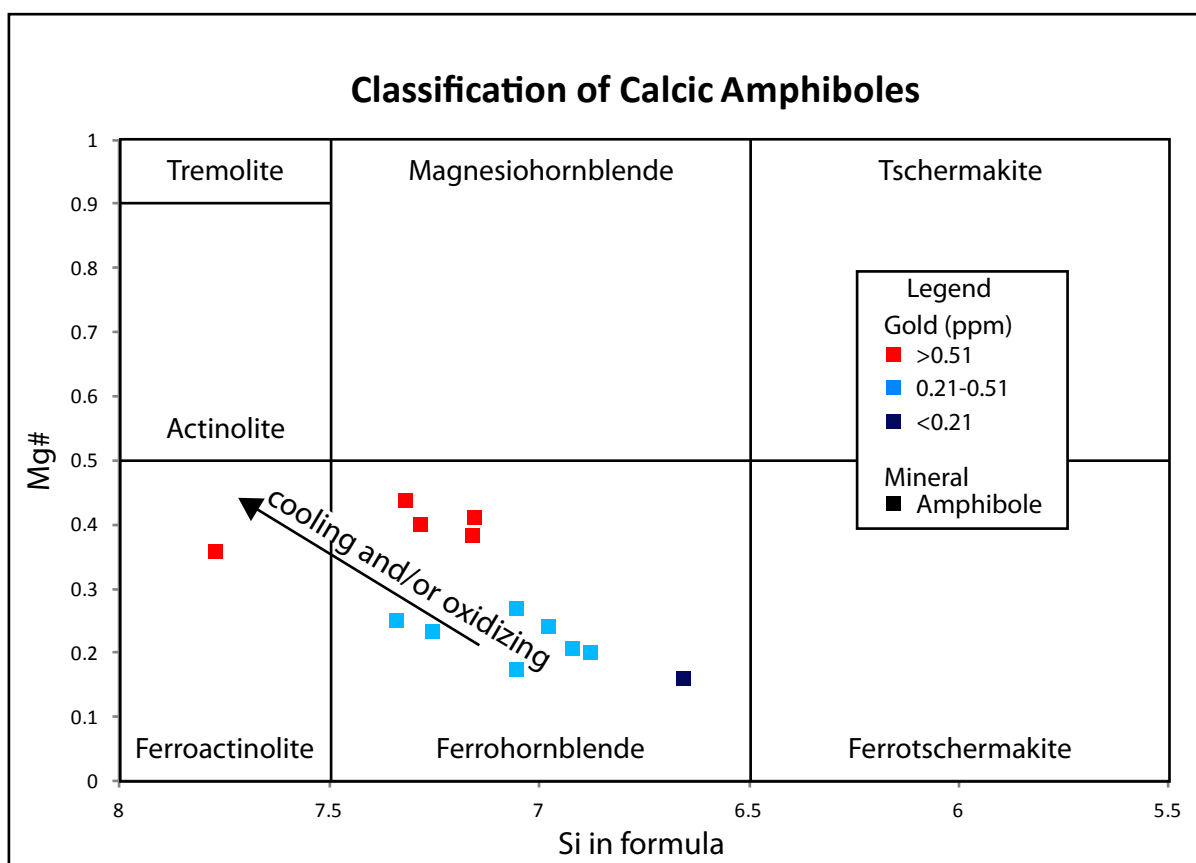
**Figure 4.8:** Classification of retrograde amphiboles from the Buckhorn Gold Skarn based on the criteria of Leake et al. (1997). The amphiboles associated with gold mineralization have elevated Mg and decreased Al, corresponding to an increase in Si, when compared to amphiboles in non mineralized skarn. This change in composition is suggestive of a cooling and oxidizing trend (Blundy and Holland, 1990; Spear, 1981; Holland and Blundy, 1994).

**Table 4.3:** Correlation matrix of major elements in amphibole and gold. Major elements determined by EMP, gold by ICP-MS.

| Correlation | Au(ppm) | SiO2(%) | TiO2(%) | Al2O3(%) | Cr2O3(%) | FeO(%) | MnO(%) | MgO(%) | CaO(%) | Na2O(%) | K2O(%) | F(%) | Cl(%) | H2O(%) |
|---|---|---|---|---|---|---|---|---|---|---|---|---|---|---|
| Au(ppm) | 1.00 | 0.77 | -0.49 | -0.55 | 0.22 | -0.97 | -0.31 | 0.95 | 0.37 | 0.15 | -0.48 | -0.44 | -0.66 | 0.47 |
| SiO2(%) | 0.77 | 1.00 | -0.40 | -0.94 | -0.12 | -0.74 | -0.03 | 0.83 | 0.74 | -0.36 | -0.76 | -0.50 | -0.62 | 0.33 |
| TiO2(%) | -0.49 | -0.40 | 1.00 | 0.32 | 0.08 | 0.67 | 0.65 | -0.59 | -0.05 | 0.31 | -0.09 | 0.84 | 0.67 | -0.29 |
| Al2O3(%) | -0.55 | -0.94 | 0.32 | 1.00 | 0.31 | 0.54 | -0.09 | -0.68 | -0.80 | 0.47 | 0.81 | 0.31 | 0.49 | -0.11 |
| Cr2O3(%) | 0.22 | -0.12 | 0.08 | 0.31 | 1.00 | -0.24 | 0.41 | 0.11 | 0.31 | 0.70 | -0.55 | -0.70 | -0.56 | 0.89 |
| FeO(%) | -0.97 | -0.74 | 0.67 | 0.54 | -0.24 | 1.00 | 0.44 | -0.97 | -0.28 | -0.19 | 0.45 | 0.44 | 0.69 | -0.42 |
| MnO(%) | -0.31 | -0.03 | 0.65 | -0.09 | 0.41 | 0.44 | 1.00 | -0.39 | 0.45 | -0.21 | -0.28 | -0.16 | 0.37 | -0.06 |
| MgO(%) | 0.95 | 0.83 | -0.59 | -0.68 | 0.11 | -0.97 | -0.39 | 1.00 | 0.41 | 0.10 | -0.60 | -0.41 | -0.65 | 0.30 |
| CaO(%) | 0.37 | 0.74 | -0.05 | -0.80 | 0.31 | -0.28 | 0.45 | 0.41 | 1.00 | -0.38 | -0.82 | -0.64 | -0.18 | 0.15 |
| Na2O(%) | 0.15 | -0.36 | 0.31 | 0.47 | 0.70 | -0.19 | -0.21 | 0.10 | -0.38 | 1.00 | 0.06 | 0.19 | 0.26 | -0.24 |
| K2O(%) | -0.48 | -0.76 | -0.09 | 0.81 | -0.55 | 0.45 | -0.28 | -0.60 | -0.82 | 0.06 | 1.00 | 0.45 | 0.20 | 0.02 |
| F(%) | -0.44 | -0.50 | 0.84 | 0.31 | -0.70 | 0.44 | -0.16 | -0.41 | -0.64 | 0.19 | 0.45 | 1.00 | 0.14 | -0.69 |
| Cl(%) | -0.66 | -0.62 | 0.67 | 0.49 | -0.56 | 0.69 | 0.37 | -0.65 | -0.18 | 0.26 | 0.20 | 0.14 | 1.00 | -0.68 |
| H2O(%) | 0.47 | 0.33 | -0.29 | -0.11 | 0.89 | -0.42 | -0.06 | 0.30 | 0.15 | -0.24 | 0.02 | -0.69 | -0.68 | 1.00 |

### 4.3.5 Discussion and Summary of Microprobe Results

The microprobe analysis shows that the pyroxene and amphibole alteration at Buckhorn is comprised of hedenbergite-augite and ferrohornblende-ferroactinolite respectively, and that these compositions fit within the range expected for reduced gold skarns (Meinert et al., 2005). The analysis also showed that there is no correlation between pyroxene composition and gold grade, but that several changes in the amphibole composition correlate with gold grade. There is a positive correlation between gold and increased magnesium and silicon content in amphibole, which corresponds with a decrease in iron and aluminum. These compositional changes in amphibole can result from cooler and/or more oxidised conditions, both of which occurred at the time of gold mineralization at Buckhorn.

## 4.4   Garnet Skarn

Garnet skarn is less abundant than pyroxene skarn, making up an approximately equal portion of the SWOZ as magnetite skarn. Garnet skarn is more abundant near the northern and eastern margins of the SWOZ, but does occur throughout it (Figure 4.2). Garnet skarn also makes up a significant portion of the Gold Bowl and the Magnetic Mine. In addition to occurring as exoskarn, garnet skarn occurs as endoskarn in the Buckhorn or Early Diorite (Figure 4.9)

Garnet is the dominant prograde mineral in garnet skarn and makes up between 40 and 80 % of the rock. Pyroxene is the next most abundant prograde mineral (average 15 %), and varies between 5 and 40 %. Magnetite content is usually below 1 %, but is locally up to 30 % of the garnet skarn (Figure 4.9). Calcite locally forms about 15 % and garnet skarn may contain trace amounts of quartz and feldspar. Amphibole is the dominant retrograde mineral and it is concentrated in areas with high pyroxene content. Amphibole alteration ranges from less than 10 % to greater than 90 % of the pyroxene having been altered to amphibole. Rare retrograde epidote alteration also occurs as a trace amount. The sulfide content (1 %) is typically lower than the pyroxene skarn. Pyrrhotite is the most abundant sulfide, with lesser amounts of pyrite, chalcopyrite and trace arsenopyrite. Several generations of veins cut the garnet skarn, calcite veins are the most abundant, but there are also rare calcite ± hydrated Fe-silicate ± garnet veins. The garnet skarn is red-brown in hand sample with minor patches of dark green amphibole, pale green pyroxene and rare black magnetite (Figure 4.9).

Pyroxene occurs as either an aggregate of 20 to 100 μm stubby, blocky crystals or as similarly sized inclusions in garnet. When not included in garnet the pyroxene crystals typically form with a polygonal to web texture. Garnet occurs as 100 μm to 5 mm anhedral to euhedral crystals that have

a wide range of optical characteristics. Based on the optical characteristics at least four generation of garnet have been identified (Figure 4.9 and Figure 4.10), which is similar to the work of Gaspar et al. (2008). The first two generations of garnet formed during prograde alteration and the last two formed during retrograde alteration. The first generation garnets are typically isotropic, anhedral and darker in plane polarized transmitted light (Figure 4.9 and Figure 4.10). The next generation of garnet forms as subhedral to anhedral crystals, or rarely as epitaxial overgrowth on the first generation of garnet. The second generation garnets are characteristically anisotropic with sector and polysynthetic twinning and oscillatory zoning (Figure 4.9). Both the first and second generation of garnet may form the majority of a sample, and both occur as minor components of pyroxene and magnetite skarn. The third and fourth generations of garnet formed during retrograde alteration and are discussed according to their place in the paragenesis. When present, magnetite occurs as 20 to 250 μm subhedral crystals that form in the intercrystalline space between garnet and pyroxene, and rarely partially impinging on garnet crystals (Figure 4.9). Arsenopyrite is rare and occurs as 50 μm near euhedral inclusions in Garnet. The texture of the prograde minerals varies from polygonal to web texture with intercrystalline calcite or less commonly quartz or feldspar (Figure 4.9).

The paragenesis of prograde alteration in garnet skarn is similar to pyroxene skarn. Pyroxene was the first mineral to form followed by garnet and magnetite (Figure 4.9). In rare instances, arsenopyrite predates garnet. As seen in Figure 4.9, some of the magnetite formed after the other prograde minerals were brittlely deformed.

Retrograde silicate alteration in the garnet skarn is dominated by the alteration of pyroxene to amphibole and lesser epidote, as well as two stages of retrograde garnet growth. Garnet is deemed to be part of the retrograde assemblage if it overgrows the second generation of garnet or if it occurs in veins that cut either of the first two stages of garnet. The retrograde garnet that overgrows the second generation of prograde garnet is characteristically isotropic and forms in near euhedral crystals (Figure 4.9 and Figure 4.10). The vein style of retrograde garnet has a more diverse character than overgrowth style, and more than one generation of retrograde garnet veins occurs. The garnet veins have about 300 μm of dilation and may contain isotropic and/or anisotropic garnets with anhedral to nearly euhedral crystal shapes (Figure 4.10). The intensity of amphibole alteration is variable and it postdates the overgrowth style of retrograde garnet, but predates the garnet veins. Locally, the retrograde amphibole alteration is nearly complete with only a trace amount of pyroxene remaining, but elsewhere it is essentially absent. Epidote alteration forms in two settings. Most of the epidote

alteration partially pseudomorphs garnet crystals, but a lesser amount forms in veins that cut garnet and pyroxene rich areas. The epidote alteration only forms a trace amount of the garnet skarn, and is more abundant in areas with minimal amphibole alteration. Sulfide alteration follows epidote alteration and is dominated by pyrrhotite with lesser chalcopyrite and trace pyrite. It forms with the same paragenesis as in the pyroxene skarn, pyrrhotite and chalcopyrite together followed by minor pyrite alteration of the pyrrhotite (Figure 4.9 and Figure 4.10). Unlike the pyroxene skarn the early stage of skeletal pyrite does not occur. A trace amount of cobaltite was found in late calcite-garnet-sulfide veins that cut retrograde alteration.
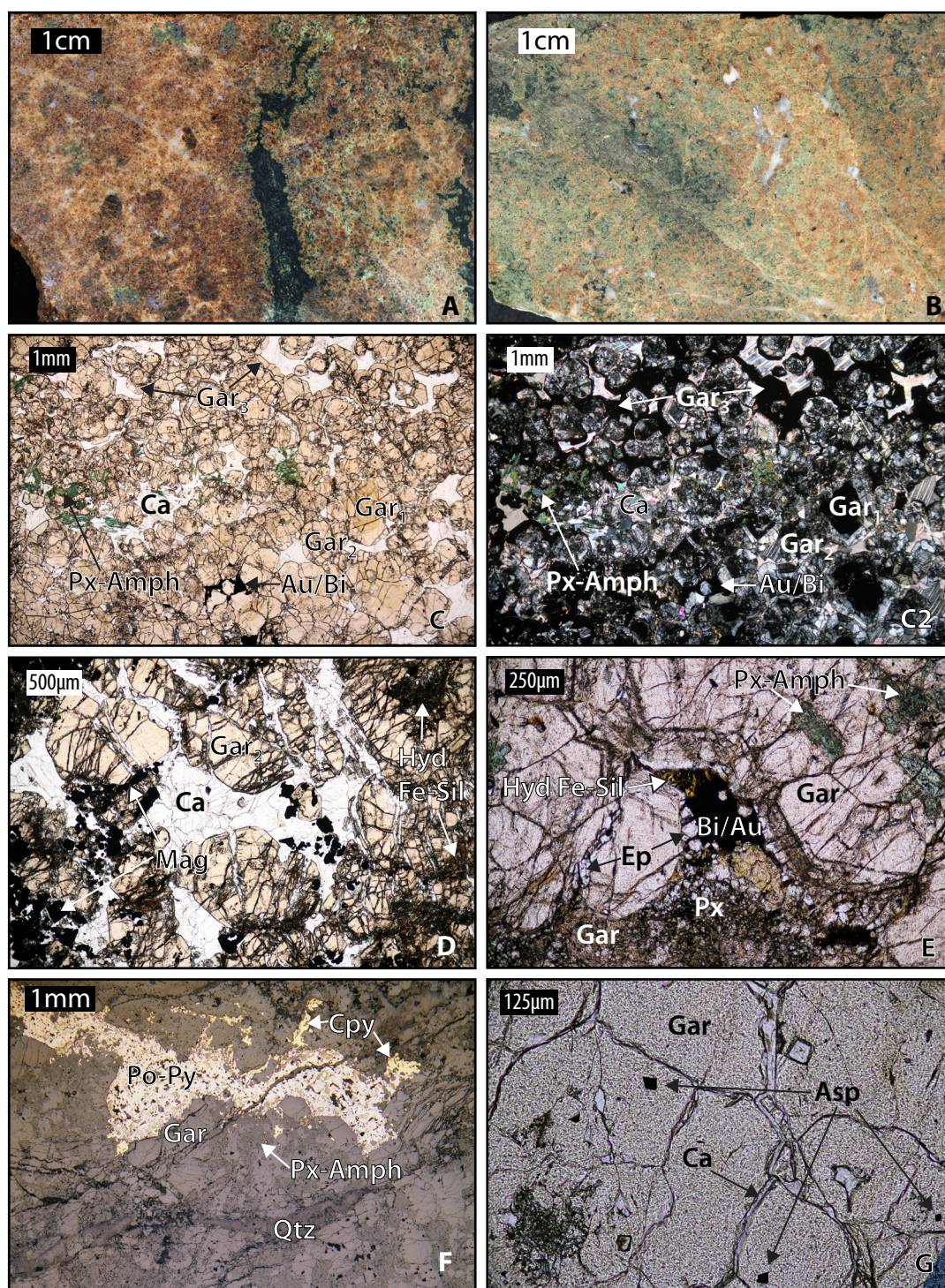
**Figure 4.9:** Examples of garnet skarn. The photographs (A, B), PPL photomicrographs (C, D, E, F), XPL photomicrograph (C2), and RL photomicrograph (G) show the mineralogy, texture and paragenesis of the prograde and retrograde alteration and gold mineralization. See text for further discussion.

The paragenesis of retrograde alteration in the garnet skarn is similar to the pyroxene skarn. Amphibole is the first retrograde mineral to form followed by epidote and sulfide minerals. The timing of

the overgrowth style of retrograde garnet is unclear, but it probably formed approximately contemporaneously with amphibole and epidote. The vein style of retrograde garnet alteration cuts the rest of the retrograde alteration and is therefore younger (Figure 4.10 A).

Gold mineralization occurs after the sulfide alteration and is accompanied by native bismuth and Bi-minerals. The majority of gold occurs in intercrystalline space between prograde and earlier retrograde minerals as well as in fractures in prograde minerals (Figure 4.10). Rarely gold mineralization is hosted entirely inside calcite that fills the remainder of the fractures and intercrystalline space. A trace amount of gold and Bi-minerals are intergrown with an early stage of hydrated Fe-silicate alteration that also fills intercrystalline space (Figure 4.10). The gold mineralization may also be hosted in calcite-garnet-sulfide veins that cut the earlier skarn alteration (Figure 4.10). Cobaltite is the most abundant sulfide in the late veins, and it is spatially associated with gold mineralization, however the gold mineralization postdates the cobaltite and occurs in brittle fractures within it (Figure 4.10).

A single sample of garnet skarn contained molybdenite (Figure 4.10). The sample has the same prograde and retrograde mineral assemblage as the typical garnet skarn, but contains a trace amount of molybdenite that occurs as 20 to 200 μm anhedral crystals. The molybdenite preferentially occurs along quartz crystal boundaries hosted in intercrystalline space between prograde and retrograde minerals. A minor amount of molybdenite rims rare pyrrhotite in the sample, and therefore molybdenite postdates the majority of retrograde alteration. The sample did not contain any gold grains so the relative timing of molybdenite and gold is uncertain. However, molybdenite and gold are presumed to be approximately coeval based on their places in the paragenetic sequence. As discussed in Chapter 3 a sample of the molybdenite-bearing garnet skarn was evaluated by Re-Os geochronology to constrain the age of skarn mineralization. The molybdenite in the garnet skarn returned an age of 162.8 ± 0.7 Ma, which confirms the temporally relationship between the skarn alteration at Buckhorn and the emplacement of the BIS (Figure 3.19 and Table 3.12).

Garnet skarn appears massive and undeformed at the hand sample scale, but has clearly been brittlely deformed when viewed in thin section. Many of the prograde garnet crystals are affected by micron scale brittle fractures that are randomly oriented and usually filled by calcite. These fractures affect most of the prograde minerals including garnet, pyroxene and magnetite, but they predate some of the prograde magnetite that fills fractures in garnet (Figure 4.9 and Figure 4.10). The retrograde

minerals are typically undeformed, although they are rarely fractured and are cut by the rare calcite-garnet-sulfide veins (Figure 4.9 and Figure 4.10).
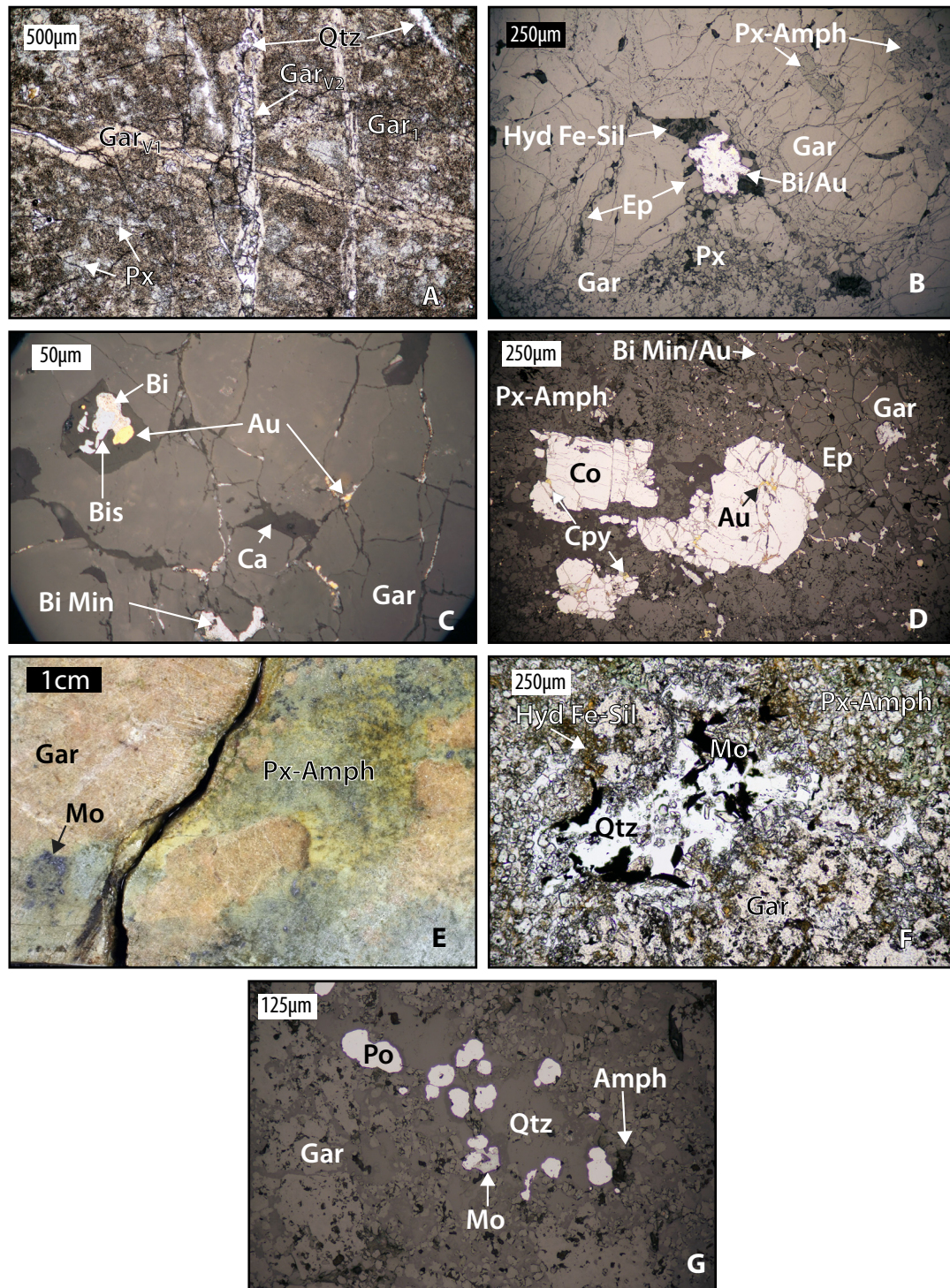


**Figure 4.10:** Examples of garnet skarn. The PPL photomicrograph (A) show several generations of retrograde garnet veins. The RL photomicrographs (B, C, D) show the specific settings of gold mineralization. The photograph (E), PPL photomicrograph (F) and RL photomicrograph (G) show the mineralogy, texture and paragenesis of the skarn alteration in the molybdenite bearing sample. See text for further discussion.

## 4.5 Magnetite Skarn

Magnetite skarn is less abundant than pyroxene skarn in the SWOZ and like the garnet skarn it predominately occurs towards its northern and eastern sides (Figure 4.2). Magnetite skarn also forms a significant portion of the Gold Bowl and Magnetic Mine. The magnetite skarn has a consistent prograde and retrograde mineral assemblage compared to the pyroxene skarn and therefore is not divided into sub-categories.

Magnetite is the dominant prograde mineral (60 and 85 %) in magnetite skarn. Pyroxene is the next most abundant prograde mineral (<5 %), but may locally composed up to 25 % before retrograde alteration. Garnet rarely occurs (0-5 %). Amphibole is the dominant retrograde mineral; it replaces about 75 % of the prograde pyroxene, and forms 5-15 % of the rock. Retrograde alteration to epidote and hydrated Fe-silicate minerals locally occurs (>1 %). Calcite is abundant 10-20 %, and sulfide minerals (~5 %) are dominated by pyrrhotite with trace pyrite and chalcopyrite. Similar to pyroxene skarn and garnet skarn, gold mineralization is accompanied by native bismuth and Bi-minerals. In hand sample the magnetite skarn is black with rare patches of white calcite, green pyroxene, dark green amphibole and red-brown garnet (Figure 4.11).

The minor amount of pyroxene that is present in magnetite skarn occurs as 500 μm to 1.5 mm blocky, elongate, subhedral to nearly euhedral crystals (Figure 4.11). Garnet occurs as near euhedral crystals, about 200 μm across, in masses or isolated crystals (Figure 4.11). Magnetite forms as 100 μm to 2 mm equant, euhedral to subhedral crystals. Some magnetite crystals have rare 20 μm to 100 μm calcite and very rarely similarly sized pyrrhotite inclusions. The prograde minerals typically form with a polygonal texture, but where calcite is more abundant they locally have a web texture with intercrystalline calcite (Figure 4.11). Like the other skarn types, pyroxene is the first prograde mineral to form, followed by garnet, which forms at about the same time as pyroxene. Magnetite is the final prograde mineral to develop, and its formation overlaps with the end of pyroxene and garnet alteration.

Retrograde alteration in magnetite skarn is less intense than in the pyroxene skarn. Retrograde amphibole alteration is patchy and preferentially replaces pyroxene along crystals boundaries and fractures. Amphibole forms as fibrous crystals that are finer-grained than pyroxene and about 200 to 500 μm in length. A late stage of fine-grained amphibole may be locally intergrown with gold and bismuth mineralization (Figure 4.11). Epidote occurs as blocky aggregates of 10-30 μm crystals that replace garnet and pyroxene (Figure 4.11). Pyrrhotite, lesser pyrite and trace chalcopyrite occur in

fractures in the prograde minerals and to a lesser extent in the intercrystalline space between them. The sulfide minerals may rarely also occur as inclusions in magnetite. Pyrite is the first sulfide mineral to form and occurs as ~100 μm anhedral crystals (Figure 4.11). Pyrrhotite and chalcopyrite formed next as anhedral space filling crystals. There is minor late pyrite alteration after pyrrhotite as described in pyroxene skarn.

Gold occurs with native bismuth and Bi-minerals in fractures in magnetite. The gold and bismuth typical occur in distinct grains that range in size from less than 20 μm up to 200 μm, but may be intergrown (Figure 4.11). A minor amount of gold occurs as small grains (1 μm) that are intergrown with fine-grained amphibole (Figure 4.11). Gold mineralization intergrown with amphibole typically occurs in samples with high amphibole content and in the same samples that also contain the more abundant fracture-hosted style of gold mineralization. Very rarely bismuth and Bi minerals occur without gold. In theses rocks the bismuth and Bi-minerals occur in fractures in the magnetite and intergrown with amphibole, the same settings as in the gold mineralized rocks. Magnetite skarn has rare hydrated Fe-silicate alteration that occurs along the edges of pyroxene and amphibole crystals as well as in veins that cut the prograde and other retrograde minerals (Figure 4.11).

The magnetite skarn appears massive, non-foliated and generally undeformed in hand sample, but in thin section the prograde minerals show signs of brittle deformation. Magnetite, pyroxene and garnet crystals are typically pervasively fractured. This fracturing occurs before the retrograde alteration and the amphibole crystals are not affected (Figure 4.11). The fractures have minor dilation (<30 μm) and are randomly oriented. They are filled by sulfide minerals and calcite and form a crackle breccia (Figure 4.11).
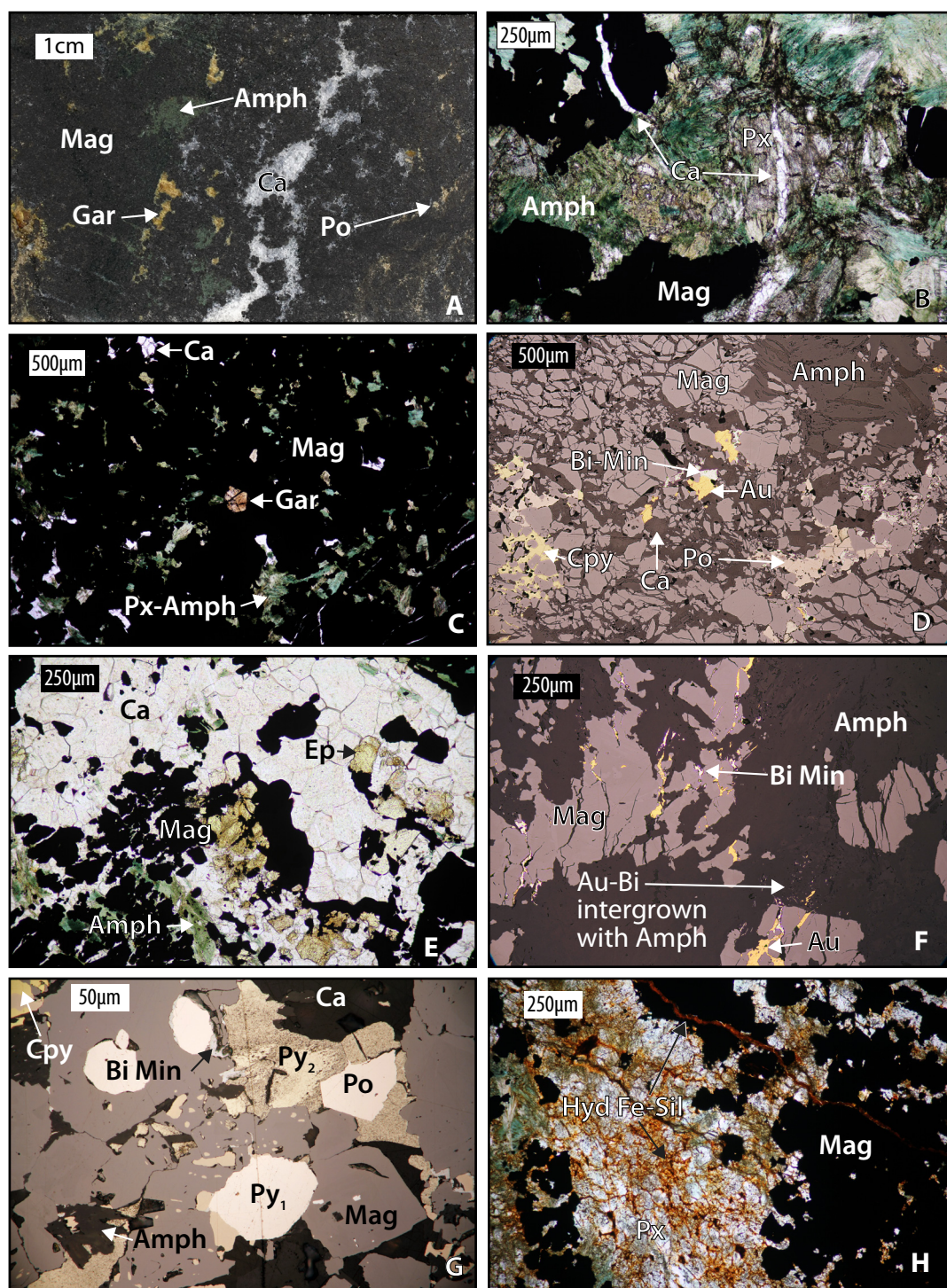
**Figure 4.11:** Examples of magnetite skarn. The photograph (A) PPL photomicrographs (B, C, E, H), and RL photomicrographs (D, F, G) show the mineralogy, texture and paragenesis of the skarn alteration and gold mineralization. See text for detailed discussion.

## 4.6   Gold Mineralization in Non Skarn-Altered Rocks

The great majority of gold mineralization occurs in skarn-altered rocks, but in rare locations (~3) significant gold mineralization has been found in rocks that are essentially not skarn-altered. The gold-bearing non skarn-altered rocks that have been identified to date all occur close to the SWOZ in hornfels-altered siliciclastic metasedimentary rocks of the BMS. In these cases, skarn alteration is limited to millimetre scale veins with centimetre scale halos that cut hornfels altered rocks. While these occurrences are rare and do not impact the economics of the deposit, they provide insight into the progression of skarn alteration and gold mineralization at Buckhorn.

The non skarn-altered rocks that host the small skarn veins are identical to the isochemical hornfels altered metasedimentary rocks in the Buckhorn area. The majority of the rock is made up of 100 to 500 μm subhedral quartz, feldspar, amphibole, and pyroxene. Lesser, similarly-sized epidote and finer-grained hydrated Fe-silicate minerals also occur (Figure 4.12). The mineralogy is variable from sample to sample, and is indistinguishable from samples of non-gold mineralized hornfels (Figure 4.12). The vein hosted skarn alteration is composed of pyroxene, amphibole, epidote, chlorite, minor sulfides (pyrrhotite, chalcopyrite, pyrite, sphalerite, and cobaltite), and gold (Figure 4.12). The alteration occurs in the veins and in the vein halos, but with less intensity, and follows the same paragenetic sequence as described in the amphibole-pyroxene skarn section.

Gold is accompanied by bismuth mineralization in the form of native bismuth, bismuthinite and other Bi-minerals. Gold and bismuth form a much greater portion of the vein hosted skarn than the typical skarn, and locally gold and bismuth minerals make up close to 1 % of the rock. Gold occurs within the skarn veins and skarn alteration halos in intercrystalline space between and fractures in pyroxene, amphibole and epidote, as well as intergrown with amphibole (Figure 4.12). In samples with extremely high gold content (~1% Au/Bi by visual estimate), gold may also be intergrown with epidote and pyroxene, and also along internal boundaries in calcite crystals (Figure 4.12).

Gold mineralization in non skarn-altered rock is relatively undeformed, with slight brittle deformation at the mineral scale, and several generations of brittle veins. The orientation and relative timing of the different skarn veins could not be determined, as the samples have ambiguous cross-cutting relationships. The gold bearing non skarn-altered rocks lack ductile deformation (Figure 4.12).
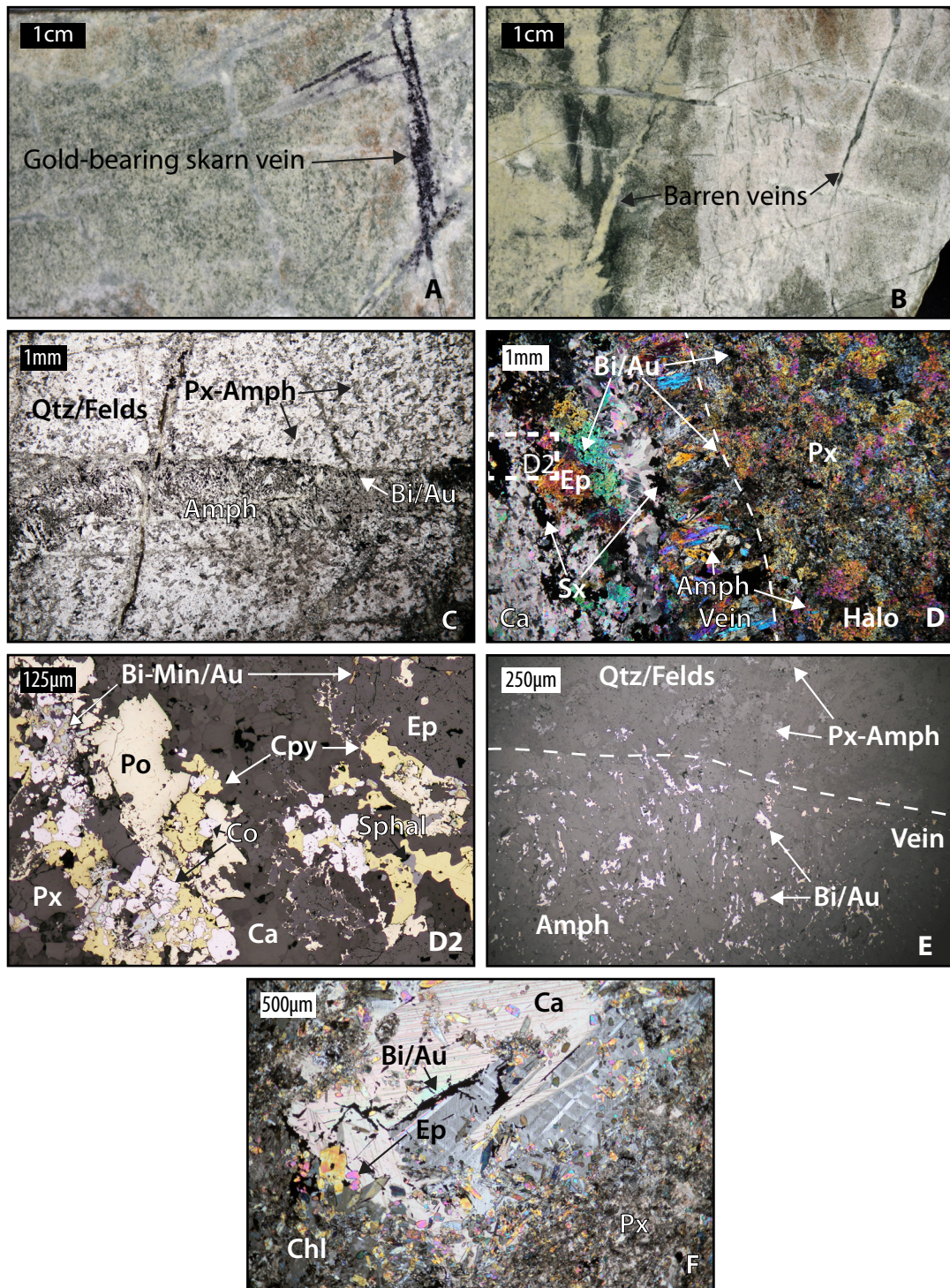
**Figure 4.12:** Examples of gold-bearing skarn veins in hornfels altered rock. The photographs (A, B), PPL photomicrograph (C), PPL photomicrographs (D, F), and RL photomicrographs (D2, E) show the mineralogy, texture and paragenetic sequence of the skarn veins and gold mineralization. See text for further discussion.

## 4.7 Discussion and Conclusions

### 4.7.1 Skarn Alteration

Skarn alteration at Buckhorn is divisible into three major alteration assemblages based on their prograde mineralogy: pyroxene skarn, garnet skarn, and magnetite skarn. The descriptions presented in this work are a detailed and accurate characterization of the skarn alteration assemblages and the variation within them. These descriptions are summarized in Table 4.4.

**Table 4.4:** Characteristics of the skarn classifications

| | Pyroxene Skarn | | | Garnet Skarn | Magnetite Skarn |
|---|---|---|---|---|---|
| | Amphibole-Pyroxene | Magnetite-Pyroxene | Epidote-Pyroxene | | |
| Prograde Mineralogy | Px > Mag - Gar | Px - Mag > Gar | Px | Gar > Px > Mag | Mag > Px > Gar |
| Retrograde Alteration Intensity | High | Moderate | High | Low | Low |
| Retrograde Mineralogy | Amph > Sx > Ca > Hyd Fe-Sil > Ep | Amph > Ca > Sx > Hyd Fe-Sil - Ep | Ep > Hyd Fe-Sil > Amph | Amph > Ca > Gar > Sx > Ep > Hyd Fe-Sil | Amph > Ca > Sx > Hyd Fe-Sil > Ep |
| Sulfide Mineralogy | Po > Py > Cpy > Sphal | Po > Py > Cpy | (Mo > Po - Cpy) | Po > Py > Cpy > Aspy > (Co - Mo) | Po > Py > Cpy |
| Sulfide Content (%) | 5-10% | <5% | Trace | 1% | 5% |
| Ore Mineralogy | Bi > Bis > Au | Bi > Bis > Au | None | Bi > Bis > Au | Bi > Bis > Au |
| Setting of Gold Mineralization | Intercryst > Intergrown > Fracture > Base Metal | Fracture > Intercryst > Intergrown | None | Intercryst > Fracture > Intergrown | Fracture > Intercryst > Intergrown |
| Size of Gold Grains | | | None | | |
| Range of Gold Grade (ppm) | <0.1 - 117.5 | <0.1 - 51.1 | <0.1 | <0.1 - 53.7 | <0.1 - 22.5 |
| Vein Assemblage | Ca > Ca-Hyd Fe-Sil>Sx | Ca | Ca-Qtz > Ep | Ca > Ca-Hyd Fe-Sil > Gar - Sx | Ca-Hyd Fe-Sil |
| Protolith | Metavolcanic - Metacarbonate - Metasedimentary | Metavolcanic - Metacarbonate - Metasedimentary | Metavolcanic - Metacarbonate - Metasedimentary | Metavolcanic > Metacarbonate > Metasedimentary | Metacarbonate > Metavolcanic > Metasedimentary |
| Styles of Deformation | Fractures / Foliations / Pseudo-foliations | Fractures | Fractures | Fractures | Fractures |

()=very rare minerals

### 4.7.1.1 Zonation and Paragenesis of Skarn Alteration

The skarn alteration at Buckhorn varies from garnet- and magnetite-dominated in the Magnetic Mine area, to roughly equal proportions of garnet, magnetite and pyroxene in the Gold Bowl, and finally pyroxene-dominated in the SWOZ (Figure 4.2). This zonation, from garnet- to pyroxene-dominated, has been noted at other gold skarns where it has been interpreted to represent an oxidised to reduced trend from proximal garnet to distal pyroxene (Meinert et al., 2005).

The skarn zonation pattern at Buckhorn suggests that the mineralizing fluids were sourced from the Buckhorn Granodiorite and Buckhorn Diorite near the Magnetic Mine and travelled to the south forming the Magnetic Mine, the Gold Bowl and ultimately the SWOZ. The same zonation can be seen at a smaller scale in the SWOZ where the northern and eastern margins have more abundant garnet and magnetite skarn than the southern and western margins. This secondary zonation is likely due to the presences of the Footwall Mylonite that channelled skarn forming fluids and allowed them to travel a greater distance with less interaction with the host rocks.

In addition to being zoned in space, prograde mineralogy in the SWOZ is also zoned in time. As the most distal part of the Buckhorn skarn system, skarn alteration in the SWOZ was likely originally composed entirely of pyroxene. However, as skarn alteration progressed, the zones of garnet and magnetite skarn expanded outward and overprinted the pyroxene alteration. This overprinting is reflected in the paragenetic sequence documented in samples collected from the SWOZ where pyroxene predates garnet and magnetite alteration (Figure 4.13).

In addition to forming at the metre scale, skarn alteration also forms in veins at the centimetre scale. These skarn veins have the same alteration assemblages, follow the same paragenesis, and have the same mineralization style as the more typical metre scale amphibole-pyroxene skarn alteration. They are found cutting prograde and retrograde skarn, as well as non skarn-altered rocks. Based on these observations the vein-hosted skarn is interpreted as the youngest and/or most distal stage of skarn alteration and gold mineralization at Buckhorn. Similar conclusions have been made regarding skarn veins in other skarn deposits (Einaudi, 1977; Ewers and Sun, 1989; Meinert et al., 2005).

The timing of skarn alteration relative to deformation has been disputed in the past (Gaspar, 2005; Hickey, 1990, 1992; McMillen, 1979), but petrography shows that much of the skarn alteration was affected by brittle and/or ductile deformation. In the SWOZ most of the prograde minerals and many of the retrograde minerals are brittlely and ductilely deformed respectively. The brittle

deformation manifests as fractures in the prograde minerals and the ductile deformation as a foliation in the retrograde minerals. The foliation is relatively flat-lying and is presumably equivalent to the low angle foliation in the host rocks. This conclusion is supported by work presented in Chapter 2 and Chapter 3 that showed that the deformation events responsible for the low angle foliations are younger than the Granodiorite dikes which acted as fluid conduits for skarn forming fluids (Figure 2.10, Figure 2.11, and Figure 3.15).
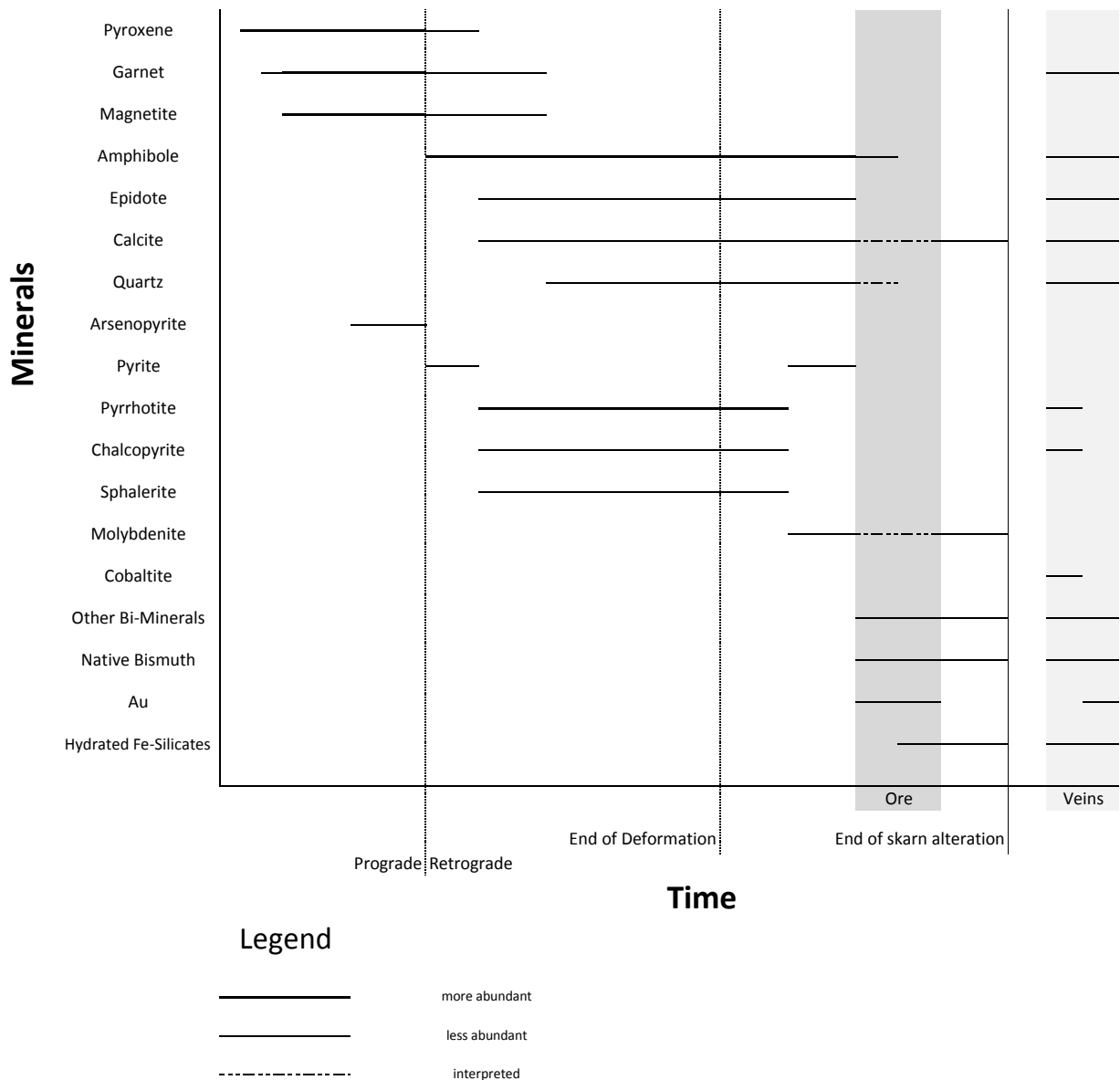


**Figure 4.13:** Paragenetic sequence of skarn alteration, deformation, and gold mineralization at Buckhorn

#### 4.7.1.2 Physicochemical Conditions of Skarn Alteration

The physicochemical conditions of prograde skarn alteration at Buckhorn can be constrained by the prograde mineralogy. The absence of graphite and pyrite and the presence of hedenbergite, andradite and magnetite in the prograde assemblage limits the log $fO_2$ conditions to between -26 and -20 (Figure 4.14). Figure 4.15 further constrains the minimum $fO_2$ to -25 based on the lack of graphite. The presence of pyrrhotite rather than pyrite and arsenopyrite rather than lollingite constrains the log $fS_2$ conditions of the prograde alteration to between -4.5 and -8 (Figure 4.15). Figure 4.14 also constrains the minimum temperature of prograde skarn alteration to approximately 430°C based on the reactions of andradite + $CO_2$ = magnetite + quartz + calcite + $O_2$ and hedenbergite + $O_2$ + $CO_2$ = magnetite + quartz + calcite. The maximum temperature of prograde alteration is limited to 500°C based on maximum temperature estimates from other skarn systems (Meinert, 2000). The figures show that Buckhorn formed under more oxidized (higher $fO_2$) and more sulfur rich (higher $fS_2$) conditions than Nickel Plate (Figure 4.15) (Ettlinger et al., 1992).
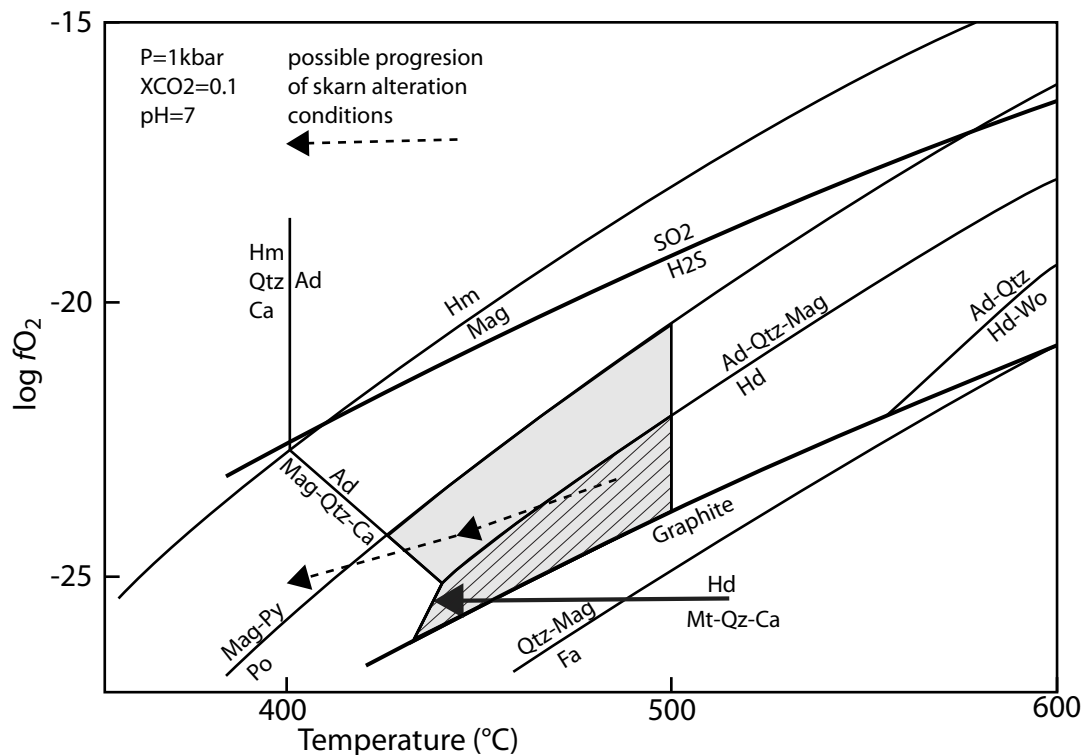


**Figure 4.14:** Temperature versus log $fO_2$ diagram showing the stability fields of major skarn silicate, oxide, and sulfide minerals. The grey box indicates the range of possible conditions for the formation of prograde alteration at Buckhorn. Stability field for prograde alteration at Nickel Plate shown with the diagonal lines. Note that the stability field for the Buckhorn skarn extends to more oxidised conditions. Modified from Einaudi et al. (1981).
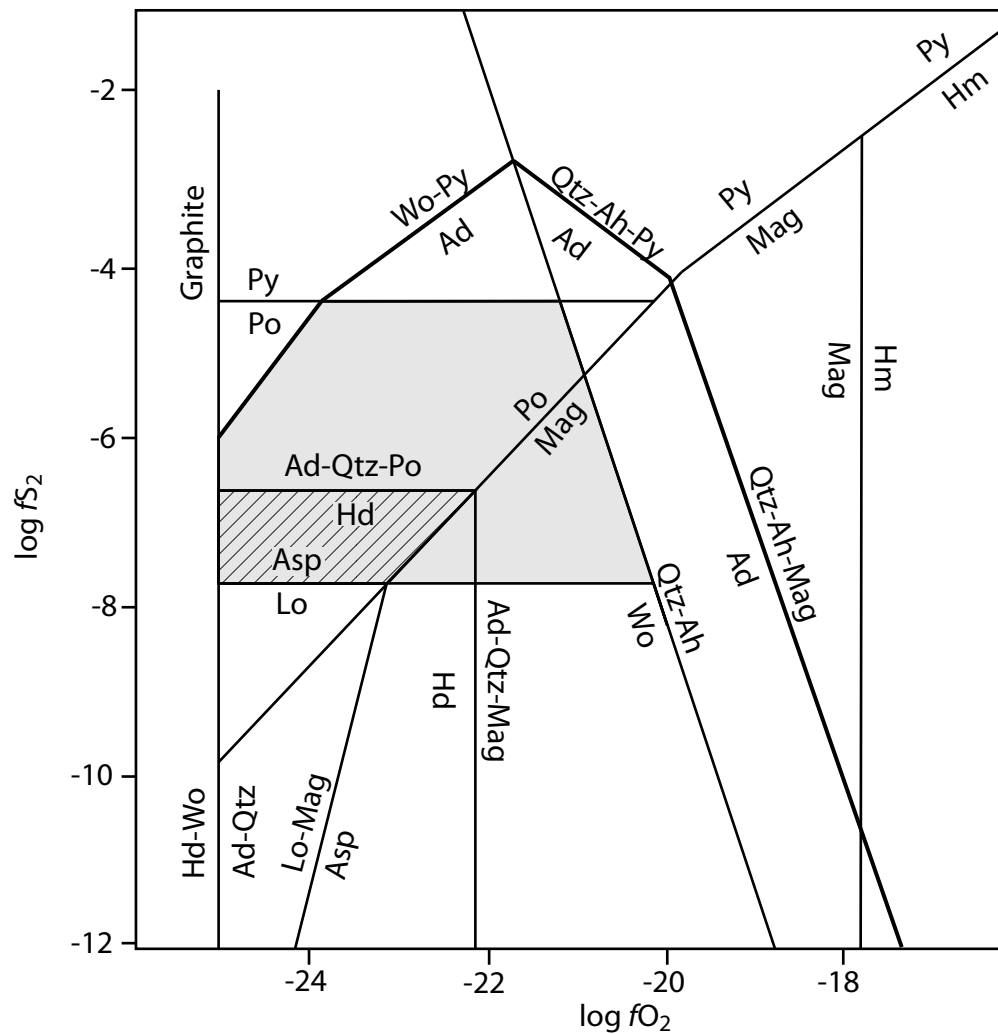
**Figure 4.15:** Log $fO_2$ versus log $fS_2$ diagram showing the stability fields of major calc-silicate and sulfide prograde minerals at T=+500°C, $XCO_2$=0.1, and P (fluid) =0.5 Kbar. Stability field for skarn alteration at Buckhorn shown as the shaded area. Stability field of the Nickel Plate shown with the diagonal lines. Note that the stability field for the Buckhorn skarn extends to more oxidised and sulfur rich conditions. Nickel Plate stability field from Ettlinger (1992). Mineral stabilities from Ettlinger (1992) and Bowman (1998).

The conditions of retrograde skarn alteration at Buckhorn can also be constrained by the mineralogy. The lack of garnet and pyroxene (andradite and hedenbergite) indicates that retrograde alteration occurred at temperatures below 430°C (Figure 4.14), and the hydrated Fe-silicate assemblage of grunerite, greenalite, and minnesotaite (Table 4.2) indicates a temperature of approximately 300°C for the later stages of retrograde alteration (Rasmussen et al., 1998). The log $fO_2$ and log $fS_2$ conditions of retrograde alteration and gold mineralization can be constrained by the sulfide mineral assemblage. The presence of arsenopyrite rather than lollingite and chalcopyrite rather than bornite limits the

log $fS_2$ to between approximately -6 and -15 (Figure 4.16). Figure 4.16 also provides the maximum log $fO_2$ of -26 based on the lack of hematite in the retrograde alteration assemblage. Figure 4.14 and Figure 4.16 demonstrate that the mineralogical changes from prograde to retrograde alteration can be explained by a cooling and reducing trend. These figures also show that similar to the prograde alteration the retrograde alteration at Buckhorn formed under more oxidized (higher $fO_2$) and more sulfur rich (higher $fS_2$) conditions than the retrograde alteration at Nickel Plate (Ettlinger et al., 1992).
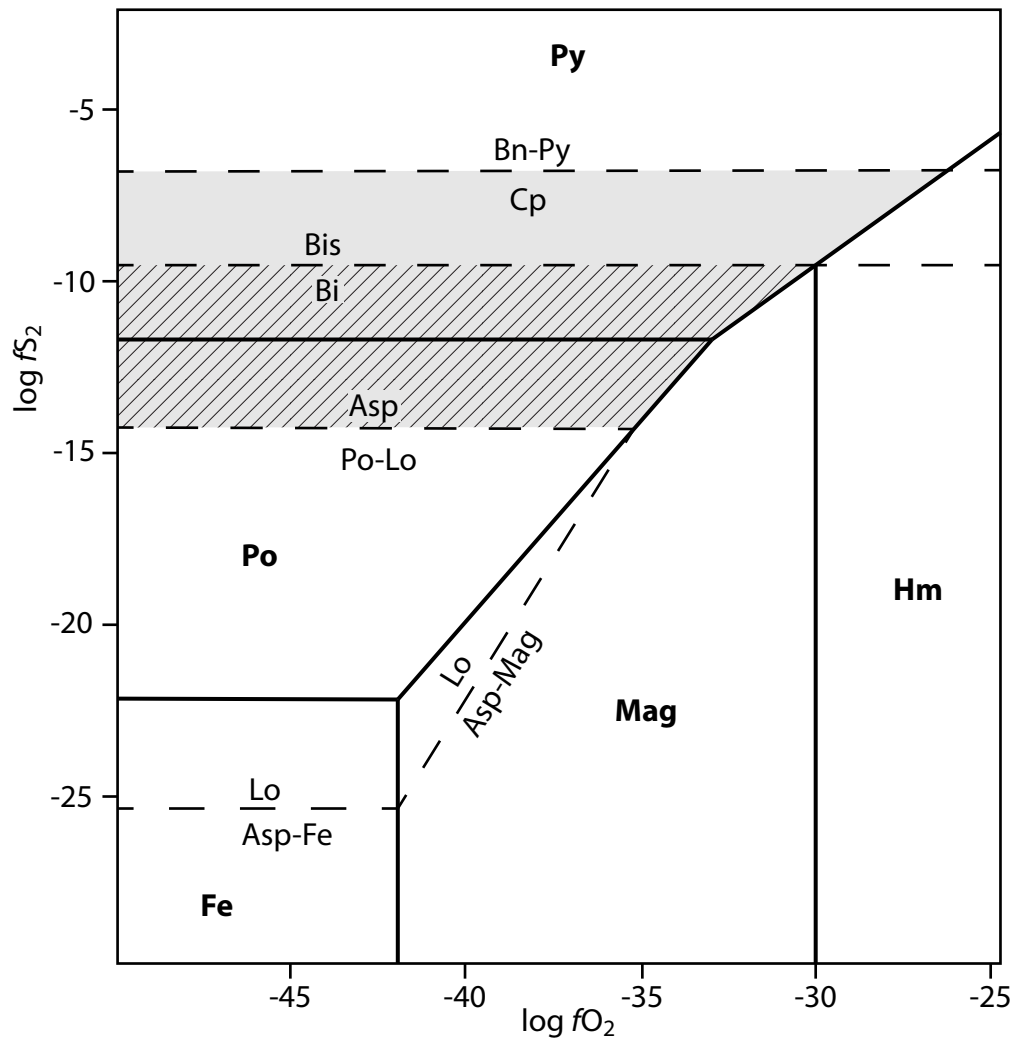


**Figure 4.16:** Log $fO_2$ versus log $fS_2$ diagram showing the stability fields of major sulfide and bismuth minerals formed during retrograde alteration at T=300°C. Stability field for skarn alteration at Buckhorn shown as the shaded area. Stability field of Nickel Plate shown with the diagonal lines. Note that the stability field for the Buckhorn skarn extends to more oxidised and sulfur rich conditions. Nickel Plate stability field from Ettlinger (1992). Mineral stabilities from Ettlinger (1992), Barton and Skinner (1979) and references therein.

### 4.7.2 Gold Mineralization

Gold mineralization in skarn alteration at Buckhorn has been known since the late 1980's, but the precise location of the gold grains within the skarn alteration had not been determined. This work shows that gold occurs in five distinct settings at the Buckhorn gold skarn: (1) in intercrystalline space between prograde and retrograde minerals, (2) in fractures in prograde minerals, (3) intergrown with retrograde minerals, (4) in skarn veins through skarn and non skarn-altered rocks, and (5) in chalcopyrite mineralization.

The first four styles of gold mineralization postdate all of the prograde and most of the retrograde alteration. In all cases, gold is accompanied by significant bismuth mineralization, which may be intergrown with gold, or occur in the same setting. The bismuth mineralization occurs as native bismuth, bismuthinite and other Bi-minerals (Table 4.2). The majority of the bismuth mineralization is made up of equal proportions of native bismuth and bismuthinite, and the remainder is composed of a minor amount of other Bi-minerals. The fifth style of gold mineralization is very rare and has only been documented in a single sample. Unlike the other styles, gold does not exist as free gold, but occurs in chalcopyrite. The gold bearing chalcopyrite predates the first four styles of gold mineralization.

The first two styles of gold mineralization, intercrystalline and fracture-hosted, are similar and likely formed at the same time. In both styles, gold precipitated in pre-existing space, either in fractures in prograde minerals or in intercrystalline space between the prograde and/or retrograde minerals. Gold is accompanied by calcite and rare quartz in both settings, and in some samples it is enclosed in these gangue minerals. Pyrrhotite, chalcopyrite and pyrite also occur in similar settings, but they are petrographically shown to predate gold mineralization. Intercrystalline and fracture-hosted gold are the dominant form of mineralization in magnetite and garnet skarn, and also from a moderate portion of the mineralization in pyroxene skarn. The third setting for gold mineralization, gold intergrown with retrograde minerals, is less abundant than the first two settings and probably younger, but the relative timing is uncertain. Amphibole is by far the most common retrograde mineral intergrown with gold, but locally gold is also intergrown with hydrated Fe-silicate minerals. This setting of gold mineralization is more abundant in pyroxene skarn, but does occur in all styles of skarn alteration. The amphibole that is intergrown with gold may be finer- or coarser-grained than the rest of the amphibole in the rock, but is typically visually distinct. The hydrated Fe-silicates are usually coarser-grained, but optically similar, to the rest of the hydrated Fe-silicates in the rock. In both cases the gold-bearing

retrograde minerals postdate deformation. More than one of the first three styles of mineralization can occur in the same sample, and this is prevalent in samples with high gold grade (>30ppm).

The vein style of gold mineralization is much rarer than the first three styles and was only found in garnet skarn and non-skarn altered rocks. It is presumed to be the result of the youngest and/or most distal expression of mineralization, so there should be no reason why it could not also occur in magnetite or pyroxene skarn. The skarn veins are made up of calcite ± quartz ± amphibole ± epidote ± pyroxene ± garnet ± sulfides, and the skarn alteration in the halos has a similar mineralogy. Gold in the vein style of mineralization is confined to skarn alteration in the vein and the vein halo, and occurs in any or all of the three aforementioned settings.

Gold mineralization in chalcopyrite has only been documented in a single sample of amphibole-pyroxene skarn, but as the gold-bearing chalcopyrite cannot be optically distinguished from barren chalcopyrite it may be more prevalent than currently known. The gold-bearing chalcopyrite formed during retrograde alteration before the first four styles of mineralization. The location of gold grains within the chalcopyrite is unclear, but their presence was indicated by an elemental map produced by Energy-Dispersive X-Ray Spectroscopy (EDS) (Figure 4.3).

### 4.7.2.1        Physicochemical Conditions of Gold Mineralization

The physicochemical conditions of gold mineralization at Buckhorn can be constrained by the retrograde calc-silicate, sulfide and bismuth mineralogy. The temperature of gold mineralization can be estimated at approximately 300°C based on the stability of the hydrated Fe-silicate mineral assemblage that is locally intergrown with gold (Rasmussen et al., 1998). This temperature is higher than that minimum temperature of 241°C estimated from eutectic point on the Au-Bi phase diagram (Figure 4.17). The Bi/Te+Se+S ($R_{Bi/Te}$) ratio of bismuth minerals can be used as a proxy for the Redox conditions of a system with $R_{Bi/Te}$>1 characteristic of a reduced environment and $R_{Bi/Te}$ <1 characteristic of an oxidised environment (Ciobanu et al., 2005, and references therein). The bismuth mineralogy at Buckhorn has approximately equal proportions of native bismuth (Bi), which is typically intergrown with gold, and bismuthinite ($Bi_2S_3$), which typically rims the gold and native bismuth (Figure 4.3). This mineral assemblage and texture suggests that gold precipitated in a reduced environment followed by an increase in oxidation state. This change in bismuth mineralogy matches the change in iron sulfide mineralogy from pyrrhotite to pyrite/marcasite that indicates log $fO_2$ conditions from approximately -36 to -42 (Figure 4.18). The bismuth mineralogy also indicates a similar change in the

sulfur fugacity, from low $fS_2$ during gold and native bismuth mineralization to higher during bismuthinite mineralization (Figure 4.16). This texture is also indicative of cooling as bismuthinite is stable under cooler conditions (Tooth et al., 2011). The pH of alteration and gold mineralization in skarns is generally near neutral to slightly acidic, buffered by the presence of calcite.

The intimate relationship between gold and bismuth suggests that gold was collected in a bismuth melt. Bismuth collection or bismuth scavenging as it is also known, occurs in deposits where a bismuth melt is stable and coexists with a hydrothermal fluid (Tooth et al., 2008). In these situations the gold concentration in the bismuth melt is several orders of magnitude higher than in the fluid (Tooth et al., 2008). Evidence for bismuth scavenging is seen in the petrography where gold and bismuth mineralization is associated with retrograde minerals formed in oxidation reactions ($Fe^{2+}$ bearing pyroxene replaced by $F^{3+}$ bearing amphibole, epidote, and hydrated Fe-silicate minerals and pyrrhotite replaced by pyrite/marcasite). Bismuth scavenging preferentially occurs in reduced, acidic, and low sulfur conditions; like those that occurred during retrograde alteration and gold mineralization at Buckhorn (Tooth et al., 2008). Bismuth scavenging has been suggested to aid in the formation of gold skarns and other deposits including epithermal and volcanic hosted massive sulfide deposits (Cepedal et al., 2006; Cook and Ciobanu, 2004; Törmänen and Koski, 2005).

At the conditions that occurred during retrograde alteration and gold mineralization gold was likely transported as bisulfide complexes before being scavenged by a bismuth melt (Figure 4.18). Bisulfide transportation of gold has been proposed previously at Buckhorn (Gaspar, 2005) and also at other gold skarns (Meinert, 2000).

Gold precipitation from a bismuth melt was caused by cooling and/or local oxidation reactions during retrograde alteration, both of which occurred during gold mineralization at Buckhorn (Tooth et al., 2011). Gold precipitation due to cooling results in gold-bismuth grains being rimmed by bismuthinite as bismuthinite is more stable under cooler conditions (Tooth et al., 2011). Such textures (gold-bismuth rimmed by bismuthinite) occur at Buckhorn and are more prevalent in the fracture and intercrystalline styles of gold mineralization (Figure 4.3). Gold precipitation caused by local oxidation reactions resulted in the intergrowth of gold-bismuth with retrograde minerals (Tooth et al., 2011), and this texture is characteristic of the intergrowth style of gold mineralization at Buckhorn (Figure 4.3, Figure 4.5, Figure 4.10, and Figure 4.11). The gold mineralization hosted in skarn veins

was precipitated by both mechanisms and is contains the fracture-hosted, intercrystalline, and inter-growth styles of gold mineralization (Figure 4.12).

The physicochemical conditions of skarn alteration and gold mineralization are now determined and summarized in Table 4.5. The system is progressed to cooler, lower oxygen fugacity, and lower sulfur fugacity conditions from prograde to retrograde alteration and gold mineralization.
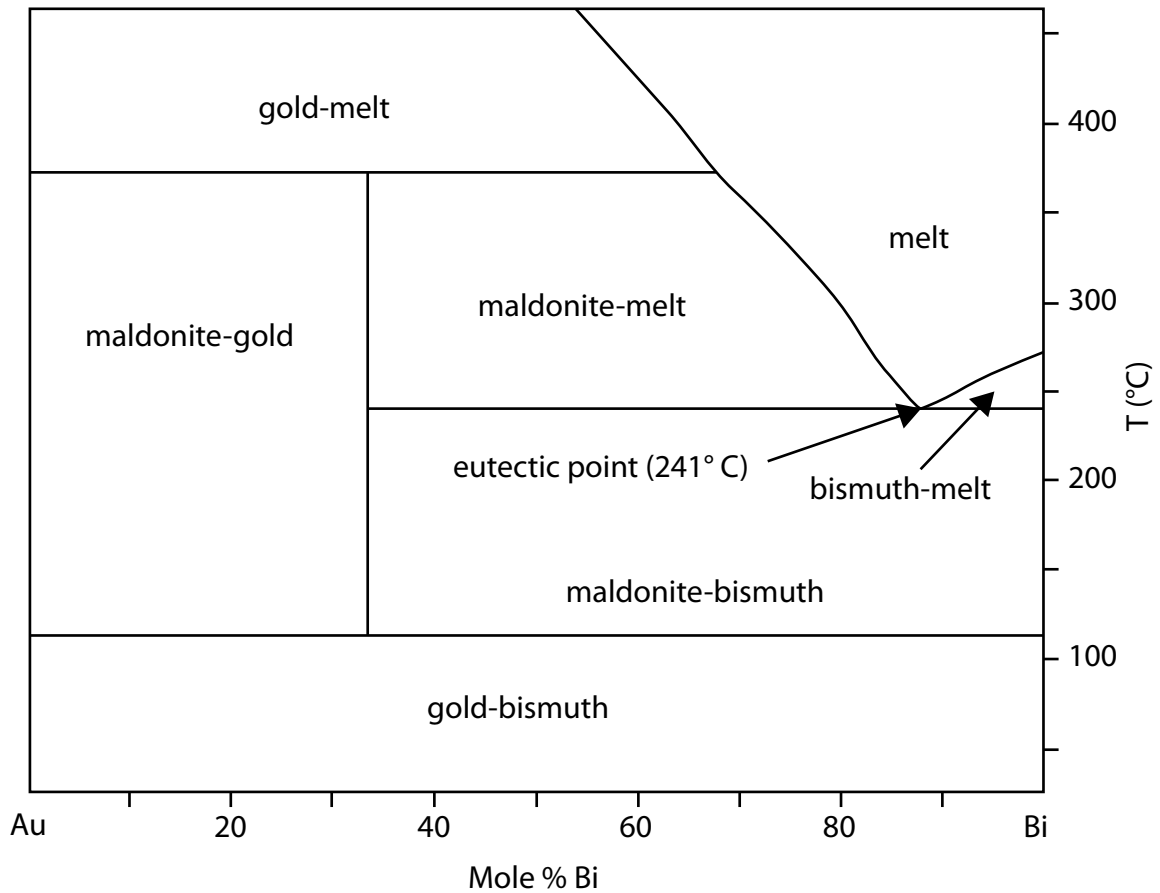
**Figure 4.17:** Phase diagram of Au-Bi at 1 bar that demonstrates the eutectic point at 241°C. Modified from Tooth et al. (2008)
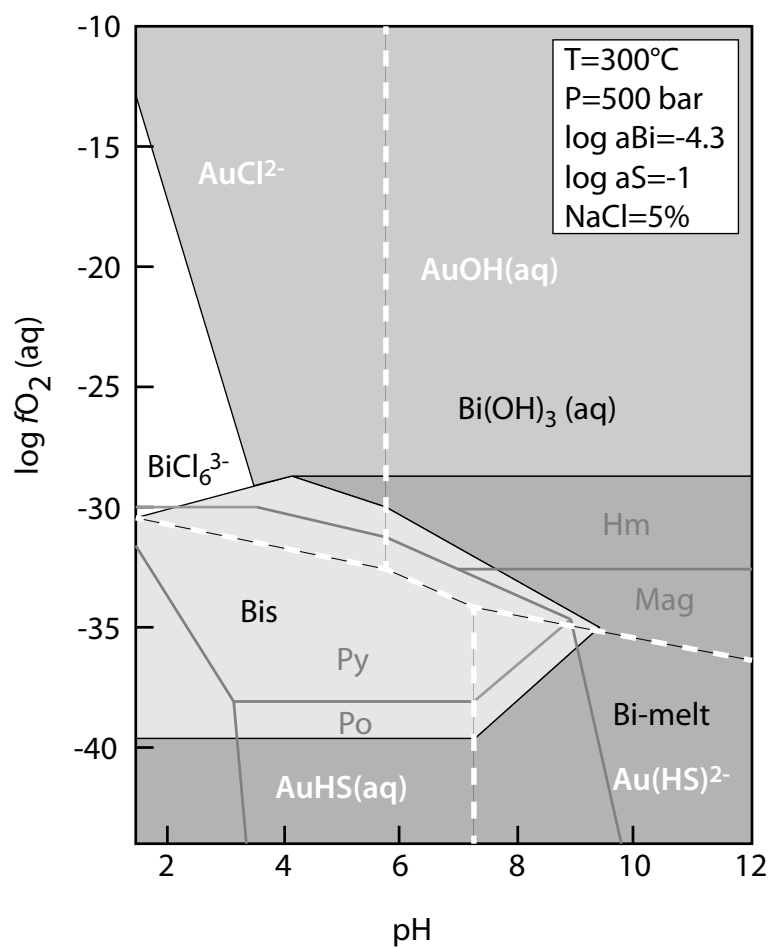
**Figure 4.18:** Log $fO_2$ versus pH diagram showing the stability fields of Au, Bi, and Fe phases and aqueous complexes at the conditions of retrograde alteration and gold mineralization at Buckhorn (pH=6-8, log $fO_2$=-36 to -42). Modified from Tooth et al. (2008).

**Table 4.5:** Summary of physicochemical conditions of skarn alteration and gold mineralization

|  | Prograde | Retrograde | Gold Mineralization |
|---|---|---|---|
| Temperature (°C) | 430 to 500 | 300 to 430 | 241 to 300 |
| $fO_2$ | -25 to -20 | < -26 | -42 to -36 |
| $fS_2$ | -8 to -4.5 | -15 to -6 | -15 to -6 |
| pH | 6 to 8 | 6 to 8 | 6 to 8 |

### 4.7.3 Comparison to Nickel Plate

The Nickel Plate deposit in the Hedley mining district is the largest gold skarn in Canada, and was the only known economic gold skarn until the early 1970's (Meinert, 2000). Production from the deposit totalled 2.3 Moz of gold at an average grade of 5.4 g/t Au, this includes almost 1.3 Moz of gold that was mined underground at a grade of 14 g/t (Ray et al., 1996). Similar to the Buckhorn gold skarn, the Nickel Plate deposit lies in the accreted Quesnel terrane. The Nickel Plate deposits is located in the Late Triassic Nicola Group, which is made up of arc related volcanic and sedimentary rocks, the latter of which are dominant in the Hedley area (Ray et al., 1996). As discussed in Chapter 2, the metavolcanic rocks of the BMV that host part of the Buckhorn gold skarn are correlated with the Nicola Group. The Nickel Plate deposit is hosted in the Late Triassic Hedley formation of the Nicola Group, which consists of limestone and thinly bedded, turbiditic, calcareous siltstone and lesser amounts of calcareous argillite, tuff and conglomerate (Ray et al., 1996). While the Hedley formation is younger than the Permian Anarchist Group rocks that host the Buckhorn gold skarn it has a similar assemblage of lithologies and probably formed in a comparable depositional environment. Similar to the Buckhorn area, the Hedley mining district was intruded by a variety of alkaline to sub-alkaline, intermediate to shallow depth, gabbro to granodiorite bodies. The intrusions in the Hedley area coincide with the end of volcanism in the Nicola Group, and the oldest of these intrusions, the Hedley intrusive suite, is genetically linked to local gold skarn alteration (Ray et al., 1996). The Hedley intrusive rocks form a number of major stocks as well as sills and minor dikes that are quartz diorite to gabbro in composition and have a reduced oxidation state (Ray et al., 1996). Ranging in age from 212 to 194 Ma, the mineralizing intrusions in the Hedley area are notably older than those at Buckhorn, but they are compositionally similar and have a similar intrusive style.

In broad terms, the skarn alteration at Nickel Plate is similar to that at Buckhorn. The prograde assemblage is predominately made up of iron-rich pyroxene and garnet, while the sulfide alteration is dominated by pyrrhotite (Ray et al., 1996). However, the skarn alteration at Nickel Plate differs from the skarn alteration at Buckhorn in several ways. At Nickel Plate the skarn contains significant scapolite alteration, which is absent from the Buckhorn skarn assemblage (Ray et al., 1996). The scapolite at Nickel Plate formed with the lower temperature gold-sulfide mineralization and is presumed to be the by-product of calcic-sodic metasomatism of diorite (Ettlinger et al., 1992). Ray et al. (1990) suggest that the scapolite alteration at Nickel Plate indicates that chloride complexes may have been important for the transportation and precipitation of gold in the system. The lack of scapolite

alteration and the physicochemical conditions for gold mineralization at Buckhorn suggest that while chloride complexes may have been important for gold mineralization in some skarn systems they are not necessary to produce an economic deposit.

Other major differences between the two skarns exist in the opaque mineral assemblage. The Nickel Plate skarn has abundant arsenopyrite, trace chalcopyrite and negligible magnetite (Ettlinger et al., 1992), whereas Buckhorn has nearly the opposite abundances of these minerals. The presence of magnetite at Buckhorn suggests that parts of it formed under more oxidising conditions than the Nickel Plate skarn (Figure 4.15). The higher chalcopyrite content at Buckhorn is also similar to so-called oxidised gold skarns (Meinert et al., 2005).

Another difference between the Nickel Plate and Buckhorn gold skarns exists in the intensity of retrograde alteration. Retrograde alteration to hydrous phases is relatively minor at the Nickel Plate deposit, (Ettlinger et al., 1992), and is characterized by minor amounts of ferrowollastonite and epidote, which locally replace prograde pyroxene. The retrograde alteration at Buckhorn is more intense than at Nickel Plate, and it features a different mineral assemblage consisting of ferroactinolite, epidote and hydrated Fe-silicates (Table 4.4).

Gold mineralization at both deposits is accompanied by various bismuth minerals, but the specific mineralogy is different for each deposit. At Nickel Plate, hedleyite ($Bi_2+xTe_{1-x}$), native bismuth and maldonite ($Au_2Bi$) are the most abundant bismuth phases (Ettlinger et al., 1992). At Buckhorn the bismuth minerals tend to be sulfur and/or tellurium bearing and include native bismuth, bismuthinite ($Bi_2S_3$), joseite ($Bi_4TeS_2$), and pilsenite ($Bi_4Te_3$) among others (Gaspar, 2005). The greater sulfur and tellurium content suggests that the mineralization at Buckhorn occurred at more oxidised conditions (Ciobanu et al., 2005, and references therein).

The setting of gold mineralization at Nickel Plate is also different from that at Buckhorn. At Nickel Plate the majority of gold and bismuth mineralization is contemporaneous with arsenopyrite and occurs as inclusions within it (Ettlinger et al., 1992). This differs from the Buckhorn gold skarn where gold mineralization postdates the sulfide deposition and occurs in intercrystalline space between and fractures in prograde and retrograde minerals, or intergrown with retrograde minerals.

Comparison of the Buckhorn and Nickel Plate gold skarns indicates that despite the many similarities there are significant differences. The two deposits share many large scale characteristics including host rocks and mineralizing intrusions, they also have the same general skarn alteration and

gold mineralization assemblage. However, at the smaller scale the Buckhorn gold skarn has a more oxidised skarn assemblage, and a more sulfur-rich ore mineral assemblage.

The mineralogy and mineral chemistry at Buckhorn support its classification as a reduced gold skarn similar to other deposits around the world. However, the differences between Buckhorn and Nickel Plate clearly show that there is significant variability within this classification. This has implications for exploration strategies for similar deposits that are discussed in Chapter 6.

# Chapter 5.  Geochemistry of Skarn Alteration at Buckhorn

## 5.1  Introduction

In order to geochemically characterize the skarn alteration and gold mineralization at Buckhorn seventy-nine skarn samples and eight hornfels hosted skarn-vein samples were collected from eight drill holes through the SWOZ and Gold Bowl. Twenty-eight samples of the sedimentary, volcanic and igneous host rocks were also collected to provide geochemical context for the skarn samples. The samples came from 0.24 to 1.28 metre composite pulps from diamond drill holes and cover the three major classifications of skarn alteration: pyroxene skarn, garnet skarn and magnetite skarn (Figure 4.1 and Table 5.1). The samples were analysed by ICP-MS after four acid digestion for 55 elements, including major, trace and rare earth elements (REE). The complete results of the analysis can be found in Appendix B. The combination of four acid digestion and ICP-MS was chosen for the near complete digestion and low detection limit that allows a precise and accurate geochemical characterization of the skarn alteration.

**Table 5.1:** Summary of diamond drill holes and skarn samples selected for geochemical analysis

| Drill Hole | Location | Number of skarn samples | Samples | Types of skarn alteration | Range of Gold Grade (ppm) | Protoliths |
|---|---|---|---|---|---|---|
| D07-369 | SWOZ | 22 | BS082-84 | Pyroxene > Garnet > Magnetite | <0.1 - 62 | Metavolcanic and carbonate and clastic metasedimentary rocks |
| D08-410 | SWOZ | 21 | BS090-94 | Pyroxene > Garnet > Magnetite | <0.1 - 51.1 | Metavolcanic and carbonate metasedimentary rocks |
| D08-413 | SWOZ | 15 | BS016-17, BS085-88 | Pyroxene > Garnet > Magnetite | <0.1 - 117.5 | Metavolcanic and carbonate metasedimentary rocks |
| D08-443 | GB | 6 | BS077-79, BS089 | Pyroxene > Garnet | <0.1 - 53.7 | Clastic metasedimentary rocks and/or diorite |
| D09-536 | North of GB | 15 | BS080-81 | Pyroxene - Garnet > Magnetite | <0.1 - 0.7 | Clastic metasedimentary rocks and/or diorite |
| D10-569 | Below SWOZ | 0 | BS095-96 | Skarn veins | <0.1 - 24.1 | Clastic metasedimentary rocks |
| D10-595 | Below SWOZ | 0 | BS097-98 | Skarn veins | <0.1 - 3.5 | Clastic metasedimentary rocks |

## 5.2  Relationship between Major and Trace Elements, Skarn Alteration and Gold-Bismuth Mineralization

Geochemical analysis provides insight into the character of skarn alteration and gold mineralization. The relationship between elements in skarn alteration was investigated with a correlation matrix (Table 5.2). The correlation matrix shows that there is a positive correlation between gold and bismuth (r=0.92) and gold and silver (r=0.56), as well as a negative correlation between gold and aluminum(r=-0.5), but no correlation between gold and any other elements. The correlation matrix

also demonstrates the relationship of other elements. In addition to correlating with gold, silver also correlates with bismuth (r=0.64), lead (r=0.80), and zinc (0.68). The association of silver, lead, and zinc has been recognized in other skarns (Gemmell et al., 1992) and numerous other deposit types including epithermals (Simmons et al., 2005), porphyries (Sillitoe, 1997) and so-called intrusion related deposits (Thompson et al., 1999).

There is also a correlation between aluminum and some of the high field strength elements (HFSE). Aluminum correlates with titanium (r=0.89), zirconium (r=0.80), and niobium (r=0.84) (Table 5.2), similarly, potassium correlates with sodium (r=0.62), rubidium (r=0.87), and strontium (r=0.54) (Table 5.2). The correlation of these sets of elements suggests that they acted in a similar manner during skarn alteration likely due to their similar chemical properties.

To further investigate this relationship and geochemically distinguish the different host rocks and categories of skarn alteration a selection of major and trace elements were plotted versus bismuth (Figure 5.1). Bismuth was chosen as a proxy for gold as it has a strong correlation with gold and was precipitated with it (r=0.92, Table 5.2), but has greater range in abundances than gold.

The geochemical characterization of host rocks and skarn alteration complements the mineralogical and textural characterizations that were presented in Chapters 2 and 4 and illuminates several trends. The hornfels altered host rocks have a variable geochemical character, but generally have lower iron and manganese and higher aluminum contents than the skarn alteration (Figure 5.1). The carbonate host rocks have a different geochemical character, with higher calcium and lower iron, manganese, aluminum, and titanium content compared to the other host rocks and skarn alteration (Figure 5.1). The Quartz Porphyry dikes were also analysed and have the same general geochemical characteristics as the metasedimentary and metavolcanic rocks, but with lower bismuth content (Figure 5.1).

There is significant overlap in the geochemistry of the different skarn alteration assemblages, but some general trends can be identified. Garnet skarn tends to have higher calcium, manganese, and zirconium content, whereas magnetite skarn has high iron content and has low amounts of the other elements. The geochemical signature of pyroxene skarn is more variable, and overlaps with both magnetite and garnet skarn (Figure 5.1). The negative correlation between bismuth and aluminum is visible (r=-0.52), and the correlation is stronger in pyroxene skarn than in the other categories of skarn.

**Table 5.2:** Base 10 correlation matrix of select elements from geochemical analysis of skarn alteration at Buckhorn

| Log 10 | Au | Ag | Bi | Fe | Ca | P | Mg | Mn | Cr | Ti | Al | Na | K | S |
|---|---|---|---|---|---|---|---|---|---|---|---|---|---|---|
| Au | 1.00 | 0.56 | 0.92 | 0.16 | 0.09 | -0.15 | 0.16 | -0.18 | 0.10 | -0.40 | -0.50 | -0.10 | -0.21 | 0.16 |
| Ag | 0.56 | 1.00 | 0.64 | -0.06 | 0.19 | -0.03 | -0.01 | -0.13 | -0.32 | -0.08 | -0.17 | -0.13 | 0.02 | 0.25 |
| Bi | 0.92 | 0.64 | 1.00 | 0.22 | -0.04 | -0.14 | 0.18 | -0.27 | 0.07 | -0.41 | -0.52 | -0.13 | -0.20 | 0.19 |
| Fe | 0.16 | -0.06 | 0.22 | 1.00 | -0.42 | -0.27 | -0.03 | -0.12 | 0.41 | -0.55 | -0.59 | -0.13 | -0.31 | 0.62 |
| Ca | 0.09 | 0.19 | -0.04 | -0.42 | 1.00 | -0.15 | -0.28 | 0.51 | -0.17 | 0.12 | 0.22 | -0.47 | -0.30 | -0.29 |
| P | -0.15 | -0.03 | -0.14 | -0.27 | -0.15 | 1.00 | -0.30 | 0.15 | 0.17 | 0.74 | 0.66 | 0.36 | 0.49 | -0.04 |
| Mg | 0.16 | -0.01 | 0.18 | -0.03 | -0.28 | -0.30 | 1.00 | -0.33 | -0.20 | -0.30 | -0.33 | 0.16 | -0.11 | 0.11 |
| Mn | -0.18 | -0.13 | -0.27 | -0.12 | 0.51 | 0.15 | -0.33 | 1.00 | 0.22 | 0.25 | 0.33 | -0.16 | -0.30 | -0.23 |
| Cr | 0.10 | -0.32 | 0.07 | 0.41 | -0.17 | 0.17 | -0.20 | 0.22 | 1.00 | -0.08 | -0.07 | 0.11 | -0.09 | 0.22 |
| Ti | -0.40 | -0.08 | -0.41 | -0.55 | 0.12 | 0.74 | -0.30 | 0.25 | -0.08 | 1.00 | 0.89 | 0.27 | 0.51 | -0.29 |
| Al | -0.50 | -0.17 | -0.52 | -0.59 | 0.22 | 0.66 | -0.33 | 0.33 | -0.07 | 0.89 | 1.00 | 0.16 | 0.39 | -0.34 |
| Na | -0.10 | -0.13 | -0.13 | -0.13 | -0.47 | 0.36 | 0.16 | -0.16 | 0.11 | 0.27 | 0.16 | 1.00 | 0.62 | 0.09 |
| K | -0.21 | 0.02 | -0.20 | -0.31 | -0.30 | 0.49 | -0.11 | -0.30 | -0.09 | 0.51 | 0.39 | 0.62 | 1.00 | 0.09 |
| S | 0.16 | 0.25 | 0.19 | 0.62 | -0.29 | -0.04 | 0.11 | -0.23 | 0.22 | -0.29 | -0.34 | 0.09 | 0.09 | 1.00 |
| Cu | 0.08 | 0.45 | 0.03 | 0.17 | 0.00 | -0.06 | -0.03 | -0.33 | -0.12 | -0.07 | -0.11 | 0.03 | 0.24 | 0.61 |
| Pb | 0.49 | 0.80 | 0.62 | -0.26 | 0.14 | 0.04 | 0.01 | -0.13 | -0.44 | 0.03 | -0.09 | -0.08 | 0.09 | -0.11 |
| Zn | 0.13 | 0.68 | 0.29 | -0.39 | 0.04 | 0.23 | 0.09 | 0.00 | -0.46 | 0.29 | 0.17 | 0.10 | 0.27 | -0.06 |
| As | 0.15 | 0.04 | 0.29 | -0.04 | -0.08 | 0.20 | -0.07 | -0.10 | 0.17 | 0.11 | 0.01 | -0.05 | -0.14 | -0.21 |
| Mo | -0.29 | 0.16 | -0.22 | -0.15 | 0.11 | 0.30 | -0.32 | 0.20 | -0.07 | 0.49 | 0.36 | 0.05 | 0.32 | 0.09 |
| W | -0.13 | 0.03 | -0.11 | -0.03 | 0.33 | 0.04 | -0.42 | 0.02 | 0.15 | 0.15 | 0.14 | -0.06 | 0.05 | 0.11 |
| Co | 0.44 | 0.32 | 0.53 | 0.38 | -0.24 | 0.16 | -0.07 | -0.10 | 0.39 | -0.12 | -0.29 | 0.08 | -0.06 | 0.43 |
| Ni | -0.02 | 0.29 | 0.04 | 0.05 | -0.17 | 0.47 | -0.24 | 0.03 | 0.18 | 0.33 | 0.22 | 0.28 | 0.31 | 0.44 |
| Rb | -0.11 | 0.13 | -0.02 | -0.32 | -0.33 | 0.47 | 0.05 | -0.38 | -0.12 | 0.41 | 0.33 | 0.53 | 0.87 | 0.15 |
| Sr | -0.10 | 0.17 | 0.03 | -0.50 | -0.12 | 0.54 | -0.03 | -0.23 | -0.07 | 0.54 | 0.49 | 0.34 | 0.54 | -0.10 |
| Zr | -0.45 | -0.16 | -0.50 | -0.54 | 0.27 | 0.54 | -0.36 | 0.37 | -0.07 | 0.85 | 0.80 | 0.11 | 0.34 | -0.33 |
| Nb | -0.47 | -0.28 | -0.49 | -0.39 | 0.00 | 0.62 | -0.29 | 0.25 | -0.05 | 0.71 | 0.84 | 0.10 | 0.36 | -0.33 |
| Sn | -0.18 | -0.05 | -0.25 | 0.04 | 0.27 | 0.26 | -0.61 | 0.23 | 0.40 | 0.30 | 0.40 | -0.15 | 0.20 | 0.19 |
| Sb | 0.36 | 0.31 | 0.46 | -0.08 | -0.22 | 0.33 | 0.14 | -0.29 | 0.03 | 0.11 | 0.04 | 0.20 | 0.15 | 0.09 |

| Log 10 | Cu | Pb | Zn | As | Mo | W | Co | Ni | Rb | Sr | Zr | Nb | Sn | Sb |
|---|---|---|---|---|---|---|---|---|---|---|---|---|---|---|
| Au | 0.08 | 0.49 | 0.13 | 0.15 | -0.29 | -0.13 | 0.44 | -0.02 | -0.11 | -0.10 | -0.45 | -0.47 | -0.18 | 0.36 |
| Ag | 0.45 | 0.80 | 0.68 | 0.04 | 0.16 | 0.03 | 0.32 | 0.29 | 0.13 | 0.17 | -0.16 | -0.28 | -0.05 | 0.31 |
| Bi | 0.03 | 0.62 | 0.29 | 0.29 | -0.22 | -0.11 | 0.53 | 0.04 | -0.02 | 0.03 | -0.50 | -0.49 | -0.25 | 0.46 |
| Fe | 0.17 | -0.26 | -0.39 | -0.04 | -0.15 | -0.03 | 0.38 | 0.05 | -0.32 | -0.50 | -0.54 | -0.39 | 0.04 | -0.08 |
| Ca | 0.00 | 0.14 | 0.04 | -0.08 | 0.11 | 0.33 | -0.24 | -0.17 | -0.33 | -0.12 | 0.27 | 0.00 | 0.27 | -0.22 |
| P | -0.06 | 0.04 | 0.23 | 0.20 | 0.30 | 0.04 | 0.16 | 0.47 | 0.47 | 0.54 | 0.54 | 0.62 | 0.26 | 0.33 |
| Mg | -0.03 | 0.01 | 0.09 | -0.07 | -0.32 | -0.42 | -0.07 | -0.24 | 0.05 | -0.03 | -0.36 | -0.29 | -0.61 | 0.14 |
| Mn | -0.33 | -0.13 | 0.00 | -0.10 | 0.20 | 0.02 | -0.10 | 0.03 | -0.38 | -0.23 | 0.37 | 0.25 | 0.23 | -0.29 |
| Cr | -0.12 | -0.44 | -0.46 | 0.17 | -0.07 | 0.15 | 0.39 | 0.18 | -0.12 | -0.07 | -0.07 | -0.05 | 0.40 | 0.03 |
| Ti | -0.07 | 0.03 | 0.29 | 0.11 | 0.49 | 0.15 | -0.12 | 0.33 | 0.41 | 0.54 | 0.85 | 0.71 | 0.30 | 0.11 |
| Al | -0.11 | -0.09 | 0.17 | 0.01 | 0.36 | 0.14 | -0.29 | 0.22 | 0.33 | 0.49 | 0.80 | 0.84 | 0.40 | 0.04 |
| Na | 0.03 | -0.08 | 0.10 | -0.05 | 0.05 | -0.06 | 0.08 | 0.28 | 0.53 | 0.34 | 0.11 | 0.10 | -0.15 | 0.20 |
| K | 0.24 | 0.09 | 0.27 | -0.14 | 0.32 | 0.05 | -0.06 | 0.31 | 0.87 | 0.54 | 0.34 | 0.36 | 0.20 | 0.15 |
| S | 0.61 | -0.11 | -0.06 | -0.21 | 0.09 | 0.11 | 0.43 | 0.44 | 0.15 | -0.10 | -0.33 | -0.33 | 0.19 | 0.09 |
| Cu | 1.00 | 0.08 | 0.09 | -0.31 | 0.21 | 0.27 | 0.10 | 0.34 | 0.15 | -0.10 | -0.04 | -0.15 | 0.29 | -0.08 |
| Pb | 0.08 | 1.00 | 0.75 | 0.12 | 0.08 | -0.04 | 0.13 | 0.05 | 0.21 | 0.29 | -0.11 | -0.15 | -0.26 | 0.34 |
| Zn | 0.09 | 0.75 | 1.00 | 0.14 | 0.31 | -0.07 | 0.10 | 0.29 | 0.38 | 0.42 | 0.16 | 0.02 | -0.22 | 0.31 |
| As | -0.31 | 0.12 | 0.14 | 1.00 | -0.05 | 0.12 | 0.61 | 0.19 | 0.04 | 0.17 | 0.06 | -0.07 | -0.10 | 0.14 |
| Mo | 0.21 | 0.08 | 0.31 | -0.05 | 1.00 | 0.27 | 0.04 | 0.35 | 0.24 | 0.21 | 0.50 | 0.28 | 0.43 | -0.01 |
| W | 0.27 | -0.04 | -0.07 | 0.12 | 0.27 | 1.00 | 0.05 | 0.18 | 0.08 | 0.06 | 0.15 | -0.04 | 0.53 | -0.15 |
| Co | 0.10 | 0.13 | 0.10 | 0.61 | 0.04 | 0.05 | 1.00 | 0.62 | 0.11 | 0.00 | -0.23 | -0.37 | 0.05 | 0.13 |
| Ni | 0.34 | 0.05 | 0.29 | 0.19 | 0.35 | 0.18 | 0.62 | 1.00 | 0.39 | 0.25 | 0.22 | 0.01 | 0.27 | -0.04 |
| Rb | 0.15 | 0.21 | 0.38 | 0.04 | 0.24 | 0.08 | 0.11 | 0.39 | 1.00 | 0.66 | 0.21 | 0.22 | 0.07 | 0.21 |
| Sr | -0.10 | 0.29 | 0.42 | 0.17 | 0.21 | 0.06 | 0.00 | 0.25 | 0.66 | 1.00 | 0.30 | 0.35 | 0.07 | 0.55 |
| Zr | -0.04 | -0.11 | 0.16 | 0.06 | 0.50 | 0.15 | -0.23 | 0.22 | 0.21 | 0.30 | 1.00 | 0.67 | 0.37 | -0.11 |
| Nb | -0.15 | -0.15 | 0.02 | -0.07 | 0.28 | -0.04 | -0.37 | 0.01 | 0.22 | 0.35 | 0.67 | 1.00 | 0.36 | 0.14 |
| Sn | 0.29 | -0.26 | -0.22 | -0.10 | 0.43 | 0.53 | 0.05 | 0.27 | 0.07 | 0.07 | 0.37 | 0.36 | 1.00 | -0.12 |
| Sb | -0.08 | 0.34 | 0.31 | 0.14 | -0.01 | -0.15 | 0.13 | -0.04 | 0.21 | 0.55 | -0.11 | 0.14 | -0.12 | 1.00 |
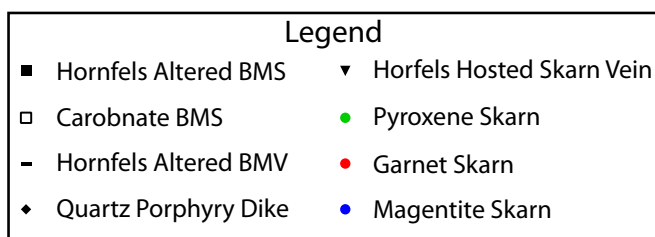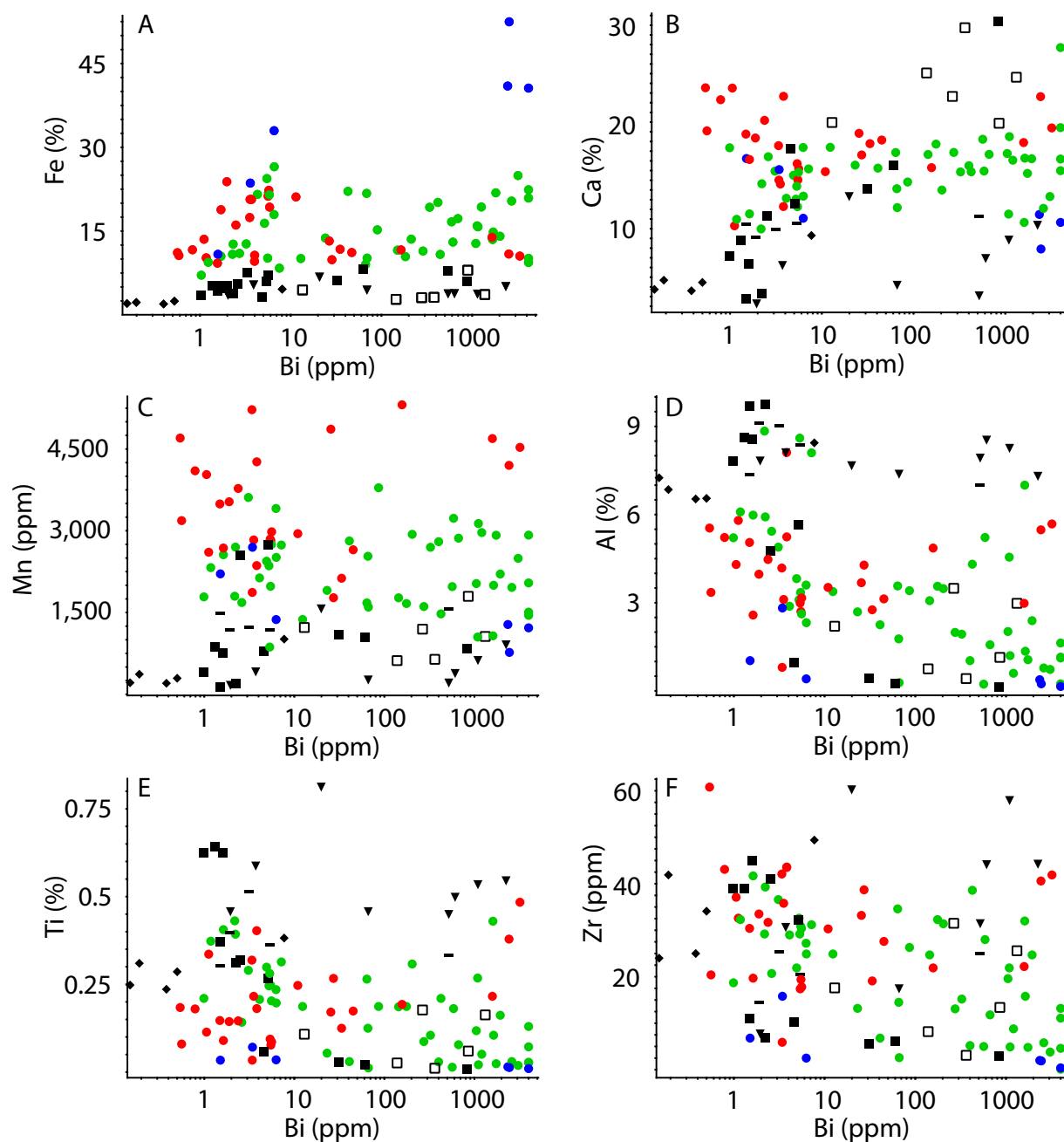
**Figure 5.1:** Plots of bismuth versus select major and trace elements (Fe, Ca, Mn, Al, Ti, and Zr) that demonstrate the geochemical character of the BMS, BMV, and skarn alteration. See text for further discussion.

Legend

- ■ Hornfels Altered BMS
- □ Carobnate BMS
- – Hornfels Altered BMV
- ◆ Quartz Porphyry Dike
- ▼ Horfels Hosted Skarn Vein
- ● Pyroxene Skarn
- ● Garnet Skarn
- ● Magentite Skarn

### 5.3 Relationship between Gold Mineralization and Sulfide Forming Elements

Gold content of the skarn and hornfels hosted skarn veins was plotted against silver, bismuth, and a selection of sulfide forming elements (S, Cu, Pb, Zn, As, Mo, and Co) to determine their relationship.

Figure 5.2 illustrates the positive correlation between and gold-bismuth (r=0.92, Table 5.2), where the samples plot along a single trend. The relationship between gold and silver is more complex (Figure 5.2). The silver analysis falls into two populations, those with high Au/Ag ratios (>4) form a tight trend, whereas those with lower Au/Ag ratios have a more diffuse pattern. Figure 5.2 also demonstrates the lack of correlation between gold and the sulfide forming elements that was noted with the correlation matrix (Table 5.2). There is also no relationship between metal content and the skarn alteration categories, and the hornfels hosted skarn veins plot in the same area as the rest of the skarn alteration.

The correlation between gold and silver suggests that some of the gold occurs as electrum, which fits with microprobe analysis performed by Gaspar (2005). The two populations defined by the difference in Au/Ag ratios have not been previously noted and their character is investigated further in section 5.4.
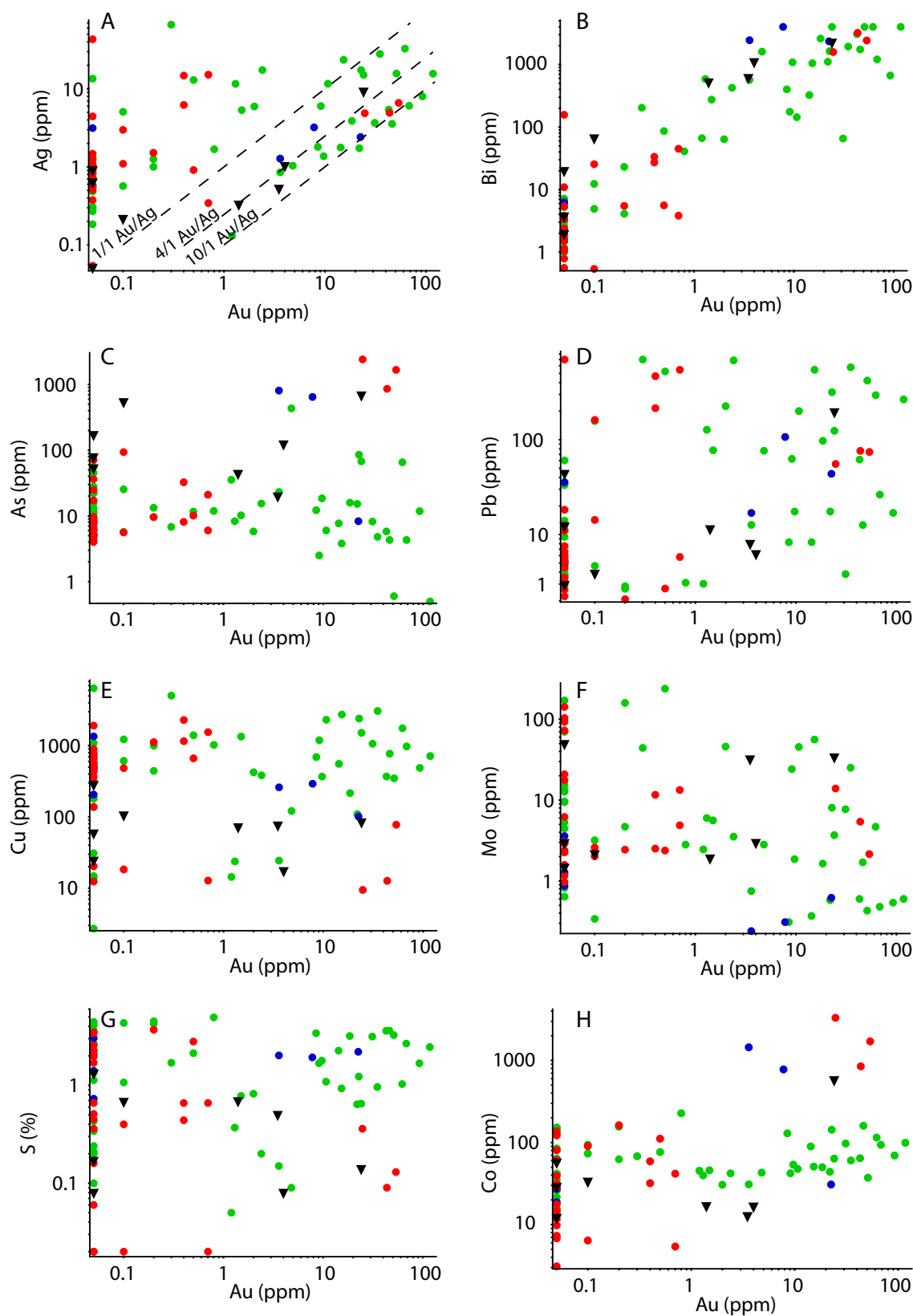
**Figure 5.2:** Graphs of Au vs. Ag, Bi, As, Pb, Cu, Mo, S, and Co. The graphs show that there is a moderate correlation between Au-Ag, a strong correlation between Au-Bi, and no correlation between gold and the other elements. Legend on Figure 5.1. See text for further discussion

## 5.4   High and Low Base Metal Gold Mineralized Populations

Au/Ag ratios were plotted versus select elements to further investigate the character of the two gold mineralized populations at Buckhorn (Figure 5.3 and Figure 5.4). In Figure 5.3 and Figure 5.4 the distribution of samples falls into two categories. Points on the Au/Ag vs gold, bismuth and arsenic graphs plot throughout the diagrams, whereas, the points on the Au/Ag vs base metal (Pb, Cu, and Mo) graphs predominately plot along the X and Y axes. Based on the latter graphs there are two interpreted populations of mineralized samples, one with high Au/Ag ratios and low base metal content, which plots along the x-axis, and a second with low Au/Ag ratios and higher base metal content that plots along the y-axis. The two populations are less distinct on the Au/Ag vs gold graph, but they appear as two sub-vertical arrays at high and low Au/Ag ratios (Figure 5.3 and Figure 5.4). The two are referred to as the low and high base metal populations.

The low base metal population is characterized by Au/Ag ratios greater than four and low base metals content. This population contains samples that have a wide range of gold grades (4.7 to >100 ppm, Figure 5.3 and Figure 5.4), come from all categories of skarn alteration including the vein hosted style (Figure 5.3 and Figure 5.4), and come from both the SWOZ and Gold Bowl (Table 5.1). In contrast, the high base metal population has Au/Ag ratios below four and higher base metal content (Figure 5.3 and Figure 5.4). Similarly, the high base metal population occurs over a wide range of gold grades (<0.06 to >50 ppm), in all categories of skarn alteration and in both the SWOZ and Gold Bowl (Table 5.1, Figure 5.3 and Figure 5.4).

Based on the metal content and petrographic analysis the low base metal population is interpreted as the main gold mineralizing event, whereas the high base metal population is interpreted as the earlier sulfide phase of retrograde alteration.
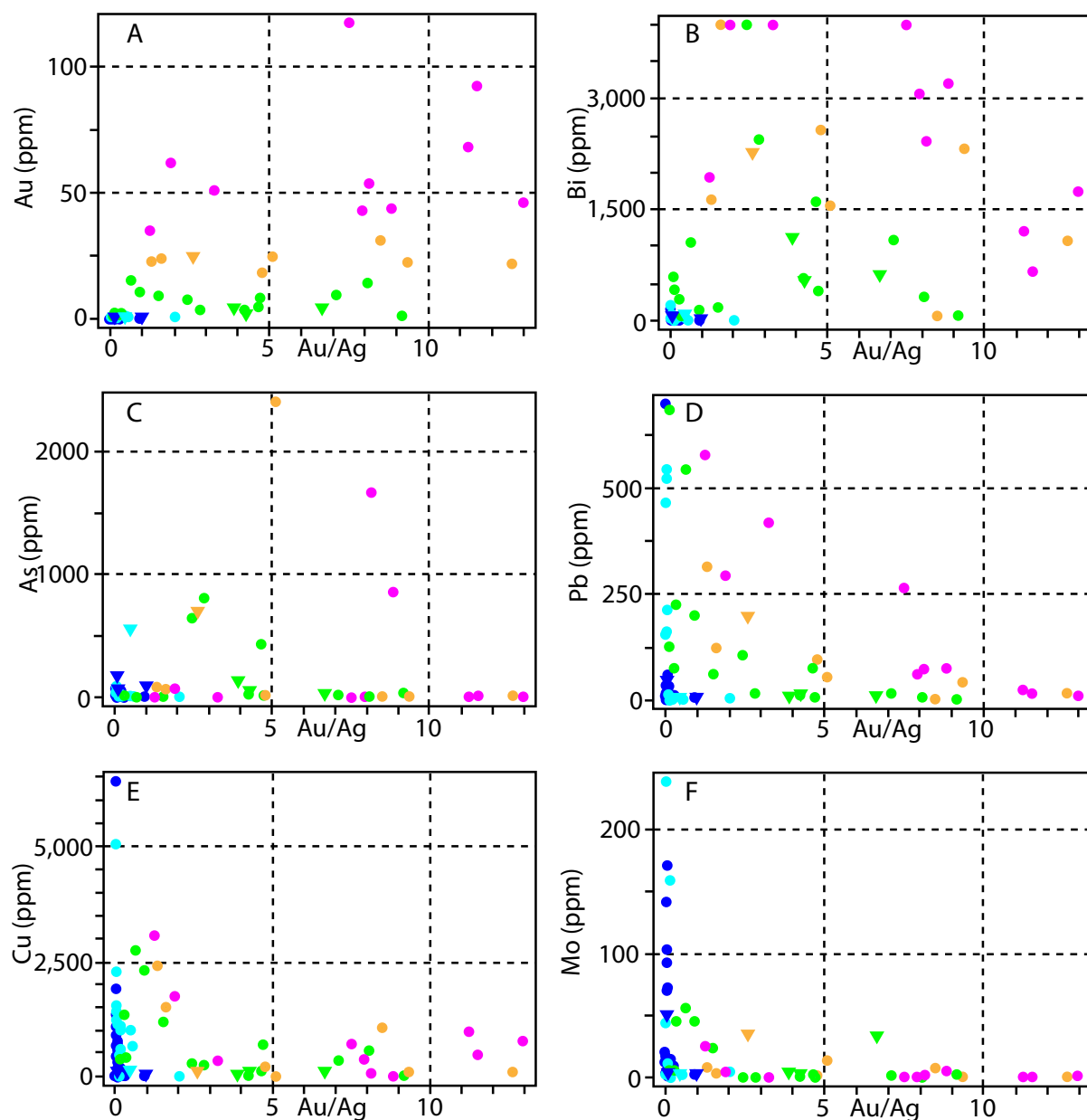
**Figure 5.3:** Graphs of Au/Ag vs Au, Bi, As, and base metals (Pb, Cu, and Mo). The graphs show two distinct populations. See text for further discussion.
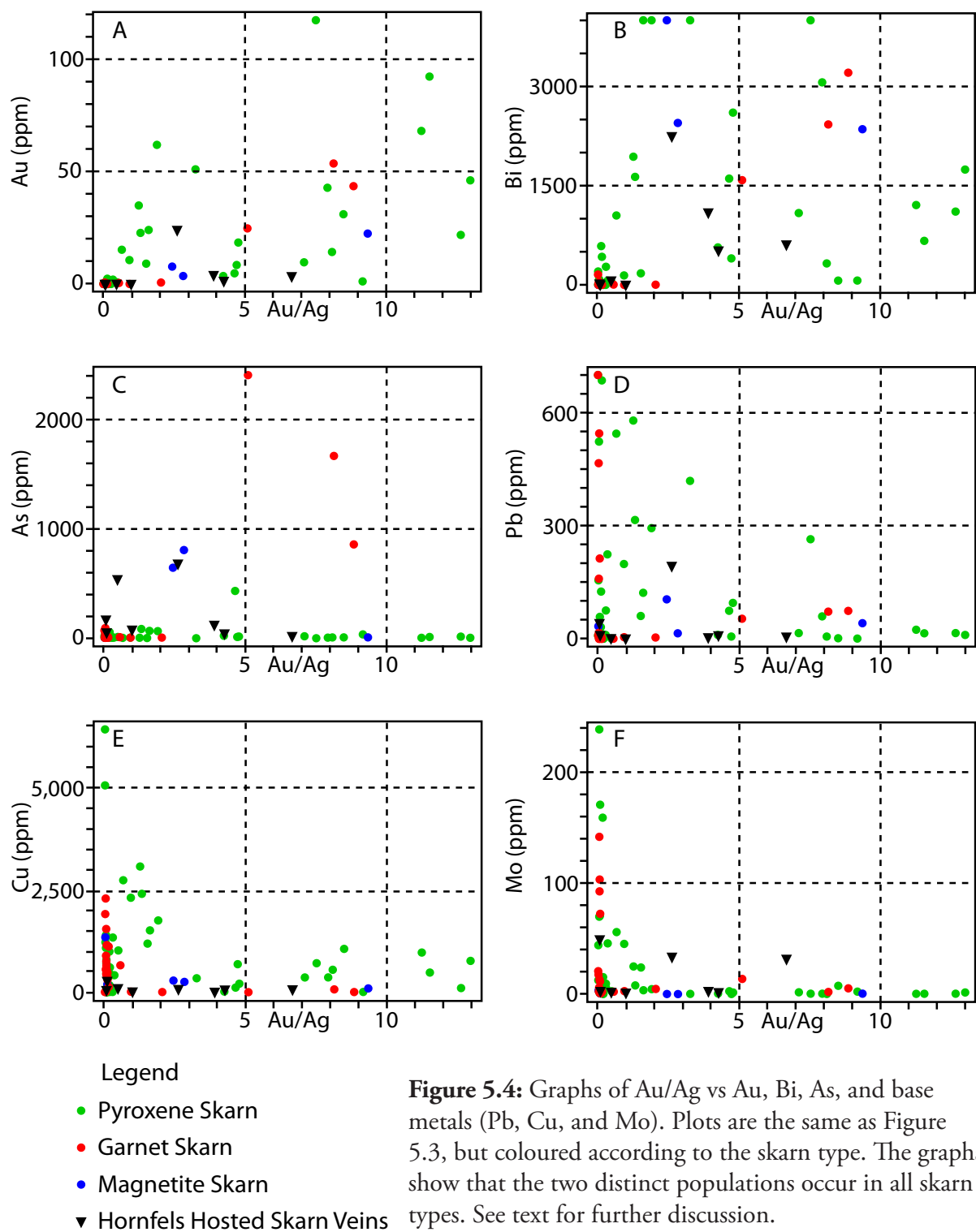
**Figure 5.4:** Graphs of Au/Ag vs Au, Bi, As, and base metals (Pb, Cu, and Mo). Plots are the same as Figure 5.3, but coloured according to the skarn type. The graphs show that the two distinct populations occur in all skarn types. See text for further discussion.

Legend

- Pyroxene Skarn
- Garnet Skarn
- Magnetite Skarn
- ▼ Hornfels Hosted Skarn Veins

## 5.5   High Field-Strength Elements as a Proxy for Protolith

Based on its position in the mine scale stratigraphy, skarn alteration at Buckhorn is presumed to replace both metavolcanic and carbonate metasedimentary rocks (Figure 2.2). However, in most locations due to the intensity of skarn alteration and its texturally destructive nature it is not possible to visually or petrographically determine the protolith of individual skarn samples. In order to geochemically determine the protolith of specific skarn samples the abundance of select high field-strength elements (HFSE) (Ti, Zr and total HREE (Gd-Lu)) were used as proxies for the protolith. These elements were chosen because they are typically immobile in hydrothermal systems (Bau, 1991; MacLean and Kranidiotis, 1987). Major elements were not useful for determining the protolith because during hydrothermal alteration they are typically mobile (Humphris and Thompson, 1978; Lentz and Gregoire, 1995).

Figure 5.5 shows a plot of Ti, Zr and total HREE vs depth for three skarn intercepts through the SWOZ; the ore body where the stratigraphy is best known. As seen in Figure 5.5 there is a noticeable decrease in these elements within the skarn alteration and gold mineralization. This decrease is most clearly seen in hole D08-413, but it is present in all three holes as marked by the different horizontal black lines. The metavolcanic rocks have higher abundances of these immobile elements than the carbonate rocks (Gaspar, 2005), so this drop is interpreted to mark the contact between the metavolcanic rocks and the underlying carbonate rocks. The proposed contact is different depending on which element is used as a proxy for protolith. In two of the three holes (D07-369 and D08-413) the proposed contacts are within 1.5 metres of each other, but in the remaining hole, D08-410, the differences between them is greater. The difference may be due to local mobility of the HFSE or local deviation from the expected volcanic rocks over carbonate rocks stratigraphy. The graphs also show local perturbations in the immobile element content, such as points A, B and C, which are interpreted as variations in the protolith lithology. The elevated immobile element content at points A and C is probably due to local siliciclastic-rich layers in the upper carbonate member of the BMS, whereas, the presence of Quartz Porphyry dike is clearly responsible for the locally high immobile element content at point B.

These graphs also demonstrate that, while the thickness of skarn alteration in the metavolcanic and the carbonate rocks is variable, the skarn alteration affects both rock types to a similar extent. Figure 5.5 also shows that protolith may partially control the type of skarn alteration that forms. In the samples analysed, garnet skarn solely forms from a metavolcanic protolith and magnetite skarn forms

predominately from a carbonate protolith. Pyroxene skarn is the most abundant variety analyzed and forms equally from both protoliths (Figure 5.5). The analysis also shows that both protoliths host gold mineralization to some degree, but that in two of the three drill holes the mineralized interval is almost entirely in the carbonate protolith (Figure 5.5).
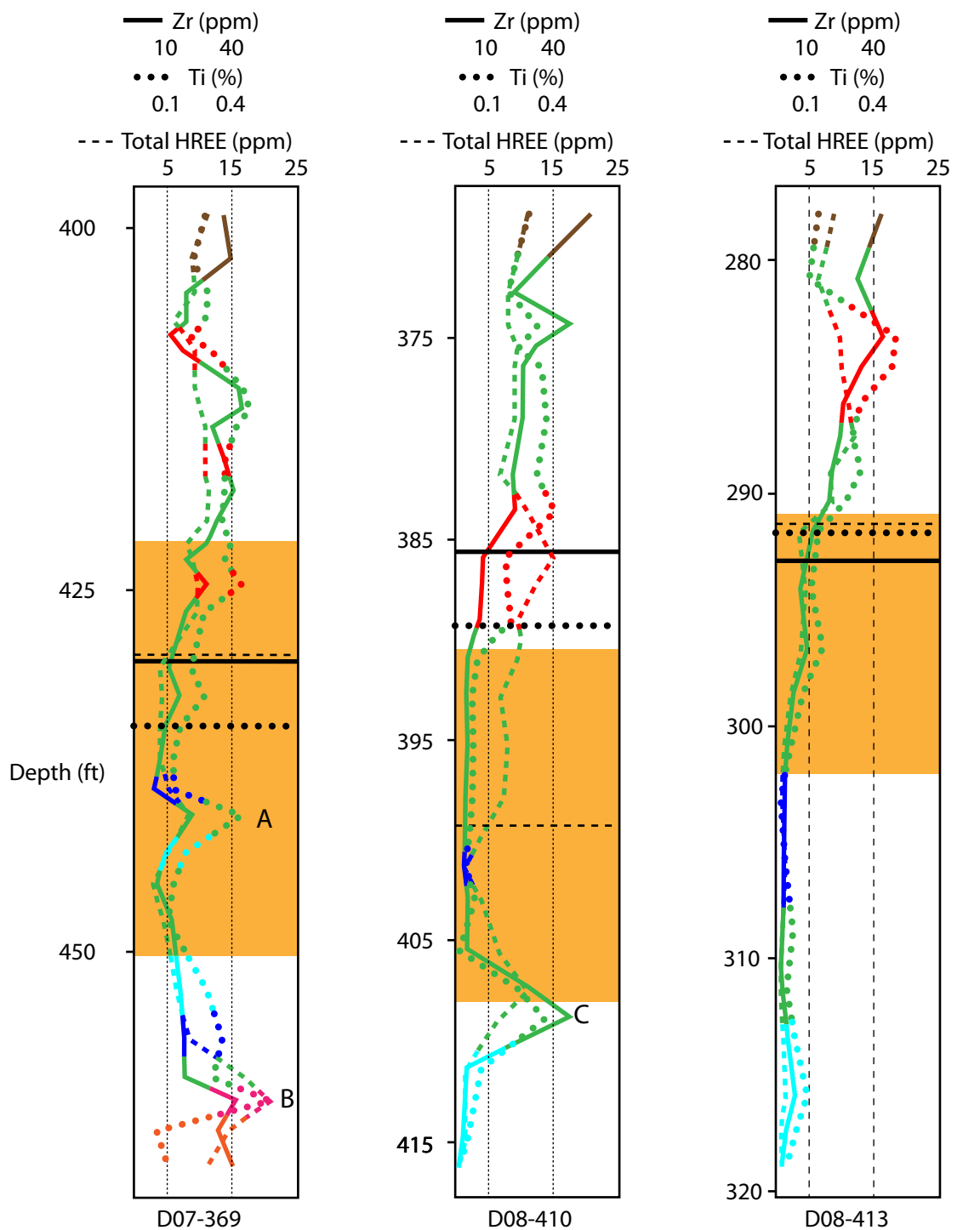
**Figure 5.5:** Immobile HFSE (Zr, Ti and total HREE content versus depth for three skarn intercepts through the SWOZ. The contact between the volcanic and carbonate rocks is picked based on a decrease in the immobile elements. Horizontal black lines mark the interpreted contacts between the BMV and the upper carbonate member of the BMS

## 5.6   Gold/Copper and Gold/Silver Ratios for Gold Bearing Skarns

In addition to determining the geochemical character of skarn alteration and gold mineralization at Buckhorn, the geochemical analysis was also used to compare Buckhorn to other skarn deposits around the world including other gold skarns (Table 5.3). To do this the Au (ppm)/Cu (%) and Au (ppm)/Ag (ppm) ratios were plotted against contained gold for numerous skarn deposits.

As Figure 5.6 shows there are notable differences between the types of skarns in terms of their Au/Cu ratio. Gold skarns typically have higher Au/Cu ratios, but not necessarily higher gold content compared to copper skarns and porphyry copper skarns. The graph also shows that it is difficult to distinguish skarn deposit types on the basis of Au/Cu ratios, as there is significant overlap between the iron skarns, lead-zinc skarns and copper skarns.

The Au/Cu ratios were also plotted in an attempt to distinguish reduced from oxidized gold skarns. Oxidised gold skarns characteristically have minor ubiquitous chalcopyrite mineralization, which is not typically a feature of reduced gold skarns (Meinert et al., 2005). The graph shows that gold skarns can have variable Au/Cu ratios that range from about 1 to 1000 Au (ppm)/Cu (%) and that there is no relationship between the Au/Cu ratio and the reduced-oxidised gold skarn distinction.

The Au/Ag ratio from the same set of gold skarns was also plotted against contained gold to try and geochemically distinguish reduced from oxidised gold skarns. Figure 5.7 shows that gold skarns may have a wide range of Au/Ag ratios, and that similar to the Au/Cu ratios, there is no relationship between the oxidised-reduced gold skarn distinction and the Au/Ag ratio. Figure 5.6 and Figure 5.7 also show that while there are significant differences between Buckhorn and the Nickel Plate gold skarn as described in Chapter 4, in terms of Au/Cu and Au/Ag ratios the deposits are similar.

**Table 5.3:** Summary of gold skarns compared based on the Au/Ag and Au/Cu ratios

| Name | Location | | Tonnage (t x 1000) | Gold (ppm) | Contained Gold (kg) | Accessory Metals | Au/Ag | Au/Cu (ppm/%) | Skarn Oxidation State | References |
|---|---|---|---|---|---|---|---|---|---|---|
| | Latitude | Longitude | | | | | | | | |
| Nambija, District, Ecuador | 4°3'54"S | 78°46'59"W | 8300-10400 | 15.0 | ~140,000 | Ag (~2.5ppm), Cu (0.01%) | 6.00 | 1500 | Oxidised | Markowski et al (2006), Fontbote et al (2004), Meinert (1998) |
| La Luz/Siuna, Nicaragua | 13°44'19"N | 84°47'06"W | 27700 | 3.4 | 94,762 | Ag(1.2ppm), Cu(0.44%) | 2.85 | 7.78 | Oxidised | Venable (1994), Theodore et al., (1991) |
| Fortitude, Nevada, USA | 40°32'54"N | 117°07'57"W | 10900 | 7.2 | 77,968 | Ag (28.2ppm), Cu (0.79%) | 0.24 | 9.05 | Reduced | Meinert (2000), Wotruba et al. (1986), Theodore et al. (1973) |
| Nickel Plate, BC, Canada | 49°21'55"N | 120°02'04"W | 13400 | 5.3 | 71,020 | Ag (1.74ppm), Cu (0.029%) | 3.04 | 183 | Reduced | Ray et al. (1993), Ettlinger et al. (1992) |
| El Valle - Boinas, Spain | 43°16'56"N | 6°18'19"W | 14200 | 4.3 | 61,202 | Ag(12.27ppm), Cu(0.41%) | 0.35 | 10.50 | Reduced | Cepedal et al. (2000), Martin-Izard et al. (2000a) |
| Red Dome, Australia | 17°07'00"S | 144°24'00"E | 15000 | 2.6 | 39,000 | Ag(5.25ppm), Cu(0.46%), Zn(1%) | 0.50 | 5.65 | Oxidised | Ewers and Sun(1989), Theodore et al., (1991) |
| Buckhorn, Washington, USA | 48°57' N | 118° 59' W | 2147.3 | 14.0 | 30,051 | Ag (3.42ppm), Cu (0.09%) | 4.09 | 156 | Reduced | Cooper et al. (2008), Gaspar (2005), This Study |
| Phoenix, BC, Canada | 49°05'36"N | 118°35'42"W | 26956 | 1.1 | 29,652 | Ag(7.1 ppm), Cu(0.9%) | 0.16 | 1.22 | Oxidised | Church (1986) |
| Beal, Montana, USA | 45°57'08"N | 112°52'56"W | 14800 | 1.5 | 23,100 | Ag (1.5ppm) | 1.00 | | Reduced | Meinert (2000), Wilkie (1996) |
| McCoy, Nevada, USA | 40°19'51"N | 117°13'34"W | 15600 | 1.4 | 22,464 | Ag(0.1ppm), Cu(0.1%) | 14.40 | 14.40 | Oxidised | Brooks (1994), Meinert (2000), Meinert (1989) |
| Bau, Malaysia | 1°24'07"N | 110°08'45"E | 2400 | 7.2 | 17,280 | Ag(0.1ppm) | 72.00 | | Reduced | Theodore et al., (1991), Meinert (1989), Bowles (1984) |

| Name | Location | | Tonnage (t x 1000) | Gold (ppm) | Con-tained Gold (kg) | Accessory Metals | Au/Ag | Au/Cu (ppm/%) | Skarn Oxidation State | References |
|---|---|---|---|---|---|---|---|---|---|---|
| | Latitude | Longitude | | | | | | | | |
| Nui Phao, Vietnam | 21°38'52"N | 105°39'55"E | 87900 | 0.2 | 16,701 | WO3(0.19%), CaF2(7.95%), Cu(0.18%), Bi(0.09%) | | 1.06 | Reduced | Richards et al (2003), Winter (2001) |
| Carles, Spain | 43°21'43"N | 6°14'45"W | 5300 | 3.0 | 15,900 | Ag(5.84 ppm), As(0.2-2.2%), Cu(0.42%) | 2.72 | 37.90 | Reduced | Martin-Izard et al (2000b), Meinert (2000) |
| Mt. Hamilton, Nevada, USA | 39°15'14"N | 115°33'27"W | 12617 | 1.0 | 12,164 | Ag(17.2ppm) | 0.06 | | Oxidised | Dennis et al., (1989), Theodore et al., (1991) |
| Minnie-Tomboy, Nevada, USA | 40°31'21"N | 117°07'23"W | 3900 | 2.8 | 10,920 | Ag(9ppm), Cu(0.3%) | 0.31 | 9.33 | Reduced | Blake et al., (1984), Meinert (1989) |
| QR, BC, Canada | 52°40'08"N | 121°47'11"W | 2372 | 4.6 | 10,800 | Ag(1.05ppm) | 4.34 | | Oxidised | Meredith-Jones, (2010) ( MINFILE No 093A 121) |
| Junction Reef, Australia | 33°37'28"S | 148°59'45"E | 2370 | 3.2 | 7,683 | Ag(0.5ppm), Cu(0.06%) | 0.65 | 54 | Reduced | Gray et al., (1995) |
| Nixon Fork, Alaska, USA | 63° 14' 18" N | 154° 45' 59"W | 167.618 | 39.4 | 6,608 | Ag(6.7ppm), Cu(0.6%) | 5.88 | 65.70 | Oxidised | Newberry et al., (1997), Bundtzen and Miller (1997) |
| Surprise, Nevada, USA | 40°37'05"N | 117°01'25"W | 1530 | 2.8 | 4,238 | Ag(23.1ppm), Cu(0.85%) | 0.12 | 3.26 | Oxidised | Theodore et al., (1991) |
| Marn, Yukon, Canada | 64° 29' 37" N | 138° 47' 38"W | 272.155 | 8.6 | 2,330 | Ag(17.12ppm), Cu(1%), W(0.1%) | 0.50 | 8.56 | Reduced | Brown and Nesbitt (1987) |
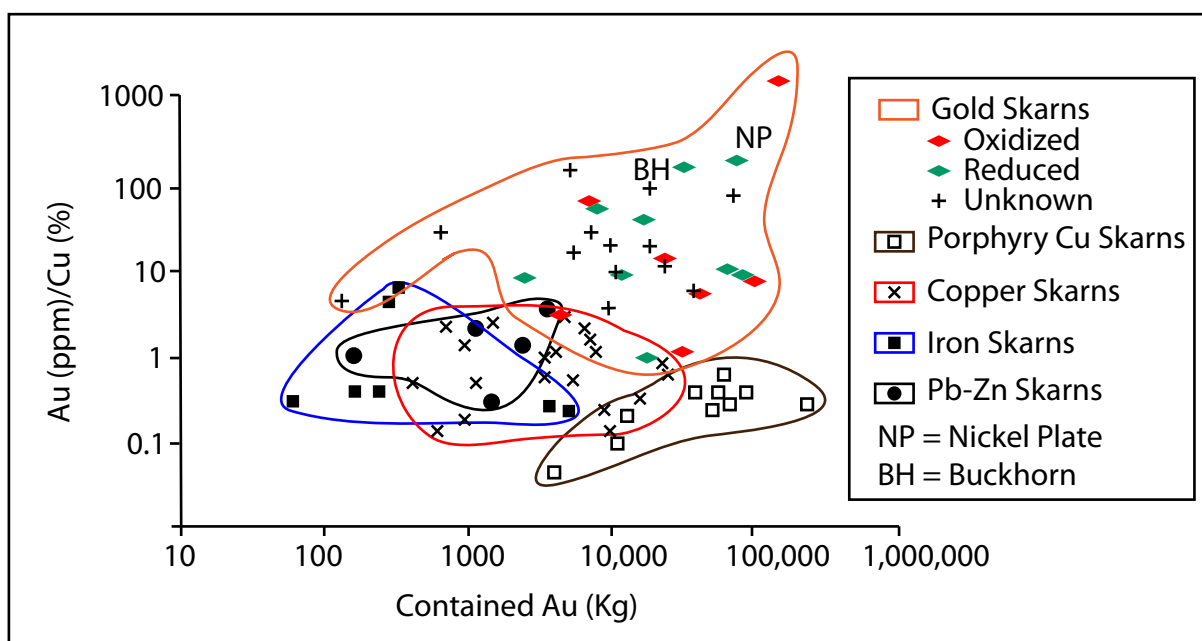
**Figure 5.6:** Plot of Au (ppm)/Cu (%) vs Contained Au (Kg) for a selection of gold, porphyry copper, copper, iron, and lead-zinc skarns. Coloured points from Table 5.3, remainder from Meinert (1989). See text for further discussion.
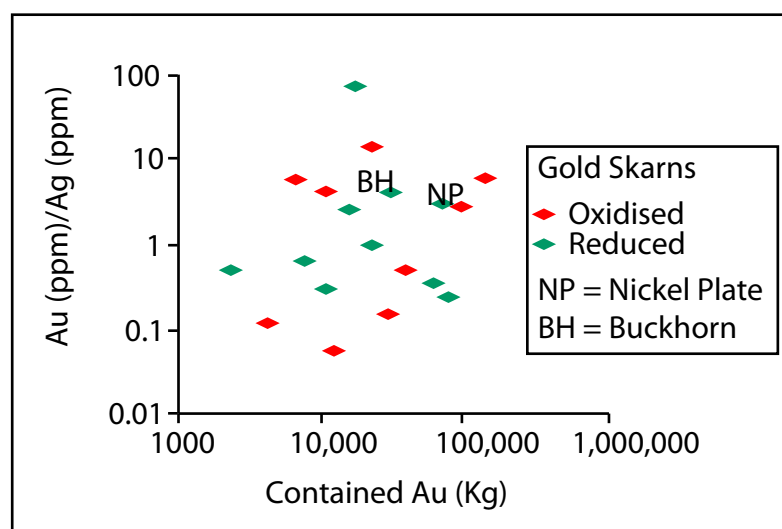


**Figure 5.7:** Plot of Au/Ag vs Contained Au (Kg) for a selection of gold skarns. See text for further discussion.

## 5.7 Discussion and Conclusions

Geochemical analysis of skarn alteration at Buckhorn supports many of the conclusions drawn from the detailed petrography. The correlation between gold and bismuth (r=0.92), which was demonstrated with both the correlation matrix and Au-Bi plot, matches with the petrography that described the intergrowth of gold and bismuth minerals (Chapter 4). The correlation between gold and

silver (r=0.56) fits with the presence of electrum detected in a previous microprobe study (Gaspar, 2005). The lack of a strong correlation between gold or bismuth and the major and trace elements fits with the petrographic analysis presented in Chapter 4, which showed that gold mineralization post-dates the majority of silicate skarn alteration. This implies that the host rock chemistry and therefore the mineralogy and the type of skarn alteration does not impact the location or grade of gold mineralization. Similarly, the lack of correlation between gold and the sulfide forming elements suggests that the sulfide mineralogy does not impact the location or grade of gold mineralization. This conclusion fits with the petrography, which demonstrated that the majority of sulfide alteration predates and is unrelated to gold mineralization (Chapter 4). Notable exceptions to this conclusion are the examples of gold-bearing chalcopyrite; however, these form a minor portion of the total sulfide alteration and therefore do not have a significant impact on the correlation between gold and copper.

The negative correlation between gold and aluminum suggests that aluminum poor protoliths are more prospective for gold mineralization, as aluminum is presumed to be less mobile during skarn alteration than the other major elements based on its correlation with the HFSE (Table 5.2); hence, the aluminum content of the skarn alteration reflects the aluminum content of the protolith. The negative correlation between gold and aluminum is also consistent with variation in amphibole chemistry presented in Chapter 4.

The relationships between gold and other elements described in this chapter confirm those previously documented at Buckhorn (Hickey, 1990, 1992) and are similar to those at other gold skarn deposits such as Nickel Plate (Ray et al., 1996) and Junction Reefs (Gray et al., 1995).

The geochemical analysis also matches the petrographic observation that gold and base metal mineralization at Buckhorn occurred in two distinct events. The base metal event is characterized by high base metal content and low Au/Ag ratios (<4). It may contain a minor amount of gold mineralization, as indicated by EDS elemental maps of gold bearing chalcopyrite (Figure 4.3). Base metal mineralization can be petrographically shown to be part of the retrograde alteration that predates the gold mineralization. The gold mineralizing event has low base metal contents and high Au/Ag ratios (>4). The bulk of gold mineralization at Buckhorn was deposited during this event, and the gold occurs solely in the fracture, intercrystalline and intergrowth settings outlined in Chapter 4. Petrography in Chapter 4 showed that both the base metal and gold mineralizing events occurred during retrograde skarn alteration, and that in some locations the gold mineralizing event overprint the base metal

event. However, the presence of base metal rich samples without gold shows that the two mineralizing events were not necessarily spatially coincident. Both mineralizing events occur in the SWOZ and Gold Bowl and are not dependent on the skarn mineralogy (Table 5.1 and Figure 5.4).

The geochemical analyses also lead to conclusions regarding the character of the host rocks and the skarn alteration categories. It showed that the host rocks have a different major and trace element signature from the skarn alterations, but there is significant overlap between the two and the host rocks cannot be distinguished from the skarn alteration on the basis of the major and trace elements. Similarly, the overlap in the geochemical signature of the three skarn alteration assemblages is too great to conclusively distinguish them. However they can be easily distinguished based on their mineralogy (Chapter 4).

Geochemical analysis of HFSE in the skarn alteration at Buckhorn was able to help determine the protolith of skarn alteration in the SWOZ, a task that is not possible petrographically. The protoliths are distinguished based on their place in the stratigraphy and HFSE content. The HFSE are immobile during skarn alteration and the BMV has notably higher HFSE content than the carbonate member of the BMS, hence, skarn alteration with a BMV protolith has higher HFSE. By determining the protolith this work was able to show that the carbonate member of the BMS host a higher proportion of the skarn alteration and gold mineralization than the other protoliths (Figure 5.5). Determining the protolith also showed that garnet skarn preferentially forms from a metavolcanic protolith and that magnetite skarn forms preferentially from a carbonate protolith

The multi-element geochemical analysis of skarn alteration also used to compare Buckhorn to other skarns. This comparison showed that there are differences between some skarn deposits types in terms of Au/Cu ratios, but that there is also significant overlap between other types of skarns. The analysis also showed that, although, the reduced and oxidized gold skarns have different sulfide assemblages there is no difference between them in terms of their Au/Cu or Au/Ag ratios.

# Chapter 6.   Summary

The Buckhorn gold skarn is hosted in Permian Anarchist Group metasedimentary rocks disconformably overlain by Jurassic Elise Formation metavolcanic rocks. The Anarchist Group was deposited in a back-arc setting and is locally comprised of a lower member of fine-grained siliciclastic rocks and a conformable upper member of carbonate rocks. The Jurassic Elise Formation metavolcanic rocks were deposited sub-aerially in a continental arc setting and are locally made up of basaltic flows and autobreccias. This stratigraphy is intruded by two suites of granitoids. The Middle Jurassic post-accretionary Buckhorn Intrusive Suite (BIS) is genetically related to the skarn alteration and gold mineralization and comprised of a granodiorite stock (170.4 ± 1.7 Ma), marginal diorite (168.9 ± 0.9 Ma), and several generations of dikes: mafic diorite dikes, Early Diorite dikes (168.2 ± 0.7 Ma), Granodiorite dikes (167.5 ± 0.7 Ma), and Quartz Porphyry dikes (163.6 ± 0.8 Ma). The Eocene Roosevelt Intrusive Suite (50.5 ± 2.9 Ma) is comprised of a small (~0.03 km$^2$) granodiorite stock that post-dates skarn alteration and gold mineralization.

Skarn alteration at Buckhorn is divided into three categories based on the prograde mineralogy: pyroxene skarn, garnet skarn, and magnetite skarn. Pyroxene skarn is further subdivided based on the retrograde mineralogy: amphibole-pyroxene skarn, magnetite-pyroxene skarn, and epidote-pyroxene skarn. The location of skarn alteration and gold mineralization at Buckhorn is spatially controlled by shear zones and Granodiorite dikes that acted as conduits for hydrothermal fluids. The skarn alteration is zoned from dominantly magnetite and garnet skarn in the proximal Magnetic Mine, to equal portions of magnetite, garnet, and pyroxene skarn in the Gold Bowl, and pyroxene skarn dominated in the distal Southwest Ore-Zone (SWOZ). The SWOZ contains the majority of the gold mineralization and consists of a 1-15 metre thick sub-horizontal layer of massive calcic, Fe-rich, reduced skarn alteration. The SWOZ occurs along a low-angle shear zone at the contact between the carbonate metasedimentary rocks and overlying metavolcanic rocks. Skarn alteration also occurs in millimetre scale veins that cut the skarn and hornfels alteration and are interpreted and the youngest and/or most distal expression of skarn alteration.

Based on the mineralogy the hydrothermal fluids that caused prograde alteration were between 430-500° C, $fO_2$=-25 to -20, $fS_2$=-8 to -4.5, and near neutral to slightly acidic pH. Fluids responsible for retrograde alteration were cooler (300-430° C), more reduced ($fO_2$<-26), and had lower sulfur fugacity ($fS_2$=-15 to -6) than fluids responsible for prograde alteration. The physicochemical conditions for prograde and retrograde alteration at Buckhorn are more oxidised and sulfur rich than those

proposed for skarn alteration at the Nickel Plate gold skarn in the nearby Hedley district (90 km to the north-west) (Ettlinger et al., 1992).

Gold mineralization at Buckhorn occurs in fractures in and intercrystalline space between prograde and retrograde minerals as well as intergrown with retrograde minerals. The gold mineralization is intimately associated and intergrown with bismuth. The intergrowth textures of gold-bismuth and gold-retrograde minerals suggest that gold was scavenged by a bismuth melt from a hydrothermal fluid (Tooth et al., 2011). Based on the conditions of retrograde alteration gold was transported as bisulfide complexes in the fluid. Bismuth scavenging preferentially occurs in reduced, acidic, and low sulfur conditions (Tooth et al., 2008); like those that occurred during retrograde alteration and gold mineralization at Buckhorn.

Before this study the mechanism for gold precipitation at Buckhorn was unknown. This work shows that gold precipitation was induced two physicochemical changes. The most prevalent was cooling that results in gold intergrown with bismuth and rimmed by bismuthinite (Tooth et al., 2011), a texture that is abundant in the intercrystalline and fracture hosted settings of gold mineralization. Gold precipitation caused by local retrograde oxidation reactions formed a lesser portion of the gold mineralization. This mechanism forms gold-bismuth mineralization that is intergrown with retrograde minerals (Tooth et al., 2011), the diagnostic texture of the intergrowth style of gold mineralization. The mechanism for gold precipitation in gold skarns has been disputed in the past (Meinert, 2000), but this research at Buckhorn suggests that it may be a combination of cooling and local retrograde oxidation reactions.

Re-Os geochronology of molybdenite bearing skarn constrains age of skarn alteration and gold mineralization at Buckhorn to a 4.7 million year window in the Middle Jurassic between 167.5 Ma and 162.8 Ma, and confirms its association with the BIS.

## 6.1  Exploration Implications

There are significant differences between Buckhorn and Nickel Plate, which has served as the de facto exploration model for gold skarns (Meinert et al., 2005), and an exploration program focused on finding reduced gold skarns should not discount rocks because they do not fit the Nickel Plate model. Some of the exploration implications that come out of the better understanding of Buckhorn and the variation within reduced gold skarns include:

- Prior to this study the age of skarn alteration and gold mineralization was unclear. However local mapping, U-Pb geochronology of the host and intrusive rocks, and Re-Os of molybdenite in skarn alteration showed that the skarn alteration and gold mineralization was genetically related to the post-accretionary Middle Jurassic BIS. This means that post-accretionary plutons are also prospective for the development of gold skarns, and not only syn-accretionary plutons, such as those responsible for gold skarn formation at Nickel Plate.

- Skarn alteration with carbonate metasedimentary protolith should be targeted because at Buckhorn skarn alteration with a such a protolith hosts proportions more gold mineralization than skarn from other protoliths. This contrasts other gold skarns where mineralization is predominately hosted in siliciclastic and volcaniclastic protoliths (Meinert, 2000). This study showed that the content of certain immobile HFSE can be used to distinguish the protoliths of skarn alteration.

- Syn-mineralization shear zones and dikes acted as fluid conduits and controlled the location of skarn alteration and gold mineralization at Buckhorn, and should therefore be targets for exploration. The orientation of some of the dikes at Buckhorn may have been influenced by syn-sedimentary faults in the metasedimentary host rocks. Therefore, when exploring for reduced gold skarns the orientation of any structures should be determined because the orientation of skarn alteration can be controlled by both pre- and syn-mineralization features.

- Scapolite and arsenopyrite are vectors for gold mineralization at Nickel Plate, but they are not necessarily indicative of gold mineralization in all reduced skarns, as scapolite is not present and arsenopyrite is rare and neither is associated with gold mineralization at Buckhorn.

- Magnetite and chalcopyrite are nearly absent from Nickel Plate, but can be present in significant amounts in other reduced gold skarns such as at Buckhorn. Therefore their presences should not be used to reject an exploration target.

- At Buckhorn gold precipitated at the end of retrograde alteration, and was induced by cooling and local retrograde oxidation reactions. This change in physical conditions is expressed as a decrease in aluminum and iron content in amphibole, the development of epidote, pyrite, and hydrated Fe-silicate minerals. The latter mineralogical changes can be detected during core logging and indicate that the physicochemical conditions for gold precipitation occurred.

- Millimetre to centimetre scale skarn veins are the youngest and/or most distal expression of skarn alteration at Buckhorn. Their identification in otherwise non skarn-altered rocks suggests that an area is prospective for gold skarn mineralization.

- Economic gold skarns can occur within the same skarn system as uneconomic skarn alteration (ie. The SWOZ vs. The Magnetic Mine). It is therefore important to understand the characteristics of gold skarn alteration and properly characterize any known uneconomic skarn alteration to determine if it is part of a larger gold skarn system. This could be done using the following tools:

  ○ Property scale mapping and thin section petrography could be done to determine the character and distribution the skarn alteration assemblages, host rocks, and local intrusions. At Buckhorn such mapping would show that the most distal exposed skarn alteration is made up of roughly equal portions of garnet and pyroxene (ie. The Gold Bowl), which suggests that a more distal and more prospective pyroxene dominated zone may exist (ie. The SWOZ).

  ○ Whole rock multi-element geochemical analysis could characterize the mineralization and determine which elements correlate with gold. Based on the work at Buckhorn and other deposits reduced gold skarns are characterized by a gold - bismuth ± tellurium ± arsenic ± cobalt signature and have a high (>1) Au (ppm)/Cu (%) ratio.

  ○ Several techniques could be used to determine the composition of the skarn minerals, with iron and calcium rich pyroxene, garnet and amphibole alteration being indicative of reduced gold skarns. Microprobe analysis could be used, but it is likely prohibitively costly and time consuming for mineral exploration. Elemental analysis by EDS is more cost effective, but less precise that microprobe analysis, but it would still provide sufficient information for mineral exploration. X-Ray diffraction could also be used and in some cases the optical properties of the minerals may also be useful for distinguishing the mineral species.

## 6.2 Future Research

During the course of this study several questions arose that have been left unanswered, but would be worthwhile investigating with future research.

The spatial relationship of the different settings of gold mineralization is currently unknown, and it is unknown if their distribution is impacted by larger structures and/or other features. Determining the distribution of the different settings of gold mineralization could help identify fluid pathways and/or other controls on mineralization. This could potentially be used to fine tune the milling process to account for the different types of gold mineralization and improve the efficiency of gold recovery.

The age of the mafic diorite is yet to be determined, it cross-cuts the Buckhorn Granodiorite and is therefore younger than 170.4 Ma (Figure 3.10), but its age has not been further constrained because it was not found in contact with any other intrusions and did not contain any zircons for U-Pb geochronology. Ar-Ar geochronology could be used to further constrain the age of the mafic diorite, which would help describe the genesis of the BIS.

The current constraints on the age of skarn alteration and gold mineralization suggest that it took place over an extended period of time, between 167.5 and 162.8 Ma. Dating the prograde garnet by Lu-Hf geochronology and retrograde amphibole by Ar-Ar geochronology could possibly further constrain the age of skarn alteration and gold mineralization. This could lead to a better understanding of timing and duration of the skarn alteration system at Buckhorn, and help develop a better deposit model for reduced gold skarns.

# Chapter 7.   Conclusions

Work in the six preceding chapters leads to conclusions regarding the Buckhorn host rocks, skarn alteration, gold mineralization, and the classification as a reduced gold skarn.

## 7.1   Host Rocks

- The metasedimentary host rocks are correlated with the Permian Anarchist Group and are equivalent to other rocks in the southern Canadian cordillera including the Harper Ranch Group, Attwood Group, and the Mount Roberts Formation. This correlation is based on the lithological similarities and the Permian fossil ages previously determined.

- The metavolcanic host rocks unconformably overly the metasedimentary host rocks and are correlated with the Jurassic Elise formation of the Nelson-Rossland area. The Elise formation is age equivalent to other early Mesozoic arc related volcanic rocks in the southern Canadian cordillera including the Nicola Group in the Hedley area and the Brooklyn Formation in the Greenwood area. The correlation of the metavolcanic rocks at Buckhorn with the Jurassic Elise formation is based on the similarity in lithologies and the Early Jurassic (192.4 ± 1.0 Ma) age determined for a monzodiorite dike comagmatic with the metavolcanic sequence.

- The Buckhorn Intrusive Suite (BIS) is correlated with a number of age equivalent intrusive suites including the Cahill Creek Pluton (168.9 ±9 Ma) in the Hedley district; The Nelson (167 Ma), Trail (169±3 Ma) and Bonnington (167 Ma) Plutons and the Rossland Monzonite (167.5±0.5 Ma) in the Nelson-Rossland area. The BIS is also shown to be more complex than previously known:

  - Different generations of granodiorite that are texturally and mineralogically similar are distinguished on the basis of age (BS048 170.4 ± 1.1 Ma, BS074 167.8 ± 1.5 Ma, BS057 166.0 ± 1.0 Ma).

  - The Buckhorn Diorite (BS060 169.0 ± 0.9 Ma) is now shown to be a marginal phase of the Buckhorn Granodiorite based on the gradational contact between the two and the similarity in age.

- The Early Diorite dikes (BS075 169.4 ± 1.3 Ma, BS046 168.2 ± 0.7 Ma) are now distinguished from the Buckhorn Diorite on the basis of texture, but were shown to be the same age.

- The Granodiorite dikes are shown to host both the two low angle and steeply dipping foliations, this means that the foliations occurred after the emplacement of the dikes in the Middle Jurassic (BS059 167.4 ± 0.8). This contrasts earlier work that proposed that only the steeply dipping foliation post-dated the igneous rocks and affected the skarn alteration.

- The Early Eocene age and complex melting and emplacement history of the Roosevelt Granodiorite is confirmed on the basis of the diverse inherited zircon population discovered in the geochronological sample.

## 7.2  Skarn Alteration

- Skarn alteration is associated with the low angle shear zones and Granodiorite dikes, both of which acted as fluid pathways and control the location and intensity of skarn alteration.

- Skarn alteration overprints metavolcanic, carbonate, and to a minor extent clastic meta-sedimentary rocks. The first two host approximately equal portions of skarn alteration and gold mineralization. The protolith of skarn alteration was determined by using the HFSE content as a proxy for the protolith. This analysis also shows that garnet skarn is more prevalent in a metavolcanic protolith, magnetite in a carbonate protolith, whereas pyroxene skarn forms in all protoliths.

- Skarn alteration at Buckhorn is now split into three major alteration assemblages based on the prograde mineralogy: pyroxene skarn, garnet skarn, and magnetite skarn. Pyroxene skarn is further subdivided based on the specific prograde and retrograde alteration assemblage: amphibole-pyroxene skarn, magnetite-pyroxene skarn, and epidote-pyroxene skarn.

- The skarn alteration is zoned from garnet and magnetite dominated in the Magnetic Mine to pyroxene dominated in the SWOZ. This zonation suggests that skarn forming fluids were sourced from the Buckhorn Granodiorite and Buckhorn Diorite near the Magnetic Mine and travelled to the south forming the Magnetic Mine, the Gold Bowl and ultimately the SWOZ, cooling and become more reduced along the way.

166

- A similar zonation can be seen from east to west in the SWOZ, implying that the fluids that caused skarn alteration on the east side of the SWOZ were more oxidised that expected based on the larger scale zonation. This secondary zonation is likely due to the presences of the Footwall Mylonite that channelled skarn forming fluids and allowed them to travel a greater distance with less interaction with the host rocks.

- The physicochemical conditions of prograde and retrograde skarn alteration are constrained based on the mineralogy. Prograde alteration occurred between 430-500° C, $fO_2$=-25 to -20, $fS_2$=-8 to -4.5, and near neutral to slightly acidic pH. Retrograde alteration occurred at cooler (300-430° C), more reduced ($fO_2$<-26), and lower sulfur fugacity ($fS_2$=-15 to -6) conditions than prograde alteration.

- In addition to forming at the metre scale, skarn alteration is also documented to form in veins at the centimetre scale. Based on the cross-cutting relationships the skarn veins are the youngest and/or most distal stage of skarn alteration and gold mineralization at Buckhorn.

- Much of the skarn alteration is affected by deformation that manifests as brittle fractures in the prograde minerals and as low angle foliations in the retrograde minerals. Based on the similarities in appearance and the comparable age constraints, the deformation in the skarn is equivalent foliations in the host rocks.

## 7.3   Gold Mineralization

- Gold mineralization occurs in five distinct settings at the Buckhorn gold skarn: (1) in intercrystalline space between prograde and retrograde minerals, (2) in fractures in prograde minerals, (3) intergrown with retrograde minerals, (4) in skarn veins through skarn and non skarn-altered rocks, and (5) in chalcopyrite mineralization.

- Gold hosted in chalcopyrite formed first, followed by the fracture and intercrystalline gold, then the gold intergrown with retrograde minerals, and finally the skarn vein hosted gold. More than one setting of gold mineralization may occur in a single sample.

- In all settings gold mineralization is accompanied by bismuth mineralization in the form of native bismuth, bismuthinite, and other bismuth minerals.

- Gold mineralization is part of retrograde alteration and postdates the majority of the calc-silicate skarn alteration, and all of the foliations.

- Gold has a positive correlation with bismuth (r=0.92) and silver (r=0.56), and negative correlation with aluminum (r=-0.50), but has no significant correlation with any other major, trace or rare earth elements. The lack of correlation matches with the petrography and geochemical analysis that shows that gold mineralization is spatially, texturally, and geochemically distinct from the prograde and base metal sulfide alteration.

- Gold mineralization is spatially associated with more magnesium rich and aluminum poor amphiboles, which suggests that they formed under cooler and/or more oxidised conditions, both of which occurred towards the end of retrograde alteration at Buckhorn.

- Gold was transported as bisulfide complexes in the hydrothermal fluid between 241-300°C, $fO_2$=-42 to -36, and pH=6 to 8, before being scavenged by a bismuth melt. Precipitation of the gold-bismuth melt was induced by cooling and retrograde oxidation reactions. Precipitation caused by cooling is responsible for the fracture and intercrystalline hosted gold. Gold intergrown with retrograde minerals resulted from gold precipitation caused by that retrograde reaction.

- The maximum age of gold mineralization is constrained by the Granodiorite dikes to 167.5 ± 0.8 Ma and the minimum age is constrained by the molybdenite that postdates the retrograde alteration at 162.8 ± 0.7 Ma.

## 7.4 Comparison to Other Gold Skarns

- Buckhorn is classified as a reduced gold skarn based on the skarn mineralogy (pyroxene > garnet + magnetite, pyrrhotite > pyrite + chalcopyrite), mineral compositions (pyroxene = hedenbergite-augite, amphibole = ferrohornblende-ferroactinolite), and gold mineralization elemental assemblage (gold-bismuth).

- Other characteristics of the skarn alteration at Buckhorn are similar to so-called oxidised gold skarns (high magnetite content, minor pervasive chalcopyrite), suggesting that there is there is a continuum between reduced and oxidised gold skarns

- The oxygen and sulfur fugacity conditions for prograde and retrograde skarn alteration at Buckhorn also show that it formed at more oxidised conditions than Nickel Plate, and is further evidence that there may be a continuum between reduced and oxidised gold skarns.

- When compared to the Nickel Plate deposit, one of the largest and best studied reduced gold skarns, there are significant differences between the two deposits.

  - Buckhorn does not contain scapolite, which is spatially and temporally associated with gold mineralization at Nickel Plate where it indicates that gold was transported as chloride complexes. The lack of scapolite at Buckhorn and the physicochemical conditions determined suggest that while chloride complexes may be important for gold mineralization in some skarn systems they are not necessary to produce an economic deposit.

  - At Buckhorn the majority of gold mineralization postdates the iron-sulfide (Po>Py) alteration, whereas at Nickel Plate gold occurs as inclusions in arsenopyrite and predates the iron-sulfide (Po>Py) alteration.

# References

Barton, P. B., Jr., and Skinner, B. J., 1979, Sulfide mineral stabilities: Geochemistry of hydrothermal ore deposits, 1979, p. 278-403.

Bau, M., 1991, Rare-earth element mobility during hydrothermal and metamorphic fluid-rock interaction and the significance of the oxidation state of europium: Chemical Geology, v. 93, p. 219-230.

Beatty, T. W., 2003, Stratigraphy of the Harper Ranch Group and tectonic history of the Quesnal Terrane in the area of Kamloops, British Columbia, Simon Fraser University, 168 p.

Billingsley, P. R., and Hume, C. B., 1941, The Ore Deposits of Nickel Plate Mountain, Hedley, British Columbia, Canadian Institute of Mining and Metallurgy, Montreal, QC, Canada.

Blake, D. W., Wotruba, P. R., and Theodore, T. G., 1984, Zonation in the skarn environment at the Minnie-Tomboy gold deposits, Lander County, Nevada; Gold and silver deposits of the Basin and Range Province, Western U.S.A: Arizona Geological Society Digest, v. 15, p. 67-72.

Blundy, J. D., and Holland, T. J. B., 1990, Calcic amphibole equilibria and a new amphibole-plagioclase geothermometer: Contributions to Mineralogy and Petrology, v. 104, p. 208-224.

Bowles, J. F. W., 1984, The distinctive low-silver gold of Indonesia and East Malaysia; Gold '82; the geology, geochemistry and genesis of gold deposits: Gold '82; the geology, geochemistry and genesis of gold deposits, Harare, Netherlands (NLD), 1984, 1984.

Bowman, J. R., 1998, Basic aspects and applications of phase equilibria in the analysis of metasomatic Ca-Mg-Al-Fe-Si skarns: Short Course Handbook, v. 26, p. 1-49.

Brooks, J. W., 1994, Petrology and geochemistry of the McCoy gold skarn, Lander County, Nevada, Washington State University, Pullman, WA, United States (USA).

Broughton, W. A., 1943, Buckhorn iron deposits of Okanogan County, Washington: Washington State Department of Conservation and Development -- Division of Geology -- Report Investigations, p. 21.

Brown, I. J., and Nesbitt, B. E., 1987, Gold-copper-bismuth mineralization in hedenbergitic skarn, Tombstone Mountains, Yukon: Canadian Journal of Earth Sciences = Revue Canadienne des Sciences de la Terre, v. 24, p. 2362-2372.

Bundtzen, T. K., and Miller, M. L., 1997, Precious metals associated with Late Cretaceous-early Tertiary igneous rocks of Southwestern Alaska; Mineral deposits of Alaska: Economic Geology Monographs, v. 9, p. 242-286.

Campbell, I. H., Ballard, J. R., Palin, J. M., Allen, C., and Faunes, A., 2006, U-Pb Zircon Geochronology of Granitic Rocks from the Chuquicamata-El Abra Porphyry Copper Belt of Northern Chile: Excimer Laser Ablation ICP-MS Analysis: Economic Geology, v. 101, p. 1327-1344.

Carr, S. D., 1992, Tectonic setting and U-Pb geochronology of the Early Tertiary Ladybird Leucogranite Suite, Thor-Odin - Pinnacles Area, Southern Omineca Belt, British Columbia: Tectonics, v. 11, p. 258-278.

Cepedal, A., Fuertes-Fuente, M., Martín-Izard, A., González-Nistal, S., and Rodríguez-Pevida, L., 2006, Tellurides, selenides and Bi-mineral assemblages from the Río Narcea Gold Belt, Asturias, Spain: genetic implications in Cu–Au and Au skarns: Mineralogy and Petrology, v. 87, p. 277-304.

Cepedal, A., Martin-Izard, A., Reguilon, R., Rodriguez-Pevida, L., Spiering, E. D., and Gonzalez-Nistal, S., 2000, Origin and evolution of the calcic and magnesian skarns hosting the El Valle-Boinas copper-gold deposit, Asturias (Spain); Gold exploration in NW Iberian Peninsula: Gold exploration and mining in NW Spain, Asturias, Spain, Sept. 1998, v. 71, p. 119-151.

Cheney, E. S., Rasmussen, M. G., and Miller, M. G., 1994, Major Faults, Stratigraphy, and Identity of Quesnellia in Washington and Adjacent British Columbia, in Resources, W. S. D. O. N., ed., 80: Olympia, WA, Washington Division Of Geology and Earth Resources, p. 49-71.

Cherniak, D. J., and Watson, E. B., 2001, Pb diffusion in zircon: Chemical Geology, v. 172, p. 5-24.

Church, B. N., 1986, Geological Setting And Mineralization In The Mount Attwood-Phoenix Area Of The Greenwood Mining Camp, in Division, G. S. B. M. R., ed., 1986: Victoria, Ministry of Energy, Mines and Petroleum Resources, p. 65.

Ciobanu, C. L., and Cook, N. J., 2004, Skarn textures and a case study: the Ocna de Fier-Dognecea orefield, Banat, Romania: Metamorphic processes in ore formation and transformation: A thematic series of papers, v. 24, p. 315-370.

Ciobanu, C. L., Cook, N. J., and Pring, A., 2005, Bismuth tellurides as gold scavengers, in Mao, J., and Bierlein, F. P., eds., Mineral Deposit Research: Meeting the Global Challenge, Springer Berlin Heidelberg, p. 1383-1386.

Colpron, M., Nelson, J. A. L., and Murphy, D. C., 2007, Northern Cordilleran terranes and their interactions through time: GSA Today, v. 17, p. 4-10.

Colpron, M., and Nelson, J. L., 2011, A Digital Atlas of Terranes for the Northern Cordillera, BCGS GeoFile 2011-11, British Columbia Ministry of Energy and Mines.

Cooper, P., Roberts, L., Jimmerson, S., Eppers, K., and Darton, B., 2008, 2007 Mineral Resource and Reserve Report for the Kettle River Operations Buckhorn Mine: Republic, WA, Kinross Gold Corporation, p. 161.

Corfu, F., Hanchar, J. M., Hoskin, P. W. O., and Kinny, P. D., 2003, Atlas of zircon textures: Reviews in Mineralogy and Geochemistry, v. 53, p. 469-500.

Creaser, R. A., Papanastassiou, D. A., and Wasserburg, G. J., 1991, Negative thermal ion mass spectrometry of osmium, rhenium, and iridium: Geochimica et Cosmochimica Acta, v. 55, p. 397-401.

Dennis, M. D., Myers, G., Wilkinson, W. H., and Wendt, C. J., 1989, Precious metal mineralization at Mt. Hamilton, White Pine County, Nevada: Mining Engineering, v. 41, p. 1029-1031.

Dostal, J., Church, B. N., and Hoy, T., 2001, Geological and geochemical evidence for variable magmatism and tectonics in the southern Canadian Cordillera: Paleozoic to Jurassic suites, Greenwood, southern British Columbia: Canadian Journal of Earth Sciences, v. 38, p. 75-90.

Driver, L. A., Creaser, R. A., Chacko, T., and Erdmer, P., 2000, Petrogenesis of the Cretaceous Cassiar batholith, Yukon-British Columbia, Canada: Implications for magmatism in the North American Cordilleran Interior: Geological Society of America Bulletin, v. 112, p. 1119-1133.

Einaudi, M. T., 1977, Petrogenesis of the copper-bearing skarn at the Mason Valley Mine, Yerington District, Nevada: Economic Geology, v. 72, p. 769-795.

Einaudi, M. T., Meinert, L. D., and Newberry, R. J., 1981, Skarn deposits: Economic geology; Seventy-fifth anniversary volume; 1905-1980, 1981, p. 317-391.

Ettlinger, A. D., Meinert, L. D., and Ray, G. E., 1992, Gold skarn mineralization and fluid evolution in the Nickel Plate Deposit, British Columbia: Economic Geology and the Bulletin of the Society of Economic Geologists, v. 87, p. 1541-1565.

Ewers, G. R., and Sun, S. S., 1989, Genesis of the Red Dome gold skarn deposit, Northeast Queensland; The geology of gold deposits; the perspective in 1988: Economic Geology Monographs, v. 6, p. 218-232.

Fontbote, L., Vallance, J., Markowski, A., and Chiaradia, M., 2004, Oxidized gold skarns in the Nambija district, Ecuador; Andean metallogeny; new discoveries, concepts, and updates: Special Publication (Society of Economic Geologists (U.S.)), v. 11, p. 341-357.

Fyles, J. T., 1990, Geology of the Greenwood-Grand Forks area, British Columbia; NTS 82E/1,2, British Columbia Ministry of Energy, Mines and Petroleum Resources, Vancouver, BC, Canada, 19 p.

Gabrielse, H., 1991, Structural styles, in Gabrielse, H., and Yorath, C. J., eds., Geology of the Cordilleran Orogen in Canada, 4, Geological Survery of Canada, p. 571-675.

Gaspar, L. M., 2005, The Crown Jewel gold skarn deposit, Washington State University, Pullman, WA, United States (USA).

Gaspar, M., Knaack, C., Meinert, L. D., and Moretti, R., 2008, REE in skarn systems; a LA-ICP-MS study of garnets from the Crown Jewel gold deposit: Geochimica et Cosmochimica Acta, v. 72, p. 185-205.

Gemmell, J. B., Zantop, H., and Meinert, L. D., 1992, Genesis of the Aguilar zinc-lead-silver deposit, Argentina; contact metasomatic vs. sedimentary exhalative: Economic Geology, v. 87, p. 2085-2112.

Ghosh, D. K., 1995, Nd–Sr isotopic constraints on the interactions of the Intermontane Superterrane with the western edge of North America in the southern Canadian Cordillera: Canadian Journal of Earth Sciences, v. 32, p. 1740-1758.

Gray, N., Mandyczewsky, A., and Hine, R., 1995, Geology of the zoned gold skarn system at Junction Reefs, New South Wales; A special issue on the metallogeny of the Tasman fold belt system of eastern Australia: Economic Geology and the Bulletin of the Society of Economic Geologists, v. 90, p. 1533-1552.

Griffin, W. L., Powell, W. J., Pearson, N. J., and O'Reilly, S. Y., 2008, Appendix A2; GLITTER; data reduction software for laser ablation ICP-MS: Short Course Series - Mineralogical Association of Canada, v. 40, p. 308-311.

Hickey, R. J., III, 1990, The geology of the Buckhorn Mountain gold skarn, Okanogan County, Washington, Washington State University, 171 p.

Hickey, R. J., III, 1992, The Buckhorn Mountain (Crown Jewel) gold skarn deposit, Okanogan County, Washington: Economic Geology and the Bulletin of the Society of Economic Geologists, v. 87, p. 125-141.

Holder, G. A. M., 1989, Geochemical character and correlation of contemporaneous volcanic, plutonic and hypabyssal igneous activity associated with Eocene regional extension, Northeast Washington, 169 p.

Holder, R. W., and McCarley Holder, G. A., 1988, The Colville batholith: Tertiary plutonism in northeast Washington associated with graben and core-complex (gneiss dome) formation: Geological Society of America Bulletin, v. 100, p. 1971-1980.

Holland, T., and Blundy, J., 1994, Non-ideal interactions in calcic amphiboles and their bearing on amphibole-plagioclase thermometry: Contributions to Mineralogy and Petrology, v. 116, p. 433-447.

Hoy, T., and Dunne, K. P. E., 1997, Early Jurassic Rossland Group Southern British Columbia: Part I - Stratigraphy and Tectonics, British Columbia Geological Survey Bulletin, 102, Geological Survey Branch, p. 124.

Hoy, T., and Dunne, K. P. E., 2001, Metallogeny and mineral deposits of the Nelson-Rossland map-area; Part II, The Early Jurassic Rossland Group, southeastern British Columbia, British Columbia Ministry of Energy and Mines, Energy and Minerals Division, Geological Survey Branch, Mineral Resources Division, Victoria, BC, Canada, 195 p.

Humphris, S. E., and Thompson, G., 1978, Trace element mobility during hydrothermal alteration of oceanic basalts: Geochimica et Cosmochimica Acta, v. 42, p. 127-136.

Hurlow, H. A., and Nelson, B. K., 1993, U-Pb zircon and monazite ages for the Okanogan Range batholith, Washington: Implications for the magmatic and tectonic evolution of the southern Canadian and northern United States Cordillera: Geological Society of America Bulletin, v. 105, p. 231-240.

Irving, E., and Thorkelson, D. J., 1990, On Determining Paleohorizontal and Latitudinal Shifts: Paleomagnetism of Spences Bridge Group, British Columbia: J. Geophys. Res., v. 95, p. 19213-19234.

Jones, D. M., 1992, Preliminary geology and exploration potential of the Crown Jewel project, Okanogan County, Washington: Tucson, Arizona, Battle Mountain Exploration Company, p. 26.

Kosler, J., and Sylvester, P. J., 2003, Present Trends and the Future of Zircon in Geochronology: Laser Ablation ICPMS: Reviews in Mineralogy and Geochemistry, v. 53, p. 243-275.

Kruckenberg, S. C., Whitney, D. L., Teyssier, C., Fanning, C. M., and Dunlap, W. J., 2008, Paleocene-Eocene migmatite crystallization, extension, and exhumation in the hinterland of the northern Cordillera: Okanogan dome, Washington, USA: Geological Society of America Bulletin, v. 120, p. 912-929.

Lawley, C. J. M., Richards, J. P., Anderson, R. G., Creaser, R. A., and Heaman, L. M., 2010, Geochronology and Geochemistry of the MAX Porphyry Mo Deposit and its Relationship to Pb-Zn-Ag Mineralization, Kootenay Arc, Southeastern British Columbia, Canada: Economic Geology, v. 105, p. 1113-1142.

Leake, B. E., Woolley, A. R., Arps, C. E. S., Birch, W. D., Gilbert, M. C., Grice, J. D., Hawthorne, F. C., Kato, A., Kisch, H. J., Krivovichev, V. G., Linthout, K., Laird, J., Mandarino, J. A., Maresch, W. V., Nickel, E. H., Rock, N. M. S., Schumacher, J. C., Smith, D. C., Stephenson, N. C. N., Ungaretti, L., Whittaker, E. J. W., and Guo Youzhi, 1997, Nomenclature of amphiboles; report of the subcommittee on amphiboles of the International Mineralogical Association, Commission on New Minerals and Mineral Names: Can Mineral, v. 35, p. 219-246.

Lentz, D. R., and Gregoire, C., 1995, Petrology and mass-balance constraints on major-, trace-, and rare-earth-element mobility in porphyry-greisen alteration associated with the epizonal True Hill granite, southwestern New Brunswick, Canada: Journal of Geochemical Exploration, v. 52, p. 303-331.

Ludwig, K. R., 2009, Isoplot 4.13.11.01.02: Berkeley, Berkeley Geocrhonology Center, p. A Geochronological Toolkit for Microsoft Excel.

MacLean, W. H., and Kranidiotis, P., 1987, Immobile elements as monitors of mass transfer in hydrothermal alteration; Phelps Dodge massive sulfide deposit, Matagami, Quebec: Economic Geology, v. 82, p. 951-962.

Markey, R., Stein, H. J., Hannah, J. L., Zimmerman, A., Selby, D., and Creaser, R. A., 2007, Standardizing Re–Os geochronology: A new molybdenite Reference Material (Henderson, USA) and the stoichiometry of Os salts: Chemical Geology, v. 244, p. 74-87.

Markowski, A., Vallance, J., Chiaradia, M., and Fontbote, L., 2006, Mineral zoning and gold occurrence in the Fortuna skarn mine, Nambija District, Ecuador: Mineralium Deposita, v. 41, p. 301-321.

Martin-Izard, A., Fuertes-Fuente, M., Cepedal, A., Moreiras, D., Nieto, J. G., Maldonado, C., and Pevida, L. R., 2000a, The Rio Narcea gold belt intrusions; geology, petrology, geochemistry and timing; Gold exploration in NW Iberian Peninsula: Gold exploration and mining in NW Spain, Asturias, Spain, Sept. 1998, v. 71, p. 103-117.

Martin-Izard, A., Paniagua, A., Garcia-Iglesias, J., Fuertes, M., Boixet, L., Maldonado, C., and Varela, A., 2000b, The Carles copper-gold-molybdenum skarn (Asturias, Spain); geometry, mineral associations and metasomatic evolution; Gold exploration in NW Iberian Peninsula: Gold exploration and mining in NW Spain, Asturias, Spain, Sept. 1998, v. 71, p. 153-175.

Massey, N. W. D., MacIntyre, D. G., Desjardins, P. J., and Cooney, R. T., 2005, Digital Geology Map of British Columbia: Whole Province, Geofile 2005-1: Victoria, BC, B.C. Ministry of Energy and Mines.

McMillen, D. D., 1979, The structure and economic geology of Buckhorn Mountain, Okanogan County, Washington, University of Washington, 68 p.

Meinert, L. D., 1989, Gold skarn deposits; geology and exploration criteria; The geology of gold deposits; the perspective in 1988: Economic Geology Monographs, v. 6, p. 537-552.

Meinert, L. D., 1998, A review of skarns that contain gold; Mineralized intrusion-related skarn systems: Short Course Handbook, v. 26, p. 359-414.

Meinert, L. D., 2000, Gold in skarns related to epizonal intrusions; Gold in 2000: Reviews in Economic Geology, v. 13, p. 347-375.

Meinert, L. D., Dipple, G. M., and Nicolescu, S., 2005, World skarn deposits, in Hedenquist, J. W., Thompson, J. F. H., Goldfarb, R. J., and Richards, J. P., eds., Economic Geology; one hundredth anniversary volume, 1905-2005: United States (USA), Society of Economic Geologists, Littleton, CO, United States (USA).

Meredith-Jones, S., 2010, MINFILE Detail Report 093A 121. MINFILE: Victoria,BC, BC Geological Survey, Ministry of Energy, Mines & Petroleum Resources, p. 5.

Moen, W. S., 1980, Myers Creek and Wauconda mining districts of northeastern Okanogan County, Washington, Washington (State), Department of Natural Resources, Division of Geology and Earth Resources, Olympia, WA, United States, 96 p.

Monger, J. W. H., and Price, R. A., 2002, The Canadian Cordillera: Geology and Tectonic Evolution: Canadian Society of Economic Geophyiscists Recorder, v. 27, p. 17.

Monger, J. W. H., Wheeler, J. O., Tipper, H. W., Gabrielse, H., Harms, T., Stuik, L. C., Campbell, R. B., Dodds, C. J., Gehrels, G. E., and O'Brien, J., 1991, Part B. Cordilleran Terranes; in Upper Devonian to Middle Jurassic assemblages, in Gabrielse, H., and Yorath, C. J., eds., Geology of the Cordilleran Orogen in Canada, 4: Ottawa, ON, Geological Survey of Canada, p. 281-327.

Mortensen, J. K., Ghosh, D. K., and Ferri, F., 1995, U-Pb Geochronology of Intrusive Rocks Associated with Cu-Au Porphyry Deposits in the Canadian Cordillera, in Schroeter, T., ed., Porphyry Deposits of the Northwestern Cordillera of North America, 46, Canadian Institute of Mining and Metallurgy, p. 142-160.

Mortimer, N., 1987, The Nicola Group: Late Triassic and Early Jurassic subduction-related volcanism in British Columbia: Canadian Journal of Earth Sciences, v. 24, p. 2521-2536.

Nelson, J. L., and Colpron, M., 2007, Tectonics and metallogeny of the Canadian and Alaskan Cordillera, 1.8 Ga to present, in Goodfellow, W. D., ed., Mineral Deposits of Canada: A Synthesis of Major Deposit Types, District Metallogeny, the Evolution of Geological Provinces, and Exploration Methods., 5: Ottawa, ON, Mineral Deposits Divison, Geological Association of Canada, Special Publications, p. 755-791.

Newberry, R. J., Allegro, G. L., Cutler, S. E., Hagen-Levelle, J. H., Adams, D. D., Nicholson, L. C., Weglarz, T. B., Bakke, A. A., Clautice, K. H., Coulter, G. A., Ford, M. J., Myers, G. L., and Szumigala, D. J., 1997, Skarn deposits of Alaska; Mineral deposits of Alaska: Economic Geology Monographs, v. 9, p. 355-395.

Pouchou, J. L., and Pichoir, F., 1985, PAP f(rZ) procedure for improved quantitative microanalysis, Microbeam Analysis, p. 104-106.

Rasmussen, M. G., Evans, B. W., and Kuehner, S. M., 1998, Low-temperature fayalite, greenalite, and minnesotaite from the Overlook gold deposit, Washington; phase relations in the system FeO-SiO 2 -H 2 O: Can Mineral, v. 36, p. 147-162.

Ray, G. E., and Dawson, G. L., 1994, The geology and mineral deposits of the Hedley gold skarn district, southern British Columbia, British Columbia Ministry of Energy, Mines and Petroleum Resources, Victoria, BC, Canada, 156 p.

Ray, G. E., Dawson, G. L., and Webster, I. C. L., 1996, The stratigraphy of the Nicola Group in the Hedley District, British Columbia, and the chemistry of its intrusions and Au skarns: Canadian Journal of Earth Sciences = Revue Canadienne des Sciences de la Terre, v. 33, p. 1105-1126.

Ray, G. E., Ettlinger, A. D., and Meinert, L. D., 1990, Gold skarns; their distribution, characteristics and problems in classification: Paper - Ministry of Energy, Mines and Petroleum Resources, p. 237-246.

Ray, G. E., Webster, I. C. L., Dawson, G. L., and Ettlinger, A. D., 1993, A geological overview of the Hedley gold skarn district, southern British Columbia; Geological fieldwork 1992; a summary of field activities and current research, in Grant, B., and Newell, J. M., eds., 1993-1: Canada (CAN), Province of British Columbia, Ministry of Energy, Mines and Petroleum Resources, Victoria, BC, Canada (CAN), p. 269-279.

Richards, J. P., Dang, T., Dudka, S. F., and Wong, M. L., 2003, The Nui Phao tungsten-fluorite-copper-gold-bismuth deposit, northern Vietnam; an opportunity for sustainable development; Sustainable mining in the 21st century; a role for geoscientists: SUM21 workshop, Burnaby, BC, Canada, May 2-3, 2002, v. 12, p. 61-70.

Rinehart, C. D., and Fox, K. F., 1972, Geology and mineral deposits of the Loomis Quadrangle, Okanogan County, Washington, Washington (State), Department of Natural Resources, Division of Geology and Earth Resources, Olympia, WA, United States, 124 p.

Romer, R. L., 1992, Vesuvianite-new tool for the U-Pb dating of skarn ore deposits: Mineralogy and Petrology, v. 46, p. 331-341.

Schuster, J. E., and Carutherers, C. G., 2005, Geologic Map of Washighton State, in Reed, K. M., and Roloff, J. M., eds., Geologic Map: Olympia, WA, Washington Department of Natural Resources Division of Geology and Earth Resources.

Selby, D., and Creaser, R. A., 2004, Macroscale NTIMS and microscale LA-MC-ICP-MS Re-Os isotopic analysis of molybdenite: Testing spatial restrictions for reliable Re-Os age determinations, and implications for the decoupling of Re and Os within molybdenite: Geochimica et Cosmochimica Acta, v. 68, p. 3897-3908.

Sillitoe, R. H., 1997, Characteristics and controls of the largest porphyry copper-gold and epithermal gold deposits in the circum-Pacific region: Australian Journal of Earth Sciences, v. 44, p. 373-388.

Simmons, S. F., White, N. C., and John, D. A., 2005, Geological characteristics of epithermal precious and base metal deposits, in Hedenquist, J. W., Thompson, J. F. H., Goldfarb, R. J., and Richards, J. P., eds., Economic Geology; one hundredth anniversary volume, 1905-2005: United States (USA), Society of Economic Geologists, Littleton, CO, United States (USA).

Sláma, J., Kosler, J., Condon, D. J., Crowley, J. L., Gerdes, A., Hanchar, J. M., Horstwood, M. S. A., Morris, G. A., Nasdala, L., Norberg, N., Schaltegger, U., Schoene, B., Tubrett, M. N., and Whitehouse, M. J., 2008, Plesovice zircon -- A new natural reference material for U-Pb and Hf isotopic microanalysis: Chemical Geology, v. 249, p. 1-35.

Smoliar, M. I., Walker, R. J., and Morgan, J. W., 1996, Re-Os Ages of Group IIA, IIIA, IVA, and IVB Iron Meteorites: Science, v. 271, p. 1099-1102.

Souther, J. G., 1991, Volcanic regimes, in Gabrielse, H., and Yorath, C. J., eds., Geology of the Cordilleran Orogen in Canada, 4, Geological Survey of Canada, p. 457-490.

Spear, F. S., 1981, An experimental study of hornblende stability and compositional variability in amphibolite: Am J Sci, v. 281, p. 697-734.

Stein, H. J., Markey, R. J., Morgan, J. W., Hannah, J. L., and Schersten, A., 2001, The remarkable Re-Os chronometer in molybdenite: How and why it works: Terra Nova, v. 13, p. 479-486.

Stoffel, K. L., 1990a, Geologic map of the Oroville 1:100,000 Quadrangle, Washington, State of Washington, Department of Natural Resources, Division of Geology and Earth Resources, Olympia, WA, United States, p. 58.

Stoffel, K. L., 1990b, Geologic map of the Republic 1:100,000 Quadrangle, Washington, State of Washington, Department of Natural Resources, Division of Geology and Earth Resources, Olympia, WA, United States, p. 62.

Suydam, J. D., and Gaylord, D. R., 1997, Toroda Creek half graben, northeast Washington: Late-stage sedimentary infilling of a synextensional basin: Geological Society of America Bulletin, v. 109, p. 1333-1348.

Tafti, R., Mortensen, J. K., Lang, J. R., Rebagliati, M., and Oliver, J. L., 2009, Jurassic U-Pb And Re-Os Ages For The Newly Discovred Xietongmen Cu-Au Porphyry District, Tibet, PRC: Implications For Metallogenic Epochs In The Southern Gangdese Belt: Economic Geology, v. 104, p. 127-136.

Theodore, T. G., Orris, G. J., Hammarstrom, J. M., and Bliss, J. D., 1991, Gold-bearing skarns, B 1930: United States (USA), U. S. Geological Survey, Reston, VA, United States (USA), p. 61.

Theodore, T. G., Silberman, M. L., and Blake, D. W., 1973, Geochemistry and potassium-argon ages of plutonic rocks in the Battle Mountain mining district, Lander County, Nevada, P 0798-A: United States (USA), U. S. Geological Survey, Reston, VA, United States (USA), p. A1-A24.

Thompson, J. F. H., Sillitoe, R. H., Baker, T., Lang, J. R., and Mortensen, J. K., 1999, Intrusion-related gold deposits associated with tungsten-tin provinces: Mineralium Deposita, v. 34, p. 323-334.

Thorkelson, D. J., and Smith, A. D., 1989, Arc and intraplate volcanism in the Spences Bridge Group: Implications for Cretaceous tectonics in the Canadian Cordillera: Geology, v. 17, p. 1093-1096.

Tooth, B., Brugger, J., Ciobanu, C., and Liu, W., 2008, Modeling of gold scavenging by bismuth melts coexisting with hydrothermal fluids: Geology, v. 36, p. 815-818.

Tooth, B., Ciobanu, C. L., Green, L., O'Neill, B., and Brugger, J., 2011, Bi-melt formation and gold scavenging from hydrothermal fluids: An experimental study: Geochimica et Cosmochimica Acta, v. 75, p. 5423-5443.

Törmänen, T. O., and Koski, R. A., 2005, Gold Enrichment and the Bi-Au Association in Pyrrhotite-Rich Massive Sulfide Deposits, Escanaba Trough, Southern Gorda Ridge: Economic Geology, v. 100, p. 1135-1150.

Tripper, H. W., Woodsworth, G. J., and Gabrielse, H., 1981, Tectonic assemblage map of the Canadian Cordillera and adjacent parts of the United States of America, Geological Survey of Canada, Ottawa, ON, Canada.

Umpleby, J. B., 1911, Geology and ore deposits of the Myers Creek mining district: Bulletin - Division of Mines and Geology (State of Washington), p. 9-52.

van Achterbergh, E., Ryan, C. G., Jackson, S. E., and Griffin, W. L., 2001, Data reduction software for LA-ICP-MS: Short Course Handbook, v. 29, p. 239-243.

Venable, M. E., 1994, A geologic, tectonic and metallogenic evaluation of the Siuna Terrane, University of Arizona, Tucson, AZ, United States (USA).

Wheeler, J. O., and McFeely, P., 1991, Tectonic assemblage map of the Canadian Cordillera and adjacent parts of the United States of America--Carte des assemblages tectoniques de la Cordillere canadienne et des parties adjacentes des Etats-Unis d'Amerique, Geological Survey of Canada, Ottawa, ON, Canada.

Wilkie, K. M., 1996, Geology and hydrothermal evolution of the Beal Mountain gold deposit, Silver Bow County, Montana, Washington State University, Pullman, WA, United States (USA).

Winter, J. D., 2001, An introduction to igneous and metamorphic petrology: United States (USA), Prentice Hall, Upper Saddle River, NJ, United States (USA).

Woodsworth, G. J., Anderson, R. G., and Armstrong, R. L., 1991, Plutonic Regimes, in Gabrielse, H., and Yorath, C. J., eds., Geology of the Cordilleran Orogen in Canada, 4, Geological Survey of Canada, p. 491-531.

Wotruba, P. R., Benson, R. G., and Schmidt, K. W., 1986, Battle Mountain describes the geology of its Fortitude gold-silver deposit at Copper Canyon: Mining Engineering, v. 38, p. 495-499.

# Appendix A.   Microprobe Analysis

**Table A.1:** Microprobe analysis of pyroxene

| Label | 090-1-10 | 090-1-11 | 090-1-2 | 090-1-6 | 090-1-7 | 090-2-2 | 090-2-4 |
|---|---|---|---|---|---|---|---|
| Mineral | Px | Px | Px | Px | Px | Px | Px |
| Au (ppm) | 0.2 | 0.2 | 0.2 | 0.2 | 0.2 | 0.2 | 0.2 |
| SiO2 | 48.769 | 49.145 | 49.476 | 49.075 | 49.252 | 49.439 | 49.086 |
| TiO2 | 0.006 | 0.000 | 0.000 | 0.061 | 0.000 | 0.046 | 0.017 |
| Al2O3 | 0.287 | 0.423 | 0.146 | 1.543 | 0.091 | 0.534 | 0.415 |
| FeO | 23.244 | 22.162 | 22.283 | 29.033 | 21.833 | 21.208 | 22.544 |
| MnO | 0.465 | 0.526 | 0.378 | 0.355 | 0.406 | 0.388 | 0.406 |
| MgO | 4.098 | 4.315 | 4.314 | 5.071 | 4.495 | 4.862 | 4.109 |
| CaO | 21.493 | 23.005 | 22.736 | 11.438 | 22.808 | 22.668 | 22.635 |
| Na2O | 0.074 | 0.056 | 0.193 | 0.166 | 0.196 | 0.246 | 0.188 |
| NiO | 0.015 | 0.000 | 0.000 | 0.000 | 0.000 | 0.055 | 0.023 |
| Cr2O3 | 0.000 | 0.014 | 0.010 | 0.000 | 0.000 | 0.000 | 0.012 |
| **Total** | **98.451** | **99.645** | **99.535** | **96.742** | **99.080** | **99.447** | **99.434** |
| Si | 1.986 | 1.969 | 1.983 | 2.052 | 1.980 | 1.973 | 1.972 |
| Al (T) | 0.014 | 0.020 | 0.007 | 0.000 | 0.004 | 0.025 | 0.020 |
| Fe3+ (T) | 0.000 | 0.011 | 0.010 | 0.000 | 0.015 | 0.002 | 0.008 |
| **Sum T** | **2.000** | **2.000** | **2.000** | **2.052** | **2.000** | **2.000** | **2.000** |
| Al (M1) | 0.000 | 0.000 | 0.000 | 0.076 | 0.000 | 0.000 | 0.000 |
| Fe3+ (M1) | 0.020 | 0.035 | 0.031 | 0.000 | 0.035 | 0.043 | 0.041 |
| Ti | 0.000 | 0.000 | 0.000 | 0.002 | 0.000 | 0.001 | 0.001 |
| Cr | 0.000 | 0.000 | 0.000 | 0.000 | 0.000 | 0.000 | 0.000 |
| Mg | 0.249 | 0.258 | 0.258 | 0.316 | 0.269 | 0.289 | 0.246 |
| Fe2+ | 0.771 | 0.697 | 0.706 | 1.015 | 0.684 | 0.663 | 0.708 |
| Mn | 0.016 | 0.018 | 0.013 | 0.013 | 0.014 | 0.013 | 0.014 |
| Ni | 0.001 | 0.000 | 0.000 | 0.000 | 0.000 | 0.002 | 0.001 |
| **Sum M1** | **1.057** | **1.008** | **1.008** | **1.422** | **1.002** | **1.012** | **1.011** |
| Ca | 0.938 | 0.988 | 0.977 | 0.512 | 0.983 | 0.969 | 0.974 |
| Na | 0.006 | 0.004 | 0.015 | 0.013 | 0.015 | 0.019 | 0.015 |
| **Sum M2** | **0.943** | **0.992** | **0.992** | **0.526** | **0.998** | **0.988** | **0.989** |
| Mg# | 0.244 | 0.270 | 0.267 | 0.237 | 0.283 | 0.304 | 0.258 |
| **Name** | Hed | Hed | Hed | aug | hed | hed | hed |

## Table A.1 Continued

| Label | 091-2-2 | 091-2-5 | 092-1-1 | 092-1-2 | 092-1-3 | 092-1-5 | 092-1-6 |
|---|---|---|---|---|---|---|---|
| Mineral | Px | Px | Px | Px | Px | Px | Px |
| Au (ppm) | 0.5 | 0.5 | 46.2 | 46.2 | 46.2 | 46.2 | 46.2 |
| | | | | | | | |
| SiO2 | 37.291 | 46.175 | 50.275 | 49.336 | 49.687 | 49.622 | 49.954 |
| TiO2 | 0.126 | 0.169 | 0.015 | 0.000 | 0.019 | 0.000 | 0.000 |
| Al2O3 | 11.295 | 5.215 | 0.030 | 0.245 | 0.425 | 0.205 | 0.145 |
| FeO | 15.623 | 28.513 | 20.856 | 24.337 | 22.037 | 22.919 | 21.227 |
| MnO | 0.585 | 0.402 | 0.667 | 0.265 | 0.477 | 0.519 | 0.525 |
| MgO | 0.039 | 4.347 | 4.930 | 2.702 | 4.098 | 3.882 | 4.571 |
| CaO | 32.953 | 11.375 | 23.185 | 22.893 | 22.555 | 23.297 | 23.016 |
| Na2O | 0.000 | 0.554 | 0.013 | 0.113 | 0.193 | 0.046 | 0.171 |
| NiO | 0.000 | 0.000 | 0.009 | 0.000 | 0.044 | 0.000 | 0.000 |
| Cr2O3 | 0.006 | 0.010 | 0.010 | 0.000 | 0.022 | 0.020 | 0.000 |
| Total | 97.919 | 96.758 | 99.991 | 99.891 | 99.558 | 100.510 | 99.609 |
| | | | | | | | |
| Si | 1.497 | 1.916 | 2.000 | 1.994 | 1.993 | 1.978 | 1.996 |
| Al (T) | 0.503 | 0.084 | 0.000 | 0.006 | 0.007 | 0.010 | 0.004 |
| Fe3+ (T) | 0.000 | 0.000 | 0.000 | 0.000 | 0.000 | 0.012 | 0.000 |
| Sum T | 2.000 | 2.000 | 2.000 | 2.000 | 2.000 | 2.000 | 2.000 |
| Al (M1) | 0.032 | 0.171 | 0.001 | 0.005 | 0.013 | 0.000 | 0.002 |
| Fe3+ (M1) | 0.463 | 0.000 | 0.000 | 0.010 | 0.008 | 0.024 | 0.015 |
| Ti | 0.004 | 0.005 | 0.000 | 0.000 | 0.001 | 0.000 | 0.000 |
| Cr | | 0.000 | 0.000 | 0.000 | 0.001 | 0.001 | 0.000 |
| Mg | 0.002 | 0.269 | 0.292 | 0.163 | 0.245 | 0.231 | 0.272 |
| Fe2+ | 0.061 | 0.990 | 0.694 | 0.813 | 0.731 | 0.728 | 0.694 |
| Mn | 0.020 | 0.014 | 0.022 | 0.009 | 0.016 | 0.018 | 0.018 |
| Ni | | 0.000 | 0.000 | 0.000 | 0.001 | 0.000 | 0.000 |
| Sum M1 | 0.582 | 1.450 | 1.011 | 1.000 | 1.016 | 1.001 | 1.002 |
| Ca | | 0.506 | 0.988 | 0.991 | 0.969 | 0.995 | 0.985 |
| Na | | 0.045 | 0.001 | 0.009 | 0.015 | 0.004 | 0.013 |
| Sum M2 | 0.000 | 0.550 | 0.989 | 1.000 | 0.984 | 0.999 | 0.998 |
| | | | | | | | |
| Mg# | 0.037 | 0.214 | 0.296 | 0.167 | 0.251 | 0.241 | 0.282 |
| Name | alum ferrian subilicic essenite | alum aug | hed | hed | hed | hed | hed |

**Table A.1 Continued**

| Label | 092-1-7 | 092-2-2 | 092-2-3 | 092-2-4 | 092-2-5 | 092-2-6 | 092-2-7 |
|---|---|---|---|---|---|---|---|
| Mineral | Px | Px | Px | Px | Px | Px | Px |
| Au (ppm) | 46.2 | 46.2 | 46.2 | 46.2 | 46.2 | 46.2 | 46.2 |
| | | | | | | | |
| SiO2 | 49.490 | 49.850 | 49.229 | 49.809 | 49.156 | 49.640 | 50.972 |
| TiO2 | 0.000 | 0.003 | 0.013 | 0.003 | 0.025 | 0.000 | 0.022 |
| Al2O3 | 0.143 | 0.241 | 0.266 | 0.300 | 0.192 | 0.187 | 0.615 |
| FeO | 22.858 | 22.522 | 23.323 | 21.836 | 23.784 | 23.633 | 27.130 |
| MnO | 0.359 | 0.570 | 0.486 | 0.374 | 0.566 | 0.553 | 0.326 |
| MgO | 4.141 | 4.942 | 3.858 | 4.178 | 3.113 | 3.390 | 6.159 |
| CaO | 22.772 | 20.315 | 23.018 | 22.925 | 22.794 | 23.160 | 12.875 |
| Na2O | 0.225 | 0.126 | 0.160 | 0.091 | 0.129 | 0.078 | 0.066 |
| NiO | 0.000 | 0.000 | 0.010 | 0.009 | 0.005 | 0.017 | 0.000 |
| Cr2O3 | 0.030 | 0.000 | 0.032 | 0.000 | 0.050 | 0.002 | 0.010 |
| Total | **100.017** | **98.569** | **100.395** | **99.525** | **99.813** | **100.658** | **98.175** |
| | | | | | | | |
| Si | 1.977 | 2.018 | 1.965 | 1.998 | 1.984 | 1.983 | 2.085 |
| Al (T) | 0.007 | 0.000 | 0.013 | 0.002 | 0.009 | 0.009 | 0.000 |
| Fe3+ (T) | 0.016 | 0.000 | 0.023 | 0.000 | 0.007 | 0.008 | 0.000 |
| Sum T | **2.000** | **2.018** | **2.000** | **2.000** | **2.000** | **2.000** | **2.085** |
| Al (M1) | 0.000 | 0.011 | 0.000 | 0.012 | 0.000 | 0.000 | 0.030 |
| Fe3+ (M1) | 0.039 | 0.000 | 0.046 | 0.000 | 0.023 | 0.023 | 0.000 |
| Ti | 0.000 | 0.000 | 0.000 | 0.000 | 0.001 | 0.000 | 0.001 |
| Cr | 0.001 | 0.000 | 0.001 | 0.000 | 0.002 | 0.000 | 0.000 |
| Mg | 0.247 | 0.298 | 0.230 | 0.250 | 0.187 | 0.202 | 0.376 |
| Fe2+ | 0.709 | 0.762 | 0.710 | 0.733 | 0.772 | 0.759 | 0.928 |
| Mn | 0.012 | 0.020 | 0.016 | 0.013 | 0.019 | 0.019 | 0.011 |
| Ni | 0.000 | 0.000 | 0.000 | 0.000 | 0.000 | 0.001 | 0.000 |
| Sum M1 | **1.008** | **1.092** | **1.003** | **1.008** | **1.004** | **1.003** | **1.346** |
| Ca | 0.975 | 0.881 | 0.984 | 0.985 | 0.985 | 0.991 | 0.564 |
| Na | 0.017 | 0.010 | 0.012 | 0.007 | 0.010 | 0.006 | 0.005 |
| Sum M2 | **0.992** | **0.891** | **0.997** | **0.992** | **0.996** | **0.997** | **0.569** |
| | | | | | | | |
| Mg# | 0.258 | 0.281 | 0.244 | 0.254 | 0.195 | 0.210 | 0.288 |
| Name | hed | aug | hed | hed | hed | hed | aug |

## Table A.1 Continued

| Label | 092-2-8 | 092-3-1 | 092-3-2 | 092-3-3 | 092-3-4 | 093-1-3 | 093-2-2 |
|---|---|---|---|---|---|---|---|
| Mineral | Px | Px | Px | Px | Px | Px | Px |
| Au (ppm) | 46.2 | 46.2 | 46.2 | 46.2 | 46.2 | 51.1 | 51.1 |
| | | | | | | | |
| SiO2 | 50.330 | 49.408 | 49.819 | 49.418 | 49.616 | 50.255 | 49.891 |
| TiO2 | 0.000 | 0.013 | 0.050 | 0.000 | 0.005 | 0.000 | 0.003 |
| Al2O3 | 0.375 | 0.198 | 1.470 | 0.357 | 0.308 | 0.466 | 0.870 |
| FeO | 23.613 | 23.062 | 28.498 | 22.706 | 22.756 | 22.265 | 18.370 |
| MnO | 0.530 | 0.634 | 0.332 | 0.398 | 0.482 | 0.387 | 0.244 |
| MgO | 4.959 | 3.755 | 5.628 | 3.917 | 3.887 | 6.081 | 6.811 |
| CaO | 19.253 | 23.292 | 11.860 | 23.195 | 22.984 | 19.402 | 23.239 |
| Na2O | 0.147 | 0.117 | 0.173 | 0.121 | 0.069 | 0.109 | 0.173 |
| NiO | 0.004 | 0.031 | 0.014 | 0.000 | 0.017 | 0.000 | 0.005 |
| Cr2O3 | 0.000 | 0.024 | 0.052 | 0.014 | 0.004 | 0.006 | 0.000 |
| Total | 99.210 | 100.532 | 97.896 | 100.125 | 100.128 | 98.971 | 99.607 |
| | | | | | | | |
| Si | 2.028 | 1.970 | 2.050 | 1.975 | 1.985 | 2.014 | 1.959 |
| Al (T) | 0.000 | 0.009 | 0.000 | 0.017 | 0.015 | 0.000 | 0.040 |
| Fe3+ (T) | 0.000 | 0.020 | 0.000 | 0.008 | 0.001 | 0.000 | 0.001 |
| Sum T | 2.028 | 2.000 | 2.050 | 2.000 | 2.000 | 2.014 | 2.000 |
| Al (M1) | 0.018 | 0.000 | 0.071 | 0.000 | 0.000 | 0.022 | 0.000 |
| Fe3+ (M1) | 0.000 | 0.037 | 0.000 | 0.034 | 0.020 | 0.000 | 0.054 |
| Ti | 0.000 | 0.000 | 0.002 | 0.000 | 0.000 | 0.000 | 0.000 |
| Cr | 0.000 | 0.001 | 0.002 | 0.000 | 0.000 | 0.000 | 0.000 |
| Mg | 0.298 | 0.223 | 0.345 | 0.233 | 0.232 | 0.363 | 0.399 |
| Fe2+ | 0.796 | 0.712 | 0.981 | 0.716 | 0.740 | 0.746 | 0.548 |
| Mn | 0.018 | 0.021 | 0.012 | 0.013 | 0.016 | 0.013 | 0.008 |
| Ni | 0.000 | 0.001 | 0.000 | 0.000 | 0.001 | 0.000 | 0.000 |
| Sum M1 | 1.130 | 0.996 | 1.413 | 0.998 | 1.010 | 1.145 | 1.009 |
| Ca | 0.831 | 0.995 | 0.523 | 0.993 | 0.985 | 0.833 | 0.978 |
| Na | 0.011 | 0.009 | 0.014 | 0.009 | 0.005 | 0.008 | 0.013 |
| Sum M2 | 0.843 | 1.004 | 0.537 | 1.002 | 0.990 | 0.842 | 0.991 |
| | | | | | | | |
| Mg# | 0.272 | 0.239 | 0.260 | 0.246 | 0.238 | 0.327 | 0.421 |
| Name | aug | Wol | aug | hed | hed | aug | hed |

**Table A.1 Continued**

| Label | 093-2-7 | 093-3-1 | 094-1-2 | 094-1-8 | 094-2-3 | 094-2-6 | 094-3-6 |
|---|---|---|---|---|---|---|---|
| Mineral | Px | Px | Px | Px | Px | Px | Px |
| Au (ppm) | 51.1 | 51.1 | 51.1 | 51.1 | 51.1 | 51.1 | 51.1 |
| | | | | | | | |
| SiO2 | 48.145 | 49.710 | 49.449 | 49.101 | 47.656 | 48.509 | 48.539 |
| TiO2 | 0.020 | 0.007 | 0.059 | 0.023 | 0.017 | 0.000 | 0.026 |
| Al2O3 | 0.348 | 0.280 | 0.357 | 0.295 | 0.565 | 0.256 | 1.780 |
| FeO | 23.579 | 21.792 | 22.415 | 23.790 | 26.317 | 26.505 | 22.540 |
| MnO | 0.360 | 0.324 | 0.603 | 0.477 | 0.410 | 0.352 | 0.247 |
| MgO | 3.431 | 4.759 | 4.451 | 3.655 | 2.242 | 2.135 | 3.796 |
| CaO | 22.610 | 23.119 | 22.125 | 22.415 | 21.294 | 21.871 | 21.391 |
| Na2O | 0.103 | 0.059 | 0.075 | 0.125 | 0.302 | 0.106 | 0.773 |
| NiO | 0.013 | 0.022 | 0.000 | 0.006 | 0.001 | 0.000 | 0.000 |
| Cr2O3 | 0.004 | 0.032 | 0.032 | 0.000 | 0.000 | 0.000 | 0.014 |
| Total | **98.612** | **100.103** | **99.565** | **99.887** | **98.805** | **99.734** | **99.106** |
| | | | | | | | |
| Si | 1.962 | 1.977 | 1.984 | 1.974 | 1.956 | 1.978 | 1.945 |
| Al (T) | 0.017 | 0.013 | 0.016 | 0.014 | 0.027 | 0.012 | 0.055 |
| Fe3+ (T) | 0.021 | 0.010 | 0.000 | 0.012 | 0.016 | 0.010 | 0.000 |
| Sum T | **2.000** | **2.000** | **2.000** | **2.000** | **2.000** | **2.000** | **2.000** |
| Al (M1) | 0.000 | 0.000 | 0.001 | 0.000 | 0.000 | 0.000 | 0.029 |
| Fe3+ (M1) | 0.045 | 0.026 | 0.016 | 0.034 | 0.067 | 0.030 | 0.083 |
| Ti | 0.001 | 0.000 | 0.002 | 0.001 | 0.001 | 0.000 | 0.001 |
| Cr | 0.000 | 0.001 | 0.001 | 0.000 | 0.000 | 0.000 | 0.000 |
| Mg | 0.208 | 0.282 | 0.266 | 0.219 | 0.137 | 0.130 | 0.227 |
| Fe2+ | 0.738 | 0.689 | 0.737 | 0.754 | 0.821 | 0.864 | 0.672 |
| Mn | 0.012 | 0.011 | 0.020 | 0.016 | 0.014 | 0.012 | 0.008 |
| Ni | 0.000 | 0.001 | 0.000 | 0.000 | 0.000 | 0.000 | 0.000 |
| Sum M1 | **1.005** | **1.010** | **1.043** | **1.025** | **1.039** | **1.036** | **1.021** |
| Ca | 0.987 | 0.985 | 0.951 | 0.966 | 0.937 | 0.955 | 0.919 |
| Na | 0.008 | 0.005 | 0.006 | 0.010 | 0.024 | 0.008 | 0.060 |
| Sum M2 | **0.995** | **0.990** | **0.957** | **0.975** | **0.961** | **0.964** | **0.979** |
| | | | | | | | |
| Mg# | 0.220 | 0.290 | 0.266 | 0.225 | 0.143 | 0.131 | 0.252 |
| Name | hed | hed | hed | hed | hed | hed | hed |

| | |
|---|---|
| Label | 094-3-8 |
| Mineral | Px |
| Au (ppm) | 51.1 |

| | |
|---|---|
| SiO2 | 49.152 |
| TiO2 | 0.000 |
| Al2O3 | 0.973 |
| FeO | 23.370 |
| MnO | 0.375 |
| MgO | 3.518 |
| CaO | 21.762 |
| Na2O | 0.718 |
| NiO | 0.000 |
| Cr2O3 | 0.000 |
| **Total** | **99.867** |

| | |
|---|---|
| Si | 1.964 |
| Al (T) | 0.036 |
| Fe3+ (T) | 0.000 |
| **Sum T** | **2.000** |
| Al (M1) | 0.010 |
| Fe3+ (M1) | 0.082 |
| Ti | 0.000 |
| Cr | 0.000 |
| Mg | 0.210 |
| Fe2+ | 0.699 |
| Mn | 0.013 |
| Ni | 0.000 |
| **Sum M1** | **1.013** |
| Ca | 0.932 |
| Na | 0.056 |
| **Sum M2** | **0.987** |

| | |
|---|---|
| Mg# | 0.231 |
| Name | hed |

**Table A.2:** Microprobe analysis of amphibole

| Label | 090-1-5 | 091-1-1 | 091-1-3 | 091-1-4 | 091-2-1 | 091-2-3 | 091-2-4 |
|---|---|---|---|---|---|---|---|
| Mineral | Amph | Amph | Amph | Amph | Amph | Amph | Amph |
| Au (ppm) | 0.2 | 0.5 | 0.5 | 0.5 | 0.5 | 0.5 | 0.5 |
| SiO2 | 41.356 | 44.394 | 44.239 | 46.513 | 43.502 | 45.991 | 44.692 |
| TiO2 | 0.029 | 0.079 | 0.104 | 0.074 | 0.215 | 0.038 | 0.328 |
| Al2O3 | 9.451 | 6.001 | 5.037 | 3.894 | 7.107 | 4.717 | 5.986 |
| Cr2O3 | 0.000 | 0.012 | 0.000 | 0.035 | 0.067 | 0.019 | 0.017 |
| FeO | 28.936 | 29.316 | 28.536 | 28.475 | 29.424 | 28.781 | 30.302 |
| MnO | 0.276 | 0.276 | 0.340 | 0.357 | 0.445 | 0.370 | 0.448 |
| MgO | 2.818 | 4.444 | 4.867 | 4.823 | 3.514 | 4.377 | 3.189 |
| CaO | 10.789 | 11.349 | 11.317 | 11.514 | 11.427 | 11.485 | 11.420 |
| Na2O | 0.632 | 0.570 | 0.614 | 0.523 | 0.724 | 0.525 | 0.573 |
| K2O | 2.071 | 0.859 | 0.512 | 0.340 | 0.440 | 0.420 | 0.564 |
| F | 0.000 | 0.151 | 0.122 | 0.130 | 0.000 | 0.094 | 0.000 |
| Cl | 0.147 | 0.218 | 0.225 | 0.157 | 0.184 | 0.223 | 0.312 |
| H2O | 1.853 | 1.631 | 1.652 | 1.712 | 1.816 | 1.684 | 1.688 |
| Sum | **98.357** | **99.301** | **97.566** | **98.548** | **98.865** | **98.722** | **99.519** |
| Ideal site assignments | | | | | | | |
| Si | 6.658 | 6.983 | 7.059 | 7.344 | 6.885 | 7.262 | 7.061 |
| Al (IV) | 1.342 | 1.017 | 0.941 | 0.656 | 1.115 | 0.738 | 0.939 |
| Sum T | **8.000** | **8.000** | **8.000** | **8.000** | **8.000** | **8.000** | **8.000** |
| Al (VI) | 0.451 | 0.095 | 0.006 | 0.068 | 0.211 | 0.139 | 0.175 |
| Ti | 0.004 | 0.009 | 0.013 | 0.009 | 0.026 | 0.004 | 0.039 |
| Fe 3+ | 0.409 | 0.649 | 0.685 | 0.393 | 0.599 | 0.403 | 0.466 |
| Cr | 0.000 | 0.001 | 0.000 | 0.004 | 0.008 | 0.002 | 0.002 |
| Mg | 0.676 | 1.042 | 1.158 | 1.135 | 0.829 | 1.030 | 0.751 |
| Fe 2+ | 3.460 | 3.203 | 3.123 | 3.366 | 3.296 | 3.397 | 3.538 |
| Mn | 0.000 | 0.000 | 0.016 | 0.023 | 0.031 | 0.023 | 0.029 |
| Sum C | **5.000** | **5.000** | **5.000** | **5.000** | **5.000** | **5.000** | **5.000** |
| Fe 2+ | 0.027 | 0.004 | 0.000 | 0.000 | 0.000 | 0.000 | 0.000 |
| Mn | 0.038 | 0.037 | 0.030 | 0.024 | 0.029 | 0.027 | 0.031 |
| Ca | 1.861 | 1.913 | 1.935 | 1.948 | 1.938 | 1.943 | 1.933 |
| Na | 0.074 | 0.047 | 0.035 | 0.028 | 0.033 | 0.030 | 0.036 |
| Sum B | **2.000** | **2.000** | **2.000** | **2.000** | **2.000** | **2.000** | **2.000** |
| Na | 0.123 | 0.127 | 0.155 | 0.132 | 0.189 | 0.130 | 0.140 |
| K | 0.425 | 0.172 | 0.104 | 0.069 | 0.089 | 0.085 | 0.114 |
| Sum A | **0.548** | **0.299** | **0.259** | **0.201** | **0.278** | **0.215** | **0.254** |
| F | 0.000 | 0.008 | 0.006 | 0.007 | 0.000 | 0.005 | 0.000 |
| Cl | 0.004 | 0.006 | 0.006 | 0.004 | 0.005 | 0.006 | 0.009 |
| OH | 1.996 | 1.986 | 1.987 | 1.989 | 1.995 | 1.989 | 1.991 |
| Sum W | **2.000** | **2.000** | **2.000** | **2.000** | **2.000** | **2.000** | **2.000** |

## Table A.2 Continued

| Label | 091-2-6 | 093-2-5 | 094-2-2 | 094-2-4 | 094-3-4 | 094-3-9 |
|---|---|---|---|---|---|---|
| Mineral | Amph | Amph | Amph | Amph | Amph | Amph |
| Au (ppm) | 0.5 | 51.1 | 51.1 | 51.1 | 51.1 | 51.1 |
| SiO2 | 43.602 | 50.866 | 47.743 | 48.296 | 46.644 | 46.522 |
| TiO2 | 0.176 | 0.008 | 0.009 | 0.000 | 0.000 | 0.000 |
| Al2O3 | 6.861 | 1.343 | 4.659 | 4.121 | 5.101 | 5.056 |
| Cr2O3 | 0.000 | 0.000 | 0.041 | 0.000 | 0.000 | 0.000 |
| FeO | 29.272 | 25.404 | 24.115 | 24.055 | 25.146 | 24.517 |
| MnO | 0.327 | 0.383 | 0.318 | 0.233 | 0.345 | 0.303 |
| MgO | 3.677 | 7.526 | 7.901 | 8.544 | 7.339 | 7.843 |
| CaO | 11.418 | 11.858 | 11.568 | 11.322 | 11.606 | 11.224 |
| Na2O | 0.791 | 0.175 | 0.775 | 0.595 | 0.834 | 1.017 |
| K2O | 0.566 | 0.080 | 0.279 | 0.205 | 0.369 | 0.324 |
| F | 0.000 | 0.067 | 0.008 | 0.074 | 0.044 | 0.192 |
| Cl | 0.208 | 0.014 | 0.170 | 0.085 | 0.178 | 0.115 |
| H2O | 1.792 | 1.919 | 1.822 | 1.841 | 1.777 | 1.693 |
| Sum | **98.691** | **99.643** | **99.408** | **99.371** | **99.384** | **98.804** |
| Ideal site assignments | | | | | | |
| Si | 6.922 | 7.776 | 7.288 | 7.325 | 7.164 | 7.159 |
| Al (IV) | 1.078 | 0.224 | 0.712 | 0.675 | 0.836 | 0.841 |
| Sum T | **8.000** | **8.000** | **8.000** | **8.000** | **8.000** | **8.000** |
| Al (VI) | 0.205 | 0.018 | 0.126 | 0.062 | 0.087 | 0.076 |
| Ti | 0.021 | 0.001 | 0.001 | 0.000 | 0.000 | 0.000 |
| Fe 3+ | 0.535 | 0.188 | 0.410 | 0.569 | 0.525 | 0.557 |
| Cr | 0.000 | 0.000 | 0.005 | 0.000 | 0.000 | 0.000 |
| Mg | 0.870 | 1.715 | 1.798 | 1.932 | 1.680 | 1.799 |
| Fe 2+ | 3.352 | 3.060 | 2.660 | 2.437 | 2.705 | 2.568 |
| Mn | 0.017 | 0.018 | 0.000 | 0.000 | 0.003 | 0.000 |
| Sum C | **5.000** | **5.000** | **5.000** | **5.000** | **5.000** | **5.000** |
| Fe 2+ | 0.000 | 0.000 | 0.009 | 0.045 | 0.000 | 0.030 |
| Mn | 0.027 | 0.032 | 0.041 | 0.030 | 0.042 | 0.039 |
| Ca | 1.942 | 1.942 | 1.892 | 1.840 | 1.910 | 1.851 |
| Na | 0.031 | 0.026 | 0.058 | 0.085 | 0.048 | 0.080 |
| Sum B | **2.000** | **2.000** | **2.000** | **2.000** | **2.000** | **2.000** |
| Na | 0.213 | 0.026 | 0.172 | 0.090 | 0.200 | 0.224 |
| K | 0.115 | 0.016 | 0.054 | 0.040 | 0.072 | 0.064 |
| Sum A | **0.327** | **0.042** | **0.226** | **0.129** | **0.272** | **0.287** |
| F | 0.000 | 0.004 | 0.000 | 0.004 | 0.002 | 0.010 |
| Cl | 0.006 | 0.000 | 0.005 | 0.002 | 0.005 | 0.003 |
| OH | 1.994 | 1.996 | 1.995 | 1.994 | 1.993 | 1.987 |
| Sum W | **2.000** | **2.000** | **2.000** | **2.000** | **2.000** | **2.000** |

## Appendix B.   Four Acid Digestion ICP-MS Geochemical Analysis

**Table B.1:** Major element and mineralizing element geochemical analysis of Buckhorn skarn alteration and host rocks

| Table B.1 Hole ID | Sample ID | From | To | Lithology | Sample | Skarn Class | Au ppm | Ag ppm | Bi ppm | Fe % | Ca % | P % | Mg % | Ti % | Al % | Na % | K % | S % |
|---|---|---|---|---|---|---|---|---|---|---|---|---|---|---|---|---|---|---|
| D07-369 | BX02864 | 399 | 402 | Hornfels BMV | | | 1.3 | 2.516 | 516.42 | 7.51 | 10.27 | 0.103 | 3.01 | 0.334 | 7.01 | 1.154 | 1.56 | 0.76 |
| D07-369 | BX02865 | 402 | 404.4 | Hornfels BMV | | | 0.05 | 1.157 | 5.36 | 6.66 | 9.52 | 0.093 | 3.13 | 0.362 | 8.38 | 1.3 | 1.64 | 0.6 |
| D07-369 | BX02866 | 404.4 | 406.4 | Skarn | | Amp-Px | 0.5 | 12.981 | 86.32 | 14.82 | 13.82 | 0.042 | 1.54 | 0.187 | 3.41 | 0.034 | 0.01 | 2.13 |
| D07-369 | BX02867 | 406.4 | 407.3 | Skarn | | Amp-Px | 0.1 | 5.083 | 12.36 | 9.68 | 17.4 | 0.041 | 0.97 | 0.187 | 3.38 | 0.187 | 1.12 | 1.07 |
| D07-369 | BX02868 | 407.3 | 408.4 | Skarn | | Gar | 0.4 | 14.779 | 33.51 | 11.34 | 17.78 | 0.029 | 1.02 | 0.125 | 2.76 | 0.039 | 0.15 | 0.66 |
| D07-369 | BX02869 | 408.4 | 411 | Skarn | | Gar | 0.7 | 15.186 | 45.05 | 10.76 | 18.15 | 0.037 | 0.97 | 0.174 | 3.13 | 0.051 | 0.62 | 0.66 |
| D07-369 | BX02870 | 411 | 412.4 | Skarn | | Amp-Px | 0.05 | 0.484 | 2.22 | 12.25 | 13.64 | 0.053 | 1.38 | 0.393 | 5.92 | 0.374 | 0.51 | 0.24 |
| D07-369 | BX02871 | 412.4 | 413.7 | Skarn | | Amp-Px | 0.05 | 0.184 | 1.63 | 10.08 | 10.53 | 0.056 | 1.42 | 0.406 | 5.98 | 1.962 | 1.03 | 0.1 |
| D07-369 | BX02872 | 413.7 | 415.9 | Skarn | | Ep-Px | 0.05 | 0.289 | 3.09 | 12.3 | 14.94 | 0.048 | 1.21 | 0.29 | 4.89 | 0.066 | 0.26 | 0.43 |
| D07-369 | BX02873 | 415.9 | 418.1 | Skarn | | Gar | 0.05 | 1.013 | 1.12 | 9.81 | 9.3 | 0.059 | 1.62 | 0.336 | 5.8 | 1.014 | 2.7 | 0.36 |
| D07-369 | BX02874 | 418.1 | 420.2 | Skarn | | Ep-Px | 0.05 | 0.585 | 1.18 | 9.01 | 9.97 | 0.057 | 1.59 | 0.373 | 6.09 | 0.607 | 2.77 | 0.34 |
| D07-369 | BX02875 | 420.2 | 421.8 | Skarn | | Amp-Px | 0.3 | 66.454 | 203.92 | 13.15 | 12.99 | 0.049 | 1.48 | 0.308 | 3.48 | 0.04 | 0.16 | 1.7 |
| D07-369 | BX02876 | 421.8 | 422.9 | Skarn | | Amp-Px | 2 | 5.952 | 63.92 | 8.61 | 16.86 | 0.039 | 1.28 | 0.265 | 3.57 | 0.042 | 0.89 | 0.82 |
| D07-369 | BX02877 | 422.9 | 424.6 | Skarn | | Amp-Px | 9.1 | 6.017 | 175.95 | 10.02 | 17.73 | 0.027 | 0.91 | 0.187 | 3.56 | 0.055 | 1.43 | 1.68 |
| D07-369 | BX02878 | 424.6 | 426.5 | Skarn | | Gar | 0.4 | 6.218 | 27.23 | 9.47 | 16.61 | 0.039 | 0.94 | 0.267 | 4.28 | 0.057 | 1.36 | 0.44 |
| D07-369 | BX02879 | 426.5 | 428.6 | Skarn | | Amp-Px | 10.7 | 11.638 | 143.97 | 11.18 | 16.66 | 0.037 | 1.15 | 0.186 | 3.07 | 0.067 | 1 | 1.09 |
| D07-369 | BX02882 | 430.4 | 432.4 | Skarn | | Amp-Px | 15.3 | 23.543 | 1049.84 | 12.38 | 16.76 | 0.038 | 1.49 | 0.118 | 2.02 | 0.075 | 0.9 | 0.93 |
| D07-369 | BX02883 | 432.4 | 434.4 | Skarn | BS083 | Amp-Px | 35 | 28.03 | 1938.04 | 13.67 | 16.22 | 0.03 | 1.46 | 0.162 | 2.39 | 0.069 | 0.19 | 0.96 |
| D07-369 | BX02884 | 434.4 | 436.7 | Skarn | | Amp-Px | 22.8 | 17.405 | 1633.41 | 14.42 | 16.28 | 0.028 | 1.52 | 0.105 | 1.35 | 0.059 | 0.06 | 1.23 |
| D07-369 | BX02885 | 436.7 | 438.8 | Skarn | BS082 | Amp-Px | 1.5 | 5.339 | 274.62 | 11.02 | 16.87 | 0.02 | 2.16 | 0.087 | 1.99 | 0.072 | 0.51 | 0.78 |
| D07-369 | BX02886 | 438.8 | 440.6 | Marble BMS | | Amp-Px | 3.6 | 5.987 | 855.62 | 7.59 | 19.88 | 0.016 | 1.73 | 0.06 | 1.14 | 0.08 | 0.43 | 0.66 |
| D07-369 | BX02887 | 440.6 | 443.2 | Skarn | | Amp-Px | 2.4 | 17.437 | 425.27 | 10.42 | 14.87 | 0.008 | 2.39 | 0.21 | 4.31 | 0.133 | 0.58 | 0.2 |
| D07-369 | BX02888 | 443.2 | 445.4 | Marble BMS | | Amp-Px | 0.05 | 0.989 | 12.92 | 4.05 | 19.96 | 0.012 | 4.65 | 0.108 | 2.2 | 0.045 | 0.81 | 0.28 |
| D07-369 | BX02889 | 445.4 | 447.9 | Skarn | | Amp-Px | 24.1 | 15.078 | 4000.1 | 8.97 | 19.43 | 0.012 | 2.17 | 0.072 | 1.12 | 0.046 | 0.09 | 0.65 |

| Table B.1 Hole ID | Sample ID | From | To | Lithology | Sample | Skarn Class | Au ppm | Ag ppm | Bi ppm | Fe % | Ca % | P % | Mg % | Ti % | Al % | Na % | K % | S % |
|---|---|---|---|---|---|---|---|---|---|---|---|---|---|---|---|---|---|---|
| D07-369 | BX02890 | 447.9 | 450.2 | Skarn | BS084 | Amp-Px | 62 | 32.792 | 4000.1 | 9.71 | 27.69 | 0.008 | 2.1 | 0.13 | 1.15 | 0.03 | 0.01 | 1.03 |
| D07-369 | BX02892 | 452.7 | 456.1 | Marble BMS | | Amp-Px | 2.2 | 1.337 | 1320.03 | 3.24 | 24.63 | 0.008 | 1.07 | 0.163 | 2.98 | 0.45 | 0.3 | 0.38 |
| D07-369 | BX02893 | 456.1 | 458.8 | Marble BMS | | Amp-Px | 0.5 | 9.44 | 265.43 | 2.68 | 22.65 | 0.007 | 1.27 | 0.177 | 3.49 | 0.793 | 0.84 | 0.32 |
| D07-369 | BX02894 | 458.8 | 460.4 | Skarn | | Ep-Px | 1.3 | 11.612 | 587.14 | 12.62 | 14.95 | 0.024 | 2.08 | 0.181 | 5.22 | 0.024 | 0.01 | 0.37 |
| D07-369 | BX02895 | 460.4 | 462.5 | QP Dike | | | 0.05 | 0.248 | 7.71 | 4.2 | 8.3 | 0.009 | 1.75 | 0.382 | 8.44 | 3.096 | 2.86 | 0.07 |
| D07-369 | BX02896 | 462.5 | 465 | Hornfels BMS | | | 0.05 | 0.175 | 2.24 | 3.39 | 2.3 | 0.007 | 2.02 | 0.312 | 9.74 | 1.869 | 3.75 | 0.2 |
| D07-369 | BX02897 | 465 | 468.6 | Hornfels BMS | | | 0.05 | 0.127 | 1.5 | 3.88 | 1.73 | 0.005 | 2.11 | 0.371 | 9.68 | 1.601 | 3.36 | 0.26 |
| D08-410 | BX04561 | 368.8 | 372.7 | Hornfels | | | 0.05 | 0.615 | 3.16 | 7.08 | 8.9 | 0.116 | 3.63 | 0.515 | 9.02 | 1.259 | 2.45 | 0.22 |
| D08-410 | BX04562 | 372.7 | 374.3 | Skarn | | Amp-Px | 0.05 | 0.27 | 0.99 | 6.7 | 17.35 | 0.067 | 2.52 | 0.21 | 5.21 | 0.228 | 0.91 | 0.21 |
| D08-410 | BX04563 | 374.3 | 375.4 | Skarn | | Amp-Px | 0.05 | 0.309 | 2.18 | 10.44 | 8.98 | 0.109 | 2.56 | 0.431 | 8.84 | 1.726 | 0.43 | 0.2 |
| D08-410 | BX04564 | 375.4 | 376.4 | Skarn | | Amp-Px | 0.1 | 0.568 | 4.92 | 15.99 | 14.51 | 0.047 | 2.26 | 0.299 | 3.82 | 0.009 | 1.01 | 4.34 |
| D08-410 | BX04565 | 376.4 | 379 | Skarn | | Amp-Px | 0.05 | 0.955 | 5.44 | 21.45 | 11.27 | 0.04 | 1.51 | 0.248 | 3.35 | 0.122 | 0.35 | 4.13 |
| D08-410 | BX04566 | 379 | 381.8 | Skarn | | Amp-Px | 0.05 | 1.301 | 5.23 | 23.99 | 12.05 | 0.04 | 1.15 | 0.246 | 3.1 | 0.184 | 0.52 | 3.63 |
| D08-410 | BX04567 | 381.8 | 383.6 | Skarn | BS090 | Amp-Px | 0.2 | 1.26 | 4.11 | 21.15 | 12.14 | 0.044 | 1.28 | 0.207 | 2.88 | 0.135 | 1.3 | 4.27 |
| D08-410 | BX04568 | 383.6 | 385.9 | Skarn | | Gar | 0.05 | 1.239 | 3.54 | 20.25 | 13.61 | 0.037 | 1.28 | 0.216 | 3.11 | 0.045 | 0.13 | 3.41 |
| D08-410 | BX04569 | 385.9 | 387.3 | Skarn | | Gar | 0.05 | 1.026 | 5.39 | 20.84 | 15.71 | 0.033 | 0.72 | 0.094 | 2.99 | 0.027 | 0.05 | 3.47 |
| D08-410 | BX04570 | 387.3 | 389.1 | Skarn | BS091 | Gar | 0.5 | 0.911 | 5.6 | 18.88 | 15.17 | 0.032 | 0.98 | 0.086 | 3.16 | 0.059 | 0.09 | 2.8 |
| D08-410 | BX04571 | 389.1 | 389.9 | Skarn | | Gar | 0.2 | 1.516 | 5.49 | 21.89 | 14.04 | 0.04 | 1.06 | 0.077 | 2.7 | 0.038 | 0.04 | 3.7 |
| D08-410 | BX04572 | 389.9 | 391 | Skarn | | Amp-Px | 0.2 | 1.002 | 23.09 | 13.34 | 15.56 | 0.017 | 1.42 | 0.054 | 2.69 | 0.008 | 0.02 | 4.51 |
| D08-410 | BX04573 | 391 | 392.8 | Skarn | | Amp-Px | 0.8 | 1.683 | 40.91 | 21.71 | 15.25 | 0.02 | 1.26 | 0.03 | 2.25 | 0.044 | 0.03 | 4.94 |
| D08-410 | BX04574 | 392.8 | 395.3 | Skarn | BS092 | Amp-Px | 46.2 | 3.563 | 1743.94 | 21.44 | 14.71 | 0.024 | 1.65 | 0.024 | 1.06 | 0.073 | 0.02 | 3.62 |
| D08-410 | BX04575 | 395.3 | 397.9 | Skarn | | Amp-Px | 8.5 | 1.805 | 401.14 | 19.72 | 15.5 | 0.016 | 1.6 | 0.029 | 1.03 | 0.067 | 0.01 | 3.41 |
| D08-410 | BX04576 | 397.9 | 399.8 | Skarn | | Amp-Px | 21.9 | 1.734 | 1108.77 | 15.36 | 18.5 | 0.012 | 1.73 | 0.021 | 1.2 | 0.052 | 0.02 | 0.64 |
| D08-410 | BX04578 | 399.8 | 401.4 | Skarn | | Amp-Px | 42.9 | 5.418 | 3062.05 | 24.53 | 12.32 | 0.021 | 2.13 | 0.019 | 0.73 | 0.063 | 0.03 | 3.6 |
| D08-410 | BX04579 | 401.4 | 403 | Skarn | | Mag | 22.5 | 2.409 | 2353.82 | 40.55 | 10.47 | 0.01 | 1.57 | 0.015 | 0.38 | 0.064 | 0.05 | 2.2 |
| D08-410 | BX04580 | 403 | 405.6 | Skarn | | Amp-Px | 18.5 | 3.881 | 2604.79 | 19.97 | 11.1 | 0.023 | 2.68 | 0.03 | 0.78 | 0.08 | 0.06 | 3.19 |

| Table B.1 / Hole ID | Sample ID | From | To | Lithology | Sample | Skarn Class | Au ppm | Ag ppm | Bi ppm | Fe % | Ca % | P % | Mg % | Ti % | Al % | Na % | K % | S % |
|---|---|---|---|---|---|---|---|---|---|---|---|---|---|---|---|---|---|---|
| D08-410 | BX04581 | 405.6 | 407.5 | Skarn | BS093 BS094 | Amp-Px | 51.1 | 15.705 | 4000.1 | 21.99 | 16.19 | 0.02 | 2.42 | 0.027 | 1.63 | 0.064 | 0.08 | 3.26 |
| D08-410 | BX04582 | 407.5 | 409 | Skarn | | Amp-Px | 9.7 | 1.368 | 1086.84 | 15.53 | 10.51 | 0.083 | 3.37 | 0.268 | 4.55 | 0.09 | 0.39 | 1.79 |
| D08-410 | BX04583 | 409 | 411.5 | Skarn | | Amp-Px | 4.8 | 1.036 | 1607.57 | 13.08 | 9.65 | 0.122 | 5.12 | 0.43 | 7 | 0.012 | 0.09 | 0.09 |
| D08-410 | BX04584 | 411.5 | 415 | Marble BMS | | | 0.5 | 0.165 | 138.61 | 2.37 | 25.07 | 0.007 | 4.78 | 0.026 | 0.75 | 0.014 | 0.09 | 0.02 |
| D08-410 | BX04585 | 415 | 416.3 | Marble BMS | | | 0.4 | 0.465 | 363.53 | 2.74 | 29.74 | 0.006 | 2.34 | 0.011 | 0.42 | 0.006 | 0.03 | 0.02 |
| D08-410 | BX04586 | 416.3 | 417.6 | Hornfels BMS | | | 0.1 | 0.116 | 34.37 | 0.74 | 2.88 | 0.001 | 0.14 | 0.003 | 0.16 | 0.007 | 0.01 | 0.02 |
| D08-413 | BX04635 | 278 | 280.8 | Hornfels BMS | | | 0.05 | 0.18 | 1.91 | 4.75 | 8.09 | 0.098 | 3.69 | 0.398 | 9.11 | 1.734 | 2.15 | 0.42 |
| D08-413 | BX04636 | 280.8 | 283.3 | Hornfels | | Ep-Px | 0.05 | 0.134 | 1.5 | 5.42 | 9.49 | 0.077 | 3.47 | 0.303 | 7.35 | 1.386 | 1.34 | 0.19 |
| D08-413 | BX04638 | 283.3 | 284.6 | Skarn | | Gar | 0.05 | 0.51 | 3.82 | 9.19 | 11.29 | 0.096 | 2.75 | 0.403 | 8.11 | 1.44 | 0.51 | 0.66 |
| D08-413 | BX04639 | 284.6 | 286.2 | Skarn | | Gar | 0.05 | 0.714 | 3.38 | 17.02 | 17.57 | 0.04 | 1.01 | 0.319 | 4.18 | 0.086 | 0.15 | 2.26 |
| D08-413 | BX04640 | 286.2 | 287.6 | Skarn | | Gar | 0.05 | 0.951 | 10.93 | 20.7 | 14.89 | 0.032 | 1.09 | 0.247 | 3.52 | 0.131 | 0.22 | 2.56 |
| D08-413 | BX04641 | 287.6 | 289.1 | Skarn | | Amp-Px | 0.05 | 0.726 | 6.26 | 17.55 | 17.38 | 0.036 | 1.02 | 0.235 | 3.6 | 0.084 | 0.12 | 2.29 |
| D08-413 | BX04642 | 289.1 | 290.4 | Skarn | | Amp-Px | 0.05 | 0.847 | 5.57 | 21.09 | 14.82 | 0.043 | 1.32 | 0.203 | 2.62 | 0.116 | 0.15 | 2.67 |
| D08-413 | BX04643 | 290.4 | 291.7 | Skarn | BS085 | Amp-Px | 0.05 | 0.929 | 6.3 | 26.11 | 12.36 | 0.036 | 1.24 | 0.197 | 2.32 | 0.115 | 0.21 | 4.45 |
| D08-413 | BX04644 | 291.7 | 294.2 | Skarn | BS016 | Amp-Px | 31.1 | 3.666 | 65.7 | 21.34 | 13.13 | 0.032 | 1.35 | 0.125 | 1.77 | 0.113 | 0.15 | 3.15 |
| D08-413 | BX04645 | 294.2 | 296.8 | Skarn | BS086 | Amp-Px | 92.4 | 8.018 | 666.7 | 16.83 | 16.67 | 0.018 | 2.15 | 0.078 | 1.57 | 0.074 | 0.05 | 1.68 |
| D08-413 | BX04646 | 296.8 | 298.7 | Skarn | | Amp-Px | 14.3 | 1.77 | 325.18 | 18.86 | 14.86 | 0.036 | 1.66 | 0.105 | 1.93 | 0.095 | 0.1 | 2.26 |
| D08-413 | BX04647 | 298.7 | 300.8 | Skarn | BS087 | Amp-Px | 68.2 | 6.069 | 1207.42 | 18.91 | 16.07 | 0.033 | 2.05 | 0.051 | 0.6 | 0.084 | 0.03 | 2.67 |
| D08-413 | BX04648 | 300.8 | 303.3 | Skarn | | Amp-Px | 117.5 | 15.651 | 4000.1 | 20.51 | 14.99 | 0.019 | 2.77 | 0.028 | 0.24 | 0.068 | 0.01 | 2.46 |
| D08-413 | BX04649 | 303.3 | 306 | Skarn | | Mag-Px | 7.8 | 3.21 | 4000.1 | 40.18 | 9.65 | 0.009 | 1.38 | 0.01 | 0.15 | 0.032 | 0.01 | 1.93 |
| D08-413 | BX04650 | 306 | 308 | Skarn | BS017 | Mag | 3.6 | 1.277 | 2448.35 | 52.05 | 6.91 | 0.011 | 0.74 | 0.013 | 0.24 | 0.045 | 0.03 | 2.02 |
| D08-413 | BX04651 | 309 | 311.5 | Skarn | BS088 | Amp-Px | 3.6 | 0.85 | 567.62 | 16.25 | 18.23 | 0.009 | 3.27 | 0.014 | 0.23 | 0.057 | 0.03 | 0.15 |
| D08-413 | BX04652 | 311.5 | 313.6 | Skarn | | Amp-Px | 1.2 | 0.131 | 66.49 | 9.75 | 11.18 | 0.004 | 6.85 | 0.012 | 0.28 | 0.057 | 0.03 | 0.05 |
| D08-413 | BX04653 | 313.6 | 316.1 | Hornfels | | Amp-Px | 0.05 | 0.066 | 31.08 | 5.74 | 13.11 | 0.007 | 9.88 | 0.028 | 0.43 | 0.049 | 0.05 | 0.02 |
| D08-413 | BX04654 | 316.1 | 317.6 | Hornfels | | Amp-Px | 0.05 | 0.076 | 4.62 | 2.75 | 17.28 | 0.005 | 7.74 | 0.057 | 0.97 | 0.024 | 0.05 | 0.02 |
| D08-413 | BX04656 | 317.6 | 319 | Hornfels | | Amp-Px | 2.3 | 0.36 | 60.6 | 7.76 | 15.53 | 0.006 | 7.22 | 0.022 | 0.26 | 0.032 | 0.06 | 0.7 |

| Table B.1 Hole ID | Sample ID | From | To | Lithology | Sample | Skarn Class | Au ppm | Ag ppm | Bi ppm | Fe % | Ca % | P % | Mg % | Ti % | Al % | Na % | K % | S % |
|---|---|---|---|---|---|---|---|---|---|---|---|---|---|---|---|---|---|---|
| D08-413 | BX04657 | 319 | 321.6 | Hornfels | | Amp-Px | 5.3 | 0.764 | 834.57 | 5.6 | 30.35 | 0.005 | 1.31 | 0.008 | 0.14 | 0.013 | 0.01 | 1.6 |
| D08-443 | BX11281 | 87 | 88.8 | Hornfels | | | 0.05 | 0.149 | 1.31 | 4.85 | 7.82 | 0.119 | 1.47 | 0.642 | 8.62 | 3.097 | 1.86 | 0.27 |
| D08-443 | BX11282 | 88.8 | 90.8 | Hornfels | | | 0.05 | 0.204 | 1.61 | 4.41 | 5.38 | 0.076 | 1.43 | 0.626 | 8.55 | 3.55 | 3.07 | 0.33 |
| D08-443 | BX11283 | 90.8 | 93.4 | Skarn | | Gar | 43.6 | 4.933 | 3207.88 | 10.12 | 19.4 | 0.066 | 1.48 | 0.484 | 5.68 | 0.13 | 0.02 | 0.09 |
| D08-443 | BX11284 | 93.4 | 95.9 | Skarn | BS078 | Gar | 53.7 | 6.602 | 2425.66 | 10.49 | 22.63 | 0.06 | 1.03 | 0.379 | 5.48 | 0.021 | 0.01 | 0.13 |
| D08-443 | BX11285 | 95.9 | 98.1 | Skarn | BS079 | Gar | 24.8 | 4.873 | 1583.99 | 13.48 | 17.89 | 0.072 | 1.62 | 0.216 | 2.98 | 0.036 | 0.01 | 0.36 |
| D08-443 | BX11287 | 101 | 103.3 | Skarn | BS077 BS089 | Gar | 0.1 | 2.98 | 25.46 | 12.82 | 18.84 | 0.051 | 0.86 | 0.171 | 3.68 | 0.03 | 0.07 | 0.4 |
| D08-443 | BX11288 | 103.3 | 104.9 | Skarn | | Gar | 0.05 | 43.23 | 157.23 | 11.23 | 15.3 | 0.05 | 1.31 | 0.193 | 4.86 | 0.028 | 0.08 | 0.16 |
| D08-443 | BX11289 | 104.9 | 106 | Skarn | | Ep-Px | 0.05 | 0.736 | 7.18 | 7.96 | 15.17 | 0.038 | 0.87 | 0.314 | 8.1 | 0.022 | 0.04 | 0.02 |
| D08-443 | BX11290 | 106 | 108.6 | Skarn | | Amp-Px | 0.05 | 0.599 | 5.11 | 5.62 | 11.56 | 0.039 | 1.04 | 0.266 | 5.64 | 0.148 | 0.72 | 0.02 |
| D08-443 | BX11291 | 108.6 | 110.1 | Skarn | | Ep-Px | 0.05 | 0.052 | 2.51 | 5.07 | 10.35 | 0.063 | 1.1 | 0.319 | 4.76 | 0.532 | 1.73 | 0.02 |
| D09-526 | BX19604 | 518 | 522 | BMS | BS039 | | 0.05 | 0.141 | 0.99 | 3.04 | 6.22 | 0.065 | 1.69 | 0.626 | 7.81 | 2.604 | 1.8 | 0.49 |
| D09-536 | BX21686 | 1164 | 1167.7 | QP Dike | | | 0.05 | 0.073 | 0.38 | 1.55 | 2.6 | 0.073 | 0.7 | 0.236 | 6.53 | 3.744 | 2.93 | 0.09 |
| D09-536 | BX21687 | 1167.7 | 1170.5 | QP Dike | | | 0.05 | 1.342 | 0.5 | 2.05 | 3.46 | 0.092 | 0.66 | 0.286 | 6.55 | 3.296 | 2.76 | 0.15 |
| D09-536 | BX21688 | 1170.5 | 1174.5 | Skarn | | Ep-Px | 0.05 | 13.507 | 5.33 | 9.75 | 13.38 | 0.093 | 1.05 | 0.281 | 8.6 | 0.1 | 0.69 | 1.13 |
| D09-536 | BX21689 | 1174.5 | 1177.5 | Skarn | | Ep-Px | 0.05 | 0.984 | 2.61 | 10.6 | 16.43 | 0.046 | 2.55 | 0.142 | 5.43 | 0.04 | 0.01 | 1.35 |
| D09-536 | BX21690 | 1177.5 | 1180 | Skarn | | Gar | 0.05 | 0.911 | 0.56 | 10.22 | 19.1 | 0.003 | 3.22 | 0.08 | 3.35 | 0.032 | 0.02 | 0.45 |
| D09-536 | BX21691 | 1180 | 1183.5 | Skarn | BS081 | Mag-px | 0.05 | 0.566 | 6.28 | 32.56 | 10.08 | 0.005 | 3.87 | 0.035 | 0.41 | 0.029 | 0.01 | 0.73 |
| D09-536 | BX21692 | 1183.5 | 1187.5 | Skarn | | Mag-Px | 0.05 | 3.143 | 1.51 | 10.44 | 16.24 | 0.006 | 5.4 | 0.034 | 1.03 | 0.032 | 0.01 | 1.41 |
| D09-536 | BX21693 | 1187.5 | 1191.7 | Skarn | | Gar | 0.05 | 4.436 | 3.41 | 20.26 | 14.02 | 0.011 | 4.89 | 0.034 | 0.8 | 0.031 | 0.01 | 2.09 |
| D09-536 | BX21694 | 1191.7 | 1195.3 | Skarn | | Gar | 0.05 | 0.376 | 2.38 | 15.67 | 20.18 | 0.01 | 1.67 | 0.146 | 4.47 | 0.021 | 0.01 | 0.51 |
| D09-536 | BX21696 | 1195.3 | 1199.3 | Skarn | | Gar | 0.7 | 0.344 | 3.83 | 10.27 | 22.66 | 0.026 | 1.16 | 0.181 | 5.24 | 0.016 | 0.01 | 0.02 |
| D09-536 | BX21697 | 1199.3 | 1203.3 | Skarn | | Gar | 0.05 | 0.548 | 1.89 | 23.43 | 18.36 | 0.031 | 1.22 | 0.144 | 3.97 | 0.025 | 0.01 | 1.7 |
| D09-536 | BX21698 | 1203.3 | 1207.3 | Skarn | | Mag-Px | 0.05 | 0.693 | 3.43 | 23.18 | 15.1 | 0.013 | 2.59 | 0.071 | 2.82 | 0.05 | 0.05 | 3.03 |
| D09-536 | BX21700 | 1207.3 | 1211.3 | Skarn | | Gar | 0.05 | 0.819 | 1.63 | 18.42 | 16.14 | 0.023 | 2.99 | 0.09 | 2.58 | 0.042 | 0.03 | 1.97 |
| D09-536 | BX21701 | 1211.3 | 1215 | Skarn | BS080 | Gar | 0.05 | 0.054 | 0.79 | 11.25 | 22.31 | 0.032 | 0.57 | 0.18 | 5.22 | 0.011 | 0.01 | 0.02 |
| D09-536 | BX21702 | 1215 | 1218.9 | Skarn | | Gar | 0.05 | 1.083 | 1.06 | 13.13 | 23.51 | 0.015 | 0.36 | 0.114 | 4.3 | 0.006 | 0.01 | 0.02 |
| D09-536 | BX21703 | 1218.9 | 1222 | Skarn | | Gar | 0.1 | 1.097 | 0.54 | 10.72 | 23.54 | 0.024 | 0.58 | 0.184 | 5.54 | 0.01 | 0.01 | 0.02 |
| D09-536 | BX21704 | 1222 | 1224.9 | Skarn | | Gar | 0.05 | 1.475 | 1.49 | 8.85 | 18.76 | 0.022 | 2.17 | 0.147 | 5.05 | 0.127 | 0.47 | 0.06 |

| Hole ID | Sample ID | From | To | Lithology | Sample | Skarn Class | Au ppm | Ag ppm | Bi ppm | Fe % | Ca % | P % | Mg % | Ti % | Al % | Na % | K % | S % |
|---|---|---|---|---|---|---|---|---|---|---|---|---|---|---|---|---|---|---|
| D09-536 | BX21705 | 1224.9 | 1228.9 | QP Dike | | Amp-Px | 0.05 | 0.073 | 0.19 | 1.83 | 3.69 | 0.093 | 0.93 | 0.31 | 6.85 | 4.077 | 2.93 | 0.02 |
| D09-536 | BX21706 | 1228.9 | 1232.7 | Quartz Porphyry Dike | | | 0.05 | 0.128 | 0.15 | 1.63 | 2.74 | 0.072 | 0.54 | 0.248 | 7.25 | 2.536 | 3.39 | 0.02 |
| D10-569 | BX24565 | 201 | 203.5 | Skarn Veins | | | 0.05 | 0.633 | 3.73 | 4.94 | 5.2 | 0.078 | 2.17 | 0.587 | 8.1 | 3.108 | 2.6 | 1.32 |
| D10-569 | BX24566 | 203.5 | 207 | Skarn Veins | BS095 BS096 | | 24.1 | 9.246 | 2247.42 | 4.65 | 9.35 | 0.062 | 1.76 | 0.545 | 7.3 | 2.101 | 1.3 | 0.14 |
| D10-569 | BX24567 | 207 | 211 | Skarn Veins | | | 0.05 | 0.91 | 19.9 | 6.34 | 12.31 | 0.08 | 1.84 | 0.812 | 7.66 | 1.095 | 0.29 | 0.08 |
| D10-595 | BX25014 | 123 | 125.4 | Skarn Veins | | | 0.05 | 0.051 | 1.95 | 3.11 | 1.24 | 0.006 | 1.72 | 0.457 | 7.82 | 2.201 | 2.77 | 0.17 |
| D10-595 | BX25015 | 125.4 | 128.8 | Skarn Veins | BS097 | | 4 | 1.027 | 1094.66 | 3.31 | 7.82 | 0.024 | 2.28 | 0.534 | 8.25 | 2.375 | 1.46 | 0.08 |
| D10-595 | BX25016 | 128.8 | 131.7 | Skarn Veins | | | 1.4 | 0.329 | 519.61 | 3.35 | 2.07 | 0.039 | 1.97 | 0.449 | 7.92 | 3.596 | 2.2 | 0.69 |
| D10-595 | BX25017 | 131.7 | 134.1 | Skarn Veins | BS098 | | 3.5 | 0.526 | 611.12 | 3.38 | 5.92 | 0.022 | 1.74 | 0.498 | 8.53 | 2.804 | 1.79 | 0.5 |
| D10-595 | BX25018 | 134.1 | 137.5 | Skarn Veins | | | 0.1 | 0.216 | 66.25 | 4.02 | 3.16 | 0.021 | 2.06 | 0.457 | 7.37 | 3.09 | 1.94 | 0.68 |

**Table B.2:** Trace element geochemical analysis of Buckhorn skarn alteration and host rocks

| Table B.2 Sample ID | Mn ppm | Cr ppm | Cu ppm | Pb ppm | Zn ppm | As ppm | Mo ppm | W ppm | V ppm | Co ppm | Ni ppm | Rb ppm | Sr ppm | Y ppm | Zr ppm | Nb ppm | Sn ppm | Cs ppm |
|---|---|---|---|---|---|---|---|---|---|---|---|---|---|---|---|---|---|---|
| BX02864 | 1572 | 99 | 449.3 | 407.15 | 116.4 | 11.3 | 4.07 | 7.8 | 214 | 25.1 | 24.4 | 58 | 348 | 15.4 | 25 | 5.06 | 1.8 | 3.2 |
| BX02865 | 1174 | 88 | 300.91 | 91.96 | 201.8 | 7.6 | 3.05 | 4.5 | 226 | 29.3 | 22.8 | 60 | 390 | 12.1 | 20.4 | 3.04 | 3.7 | 7.9 |
| BX02866 | 3789 | 51 | 1402.21 | 523.89 | 925.1 | 11.6 | 238.42 | 4.4 | 91 | 76.5 | 28.7 | 0.6 | 271 | 16.4 | 26.3 | 1.95 | 3.4 | 0.2 |
| BX02867 | 1372 | 28 | 1226.66 | 156.96 | 180.3 | 25.4 | 3.19 | 200.1 | 53 | 73.4 | 27.5 | 39.4 | 335 | 12.9 | 24.9 | 1.78 | 5 | 3.3 |
| BX02868 | 2129 | 36 | 2294.64 | 466.8 | 618.6 | 32.5 | 2.51 | 30.1 | 62 | 59 | 15.1 | 6.9 | 168 | 15.9 | 19.1 | 1.57 | 10.2 | 4 |
| BX02869 | 2651 | 43 | 1550.76 | 545.46 | 286.3 | 21 | 13.32 | 24.6 | 67 | 41.7 | 8.9 | 18.9 | 122 | 18 | 27.6 | 2.28 | 10.1 | 5.5 |
| BX02870 | 2700 | 51 | 30.9 | 33.21 | 140.5 | 22.3 | 9.43 | 2.6 | 126 | 35.4 | 9.5 | 15.3 | 352 | 14.5 | 39.3 | 4.56 | 3.2 | 4.7 |
| BX02871 | 2560 | 44 | 14.27 | 12.72 | 108.8 | 5.2 | 9.61 | 2.4 | 133 | 15.3 | 8 | 26.7 | 228 | 15.3 | 41.7 | 4.77 | 1.9 | 1.9 |
| BX02872 | 3611 | 137 | 14.76 | 14.01 | 104.4 | 11.1 | 15.49 | 5.6 | 110 | 21.6 | 12.6 | 11 | 249 | 18.5 | 36.6 | 3.95 | 4.2 | 9.4 |
| BX02873 | 2606 | 46 | 450.65 | 12.6 | 144.2 | 6.8 | 2.38 | 2 | 126 | 28.6 | 15.2 | 71.6 | 217 | 16 | 32.6 | 4.23 | 1.7 | 3.5 |
| BX02874 | 2324 | 41 | 182.73 | 9.44 | 125.1 | 11.6 | 5.31 | 2 | 133 | 31.7 | 19.8 | 75.2 | 228 | 16.7 | 32.3 | 4.72 | 2.4 | 6.1 |
| BX02875 | 2935 | 33 | 5054.48 | 700 | 460.4 | 6.8 | 44.23 | 3.7 | 117 | 68 | 22.9 | 10 | 256 | 20 | 31.4 | 3.28 | 5.2 | 18.2 |
| BX02876 | 1677 | 22 | 423.18 | 225.7 | 149.7 | 5.8 | 45.89 | 1.9 | 88 | 30.6 | 11.8 | 24.6 | 265 | 14.4 | 34.6 | 3.25 | 4.2 | 4.6 |
| BX02877 | 1665 | 30 | 1194.16 | 62.71 | 116.6 | 2.5 | 24.18 | 10 | 71 | 42.2 | 14.2 | 34 | 155 | 17.5 | 32.3 | 2.22 | 8.8 | 4.2 |
| BX02878 | 1771 | 31 | 1157.83 | 214.73 | 152.4 | 8.1 | 11.62 | 12.9 | 89 | 32 | 9.2 | 41.4 | 146 | 18.4 | 38.7 | 2.95 | 9.6 | 4.5 |
| BX02879 | 1770 | 28 | 2313.42 | 200.12 | 274.7 | 6 | 45.41 | 10.8 | 85 | 47.6 | 15.4 | 24 | 178 | 18.9 | 24.7 | 1.97 | 6.6 | 4.2 |
| BX02882 | 2031 | 46 | 2740.35 | 544.9 | 331.3 | 3.8 | 56.03 | 1.1 | 51 | 50.9 | 19.3 | 23.4 | 142 | 9.9 | 19.6 | 1.37 | 3 | 6 |
| BX02883 | 2206 | 54 | 3075.11 | 579.57 | 406.9 | 4.8 | 25.11 | 1.5 | 56 | 60.4 | 19.3 | 6.4 | 182 | 9.6 | 24.7 | 2.11 | 3.8 | 5.9 |
| BX02884 | 2000 | 43 | 2409.15 | 316.56 | 301.8 | 85.2 | 8.04 | 4.6 | 38 | 143.2 | 26.2 | 3.6 | 149 | 9.2 | 15.8 | 1.19 | 2.1 | 4.1 |
| BX02885 | 1610 | 46 | 1342.34 | 77.22 | 194.2 | 10.2 | 5.61 | 0.8 | 51 | 45.8 | 9.6 | 23.3 | 195 | 9.8 | 13.1 | 0.94 | 1.9 | 7.1 |
| BX02886 | 1797 | 32 | 684.5 | 99.35 | 110.6 | 514 | 1.34 | 143.9 | 31 | 59 | 8.7 | 25.5 | 256 | 11.6 | 13.4 | 0.69 | 1.1 | 5.8 |
| BX02887 | 1475 | 70 | 383.98 | 685.67 | 182 | 15.4 | 3.53 | 3.5 | 79 | 42.1 | 9.1 | 26.2 | 310 | 14.9 | 38.6 | 2.71 | 5.7 | 1.8 |
| BX02888 | 1225 | 17 | 139.37 | 31.46 | 66.9 | 50.4 | 4.72 | 1.3 | 37 | 16.1 | 4.2 | 55.7 | 303 | 10.6 | 17.6 | 1.34 | 0.6 | 8.7 |
| BX02889 | 1448 | 39 | 1516.93 | 124.05 | 206.7 | 67.7 | 3.69 | 94.3 | 39 | 63.7 | 9.6 | 7 | 234 | 7.3 | 13.2 | 0.93 | 1.8 | 2.6 |
| BX02890 | 1507 | 42 | 1759.12 | 295.02 | 255.2 | 65.4 | 4.68 | 200.1 | 55 | 114.8 | 17.1 | 4.9 | 236 | 9.6 | 11.1 | 0.02 | 1.8 | 1.1 |
| BX02892 | 1061 | 28 | 161.64 | 49.88 | 23.1 | 162.3 | 6.99 | 32.5 | 58 | 149.8 | 8.5 | 16.4 | 519 | 11.6 | 25.6 | 2.01 | 1.1 | 2.2 |
| BX02893 | 1195 | 29 | 55.85 | 357.23 | 52.8 | 23.9 | 3.72 | 4 | 69 | 7.7 | 13.6 | 28.5 | 389 | 13.2 | 31.5 | 2.11 | 0.7 | 2.1 |
| BX02894 | 3229 | 43 | 23.71 | 127.22 | 202.3 | 8.3 | 6 | 1.7 | 74 | 39.8 | 18 | 1.6 | 300 | 45.1 | 28 | 2.2 | 3.4 | 0.1 |
| BX02895 | 1012 | 43 | 3.06 | 10.39 | 71.5 | 2.9 | 1.3 | 4.8 | 104 | 15.8 | 14.5 | 88.9 | 381 | 29.1 | 49.4 | 3.93 | 1.2 | 1.9 |

| Table B.2 Sample ID | Mn ppm | Cr ppm | Cu ppm | Pb ppm | Zn ppm | As ppm | Mo ppm | W ppm | V ppm | Co ppm | Ni ppm | Rb ppm | Sr ppm | Y ppm | Zr ppm | Nb ppm | Sn ppm | Cs ppm |
|---|---|---|---|---|---|---|---|---|---|---|---|---|---|---|---|---|---|---|
| BX02896 | 203 | 81 | 24.13 | 14.79 | 34.2 | 45 | 4.8 | 6.7 | 123 | 32.2 | 23.3 | 134.9 | 212 | 18.8 | 6.9 | 2.96 | 1.2 | 8.7 |
| BX02897 | 134 | 54 | 50.48 | 7.7 | 30.1 | 28.9 | 1.07 | 5.8 | 117 | 18.1 | 20.8 | 152.1 | 168 | 12.8 | 11 | 3.7 | 1 | 10.2 |
| BX04561 | 1227 | 156 | 112.73 | 20.91 | 78.7 | 17.3 | 1.9 | 6.4 | 294 | 40.8 | 23.9 | 106.3 | 518 | 15.4 | 25.3 | 2.97 | 2 | 12.1 |
| BX04562 | 1787 | 69 | 136.44 | 2.9 | 58 | 56.3 | 0.64 | 9.3 | 153 | 26 | 15.3 | 44 | 435 | 12.7 | 18.7 | 1.8 | 3.7 | 8.2 |
| BX04563 | 1799 | 148 | 180.58 | 5.05 | 93.9 | 45.2 | 0.82 | 6.4 | 198 | 40.7 | 18.4 | 38.1 | 373 | 12.1 | 29.2 | 2.65 | 0.8 | 13.4 |
| BX04564 | 2442 | 103 | 613.47 | 4.67 | 92.9 | 5.7 | 0.34 | 1.3 | 157 | 94 | 31.6 | 85.3 | 348 | 15.9 | 21.9 | 2.4 | 4 | 25.6 |
| BX04565 | 1981 | 134 | 713.01 | 3.8 | 69.4 | 9.2 | 4.48 | 10.8 | 123 | 125.1 | 36.6 | 19.4 | 159 | 16.4 | 30.9 | 2.23 | 13.7 | 13.7 |
| BX04566 | 2357 | 185 | 1088.63 | 4.18 | 61.6 | 28 | 69.88 | 24.2 | 125 | 152.5 | 45.8 | 10.7 | 123 | 16.4 | 32.6 | 2.24 | 14.5 | 7.5 |
| BX04567 | 2135 | 139 | 999.65 | 2.85 | 50.2 | 13.3 | 158.98 | 6.4 | 91 | 155.8 | 42.6 | 30.7 | 136 | 12.4 | 29 | 1.88 | 10.3 | 8.3 |
| BX04568 | 2832 | 144 | 899.59 | 2.23 | 38.5 | 8.4 | 141.77 | 11.4 | 130 | 122.2 | 28.1 | 9.3 | 77 | 20.3 | 35.8 | 2.85 | 12.6 | 13.3 |
| BX04569 | 2847 | 324 | 758.95 | 3.19 | 26.3 | 36.3 | 92.68 | 200.1 | 106 | 136.8 | 27.4 | 5 | 65 | 35.1 | 17.4 | 1.88 | 19.9 | 7.8 |
| BX04570 | 2981 | 335 | 665.31 | 2.69 | 39 | 10.1 | 2.38 | 12 | 113 | 111.4 | 19.2 | 4 | 71 | 29.5 | 17.8 | 1.8 | 18.1 | 4.6 |
| BX04571 | 2822 | 252 | 1122.39 | 2.08 | 40.8 | 9.6 | 2.44 | 6.3 | 99 | 162.5 | 28.7 | 5.3 | 127 | 22.9 | 19.4 | 1.42 | 15.7 | 11.9 |
| BX04572 | 1906 | 110 | 442.58 | 2.68 | 23.3 | 9.6 | 4.69 | 5.9 | 76 | 62.5 | 7.8 | 4.2 | 412 | 22.8 | 13.2 | 1.36 | 11.1 | 6.8 |
| BX04573 | 2813 | 134 | 1027.34 | 3.1 | 44.5 | 11.9 | 2.81 | 2.6 | 57 | 227.4 | 28.4 | 2.8 | 51 | 21.7 | 6.8 | 1.12 | 8.8 | 5.7 |
| BX04574 | 2918 | 112 | 772.73 | 12.57 | 67.8 | 4.3 | 1.7 | 1.9 | 39 | 160.2 | 22.8 | 1.3 | 32 | 15.8 | 4.8 | 0.78 | 3.2 | 2.7 |
| BX04575 | 2800 | 125 | 692.01 | 8.29 | 83.6 | 12.2 | 0.31 | 10.3 | 36 | 129.6 | 24.2 | 1.2 | 34 | 19.7 | 5.2 | 1 | 3.9 | 2.7 |
| BX04576 | 3133 | 199 | 109.25 | 17.49 | 78.6 | 15.2 | 0.58 | 46.4 | 37 | 44 | 9.5 | 2.5 | 68 | 25.7 | 4.9 | 0.99 | 9.1 | 5.9 |
| BX04578 | 2494 | 140 | 369.51 | 61.69 | 72.6 | 5.8 | 0.6 | 6.8 | 47 | 64.4 | 12.4 | 3.7 | 85 | 15 | 3.8 | 0.73 | 3.2 | 3.8 |
| BX04579 | 1280 | 115 | 101.23 | 43.64 | 45.4 | 8.3 | 0.62 | 1.1 | 34 | 30.8 | 2.6 | 3 | 111 | 5.8 | 2 | 0.54 | 2.2 | 3.3 |
| BX04580 | 1961 | 77 | 216.21 | 97.28 | 73.9 | 15.9 | 1.64 | 0.9 | 54 | 50 | 7.7 | 7.4 | 151 | 20 | 5.8 | 1.01 | 1.8 | 9.4 |
| BX04581 | 2043 | 78 | 349.1 | 419.96 | 90.5 | 0.6 | 0.43 | 5.4 | 28 | 37.3 | 5.3 | 7.3 | 227 | 28.4 | 0.1 | 1.14 | 4.2 | 5.4 |
| BX04582 | 1050 | 46 | 368.42 | 17.44 | 120 | 18.5 | 1.86 | 2.7 | 65 | 53.8 | 7.2 | 35.9 | 243 | 19.3 | 21.9 | 10.76 | 1.5 | 16.2 |
| BX04583 | 1073 | 149 | 121.08 | 76.48 | 151.6 | 433.3 | 2.82 | 4.4 | 105 | 43 | 3.7 | 9 | 209 | 10.8 | 32 | 13.66 | 4.4 | 4.1 |
| BX04584 | 618 | 61 | 9.1 | 11.24 | 34.6 | 23.8 | 0.61 | 0.3 | 12 | 9.8 | 3.4 | 6.7 | 241 | 7.3 | 8.2 | 0.56 | 0.3 | 1.6 |
| BX04585 | 641 | 58 | 6.25 | 22.84 | 39.4 | 324.7 | 2.8 | 0.4 | 15 | 47 | 7.6 | 2.3 | 334 | 5.3 | 3.1 | 0.25 | 0.3 | 1 |
| BX04586 | 156 | 514 | 4.53 | 4.67 | 5.1 | 8.3 | 0.32 | 0.2 | 5 | 2.4 | 4.6 | 0.5 | 34 | 2.2 | 0.3 | 0.2 | 0.1 | 0.2 |
| BX04635 | 1188 | 211 | 75.55 | 4.16 | 62.9 | 8.3 | 0.71 | 2.1 | 239 | 18.2 | 28.2 | 94 | 378 | 15.4 | 14.4 | 2.88 | 0.6 | 7.1 |
| BX04636 | 1479 | 176 | 98.66 | 3.23 | 78 | 8.9 | 1.99 | 2.2 | 245 | 25.3 | 32.1 | 63.7 | 337 | 11.7 | 11.1 | 2.18 | 0.6 | 5.7 |

| Table B.2 Sample ID | Mn ppm | Cr ppm | Cu ppm | Pb ppm | Zn ppm | As ppm | Mo ppm | W ppm | V ppm | Co ppm | Ni ppm | Rb ppm | Sr ppm | Y ppm | Zr ppm | Nb ppm | Sn ppm | Cs ppm |
|---|---|---|---|---|---|---|---|---|---|---|---|---|---|---|---|---|---|---|
| BX04638 | 2361 | 271 | 364.98 | 7.55 | 71.4 | 17.2 | 0.97 | 1.5 | 241 | 60.9 | 27.8 | 21.9 | 459 | 16.5 | 43.5 | 3.42 | 2.1 | 2 |
| BX04639 | 5221 | 225 | 540.51 | 4.48 | 63.1 | 7.9 | 72.48 | 13.5 | 120 | 60.8 | 11.2 | 3.6 | 167 | 19.3 | 42.1 | 2.76 | 7.5 | 4.4 |
| BX04640 | 2947 | 292 | 662.62 | 5.12 | 74.9 | 24.9 | 103.35 | 46.2 | 117 | 80.6 | 14.2 | 5.1 | 146 | 23.6 | 30.3 | 2.66 | 14 | 5.9 |
| BX04641 | 3409 | 187 | 490.77 | 3.59 | 58.3 | 11.3 | 170.65 | 21.5 | 125 | 63.8 | 11.9 | 3.7 | 167 | 19.8 | 27.2 | 2.33 | 9.7 | 6.1 |
| BX04642 | 2749 | 210 | 689.16 | 3.07 | 67.9 | 15.8 | 70.62 | 21.2 | 96 | 84.6 | 13.1 | 1.8 | 130 | 16.7 | 30.4 | 2.11 | 10.8 | 1.7 |
| BX04643 | 2511 | 155 | 799.6 | 3.73 | 69.5 | 6.2 | 13.43 | 12 | 79 | 149.4 | 21.6 | 1.5 | 83 | 14.9 | 24.9 | 2.08 | 9.5 | 0.5 |
| BX04644 | 2532 | 152 | 1065.53 | 3.82 | 67.8 | 8.2 | 7.7 | 2.2 | 71 | 97.2 | 12.7 | 1.1 | 88 | 6.2 | 14.5 | 1.37 | 7.3 | 0.2 |
| BX04645 | 2864 | 168 | 487.49 | 16.91 | 64.5 | 11.8 | 0.54 | 2.5 | 53 | 69.4 | 8.1 | 0.4 | 96 | 12.3 | 11.8 | 0.94 | 4.8 | 0.2 |
| BX04646 | 2697 | 201 | 555.96 | 8.3 | 63.4 | 7.7 | 0.37 | 1.4 | 51 | 89.6 | 12.2 | 1.2 | 110 | 10.9 | 15.2 | 1.13 | 5.4 | 0.2 |
| BX04647 | 2967 | 132 | 976.21 | 26.32 | 58 | 4.3 | 0.48 | 0.9 | 42 | 93.6 | 10.8 | 0.4 | 47 | 8 | 8.8 | 0.52 | 1.9 | 0.5 |
| BX04648 | 2920 | 136 | 715.81 | 265.73 | 71.9 | 0.5 | 0.6 | 1.8 | 23 | 99.3 | 11.1 | 0.6 | 40 | 3.7 | 4.6 | 0.33 | 1.1 | 0.5 |
| BX04649 | 1219 | 141 | 292.2 | 106.71 | 34 | 645.9 | 0.31 | 8.8 | 22 | 777.3 | 8.6 | 1 | 61 | 3.8 | 0.4 | 0.17 | 1 | 1.2 |
| BX04650 | 768 | 120 | 260.1 | 16.88 | 25.4 | 807.5 | 0.24 | 1.9 | 20 | 1445.5 | 13.6 | 1.6 | 61 | 5.8 | 1.9 | 0.39 | 1.6 | 2.1 |
| BX04651 | 1975 | 82 | 24.32 | 12.63 | 48.2 | 23.1 | 0.75 | 3.1 | 11 | 30.9 | 2.5 | 1.8 | 158 | 5.8 | 5 | 0.26 | 1.2 | 2.6 |
| BX04652 | 1599 | 112 | 14.35 | 3.02 | 60.3 | 35.4 | 2.46 | 0.2 | 5 | 45.3 | 2.5 | 1.7 | 57 | 3.2 | 2.6 | 0.3 | 1.5 | 2 |
| BX04653 | 1101 | 41 | 4.31 | 2.39 | 51.8 | 4.5 | 0.75 | 0.3 | 15 | 10.7 | 3.5 | 2.6 | 64 | 4.3 | 5.6 | 0.53 | 1.5 | 0.9 |
| BX04654 | 794 | 104 | 8.36 | 7.33 | 45.4 | 2.7 | 2.22 | 1.1 | 15 | 5.5 | 5.7 | 3.1 | 153 | 5.5 | 10.3 | 1.11 | 0.7 | 1 |
| BX04656 | 1041 | 54 | 173.78 | 23.52 | 59.5 | 6.5 | 0.72 | 0.5 | 8 | 23.1 | 7.8 | 3.7 | 165 | 3 | 6.2 | 0.21 | 0.5 | 1.4 |
| BX04657 | 839 | 47 | 210.93 | 18.23 | 24.7 | 44.7 | 0.56 | 0.6 | 7 | 56.9 | 6.2 | 0.9 | 293 | 4.1 | 2.9 | 0.11 | 0.7 | 0.7 |
| BX11281 | 866 | 297 | 86.1 | 9.49 | 62.4 | 41.9 | 2.35 | 1.6 | 196 | 31.9 | 16 | 45.9 | 380 | 30.5 | 38.9 | 3.89 | 1.1 | 0.6 |
| BX11282 | 762 | 275 | 123.36 | 9.32 | 58.5 | 65.6 | 3.76 | 1.6 | 167 | 20.6 | 13.2 | 70.6 | 287 | 31.5 | 44.9 | 4.21 | 0.9 | 1.1 |
| BX11283 | 4530 | 119 | 12.64 | 76.2 | 126.4 | 859.1 | 5.41 | 1.9 | 129 | 847.8 | 19.7 | 1.2 | 231 | 23 | 41.9 | 2.97 | 3.9 | 1.3 |
| BX11284 | 4200 | 168 | 77.64 | 74.22 | 70.9 | 1669.2 | 2.15 | 2.3 | 114 | 1709.5 | 25.6 | 1.6 | 55 | 27.2 | 40.6 | 2.06 | 4.9 | 1.7 |
| BX11285 | 4692 | 57 | 9.43 | 55.43 | 214.9 | 2408.9 | 13.9 | 4.4 | 59 | 3305.4 | 45.3 | 2.1 | 156 | 19.6 | 22.2 | 1.61 | 2.4 | 3.4 |
| BX11287 | 4864 | 93 | 18.31 | 161.38 | 606.7 | 93.5 | 2.6 | 2.6 | 43 | 90.5 | 8.2 | 12.3 | 112 | 18.1 | 33.2 | 2.29 | 2.2 | 18.7 |
| BX11288 | 5311 | 33 | 12.37 | 700 | 3178.6 | 71.1 | 20.86 | 1.2 | 47 | 39.3 | 15.9 | 9.2 | 387 | 15.5 | 21.9 | 2.33 | 1.5 | 17.4 |
| BX11289 | 2738 | 108 | 2.7 | 60.42 | 144.7 | 13.2 | 2.91 | 1.2 | 82 | 13.9 | 13.7 | 1.8 | 644 | 28.2 | 31.2 | 7.09 | 1.6 | 2.3 |
| BX11290 | 2736 | 153 | 1.19 | 39.63 | 137.5 | 9.3 | 3.55 | 1.9 | 75 | 11.6 | 20 | 14.4 | 328 | 28.3 | 32.2 | 4.63 | 1.2 | 0.6 |
| BX11291 | 2544 | 221 | 1.08 | 5.95 | 92.1 | 17.1 | 0.94 | 1.5 | 92 | 9 | 25.5 | 32.5 | 268 | 24.4 | 41 | 3.26 | 1.1 | 0.5 |

| Table B.2 Sample ID | Mn ppm | Cr ppm | Cu ppm | Pb ppm | Zn ppm | As ppm | Mo ppm | W ppm | V ppm | Co ppm | Ni ppm | Rb ppm | Sr ppm | Y ppm | Zr ppm | Nb ppm | Sn ppm | Cs ppm |
|---|---|---|---|---|---|---|---|---|---|---|---|---|---|---|---|---|---|---|
| BX19604 | 408 | 47 | 59.45 | 8.3 | 37.3 | 52.7 | 2.1 | 2.1 | 162 | 16.5 | 7.2 | 40 | 374 | 24.1 | 38.9 | 3.75 | 0.8 | 0.7 |
| BX21686 | 202 | 33 | 23.07 | 7.9 | 14.8 | 2.7 | 1.34 | 1 | 53 | 4.8 | 3.1 | 89.1 | 439 | 10.3 | 25 | 13.64 | 1.4 | 3.1 |
| BX21687 | 294 | 45 | 586.57 | 6.83 | 22.2 | 3.5 | 2.07 | 1.7 | 75 | 4.2 | 3.9 | 83.8 | 366 | 12.2 | 34.1 | 12.11 | 1.6 | 3.1 |
| BX21688 | 866 | 41 | 6420.05 | 11.16 | 137.9 | 22.4 | 12.7 | 2 | 72 | 41.8 | 31.6 | 42.1 | 1046 | 16.4 | 29.2 | 11.57 | 8.2 | 2.5 |
| BX21689 | 1684 | 43 | 474.57 | 5.98 | 60.1 | 22.8 | 1.26 | 5.4 | 46 | 15.3 | 6.9 | 0.9 | 640 | 8.1 | 20.7 | 5.71 | 5.4 | 0.3 |
| BX21690 | 3186 | 43 | 431.34 | 2.62 | 59.9 | 8.1 | 1.16 | 2.5 | 46 | 7.3 | 3.6 | 0.6 | 46 | 8.4 | 20.4 | 2.52 | 2.8 | 0.3 |
| BX21691 | 1371 | 21 | 205.77 | 5.19 | 70.4 | 5.1 | 1.28 | 2.5 | 34 | 28 | 10.2 | 0.8 | 20 | 1.3 | 2.5 | 0.31 | 0.8 | 0.6 |
| BX21692 | 2209 | 20 | 1348.73 | 35.58 | 141.9 | 5 | 3.59 | 2.5 | 16 | 27.3 | 8.3 | 0.6 | 27 | 2.4 | 6.8 | 0.7 | 1 | 0.6 |
| BX21693 | 1869 | 22 | 1915.28 | 10.93 | 163.2 | 4.4 | 17.67 | 0.9 | 29 | 31.4 | 10.1 | 0.7 | 26 | 1.5 | 5.9 | 0.5 | 0.9 | 0.8 |
| BX21694 | 3776 | 54 | 138.95 | 5.89 | 30.5 | 5.2 | 2.25 | 9.5 | 74 | 14.9 | 4.5 | 0.6 | 82 | 14.1 | 31.7 | 4.15 | 4.4 | 0.5 |
| BX21696 | 4265 | 75 | 12.74 | 5.79 | 23 | 6 | 4.88 | 4.6 | 67 | 5.4 | 2.3 | 0.6 | 60 | 19.8 | 43.6 | 5.78 | 4.6 | 0.8 |
| BX21697 | 3532 | 56 | 311.32 | 5.51 | 32.4 | 9.7 | 2.94 | 9.6 | 60 | 11.7 | 6.2 | 1 | 48 | 15.4 | 33.5 | 4.8 | 4.5 | 0.9 |
| BX21698 | 2697 | 33 | 494.81 | 4.84 | 41.9 | 6.2 | 0.87 | 0.8 | 47 | 18.7 | 7.9 | 1.1 | 34 | 7.7 | 15.8 | 2.08 | 1.8 | 0.6 |
| BX21700 | 2684 | 34 | 485.02 | 3.53 | 47.1 | 5 | 1.58 | 1 | 46 | 17.6 | 6.7 | 0.8 | 28 | 8.7 | 19.7 | 2.29 | 1.4 | 0.6 |
| BX21701 | 4100 | 61 | 20.25 | 6.62 | 10.2 | 5.9 | 2.92 | 10.5 | 74 | 3.1 | 3.8 | 0.1 | 51 | 24.8 | 43.1 | 5.13 | 8.1 | 0.1 |
| BX21702 | 4031 | 82 | 589.46 | 3.1 | 49.9 | 7.7 | 3.04 | 31.4 | 53 | 6.8 | 4 | 0.05 | 32 | 23.8 | 37.1 | 4.25 | 13.3 | 0.1 |
| BX21703 | 4701 | 58 | 484.13 | 14.25 | 36.4 | 5.6 | 2.02 | 3.3 | 64 | 6.4 | 5.8 | 0.1 | 33 | 30.3 | 60.8 | 5.59 | 6.1 | 0.2 |
| BX21704 | 3492 | 51 | 557.95 | 18.25 | 65.2 | 4 | 6.19 | 7.8 | 59 | 9.8 | 6.7 | 19.2 | 218 | 15.7 | 30.4 | 5.11 | 3.7 | 0.6 |
| BX21705 | 368 | 31 | 4.97 | 13.35 | 17.2 | 3.5 | 2.56 | 1.4 | 78 | 5.1 | 3.8 | 92.2 | 286 | 12.7 | 41.9 | 14.27 | 1.5 | 3.3 |
| BX21706 | 212 | 41 | 12.39 | 12.12 | 15.6 | 3.1 | 1.41 | 2.6 | 53 | 3.4 | 2.9 | 138 | 262 | 10.2 | 24 | 14.78 | 1.3 | 3.5 |
| BX24565 | 410 | 60 | 282.65 | 12.21 | 37.1 | 53 | 2.95 | 1.4 | 177 | 28.7 | 15.7 | 64.3 | 294 | 22.6 | 30.6 | 3.31 | 0.6 | 1.2 |
| BX24566 | 906 | 46 | 84.18 | 195.05 | 70.7 | 683 | 33.81 | 1.5 | 158 | 575.8 | 13.7 | 30.6 | 350 | 17.4 | 44.2 | 2.98 | 1.6 | 0.4 |
| BX24567 | 1566 | 95 | 58.73 | 43.68 | 60.1 | 170.6 | 49.42 | 1.6 | 228 | 57 | 28.6 | 7.2 | 412 | 22.2 | 60.2 | 5.01 | 2.6 | 0.2 |
| BX25014 | 163 | 80 | 24.33 | 2.94 | 26.8 | 78.3 | 1.46 | 3.3 | 137 | 12.1 | 14.4 | 102.7 | 169 | 24.1 | 7.7 | 4.8 | 1.1 | 8.3 |
| BX25015 | 619 | 147 | 17.37 | 6.22 | 29.5 | 122.8 | 2.96 | 2.2 | 174 | 16.6 | 54.4 | 52.9 | 537 | 76.7 | 57.9 | 3.79 | 1 | 4.2 |
| BX25016 | 206 | 49 | 71.68 | 11.39 | 25.2 | 43.7 | 1.9 | 1.8 | 135 | 16.8 | 12.6 | 86.6 | 275 | 48.9 | 31.4 | 3.52 | 0.1 | 11 |
| BX25017 | 380 | 74 | 75.94 | 7.98 | 21 | 19.8 | 31.94 | 3.3 | 123 | 12.7 | 17.9 | 49 | 442 | 22.4 | 44.1 | 4.09 | 0.7 | 1.8 |
| BX25018 | 261 | 48 | 105.26 | 3.87 | 27.7 | 540.1 | 2.15 | 2.2 | 99 | 33.4 | 10.1 | 62.2 | 284 | 24.8 | 17.4 | 5.18 | 0.6 | 10.2 |

**Table B.3:** Trace element geochemical analysis of Buckhorn skarn alteration and host rocks (Part 2)

| Table B.3 Sample ID | Ba ppm | Th ppm | U ppm | Ga ppm | Hf ppm | Cd ppm | Sb ppm | Be ppm | Sc ppm | Li ppm | Ta ppm |
|---|---|---|---|---|---|---|---|---|---|---|---|
| BX02864 | 626 | 1.8 | 1.5 | 13.01 | 0.81 | 0.69 | 10.38 | 0.5 | 22 | 21 | 0.3 |
| BX02865 | 1201 | 1.5 | 1.3 | 15.01 | 0.69 | 2.51 | 5.29 | 1 | 25 | 29.2 | 0.1 |
| BX02866 | 11 | 0.6 | 3.4 | 12.48 | 0.79 | 16.6 | 4.48 | 0.5 | 7.4 | 9.8 | 0.1 |
| BX02867 | 220 | 0.5 | 2.8 | 12.94 | 0.63 | 2.06 | 3.08 | 0.5 | 6.7 | 7 | 0.05 |
| BX02868 | 148 | 0.4 | 2.7 | 12.01 | 0.61 | 9.06 | 3.1 | 0.5 | 4.8 | 5 | 0.05 |
| BX02869 | 327 | 0.8 | 3.1 | 12.73 | 0.82 | 4.05 | 3.22 | 0.5 | 6.3 | 5 | 0.1 |
| BX02870 | 450 | 1.7 | 2.3 | 16.01 | 1.38 | 0.19 | 6 | 1 | 14.4 | 4.8 | 0.2 |
| BX02871 | 574 | 2 | 1.8 | 13.52 | 1.39 | 0.11 | 4.06 | 1 | 16.9 | 4.7 | 0.2 |
| BX02872 | 171 | 1.7 | 2.3 | 15.99 | 1.21 | 0.13 | 5.15 | 0.5 | 11.6 | 5 | 0.2 |
| BX02873 | 1619 | 2.1 | 1.2 | 14.14 | 1.11 | 1.04 | 5.04 | 0.5 | 13.7 | 6.2 | 0.2 |
| BX02874 | 1525 | 2.3 | 1.3 | 15.46 | 1.11 | 0.5 | 5.39 | 0.5 | 14.9 | 7.3 | 0.2 |
| BX02875 | 185 | 1.3 | 7.8 | 19.72 | 0.97 | 9.46 | 5.19 | 0.5 | 12.2 | 9.7 | 0.2 |
| BX02876 | 584 | 1.2 | 3.6 | 15.18 | 1.07 | 1.25 | 4.28 | 0.5 | 9.7 | 11.1 | 0.2 |
| BX02877 | 190 | 0.7 | 2.3 | 16.12 | 0.99 | 1.78 | 4.4 | 0.5 | 5.7 | 4.8 | 0.1 |
| BX02878 | 663 | 0.9 | 2.4 | 19.43 | 1.05 | 2.31 | 2.22 | 0.5 | 8.5 | 4.5 | 0.1 |
| BX02879 | 431 | 0.5 | 2.5 | 13.53 | 0.72 | 3.94 | 4.75 | 0.5 | 6.9 | 5.5 | 0.05 |
| BX02882 | 503 | 0.4 | 1.8 | 8.67 | 0.53 | 5.65 | 3.98 | 0.5 | 4.2 | 7.5 | 0.05 |
| BX02883 | 163 | 0.7 | 1.9 | 10.43 | 0.71 | 6.38 | 4.6 | 0.5 | 5.3 | 6.9 | 0.1 |
| BX02884 | 85 | 0.3 | 1.6 | 6.19 | 0.44 | 4.56 | 5 | 0.5 | 4.2 | 7.4 | 0.05 |
| BX02885 | 423 | 0.3 | 1.5 | 8.95 | 0.35 | 2.2 | 3.05 | 0.5 | 4 | 13.8 | 0.05 |
| BX02886 | 218 | 0.3 | 1.9 | 5.35 | 0.38 | 1.11 | 4.1 | 0.5 | 2.9 | 10.1 | 0.05 |
| BX02887 | 642 | 1.5 | 6.2 | 15.66 | 1.03 | 1.33 | 3.58 | 0.5 | 11 | 12.2 | 0.1 |
| BX02888 | 106 | 0.7 | 3 | 5.64 | 0.54 | 0.33 | 1.35 | 0.5 | 5.8 | 19.2 | 0.05 |
| BX02889 | 93 | 0.6 | 1.8 | 7.7 | 0.37 | 3.44 | 4.89 | 0.5 | 3.8 | 8.1 | 0.05 |
| BX02890 | 0.5 | 1.5 | 2.1 | 6.46 | 0.4 | 4 | 5.25 | 0.5 | 4.7 | 6.2 | 0.05 |
| BX02892 | 152 | 1.6 | 3.8 | 6.04 | 0.82 | 0.31 | 6.23 | 0.5 | 9 | 6.8 | 0.05 |
| BX02893 | 503 | 1.5 | 4.2 | 6.77 | 0.83 | 0.39 | 1.42 | 0.5 | 10 | 6.4 | 0.1 |
| BX02894 | 3 | 1.3 | 3.8 | 22.62 | 0.88 | 0.39 | 3.58 | 0.5 | 9.9 | 4.3 | 0.1 |
| BX02895 | 5056 | 3 | 0.8 | 9.96 | 1.4 | 0.1 | 1.4 | 1 | 22.7 | 6.5 | 0.2 |

| Table B.3 Sample ID | Ba ppm | Th ppm | U ppm | Ga ppm | Hf ppm | Cd ppm | Sb ppm | Be ppm | Sc ppm | Li ppm | Ta ppm |
|---|---|---|---|---|---|---|---|---|---|---|---|
| BX02896 | 1476 | 2.4 | 0.2 | 17.43 | 0.25 | 0.05 | 1 | 0.5 | 25.9 | 38.5 | 0.2 |
| BX02897 | 1133 | 2.2 | 0.3 | 18.08 | 0.29 | 0.03 | 0.71 | 1 | 24.6 | 43 | 0.2 |
| BX04561 | 1293 | 1.4 | 0.9 | 16.5 | 0.71 | 0.24 | 3.9 | 0.5 | 37.1 | 34.7 | 0.1 |
| BX04562 | 390 | 0.9 | 0.6 | 11.72 | 0.58 | 0.23 | 1.13 | 1 | 17.2 | 52.9 | 0.05 |
| BX04563 | 70 | 1.3 | 1.9 | 16.95 | 0.82 | 0.14 | 2 | 0.5 | 24.8 | 56 | 0.1 |
| BX04564 | 76 | 1.3 | 2 | 15.11 | 0.59 | 0.32 | 1.14 | 0.5 | 12.4 | 26.7 | 0.1 |
| BX04565 | 109 | 0.7 | 2.7 | 17.57 | 0.88 | 0.15 | 2.7 | 0.5 | 9.6 | 14.3 | 0.05 |
| BX04566 | 86 | 0.6 | 3.1 | 15.32 | 0.92 | 0.17 | 1.95 | 0.5 | 9.4 | 10.6 | 0.05 |
| BX04567 | 37 | 0.7 | 2.5 | 13.17 | 0.85 | 0.13 | 2.5 | 0.5 | 9.1 | 11.3 | 0.05 |
| BX04568 | 115 | 0.5 | 2.3 | 13.41 | 1.27 | 0.22 | 1.4 | 0.5 | 6.8 | 9.4 | 0.2 |
| BX04569 | 53 | 0.3 | 4.3 | 14.23 | 0.46 | 0.22 | 1.05 | 0.5 | 2.5 | 5.5 | 0.05 |
| BX04570 | 41 | 0.4 | 1.6 | 14.45 | 0.45 | 0.21 | 2.45 | 0.5 | 2.5 | 6.7 | 0.05 |
| BX04571 | 45 | 0.2 | 1.1 | 13.07 | 0.41 | 0.25 | 1.33 | 0.5 | 2.8 | 12.7 | 0.05 |
| BX04572 | 59 | 0.3 | 0.8 | 14.7 | 0.31 | 0.18 | 5.08 | 1 | 2 | 66.8 | 0.05 |
| BX04573 | 42 | 0.1 | 0.6 | 12.13 | 0.15 | 0.33 | 1.49 | 0.5 | 0.3 | 7.8 | 0.05 |
| BX04574 | 22 | 0.05 | 0.7 | 7.5 | 0.16 | 0.31 | 3.04 | 0.5 | 1.7 | 7.4 | 0.05 |
| BX04575 | 18 | 0.05 | 0.8 | 7.5 | 0.11 | 0.48 | 2.62 | 0.5 | 0.8 | 6.6 | 0.05 |
| BX04576 | 77 | 0.05 | 1.4 | 9.53 | 0.15 | 0.16 | 3.83 | 0.5 | 0.7 | 11.9 | 0.05 |
| BX04578 | 50 | 0.1 | 1.1 | 11.57 | 0.07 | 0.37 | 5.88 | 0.5 | 1 | 10.5 | 0.05 |
| BX04579 | 25 | 0.05 | 0.6 | 24.37 | 0.07 | 0.15 | 6.06 | 1 | 0.4 | 7.5 | 0.05 |
| BX04580 | 105 | 0.05 | 1.1 | 10.67 | 0.16 | 0.31 | 13.57 | 0.5 | 1.4 | 17.4 | 0.05 |
| BX04581 | 60 | 0.05 | 1.3 | 15.78 | 0.01 | 0.61 | 17.89 | 0.5 | 0.05 | 10.8 | 0.05 |
| BX04582 | 96 | 8.9 | 42.3 | 29.24 | 0.84 | 0.42 | 46.32 | 0.5 | 8.9 | 18.6 | 0.7 |
| BX04583 | 34 | 14.5 | 17.7 | 37.19 | 0.96 | 0.36 | 15.99 | 0.5 | 8.3 | 34.2 | 0.9 |
| BX04584 | 38 | 0.3 | 1.2 | 1.95 | 0.22 | 0.4 | 2.73 | 0.5 | 0.9 | 11.4 | 0.05 |
| BX04585 | 13 | 0.3 | 3 | 1.74 | 0.09 | 0.43 | 4.37 | 0.5 | 0.5 | 8.7 | 0.05 |
| BX04586 | 5 | 0.2 | 0.2 | 0.62 | 0.01 | 0.09 | 1.53 | 0.5 | 0.5 | 5.7 | 0.05 |
| BX04635 | 767 | 1.3 | 0.5 | 15.58 | 0.46 | 0.15 | 1.45 | 0.5 | 26.3 | 47.5 | 0.1 |
| BX04636 | 639 | 1 | 0.5 | 12.47 | 0.43 | 0.16 | 1.67 | 0.5 | 23.9 | 49.7 | 0.05 |

| Table B.3 Sample ID | Ba ppm | Th ppm | U ppm | Ga ppm | Hf ppm | Cd ppm | Sb ppm | Be ppm | Sc ppm | Li ppm | Ta ppm |
|---|---|---|---|---|---|---|---|---|---|---|---|
| BX04638 | 411 | 1.7 | 1.3 | 15.29 | 0.95 | 0.25 | 5.9 | 0.5 | 27.2 | 18.6 | 0.2 |
| BX04639 | 38 | 0.8 | 2.1 | 12.6 | 1.32 | 0.25 | 3.93 | 0.5 | 12.8 | 4.6 | 0.1 |
| BX04640 | 60 | 0.6 | 3.2 | 15.46 | 0.94 | 0.35 | 3.96 | 0.5 | 10.1 | 5.9 | 0.05 |
| BX04641 | 41 | 0.6 | 2.5 | 15.29 | 0.86 | 0.24 | 5.74 | 0.5 | 10.3 | 4.8 | 0.1 |
| BX04642 | 31 | 0.7 | 2.4 | 14.79 | 0.88 | 0.2 | 9.41 | 0.5 | 9.3 | 5.4 | 0.1 |
| BX04643 | 30 | 0.5 | 2.8 | 13.03 | 0.89 | 0.19 | 4.74 | 0.5 | 7.8 | 4.5 | 0.05 |
| BX04644 | 17 | 0.3 | 1.4 | 13.68 | 0.49 | 0.17 | 4.44 | 0.5 | 5.1 | 3.5 | 0.05 |
| BX04645 | 7 | 0.3 | 1 | 9.72 | 0.36 | 0.21 | 8.9 | 0.5 | 2.5 | 3.3 | 0.05 |
| BX04646 | 15 | 0.5 | 1.2 | 11.33 | 0.51 | 0.14 | 6.77 | 0.5 | 4.7 | 2.7 | 0.05 |
| BX04647 | 5 | 0.2 | 0.9 | 6.02 | 0.27 | 0.28 | 6.32 | 0.5 | 2.2 | 3.8 | 0.05 |
| BX04648 | 4 | 0.1 | 0.7 | 4.66 | 0.18 | 0.3 | 6.08 | 0.5 | 1.4 | 5.1 | 0.05 |
| BX04649 | 12 | 0.1 | 0.2 | 21.21 | 0.01 | 0.21 | 4.03 | 0.5 | 0.4 | 5 | 0.05 |
| BX04650 | 22 | 0.05 | 0.4 | 31.47 | 0.07 | 0.16 | 3.56 | 1 | 0.4 | 3.2 | 0.05 |
| BX04651 | 17 | 0.1 | 0.4 | 7.75 | 0.09 | 0.25 | 3.67 | 1 | 0.5 | 5.6 | 0.05 |
| BX04652 | 11 | 0.1 | 0.6 | 3.61 | 0.06 | 0.22 | 3.48 | 0.5 | 0.2 | 5.5 | 0.05 |
| BX04653 | 4 | 0.2 | 2.4 | 3.4 | 0.17 | 0.25 | 2.53 | 1 | 0.6 | 2.9 | 0.05 |
| BX04654 | 8 | 0.2 | 3.3 | 3.05 | 0.26 | 0.29 | 1.54 | 0.5 | 1 | 5.1 | 0.05 |
| BX04656 | 20 | 0.1 | 1.1 | 3.76 | 0.06 | 0.45 | 3.98 | 0.5 | 0.3 | 2.7 | 0.05 |
| BX04657 | 9 | 0.05 | 0.7 | 1.93 | 0.06 | 0.24 | 6.22 | 0.5 | 0.4 | 2.8 | 0.05 |
| BX11281 | 985 | 1.3 | 0.7 | 15.93 | 1.39 | 0.16 | 2.69 | 0.5 | 26.7 | 4.8 | 0.2 |
| BX11282 | 1389 | 1.6 | 1.1 | 15.64 | 1.55 | 0.11 | 1.79 | 0.5 | 27.4 | 5.1 | 0.2 |
| BX11283 | 23 | 1.7 | 3.3 | 12.2 | 1.64 | 0.28 | 7.68 | 0.5 | 22.7 | 6.5 | 0.1 |
| BX11284 | 15 | 0.8 | 1.8 | 11.88 | 1.36 | 0.35 | 3.02 | 0.5 | 16.7 | 6.8 | 0.1 |
| BX11285 | 20 | 0.6 | 1.7 | 8.99 | 0.74 | 0.2 | 4.98 | 0.5 | 9.9 | 6.5 | 0.05 |
| BX11287 | 42 | 0.9 | 1.5 | 9.16 | 0.99 | 7.63 | 4.74 | 0.5 | 7.4 | 5.7 | 0.1 |
| BX11288 | 69 | 1.2 | 2.1 | 12.61 | 0.99 | 37.18 | 9.44 | 0.5 | 8.4 | 7.6 | 0.1 |
| BX11289 | 33 | 1.8 | 1.5 | 19.53 | 1.14 | 1.31 | 7.91 | 0.5 | 15.8 | 11.1 | 0.4 |
| BX11290 | 374 | 1.3 | 1.5 | 13.88 | 1.27 | 0.47 | 6.98 | 0.5 | 13 | 11.1 | 0.2 |
| BX11291 | 811 | 1.6 | 1.9 | 9.47 | 1.42 | 0.12 | 8.3 | 0.5 | 14.3 | 4.8 | 0.1 |

| Table B.3 Sample ID | Ba ppm | Th ppm | U ppm | Ga ppm | Hf ppm | Cd ppm | Sb ppm | Be ppm | Sc ppm | Li ppm | Ta ppm |
|---|---|---|---|---|---|---|---|---|---|---|---|
| BX19604 | 831 | 1.2 | 0.4 | 17.59 | 1.45 | 0.22 | 2.92 | 0.5 | 23.1 | 3.6 | 0.2 |
| BX21686 | 841 | 5.7 | 2.2 | 18.82 | 1.08 | 0.04 | 1.26 | 2 | 5.7 | 10.9 | 0.8 |
| BX21687 | 788 | 5.9 | 2.2 | 18.49 | 1.05 | 0.18 | 1.06 | 2 | 7.2 | 10.6 | 0.6 |
| BX21688 | 205 | 8.4 | 13.9 | 39.76 | 1 | 3.38 | 39.67 | 0.5 | 8.9 | 8.5 | 0.6 |
| BX21689 | 4 | 3.9 | 8.3 | 27.08 | 0.72 | 0.61 | 23.14 | 0.5 | 4.2 | 3.6 | 0.3 |
| BX21690 | 3 | 0.2 | 1 | 10.52 | 0.45 | 0.56 | 1.95 | 0.5 | 1.5 | 2.1 | 0.05 |
| BX21691 | 3 | 0.05 | 0.1 | 8.23 | 0.03 | 0.25 | 1.15 | 0.5 | 0.4 | 1.9 | 0.05 |
| BX21692 | 2 | 0.1 | 0.2 | 4.66 | 0.14 | 2.12 | 1.11 | 1 | 0.9 | 2.8 | 0.05 |
| BX21693 | 2 | 0.05 | 0.2 | 5.33 | 0.11 | 2.94 | 1.54 | 0.5 | 0.8 | 2.6 | 0.05 |
| BX21694 | 3 | 0.3 | 2.1 | 13.13 | 0.68 | 0.24 | 2.4 | 0.5 | 2.4 | 1.9 | 0.2 |
| BX21696 | 3 | 0.5 | 3.1 | 15.28 | 0.98 | 0.15 | 1.58 | 0.5 | 3.3 | 2.6 | 0.3 |
| BX21697 | 3 | 0.4 | 2.3 | 14.38 | 0.84 | 0.18 | 2.15 | 0.5 | 3 | 2.2 | 0.2 |
| BX21698 | 3 | 0.2 | 0.6 | 10.28 | 0.28 | 0.1 | 1.37 | 0.5 | 1.6 | 2.3 | 0.05 |
| BX21700 | 2 | 0.2 | 0.5 | 9.09 | 0.4 | 0.3 | 1.4 | 0.5 | 1.5 | 2.1 | 0.05 |
| BX21701 | 1 | 0.4 | 4.2 | 14.89 | 0.97 | 0.11 | 1.94 | 0.5 | 3.5 | 1.3 | 0.2 |
| BX21702 | 2 | 0.3 | 4.4 | 13.95 | 0.79 | 0.99 | 1.33 | 0.5 | 2.2 | 1.6 | 0.2 |
| BX21703 | 2 | 0.4 | 3.4 | 14.72 | 1.54 | 0.84 | 0.86 | 0.5 | 3.7 | 2.3 | 0.3 |
| BX21704 | 200 | 1.4 | 2 | 11.79 | 0.75 | 0.91 | 2.32 | 0.5 | 3.1 | 3.9 | 0.2 |
| BX21705 | 816 | 6.1 | 2 | 18.26 | 1.37 | 0.03 | 1.27 | 2 | 7.7 | 8.5 | 0.7 |
| BX21706 | 972 | 5.6 | 2.2 | 19.44 | 1.05 | 0.07 | 0.43 | 2 | 5.7 | 12 | 0.8 |
| BX24565 | 254 | 1.2 | 0.4 | 15.48 | 1.03 | 0.17 | 2.37 | 0.5 | 24.4 | 6 | 0.2 |
| BX24566 | 617 | 1.4 | 2.5 | 15.29 | 1.44 | 0.55 | 5.98 | 0.5 | 22.2 | 4.5 | 0.1 |
| BX24567 | 129 | 1.3 | 2.4 | 16.88 | 1.82 | 0.16 | 7.86 | 0.5 | 33.7 | 5.2 | 0.2 |
| BX25014 | 699 | 2 | 0.5 | 18.03 | 0.22 | 0.02 | 0.69 | 1 | 22.6 | 50.6 | 0.2 |
| BX25015 | 635 | 1.1 | 1.9 | 15.58 | 1.66 | 0.06 | 3.06 | 1 | 24.3 | 9.7 | 0.2 |
| BX25016 | 604 | 1.2 | 2.3 | 16.83 | 0.84 | 0.05 | 7.45 | 1 | 19.2 | 38.9 | 0.2 |
| BX25017 | 796 | 1.3 | 1.4 | 16.33 | 1.53 | 0.06 | 1.96 | 1 | 20.4 | 10.5 | 0.2 |
| BX25018 | 445 | 1.3 | 0.6 | 16.96 | 0.5 | 0.06 | 1.37 | 1 | 17.1 | 29.7 | 0.3 |

**Table B.4:** Rare earth element geochemical analysis of Buckhorn skarn alteration and host rocks

Table B.4

| Sample ID | La ppm | Ce ppm | Pr ppm | Nd ppm | Sm ppm | Eu ppm | Gd ppm | Tb ppm | Dy ppm | Ho ppm | Er ppm | Tm ppm | Yb ppm | Lu ppm | Total HREE |
|---|---|---|---|---|---|---|---|---|---|---|---|---|---|---|---|
| BX02864 | 8 | 17.26 | 2.3 | 9.1 | 2.5 | 0.6 | 3.2 | 0.5 | 3.3 | 0.6 | 1.7 | 0.2 | 1.7 | 0.2 | 11.4 |
| BX02865 | 11.6 | 21.58 | 2.8 | 10.4 | 2.4 | 0.6 | 2.6 | 0.4 | 2.4 | 0.5 | 1.2 | 0.2 | 1.3 | 0.2 | 8.8 |
| BX02866 | 8.7 | 15.79 | 2.3 | 10.3 | 2.4 | 1.5 | 2.8 | 0.4 | 2.5 | 0.4 | 1.4 | 0.2 | 1.4 | 0.2 | 9.3 |
| BX02867 | 2.3 | 4.97 | 0.8 | 3.5 | 1.2 | 0.5 | 1.6 | 0.2 | 1.7 | 0.3 | 1 | 0.1 | 1.1 | 0.2 | 6.2 |
| BX02868 | 1.3 | 2.73 | 0.6 | 2.6 | 1.1 | 0.8 | 1.8 | 0.3 | 2.2 | 0.4 | 1.3 | 0.2 | 1.4 | 0.2 | 7.8 |
| BX02869 | 6 | 10.75 | 1.5 | 6.4 | 1.9 | 1 | 2.4 | 0.4 | 2.3 | 0.5 | 1.6 | 0.2 | 1.6 | 0.2 | 9.2 |
| BX02870 | 8.4 | 18.91 | 2.8 | 10.3 | 2.8 | 0.7 | 2.7 | 0.4 | 2.7 | 0.5 | 1.3 | 0.2 | 1.3 | 0.2 | 9.3 |
| BX02871 | 7.8 | 17.3 | 2.5 | 9.8 | 2.5 | 0.6 | 2.7 | 0.4 | 3.1 | 0.5 | 1.5 | 0.2 | 1.5 | 0.2 | 10.1 |
| BX02872 | 11.7 | 22.09 | 2.8 | 10.2 | 2.5 | 0.7 | 2.9 | 0.4 | 3.1 | 0.6 | 1.8 | 0.2 | 1.8 | 0.3 | 11.1 |
| BX02873 | 6.3 | 14.52 | 2.1 | 8.5 | 2.4 | 0.4 | 3 | 0.4 | 3 | 0.5 | 1.7 | 0.2 | 1.8 | 0.2 | 10.8 |
| BX02874 | 7.1 | 16.99 | 2.4 | 10 | 2.6 | 0.5 | 3.2 | 0.4 | 3.1 | 0.6 | 1.7 | 0.2 | 1.9 | 0.3 | 11.4 |
| BX02875 | 11.1 | 20.35 | 2.7 | 10.6 | 2.7 | 1.4 | 3 | 0.4 | 3.2 | 0.6 | 1.7 | 0.2 | 1.9 | 0.3 | 11.3 |
| BX02876 | 8.8 | 15.11 | 2.2 | 8.4 | 2 | 0.7 | 1.9 | 0.3 | 2.4 | 0.5 | 1.3 | 0.2 | 1.3 | 0.2 | 8.1 |
| BX02877 | 1.9 | 3.55 | 0.6 | 2.9 | 1.2 | 0.7 | 2 | 0.4 | 2.3 | 0.6 | 1.6 | 0.2 | 1.6 | 0.2 | 8.9 |
| BX02878 | 3.6 | 7.52 | 1.2 | 5.5 | 1.8 | 0.8 | 2.4 | 0.4 | 2.8 | 0.5 | 1.6 | 0.2 | 1.7 | 0.3 | 9.9 |
| BX02879 | 2.3 | 4.84 | 0.8 | 3.7 | 1.5 | 0.7 | 2.4 | 0.4 | 2.6 | 0.6 | 1.6 | 0.2 | 1.6 | 0.2 | 9.6 |
| BX02882 | 0.8 | 1.7 | 0.3 | 1.3 | 0.6 | 0.2 | 0.7 | 0.1 | 1.1 | 0.2 | 0.8 | 0.05 | 0.9 | 0.1 | 3.95 |
| BX02883 | 1 | 2.28 | 0.4 | 1.5 | 0.6 | 0.3 | 0.9 | 0.2 | 1.2 | 0.3 | 0.8 | 0.05 | 0.8 | 0.1 | 4.35 |
| BX02884 | 1 | 2.46 | 0.4 | 1.6 | 0.6 | 0.3 | 0.9 | 0.1 | 1.1 | 0.2 | 0.7 | 0.1 | 0.8 | 0.1 | 4 |
| BX02885 | 0.6 | 1.28 | 0.3 | 0.9 | 0.5 | 0.3 | 0.8 | 0.1 | 1.2 | 0.2 | 0.7 | 0.1 | 0.8 | 0.1 | 4 |
| BX02886 | 2.2 | 2.28 | 0.3 | 1.9 | 0.5 | 0.5 | 1.2 | 0.2 | 1.7 | 0.3 | 0.9 | 0.1 | 0.9 | 0.1 | 5.4 |
| BX02887 | 8.9 | 14.83 | 2 | 8.1 | 1.7 | 1 | 2.7 | 0.3 | 2 | 0.4 | 1.2 | 0.2 | 1.3 | 0.2 | 8.3 |
| BX02888 | 4.4 | 7.17 | 1.5 | 4.4 | 0.9 | 0.4 | 1.1 | 0.2 | 1.4 | 0.3 | 1 | 0.1 | 1 | 0.1 | 5.2 |
| BX02889 | 3.9 | 4.28 | 0.5 | 2.9 | 0.6 | 0.4 | 0.8 | 0.1 | 0.7 | 0.2 | 0.6 | 0.05 | 0.6 | 0.1 | 3.15 |
| BX02890 | 0.3 | 4.13 | 0.2 | 1.1 | 0.6 | 0.1 | 1.8 | 0.1 | 0.9 | 0.2 | 0.8 | 0.05 | 0.5 | 0.1 | 4.45 |
| BX02892 | 7.9 | 13.39 | 2.2 | 8.7 | 1.7 | 0.5 | 1.7 | 0.3 | 1.7 | 0.4 | 1.1 | 0.1 | 1 | 0.1 | 6.4 |
| BX02893 | 9.7 | 17.62 | 2.7 | 11.1 | 2.1 | 0.6 | 2.3 | 0.4 | 2.4 | 0.5 | 1.3 | 0.2 | 1.2 | 0.2 | 8.5 |
| BX02894 | 12.5 | 19.95 | 2.8 | 12.6 | 3 | 1.2 | 4.1 | 0.7 | 4.8 | 1.1 | 3 | 0.4 | 2.7 | 0.4 | 17.2 |

Table B.4

| Sample ID | La ppm | Ce ppm | Pr ppm | Nd ppm | Sm ppm | Eu ppm | Gd ppm | Tb ppm | Dy ppm | Ho ppm | Er ppm | Tm ppm | Yb ppm | Lu ppm | Total HREE |
|---|---|---|---|---|---|---|---|---|---|---|---|---|---|---|---|
| BX02895 | 14 | 25.54 | 3.8 | 17.5 | 3.8 | 0.3 | 7.1 | 0.8 | 5.3 | 1 | 3.1 | 0.4 | 2.8 | 0.4 | 20.9 |
| BX02896 | 14.9 | 31.73 | 5 | 22.6 | 4.5 | 1 | 5.2 | 0.7 | 3.9 | 0.8 | 1.8 | 0.2 | 1.5 | 0.2 | 14.3 |
| BX02897 | 10.5 | 21.03 | 3.1 | 14.2 | 3.2 | 0.9 | 4.2 | 0.5 | 3.1 | 0.5 | 1.3 | 0.2 | 1.1 | 0.2 | 11.1 |
| BX04561 | 7.5 | 15.3 | 2 | 9.9 | 2.5 | 0.8 | 3.5 | 0.4 | 3.2 | 0.6 | 1.5 | 0.2 | 1.5 | 0.2 | 11.1 |
| BX04562 | 5.3 | 9.66 | 1.4 | 5.7 | 1.2 | 0.4 | 2 | 0.3 | 2.3 | 0.5 | 1.4 | 0.2 | 1.2 | 0.2 | 8.1 |
| BX04563 | 14.1 | 22.21 | 2.5 | 9.6 | 1.9 | 0.9 | 2.4 | 0.3 | 2.3 | 0.4 | 1.1 | 0.1 | 1 | 0.2 | 7.8 |
| BX04564 | 23.8 | 32.63 | 3.5 | 12.7 | 2.4 | 1.1 | 2.5 | 0.4 | 2.6 | 0.5 | 1.7 | 0.2 | 1.6 | 0.2 | 9.7 |
| BX04565 | 1.8 | 3.85 | 0.7 | 3.3 | 1.3 | 0.6 | 1.8 | 0.3 | 2.5 | 0.6 | 1.6 | 0.2 | 1.9 | 0.3 | 9.2 |
| BX04566 | 1.5 | 3.66 | 0.6 | 3.6 | 1 | 0.7 | 1.7 | 0.3 | 2.5 | 0.6 | 1.7 | 0.2 | 1.8 | 0.3 | 9.1 |
| BX04567 | 1.6 | 3.48 | 0.6 | 3 | 1 | 0.4 | 1.4 | 0.2 | 2 | 0.5 | 1.3 | 0.2 | 1.1 | 0.2 | 6.9 |
| BX04568 | 1.7 | 2.72 | 0.5 | 1.9 | 0.9 | 0.7 | 2 | 0.4 | 3.1 | 0.7 | 2.2 | 0.3 | 2.1 | 0.4 | 11.2 |
| BX04569 | 1.3 | 1.97 | 0.5 | 2.6 | 1 | 1.3 | 2.4 | 0.5 | 3.8 | 0.9 | 3.4 | 0.4 | 3.2 | 0.5 | 15.1 |
| BX04570 | 1.4 | 1.64 | 0.2 | 1.6 | 1.1 | 0.9 | 2.1 | 0.4 | 3.2 | 0.9 | 2.7 | 0.4 | 2.6 | 0.4 | 12.7 |
| BX04571 | 0.6 | 0.65 | 0.4 | 0.8 | 0.5 | 0.6 | 1.4 | 0.3 | 2.5 | 0.7 | 2.1 | 0.3 | 2.2 | 0.4 | 9.9 |
| BX04572 | 1.9 | 1.88 | 0.3 | 1.1 | 0.6 | 0.5 | 1.6 | 0.3 | 2.6 | 0.6 | 2.3 | 0.3 | 2.3 | 0.3 | 10.3 |
| BX04573 | 0.3 | 0.24 | | 0.3 | 0.4 | 0.4 | 1.2 | 0.2 | 2.2 | 0.6 | 2.2 | 0.3 | 2.4 | 0.3 | 9.4 |
| BX04574 | | 0.27 | | 0.2 | 0.2 | 0.2 | 0.8 | 0.1 | 1.5 | 0.4 | 1.8 | 0.2 | 1.8 | 0.3 | 6.9 |
| BX04575 | | 0.24 | | 0.2 | 0.2 | 0.2 | 0.8 | 0.2 | 2 | 0.5 | 2.2 | 0.2 | 1.9 | 0.3 | 8.1 |
| BX04576 | 0.2 | 0.37 | | 0.5 | 0.3 | 0.5 | 1.1 | 0.2 | 2.1 | 0.6 | 1.8 | 0.2 | 1.3 | 0.2 | 7.5 |
| BX04578 | 0.6 | 0.94 | 0.2 | 0.7 | 0.3 | 0.2 | 0.6 | 0.1 | 1.1 | 0.3 | 0.9 | 0.1 | 0.7 | 0.1 | 3.9 |
| BX04579 | 0.4 | 0.78 | | 0.4 | | 0.1 | 0.3 | | 0.4 | 0.1 | 0.3 | 0.05 | 0.3 | | 1.45 |
| BX04580 | 0.5 | 0.43 | | 0.4 | 0.2 | 0.1 | 0.6 | 0.1 | 1.2 | 0.3 | 1 | 0.1 | 0.8 | | 4.1 |
| BX04581 | | 1.73 | | 0.2 | 0.5 | 0.4 | 1.6 | 0.1 | 1.2 | 0.7 | 1.6 | 0.1 | 1.3 | 0.2 | 6.8 |
| BX04582 | 43.3 | 67.37 | 7.9 | 32.6 | 5.4 | 3.1 | 4.4 | 0.5 | 3.2 | 0.5 | 1.3 | 0.1 | 1 | 0.1 | 11.1 |
| BX04583 | 17 | 29.14 | 3.2 | 12.4 | 2.1 | 1.5 | 2.1 | 0.3 | 1.6 | 0.3 | 0.9 | 0.1 | 0.9 | 0.2 | 6.4 |
| BX04584 | 2.3 | 2.8 | 0.5 | 1.8 | 0.4 | | 0.5 | | 0.3 | 0.1 | 0.3 | 0.05 | 0.3 | | 1.55 |
| BX04585 | 1.8 | 2.79 | 0.4 | 1.4 | 0.3 | 0.3 | 0.3 | | 0.4 | | 0.2 | 0.05 | 0.3 | | 1.25 |
| BX04586 | 1.1 | 2.19 | 0.3 | 1.3 | 0.2 | | 0.2 | | 0.2 | | 0.1 | 0.05 | | | 0.55 |
| BX04635 | 5.4 | 13.09 | 1.8 | 8.3 | 2.1 | 0.9 | 2.7 | 0.4 | 2.4 | 0.5 | 1.4 | 0.2 | 1.1 | 0.2 | 8.9 |

Table B.4

| Sample ID | La ppm | Ce ppm | Pr ppm | Nd ppm | Sm ppm | Eu ppm | Gd ppm | Tb ppm | Dy ppm | Ho ppm | Er ppm | Tm ppm | Yb ppm | Lu ppm | Total HREE |
|---|---|---|---|---|---|---|---|---|---|---|---|---|---|---|---|
| BX04636 | 5.3 | 12.26 | 1.7 | 7.5 | 1.7 | 0.6 | 1.6 | 0.3 | 1.7 | 0.4 | 1.2 | 0.1 | 1.1 | 0.1 | 6.5 |
| BX04638 | 27.1 | 42.13 | 4.3 | 14.9 | 3 | 1.2 | 2.8 | 0.4 | 2.8 | 0.5 | 1.5 | 0.2 | 1.4 | 0.2 | 9.8 |
| BX04639 | 3.8 | 8.65 | 1.5 | 8.7 | 2.4 | 2.1 | 2.3 | 0.4 | 2.6 | 0.6 | 2.1 | 0.2 | 1.6 | 0.3 | 10.1 |
| BX04640 | 2.5 | 5.15 | 0.9 | 4.9 | 1.3 | 1 | 2.1 | 0.4 | 2.7 | 0.7 | 2.3 | 0.3 | 2.4 | 0.4 | 11.3 |
| BX04641 | 2.3 | 4.57 | 0.8 | 3.9 | 1.2 | 0.9 | 2 | 0.3 | 3.2 | 0.7 | 2.5 | 0.3 | 2.6 | 0.4 | 12 |
| BX04642 | 1.2 | 2.79 | 0.5 | 2.8 | 1 | 0.6 | 1.6 | 0.2 | 2.1 | 0.5 | 1.9 | 0.2 | 1.8 | 0.2 | 8.5 |
| BX04643 | 0.7 | 1.97 | 0.4 | 2.2 | 0.9 | 0.5 | 1.8 | 0.3 | 2 | 0.5 | 1.8 | 0.2 | 1.9 | 0.2 | 8.7 |
| BX04644 | 0.4 | 1.33 | 0.2 | 1.1 | 0.4 | 0.2 | 0.6 | 0.1 | 1 | 0.2 | 0.7 | 0.05 | 0.7 | 0.1 | 3.45 |
| BX04645 | 0.5 | 1.09 | 0.2 | 0.9 | 0.3 | 0.3 | 0.7 | 0.1 | 1.2 | 0.3 | 0.9 | 0.1 | 1 | 0.2 | 4.5 |
| BX04646 | 0.8 | 1.88 | 0.3 | 1.2 | 0.3 | 0.3 | 0.7 | 0.2 | 0.8 | 0.3 | 0.8 | 0.1 | 0.7 | 0.2 | 3.8 |
| BX04647 | 0.4 | 0.56 | 0.1 | 0.4 | 0.2 | 0.1 | 0.3 |  | 0.5 | 0.2 | 0.5 | 0.05 | 0.6 |  | 2.15 |
| BX04648 | 0.5 | 1.03 |  | 0.4 | 0.1 |  | 0.2 |  | 0.4 |  | 0.3 | 0.05 | 0.3 |  | 1.25 |
| BX04649 | 0.4 | 0.82 |  | 0.3 |  | 0.1 | 0.1 |  | 0.3 |  | 0.3 | 0.05 | 0.2 |  | 0.95 |
| BX04650 | 0.2 | 0.44 |  | 0.2 |  |  | 0.2 |  | 0.4 | 0.1 | 0.4 | 0.05 | 0.2 |  | 1.35 |
| BX04651 | 0.6 | 0.65 | 0.2 | 0.7 |  | 0.1 | 0.2 |  | 0.3 |  | 0.2 | 0.05 | 0.2 |  | 0.95 |
| BX04652 | 0.2 | 0.28 |  | 0.2 |  |  | 0.2 |  |  |  | 0.1 | 0.05 | 0.1 |  | 0.45 |
| BX04653 | 0.6 | 1.06 | 0.1 | 0.5 | 0.2 |  | 0.3 |  | 0.2 |  | 0.3 | 0.05 | 0.2 |  | 1.05 |
| BX04654 | 1.2 | 2.27 | 0.4 | 1.8 | 0.4 | 0.1 | 0.5 |  | 0.4 |  | 0.2 | 0.05 | 0.3 |  | 1.45 |
| BX04656 | 0.5 | 0.67 | 0.1 | 0.5 |  |  | 0.2 |  | 0.2 |  | 0.1 | 0.05 | 0.1 |  | 0.65 |
| BX04657 | 0.5 | 0.69 | 0.1 | 0.7 | 0.1 | 0.1 | 0.3 |  | 0.2 |  | 0.1 | 0.05 | 0.2 |  | 0.85 |
| BX11281 | 7.9 | 23.24 | 3.4 | 16.2 | 4.2 | 1.1 | 4.6 | 0.8 | 4.9 | 1 | 2.6 | 0.4 | 2.4 | 0.4 | 17.1 |
| BX11282 | 7.7 | 22.59 | 3.5 | 16.9 | 4.3 | 0.8 | 5.1 | 0.9 | 5.2 | 1 | 3 | 0.4 | 2.9 | 0.4 | 18.9 |
| BX11283 | 26.1 | 41.75 | 5 | 18.8 | 3.3 | 1.5 | 4.1 | 0.6 | 3.7 | 0.7 | 2.3 | 0.3 | 2.1 | 0.3 | 14.1 |
| BX11284 | 6.1 | 10.86 | 1.8 | 9.2 | 2.8 | 1.6 | 3.7 | 0.6 | 3.6 | 0.8 | 2.2 | 0.3 | 2 | 0.3 | 13.5 |
| BX11285 | 3.5 | 7.65 | 1.3 | 6.9 | 2.1 | 1.2 | 2.5 | 0.4 | 2.6 | 0.5 | 1.4 | 0.2 | 1.3 | 0.2 | 9.1 |
| BX11287 | 4.5 | 7.96 | 1.2 | 6 | 1.6 | 0.7 | 2.1 | 0.4 | 2.3 | 0.5 | 1.5 | 0.2 | 1.3 | 0.2 | 8.5 |
| BX11288 | 5 | 11.23 | 1.8 | 9 | 1.7 | 0.5 | 2 | 0.3 | 2 | 0.4 | 1.2 | 0.2 | 1.3 | 0.2 | 7.6 |
| BX11289 | 5.3 | 13.64 | 2.2 | 11.8 | 2.9 | 0.4 | 4 | 0.6 | 4.2 | 0.9 | 2.5 | 0.3 | 2.2 | 0.4 | 15.1 |
| BX11290 | 4.5 | 12.15 | 2.1 | 10.5 | 2.8 | 0.3 | 3.4 | 0.7 | 4.1 | 0.8 | 2.4 | 0.4 | 2.8 | 0.4 | 15 |

| Sample ID | La ppm | Ce ppm | Pr ppm | Nd ppm | Sm ppm | Eu ppm | Gd ppm | Tb ppm | Dy ppm | Ho ppm | Er ppm | Tm ppm | Yb ppm | Lu ppm | Total HREE |
|---|---|---|---|---|---|---|---|---|---|---|---|---|---|---|---|
| BX11291 | 8.4 | 17.46 | 2.7 | 14.1 | 3 | 0.5 | 4 | 0.6 | 3.9 | 0.8 | 2.4 | 0.3 | 2.2 | 0.3 | 14.5 |
| BX19604 | 7.8 | 22.14 | 3.1 | 16.7 | 3.9 | 1.2 | 4.6 | 0.8 | 4.8 | 1 | 2.8 | 0.4 | 2.5 | 0.4 | 17.3 |
| BX21686 | 17 | 36.15 | 4.1 | 17.2 | 2.8 | 0.8 | 2.7 | 0.4 | 2.3 | 0.4 | 1.2 | 0.2 | 1.1 | 0.2 | 8.5 |
| BX21687 | 18 | 37.65 | 4.3 | 17.4 | 3.3 | 0.8 | 3 | 0.5 | 2.9 | 0.5 | 1.4 | 0.2 | 1.4 | 0.2 | 10.1 |
| BX21688 | 35.6 | 64.34 | 6.9 | 27.1 | 4.2 | 2.6 | 4 | 0.6 | 3.5 | 0.6 | 1.7 | 0.2 | 1.4 | 0.2 | 12.2 |
| BX21689 | 18.7 | 32.25 | 3.4 | 13 | 2.2 | 1.4 | 2 | 0.3 | 1.7 | 0.3 | 0.7 | 0.1 | 0.7 | | 5.8 |
| BX21690 | 0.2 | 1.11 | 0.4 | 4.7 | 1.6 | 0.7 | 1.6 | 0.2 | 1.3 | 0.2 | 0.6 | 0.05 | 0.5 | 0.1 | 4.55 |
| BX21691 | | 0.33 | | 0.5 | 0.1 | | 0.2 | | 0.2 | | | 0.05 | 0.1 | | 0.55 |
| BX21692 | 0.5 | 0.62 | 0.2 | 1.6 | 0.5 | 0.2 | 0.5 | | 0.4 | | 0.2 | 0.05 | 0.1 | | 1.25 |
| BX21693 | 0.1 | 0.49 | 0.1 | 1 | 0.3 | 0.1 | 0.3 | | 0.2 | | | 0.05 | | | 0.55 |
| BX21694 | 0.1 | 1.09 | 0.5 | 5.6 | 2.5 | 1 | 2.8 | 0.4 | 2.3 | 0.4 | 1.1 | 0.1 | 0.9 | 0.1 | 8.1 |
| BX21696 | 0.2 | 1.58 | 0.7 | 8 | 3 | 1.3 | 3.6 | 0.5 | 3.2 | 0.6 | 1.5 | 0.2 | 1.4 | 0.2 | 11.2 |
| BX21697 | 0.3 | 1.22 | 0.5 | 5.5 | 2.7 | 1.1 | 2.8 | 0.4 | 2.2 | 0.4 | 1.1 | 0.1 | 1 | 0.1 | 8.1 |
| BX21698 | | 0.55 | 0.2 | 2.8 | 1.2 | 0.5 | 1.6 | 0.2 | 1.2 | 0.2 | 0.5 | 0.05 | 0.5 | | 4.25 |
| BX21700 | 0.1 | 0.52 | 0.3 | 2.6 | 1.1 | 0.4 | 1.3 | 0.2 | 1.2 | 0.2 | 0.6 | 0.05 | 0.6 | | 4.15 |
| BX21701 | 0.4 | 2.15 | 0.7 | 8.4 | 3.4 | 2.1 | 4.3 | 0.6 | 4.1 | 0.8 | 2.1 | 0.3 | 1.9 | 0.3 | 14.4 |
| BX21702 | 0.5 | 2.69 | 0.8 | 8.4 | 3.2 | 2.6 | 4.3 | 0.6 | 3.5 | 0.7 | 1.9 | 0.3 | 1.9 | 0.3 | 13.5 |
| BX21703 | 0.3 | 1.74 | 0.6 | 8.1 | 3.5 | 2.1 | 4.6 | 0.7 | 4.6 | 0.9 | 2.5 | 0.3 | 2.5 | 0.4 | 16.5 |
| BX21704 | 2.3 | 6.11 | 1.1 | 7.6 | 2.6 | 1.1 | 2.6 | 0.4 | 2.4 | 0.4 | 1.3 | 0.2 | 1.2 | 0.2 | 8.7 |
| BX21705 | 17.3 | 38.29 | 4.2 | 18.4 | 3.1 | 0.7 | 3 | 0.5 | 2.8 | 0.6 | 1.5 | 0.2 | 1.5 | 0.2 | 10.3 |
| BX21706 | 15.4 | 34.27 | 4 | 17.5 | 3.2 | 0.7 | 3 | 0.4 | 2.5 | 0.4 | 1.3 | 0.2 | 1.2 | 0.2 | 9.2 |
| BX24565 | 6.4 | 19.08 | 2.8 | 14.3 | 3.5 | 0.9 | 4.2 | 0.6 | 4.6 | 0.8 | 2.5 | 0.3 | 2.2 | 0.3 | 15.5 |
| BX24566 | 6.2 | 15.67 | 2.3 | 11.5 | 2.6 | 0.7 | 3.3 | 0.6 | 3.7 | 0.7 | 2.2 | 0.3 | 1.9 | 0.2 | 12.9 |
| BX24567 | 18.9 | 31.99 | 3.9 | 17.4 | 3.7 | 1.2 | 4 | 0.6 | 4.5 | 0.9 | 2.7 | 0.3 | 2.3 | 0.3 | 15.6 |
| BX25014 | 13.2 | 28.44 | 3.6 | 17.2 | 3.5 | 0.8 | 4.2 | 0.6 | 4.9 | 1 | 2.6 | 0.3 | 1.9 | 0.2 | 15.7 |
| BX25015 | 9.5 | 22.23 | 4.3 | 23.9 | 6.6 | 1.3 | 9.1 | 1.5 | 10.6 | 2.3 | 7.1 | 0.8 | 6 | 0.8 | 38.2 |
| BX25016 | 13 | 30.42 | 5.4 | 29.5 | 6.6 | 1.6 | 9.5 | 1.4 | 9.4 | 1.9 | 5.6 | 0.6 | 4.6 | 0.7 | 33.7 |
| BX25017 | 6.6 | 19.86 | 3.4 | 17.5 | 4 | 1.1 | 4.6 | 0.7 | 4.3 | 1 | 2.7 | 0.3 | 2.1 | 0.3 | 16 |
| BX25018 | 8 | 22.16 | 3.3 | 16.6 | 4 | 1.2 | 4.9 | 0.8 | 6 | 1.2 | 3.6 | 0.4 | 3 | 0.3 | 20.2 |